

Performance of IPS Earth Retention System in Soft Clay

연약지반에 적용된 IPS 흠막이 시스템의 거동 특성

Kim, Nak-Kyung ¹	김 낙 경	Park, Jong-Sik ²	박 중 식
Oh, Hee-Jin ³	오 희 진	Han, Man-Yop ⁴	한 만 엽
Kim, Moon-Young ⁵	김 문 영	Kim, Sung-Bo ⁶	김 성 보

요 지

본 연구에서는 도심지 연약 지반에 적용된 IPS(Innovative Prestressed Support) 흠막이 시스템의 거동을 파악하고 안정성을 확인하였다. 새로운 IPS 흠막이 시스템은 강선의 인장 저항을 이용하여 띠장의 강성을 획기적으로 증가시켜 버팀보의 설치 간격을 대폭 증가시키는 공법이다. IPS 흠막이 시스템이 적용된 현장은 부산 북부 지역 내에 위치한 폭 28.8m, 길이 52.0m 그리고 굴착 깊이 16.1m 규모의 굴착 현장으로서 느슨한 매립토와 연약 점토로 이루어져 있으며 두께 650mm의 지중 연속벽, 5 단의 IPS 시스템과 중앙 스트럿으로 지지되어 있다. 시공이 진행되는 동안에 경사계 6 곳, 지하 수위계 4 곳, IPS 띠장에 설치된 변위계 30 곳, 스트럿에 설치된 변형율계 20 곳에서 현장 데이터를 계측 수집하였다. 연약 지반에 적용된 IPS 흠막이 공법은 성공적으로 수행되었다. IPS 흠막이 공법의 시공을 통하여 공법의 적용성을 확인하였으며 현장 계측 결과를 분석하고 예비 설계 내용과 비교하여 연약 지반에서의 IPS 흠막이 공법의 거동을 확인하고 안정성을 평가하였다.

Abstract

The performance of innovative prestressed support (IPS) earth retention system applied in soft clay was investigated and presented. The IPS wale system provides a high flexural stiffness to resist the bending by lateral earth pressure, and transfers lateral earth pressure to strut supports. The IPS wale system provides a larger spacing of support than conventional braced and anchored systems. The IPS earth retention system was selected for temporary earth support in a building construction in North Busan area. The excavation was made 28.8 m wide, 52.0 m long, and 16.1 m deep through loose fill to soft clay. The IPS system consists of 650 mm thick slurry walls, and five levels of IPS wales and struts. Field monitoring data were collected including wall deflections at six locations, ground water levels at four locations, IPS wale deflections at thirty locations, and axial loads on struts at twenty locations, during construction. The IPS earth retention system applied in soft clay performed successfully within a designed criterion. Field measurements were compared with design assumptions of the IPS earth retention system. The applicability and stability of the IPS earth retention system in soft clay were investigated and evaluated.

Keywords : Clayey soil, IPS earth retention system, Stability, Urban excavation

1 Member, Associate Prof., Dept. of Civil and Environmental Engrg., Sungkyunkwan Univ., nkkim@skku.edu, Corresponding Author

2 Member, Senior Researcher, Dept. of Geotechnical Engrg. Research, Korea Institute of Construction Tech.

3 Graduate Student, Dept. of Civil and Environmental Engrg., Sungkyunkwan Univ.

4 Prof., Dept. of Civil Engrg., Ajou Univ.

5 Prof., Dept. of Civil and Environmental Engrg., Sungkyunkwan Univ.

6 Associate Prof., Dept. of Civil Engrg., Chungbuk Univ.

1. Introduction

Innovative prestressed support (IPS) earth retention systems, which were developed as an alternative method to strut supports and anchored supports, have been applied in various excavations, for examples water lines, buildings in urban area, subway stations, and bridge piers. The basic mechanism and design method of the IPS earth retention system were proposed by Han et al. (2003), Kim et al. (2004), and Kim et al. (2005). In order to investigate a stability of IPS earth retention system, a pilot test of the IPS system was performed in a trench excavation for water lines (Kim et al. 2004) and a field monitoring of the IPS earth retention system was performed in an urban excavation site with multi-layered ground conditions (Kim et al. 2005).

The IPS earth retention system was applied in soft clay in North Busan. The excavation was 28.8 m in width, 52.0 m in length, and 16.1 m in depth. The IPS system consisted of slurry wall, thirty IPS wales, forty corner struts, and six center struts. As can be seen in Photo 1, the IPS earth retention system in soft clay performed successfully, providing larger workspace than conventional support systems.

This paper summarizes the field performance of the IPS earth retention system applied in soft clay. A field monitoring was conducted during excavation. The field performance data were collected and analyzed in order to evaluate the stability of the IPS earth retention system, and were compared with the design predictions.



Photo 1. IPS earth retention system applied in soft clay

2. IPS Earth Retention System in Soft Clay

2.1 Site Location

This project is the construction of an official building, which consists of 10 stories of super-structure and four levels of basement on pile groups. A plan view of site locations is shown in Fig. 1. The site was surrounded by the roads, 15 m wide to the north, 15 m wide to the east, and 30 m wide to the south. The eight storied building is located in the vicinity of the west side of the excavation. The Nak-Dong River is located 650 m west away from the site and flows to the south.

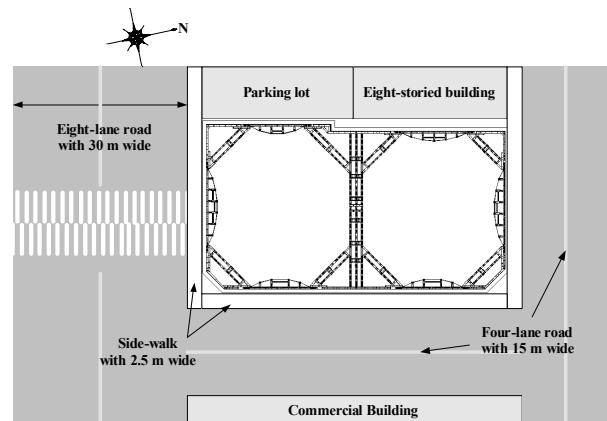


Fig. 1. Plan view of site locations

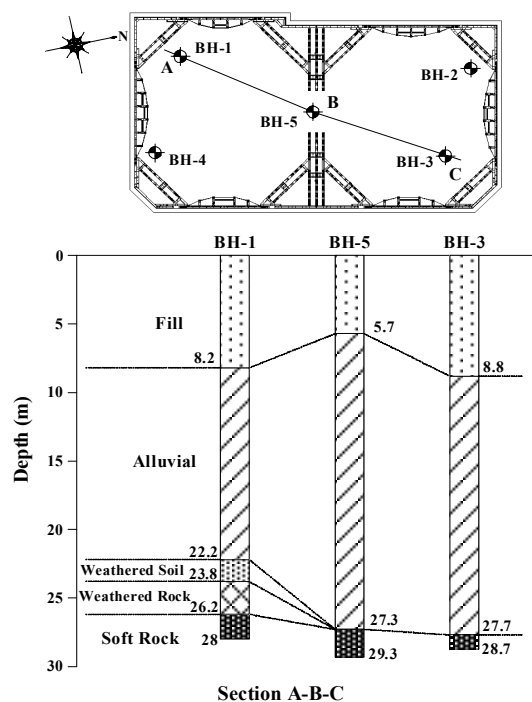


Fig. 2. Boring locations and soil profile distribution

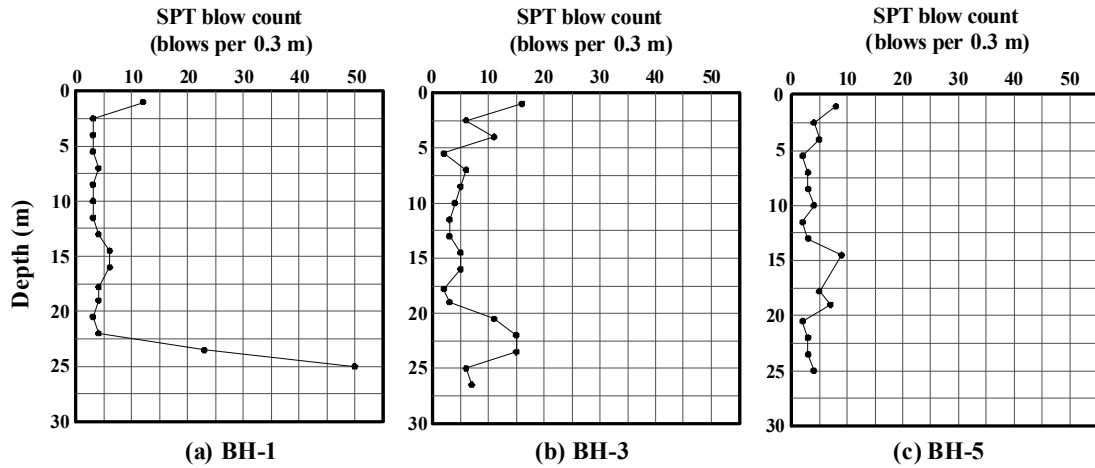


Fig. 3. Standard penetration test profile

2.2 Subsurface Conditions

The plan of borings, the soil profiles, and the standard penetration test profiles in the site were shown in Fig. 2 and Fig. 3. Five borings were drilled to identify the subsurface soil profile of the site. The subsurface soil consists of fill, silty clay, and soft rock. Fill is a composite of gravel, silty clay, and clayey sand. Dark gray silty clay with a shell underlies fill. Soft rock has gray brown color and is moderately weathered. Fill has SPT values ranging from 3 to 10. The silty clay has N values ranging from 2 to 7. Soft rock record N values less than 50 blows/50 mm. Soft rock is located at a depth of about 27.0 m below the street surface. The total unit weight of the clay is 18 kN/m^3 . The undrained shear strength of the clay is very variable, and generally ranges from 7 to 67 kPa. The sensitivity of the clay is within the range of between 1.9 and 4.3. The ground water existed at 8.25 m from the ground surface.

2.3 IPS Earth Retention System

A plan view and typical section of the excavation are shown in Figs. 4 and 5, respectively. The excavation was 28.8 m wide, 52.0 m long and 16.1 m deep. A 650 mm-thick slurry wall was used to support the retained ground and the depth of the wall was 29.0 m. The wall was internally braced with five levels of IPS wales, corner struts, and center struts.

The IPS wale consists of wale, legs to support, steel wires, and hydraulic jacks as shown in Fig. 6. Details of the IPS wale are tabulated in Table 1. Corner struts consist of two H-beams and one steel plate. Beams with $H300 \times 300 \times 10 \times 15$ (mm) were used at the first level. Beams with $H350 \times 350 \times 12 \times 19$ (mm) were used to each

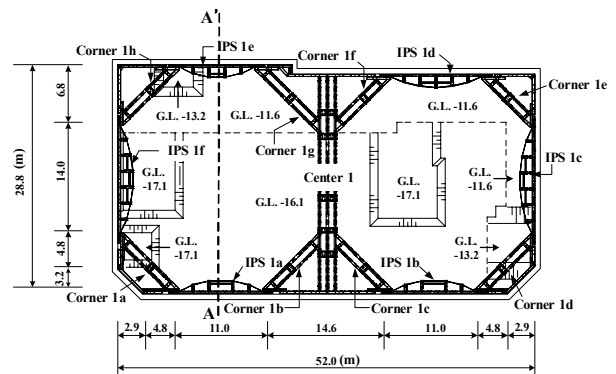


Fig. 4. Plan view of excavation

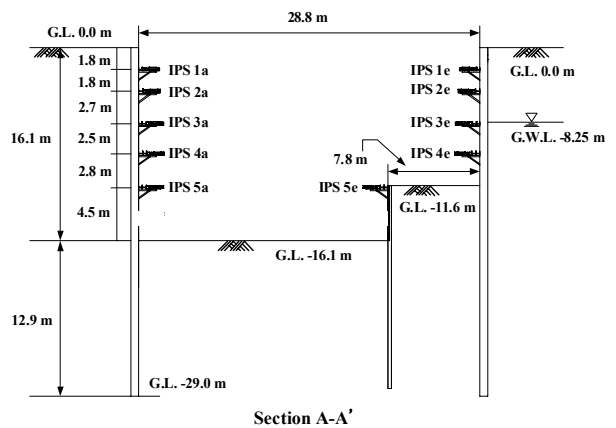


Fig. 5. Typical section of IPS wall

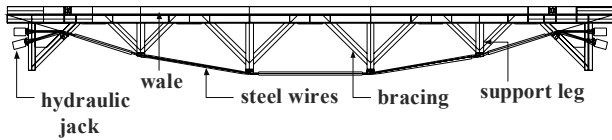


Fig. 6. Components of the IPS wale system

corner at the second to the fifth level. The length of H-beam was 5.5 m. The steel plate with 720 mm wide, 1,350 mm long, and 12 mm thick was bolted to two corner beams in order to prevent a buckling of corner beam from lateral earth pressures due to ground excavation. The center strut support consists of six H-beams and four steel plates. H-beams with H300×300×10×15 (mm) were used at the first level. Beams with H350×350×12×19 (mm) were used at the second to the sixth level. In order to prevent a buckling of the center strut support from lateral earth pressures by ground excavation, each H-beam used

was bolted with steel plate with 720 mm wide, 2,700 mm long, and 12 mm thick.

2.4 Instrumentation

The instruments for field monitoring included six inclinometers, four piezometers, twenty vibrating wire strain gauges, and thirty extensometers. The wall deflections were observed using wall inclinometers during excavation. The inclinometer casings were installed just behind the wall located at the mid-span of the IPS wales and embedded to the depth of 20.0 m to 24.0 m below the ground surface. The ground water level was monitored using piezometers. Vibrating wire strain gauges were used to measure the changes in strut loads, and were attached on the corner struts and center strut installed at each floor. The extensometers were installed at the mid-span of the

Table 1. IPS wale data

IPS wales		H-beam	Steel wires	Length of wales	Length of legs
1st level	IPS 1a, b	H300×300×10×15	φ15.2 mm, 7EA	11.0 m	1.29 m
	IPS 1c	H300×300×10×15	φ15.2 mm, 8EA	14.0 m	1.54 m
	IPS 1d	H300×300×10×15	φ15.2 mm, 7EA	13.0 m	1.44 m
	IPS 1e	H300×300×10×15	φ15.2 mm, 6EA	11.0 m	1.24 m
	IPS 1f	H300×300×10×15	φ15.2 mm, 8EA	14.0 m	1.54 m
2nd level	IPS 2a, b	H350×350×12×19	φ15.2 mm, 13EA	11.0 m	1.29 m
	IPS 2c	H350×350×12×19	φ15.2 mm, 17EA	14.0 m	1.54 m
	IPS 2d	H350×350×12×19	φ15.2 mm, 16EA	13.0 m	1.44 m
	IPS 2e	H350×350×12×19	φ15.2 mm, 11EA	11.0 m	1.24 m
	IPS 2f	H350×350×12×19	φ15.2 mm, 17EA	14.0 m	1.54 m
3rd level	IPS 3a, b	H350×350×12×19	φ15.2 mm, 15EA	11.0 m	1.29 m
	IPS 3c	H350×350×12×19	φ15.2 mm, 18EA	14.0 m	1.54 m
	IPS 3d	H350×350×12×19	φ15.2 mm, 18EA	13.0 m	1.49 m
	IPS 3e	H350×350×12×19	φ15.2 mm, 15EA	11.0 m	1.29 m
	IPS 3f	H350×350×12×19	φ15.2 mm, 18EA	14.0 m	1.54 m
4th level	IPS 4a, b	H350×350×12×19	φ15.2 mm, 27EA	11.0 m	1.29 m
	IPS 4c	H350×350×12×19	φ15.2 mm, 34EA	14.0 m	1.54 m
	IPS 4d	H350×350×12×19	φ15.2 mm, 33EA	13.0 m	1.49 m
	IPS 4e	H350×350×12×19	φ15.2 mm, 27EA	11.0 m	1.29 m
	IPS 4f	H350×350×12×19	φ15.2 mm, 34EA	14.0 m	1.54 m
5th level	IPS 5a	H350×350×12×19	φ15.2 mm, 27EA	13.0 m	1.49 m
	IPS 5b	H350×350×12×19	φ15.2 mm, 15EA	8.0 m	1.04 m
	IPS 5c	H350×350×12×19	φ15.2 mm, 25EA	12.0 m	1.44 m
	IPS 5d	H350×350×12×19	φ15.2 mm, 19EA	10.0 m	1.24 m
	IPS 5e	H350×350×12×19	φ15.2 mm, 30EA	16.0 m	1.54 m
	IPS 5f	H350×350×12×19	φ15.2 mm, 19EA	9.0 m	1.14 m

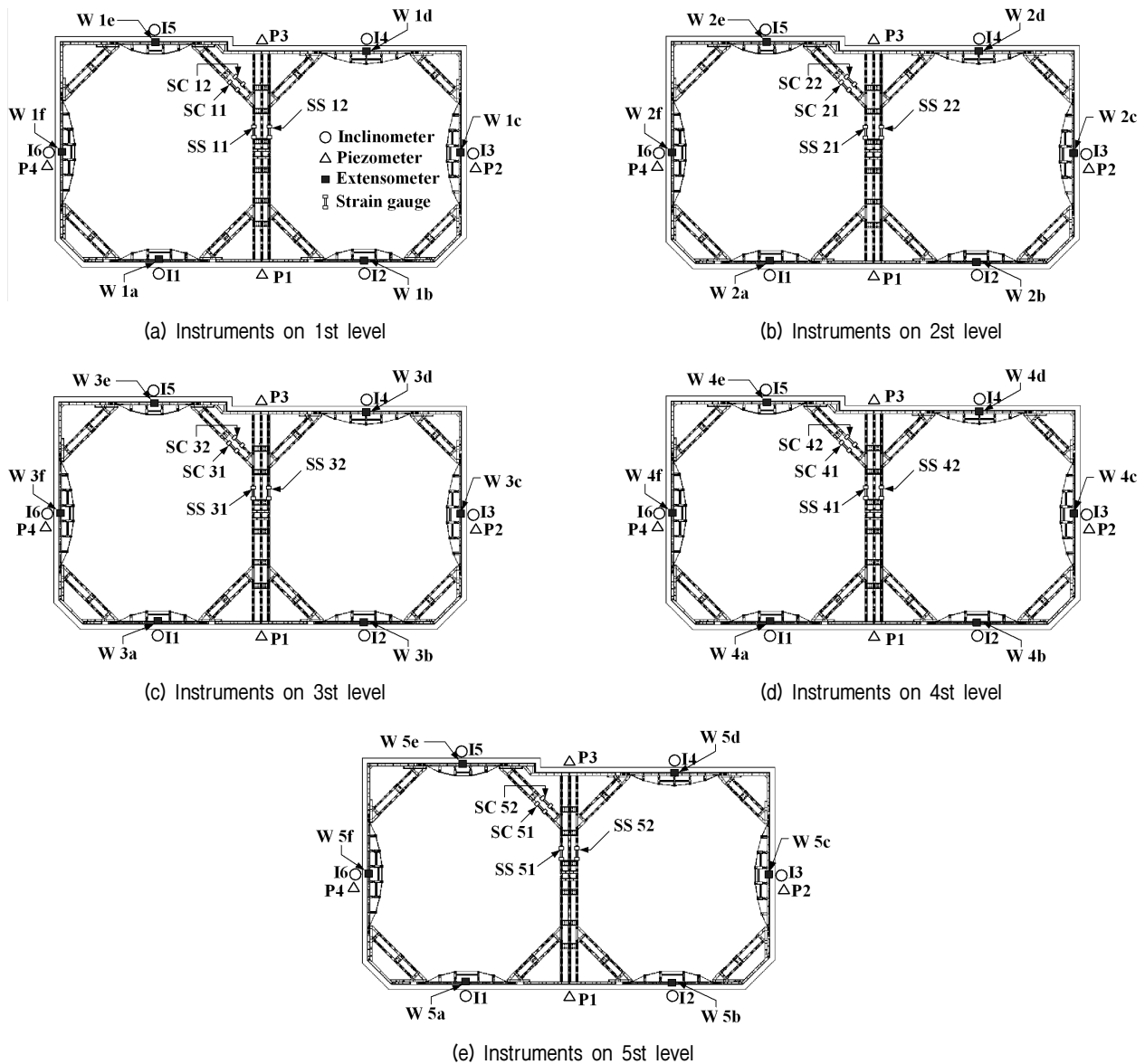


Fig. 7. Instrumentation layout

IPS walers in order to measure the horizontal deflections of the IPS walers during excavation. The location of the instruments is schematically described in Fig. 7.

2.5 Construction Sequence

Fourteen major construction stages are tabulated in Table 2. Prestresses on steel wires of the IPS walers and preloads on the corner struts and center struts are tabulated in Table 3.

3. Measured Performance

Field observation of the IPS earth retention system is summarized. The field monitoring began with the start of the slurry wall installation and was conducted in sequence up to the completion of the final ground excavation. The trends of the IPS wall deflection profiles obtained from the inclinometers were analyzed. The lateral deflections of the IPS walers from the extensometers were measured and compared with the designed assumptions. The loads on corner struts and center struts were observed and compared with the design predictions.

Table 2. Construction sequences

Step 1	Install the slurry wall.	Day 30
Step 2	Excavate to the depth of 2.8 m.	Day 38
Step 3	Install the IPS wales, corner struts, and center support at 1.8 m from the top of the wall. Prestress the IPS wales and preloading the center support.	Day 44
Step 4	Excavate to the depth of 4.8 m.	Day 50
Step 5	Install the IPS wales, corner struts, and center support at 3.6 m from the top of the wall. Prestress the IPS wales and preloading the center support.	Day 52
Step 6	Excavate to the depth of 7.3 m.	Day 59
Step 7	Install the IPS wales, corner struts, and center support at 6.3 m from the top of the wall. Prestress the IPS wales and preloading the center support.	Day 64
Step 8	Excavate to the depth of 9.8 m.	Day 81
Step 9	Install the IPS wales, corner struts, and center support at 8.8 m from the top of the wall. Prestress the IPS wales and preloading the center support.	Day 85
Step 10	Excavate to the depth of 12.6 m.	Day 91
Step 11	Install the IPS wales, corner struts, and center support at 11.6 m from the top of the wall. Prestress the IPS wales and preloading the center support.	Day 93
Step 12	Excavate to the depth of 16.1 m.	Day 102
Step 13	Install the center support at 13.8 m from the top of the wall and preloading the center support.	Day 112
Step 14	Excavate partially to the depth of 17.1 m.	Day 119

Table 3. Prestresses conditions of IPS earth retention system

Unit (kN)

		IPS a	IPS b	IPS c	IPS d	IPS e	IPS f	Corners	Center
1st level	Design	1,205	1,205	1,533	1,424	1,205	1,533	1,402	2,803
	Actual	929	834	1,164	980	784	1,156	1,764	2,646
2nd level	Design	2,790	2,790	3,550	3,297	2,790	3,550	2,320	6,492
	Actual	1,980	1,980	2,440	2,254	1,611	2,440	1,764	3,528
3rd level	Design	3,482	3,482	4,431	4,115	3,482	4,431	2,896	8,102
	Actual	2,150	2,150	2,663	2,570	2,136	2,667	2,646	4,410
4th level	Design	3,482	3,482	4,431	4,115	3,482	4,431	2,896	8,102
	Actual	3,914	3,884	4,766	4,678	3,904	4,719	2,646	4,410
5th level	Design	3,956	2,434	3,652	3,043	4,809	2,739	2,784	7,790
	Actual	3,796	2,222	3,623	2,789	4,113	2,751	2,646	4,410
6th level	Design	–	–	–	–	–	–	–	6,855
	Actual	–	–	–	–	–	–	–	4,410

3.1 Lateral Deflections

The lateral wall deflection profile developed during main construction activities was shown in Fig. 8. The lateral wall deflections were measured by inclinometers 1 and 2, which were installed just behind the wall located at the mid-span of the IPS wales. When the excavation reached final grade, the maximum lateral wall deflections were 28.1 mm at the location of I1 and 31.2 mm at the location of I2, respectively. These results indicated that the maximum lateral wall deflections were less than 0.2%

of excavation depth. The maximum lateral deflection of the IPS wall was 0.18% of the excavation depth. It was less than the deflection predicted using the Clough and O'Rourke (1990) chart for excavation cases in soft to medium clay. The maximum lateral deflection was less than the 0.2%H – 0.5%H reported by Ou et al. (1993) for excavations with a high factor of safety against basal heave, and was less than the results of numerical experiments reported by Hashash and Whittle (1996) for a braced diaphragm wall in a deep clay deposit. It was less than 0.2%H suggested by Wong et al. (1997) for

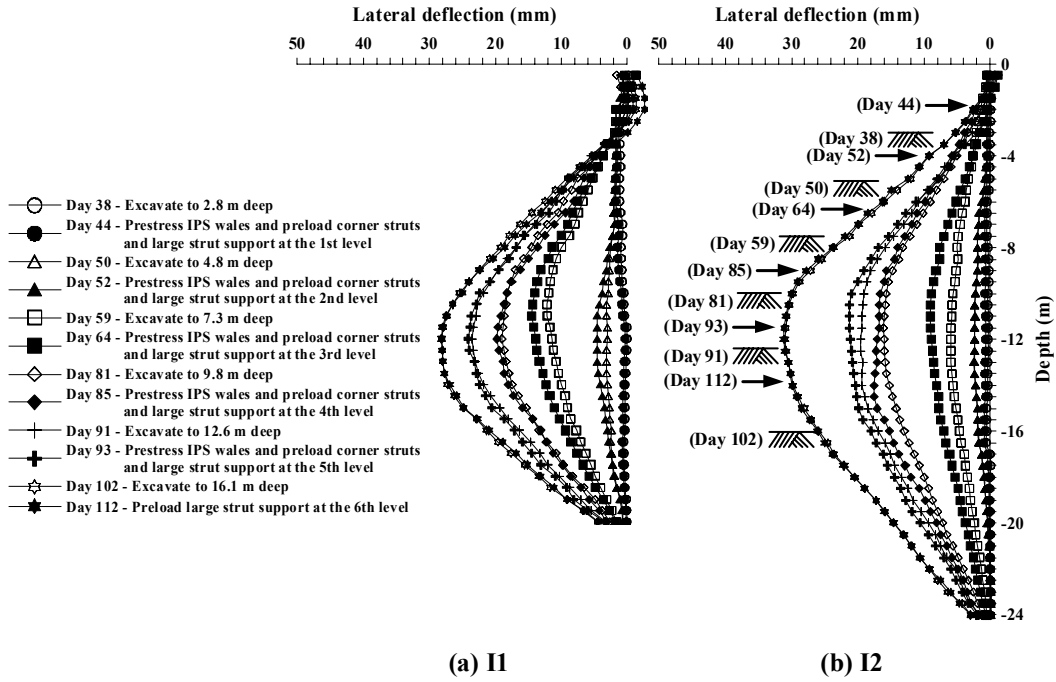


Fig. 8. Lateral deflection profiles of IPS wall during construction (a) inclinometer 1, and (b) inclinometer 2

excavations supported by rigid walls, with a combined thickness of soft-soil layers of less than 90% of the depth of excavation overlying stiff soils. The measured lateral wall deflection profiles represented a bulged fashion at 4.0 m above the soft clay stratum. This pattern for the IPS wall is comparable with wall deflection performances in soft clay reported in the literature (Lee et al. 1998; Finno et al. 2002).

The lateral deflection measured at the center location of the IPS wale during construction was shown in Fig. 9. The measured lateral deflections gradually increased throughout construction, excepting that the measurement

at the location of W2a on the center of the IPS 2a remained constant with few variations. The maximum lateral deflection measured at the center of the IPS wale by the extensometer was 6.7 mm at the location of W2b, 12.6 mm at the location of W 3b, and 12.2 mm at the location of W 4b. The measured deflection was within about 30% of the design assumption by Han et al. (2003).

3.2 Apparent Pressure Envelope by Loads on Struts

The axial loads measured on corner strut 1g to 5 g during construction are shown in Fig. 10. The loads at the location of corner 1g were measured from 620 kN

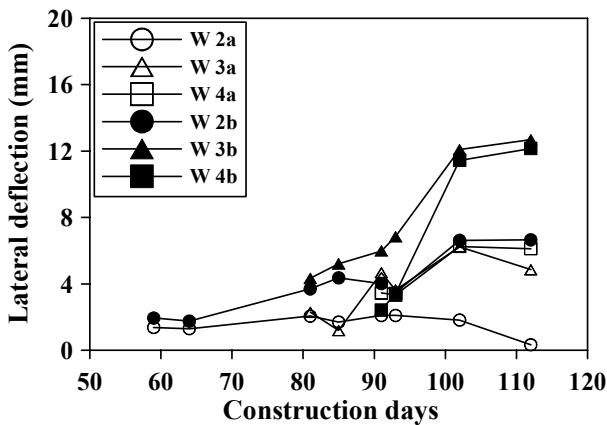


Fig. 9. Lateral deflections of the IPS wales during construction

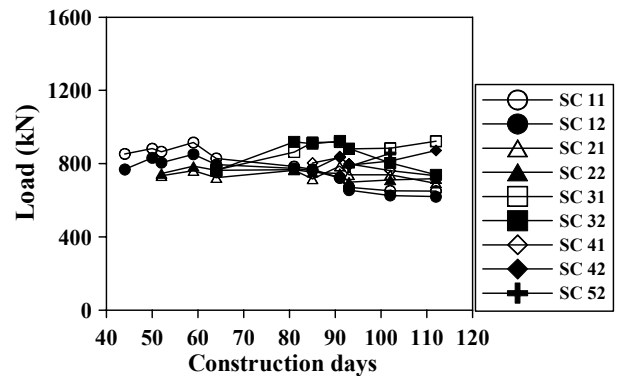


Fig. 10. Loads on corner struts during construction

to 916 kN. The loads measured at the location of corner 2 g ranged from 693 kN to 786 kN. At the location of corner 3 g, the measured loads varied from 761 kN to 924 kN. The loads at the location of corner 4 g were measured from 762 kN to 872 kN. The loads measured at the location of corner 5g ranged from 784 kN to 856 kN.

The axial load measured on center strut 1 to 5 is shown in Fig. 11. The loads measured at the location of center 1 ranged from 668 kN to 858 kN. The loads at the location of center 2 were measured from 771 kN to 940 kN. At the location of center 3, the measured loads ranged from 857 kN to 1021 kN. The loads measured at the location of center 4 varied from 898 kN to 1005 kN. The loads at the location of center 5 were measured from 855 kN to 917 kN.

The maximum strut loads after final excavation were

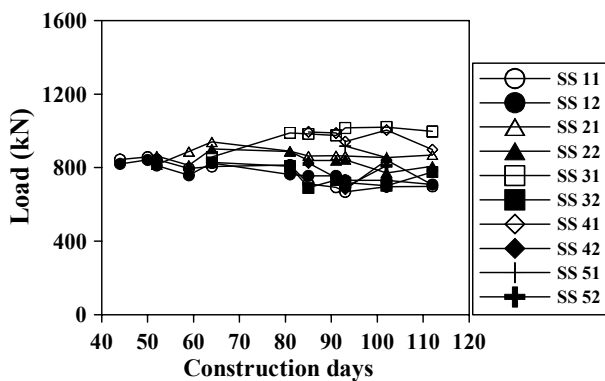


Fig. 11. Loads on center struts during construction

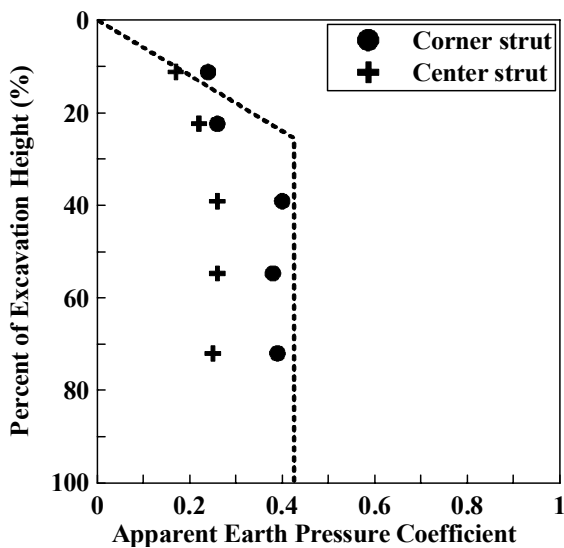


Fig. 12. Comparison of measured and the Terzaghi and Peck's design earth pressure envelope (1967)

converted into apparent pressures and compared with the Terzaghi and Peck's apparent earth pressure envelope for a soft to medium clay, as illustrated in Fig. 12. The pressures on struts at the first level ranged from 89% to 126% of the Terzaghi and Peck's apparent earth pressure envelope. The pressures at the first level exceeded the Terzaghi and Peck's apparent earth pressure envelope. This trend may have been caused by application of preload as much as approximately 126% of the design prediction. The pressures on struts at the second level varied from 58% to 68% of the apparent earth pressure by Terzaghi and Peck (1967). At the third level, the pressures on struts ranged from 62% to 95% of the Terzaghi and Peck's apparent earth pressure envelope. The pressures on struts at the fourth level varied from 62% to 90% of the Terzaghi and Peck's apparent earth pressure envelope. The pressures on struts at the fifth level ranged from 60% to 93% of the Terzaghi and Peck's apparent earth pressure envelope.

4. Discussion of Results

The behavior of members of the IPS earth retention system was investigated from analyzing the results of field measurements. The deflection behavior of the IPS wall showed a bulged shape which is quite common in soft clay. The IPS wale system proved to restrict wall deflection by the application of the prestress load.

For maximum lateral deflection of the IPS wall, the measured data was within the recommendations by other researchers for braced and anchored walls. It was notified that the deflection behavior of the IPS wall was similar to those of the braced and anchored walls.

The apparent earth pressures converted from loads on struts in the IPS wall matched with the Terzaghi and Peck's apparent earth pressure diagram. It was recognized that the earth pressure behavior on the IPS wall was similar to those of the braced and anchored walls.

5. Conclusions

The stability and applicability of the IPS earth retention system applied in soft clay were evaluated. Field monitoring

data such as the lateral wall deflection, the ground water level, the IPS wale deflection, and the strut support load were collected during excavation. Based on the measurements, the following conclusions can be drawn:

- (1) The IPS earth retention system in soft clay performed successfully. The IPS earth retention system proved to provide a large workspace. The amount of steel beams reduced 30% compared to strutted excavation in quantity.
- (2) The maximum lateral wall deflection of the IPS wall represented to be 0.18% of the excavation depth. The results were less than the deflection predicted by other researchers (Clough and O'Rourke 1990; Ou et al. 1993; Hashash and Whittle 1996; Wong et al. 1997). The lateral wall deflection profile showed a bulged fashion above the soft clay stratum. This trend is comparable with the results reported by Lee et al. (1998) and Finno et al. (2002) for wall deflection performance in deep excavation.
- (3) The maximum strut loads after final excavation were converted into apparent pressures and compared with the Terzaghi and Peck's apparent earth pressure envelope for a soft to medium clay. The pressures on struts ranged from 89% to 126% at the first level, and ranged from 58% to 68% at the second level, and ranged from 62% to 95% at the third level, and ranged from 62% to 90% at the fourth level, and ranged from 60% to 93% at the fifth level, when compared with the Terzaghi and Peck's apparent earth pressure envelope.
- (4) The excessive stresses or buckling of strut members were not observed. The axial compressive stresses on struts were within the allowable stresses.

Acknowledgments

This work was supported by grant No. (R01-2003-000-11630-0) from the Basic Research Program of the Korea Science & Engineering Foundation.

References

1. Clough, G. W., and O'Rourke, T. D. (1990), "Construction Induced Movements of In Situ Walls", *Proc., ASCE Conf. on Des. and Perf. of Earth Retaining Struct., Geotech. Spec. Publ. No.25*, ASCE, New York, pp. 439-470.
2. Finno, R. J., Bryson, S., and Calvello, M. (2002), "Performance of a Stiff Support System in Soft Clay", *Jour. Geotech. and Geoenvir.*, ASCE, Vol.128, No.8, pp. 660-671.
3. Han, M. Y., Kim, M. Y., Kim, S. B., and Park, D. H. (2003), "Theoretical Study on Flexural Stiffness of Innovative Prestressed Wale", *Proceedings of the KSCE Annual Conference 2003*, KSCE, pp. 3754-3759.
4. Hashash, Y. M. A., and Whittle, A. J. (1996), "Ground Movement Prediction for Deep Excavations in Soft Clay", *Jour. Geotech.*, ASCE, Vol.122, No.6, pp. 474-486.
5. Kim, N. K., Park, J. S., Han, M. Y., Kim, M. Y., and Kim, S. B. (2004), "Development of Innovative Prestressed Support Earth Retention System", *Jour. of the KGS*, Vol.20, No.2, March 2004, pp. 1-7.
6. Kim, N. K., Park, J. S., Jang, H. J., Han, M. Y., Kim, M. Y., and Kim, S. B. (2005), "Performance of Innovative Prestressed Support Earth Retention System in Urban Excavation", *Jour. of the KGS*, Vol.21, No.2, March 2005, pp.1-10.
7. Kim, S. B., Han, M. Y., Kim, M. Y., Kim, N. K., and Ji, T. S. (2005), "Analysis and Design of Wale in Innovative Prestressed Support (IPS) System", *Jour. of the Computational Structural Engineering Institute of Korea*, Vol.18, No.1, pp. 79-91.
8. Lee, F. H., Yong, K. Y., Quan, K. C. N., and Chee, K. T. (1998), "Effect of Corners in Strutted Excavations: Field Monitoring and Case Histories", *Jour. Geotech. and Geoenvir.*, ASCE, Vol.124, No.4, pp. 339-349.
9. Ou, C. Y., Hsien, P. G., and Chiou, D. C. (1993), "Characteristics of Ground Surface Settlement During Excavation", *Can. Geotech. J.*, Ottawa, Vol.30, pp. 758-767.
10. Terzaghi, K., and Peck, R. B. (1967), *Soil mechanics in engineering practice*, 2nd Ed., John Wiley & Sons, Inc., New York, N. Y.
11. Wong, I. H., Poh, T. Y., and Chuah, H. L. (1997), "Performance of Excavations for Depressed Expressway in Singapore", *Jour. Geotech. and Geoenvir. Engrg.*, ASCE, Vol.123, No.7, pp. 617-625.

(received on Mar. 11, 2006, accepted on Jan. 9, 2007)

Effect of Stress-Dependent Modulus and Poisson's Ratio on Rutting Prediction in Unbound Pavement Foundations

도로기초의 Rutting 예측에 미치는 응력의존 탄성계수와 포와송비의 영향

Park, Seong-Wan¹

박 성 완

요 지

본 논문은 도로기초 입상재료의 응력의존적인 특성을 고려한 응력의존적 재료 상수의 적용을 통하여 층 변형에 측을 수행하는 간편한 방식을 소개한다. 이 방법은 Unbound지반재료에 대하여 회복변형과 영구변형을 구분하여 고려하며 두 변형의 상호작용을 적용하지 않는 방식이다. 그 결과 회복변형 탄성계수와 포와송비를 포함한 해석모형은 상호작용이 고려되지 않아도 현장에서의 도로기초 변형을 예측할 수 있음을 잘 보여주고 있다. 또한 응력의존 탄성계수와 응력의존 포와송 비 모형에서 가장 영향을 많이 미치는 계수를 찾기 위하여 민감도 분석을 실시하였다. 이러한 분석결과를 토대로 응력의존에 의하여 변형 예측시 나타나는 경향을 살펴보았다.

Abstract

This paper will present a simple approach for predicting layer deformation of unbound pavement materials with stress-dependent material properties. The approach is based on an uncoupled formulation in which the resilient and deformation response of unbound materials are considered separately. As a result, an uncoupled approach incorporating a resilient stiffness and Poisson's ratio model is able to simulate field measured deformation in pavement foundations. In addition, a sensitivity analysis is conducted to identify the significant factors in the stress-dependent modulus and Poisson's ratio model. The predicted trends of deformation from this analysis are presented and discussed.

Keywords : Finite element analysis, Layer deformation, Pavement foundations, Stress-Dependent Modulus

1. Introduction

When pavement materials are subjected to repetitive loadings, both elastic and plastic strains are developed. Plastic strains are unrecoverable and manifest themselves in surface ruts, which represent the accumulated deformation in the underlying layers. For timely and cost-effective maintenance of road infrastructure, the prediction of permanent deformation is very important matter.

In general, the understanding and prediction of permanent deformation of unbound pavement geomaterials has lagged

far behind than in the area of resilient responses. From the permanent deformation behavior and models perspective, it is obvious that some models are less satisfactory in cases when a soil is near failure. Consequently, the more elaborate models or approaches can improve the prediction of permanent deformation in unbound pavement materials. However, this may lead to more difficulties in quantifying model parameters for practical applications. Therefore, the model and approach should be reasonable and simple to use. For this, a simplified uncoupled formulation is presented to predict deformations on conventional flexible

¹ Member, Assistant Prof., Dept. of Civil & Environmental Engrg., Dankook Univ., Seoul, spark@dankook.ac.kr

pavements under repeated loadings. In addition, a sensitivity analysis is conducted to identify the significant factors in the stress-dependent modulus and Poisson's ratio model of unbound geomaterials.

2. Permanent Deformation on Unbound Pavement Materials

For practical purposes, deformation or rutting has been indirectly considered through the use of empirical or semi-empirical relationships based on limiting the vertical compressive strain at the top of the pavement subgrade. This approach implies that no rutting occurs within the pavement layers above the subgrade. However, serious rutting can occur within the unbound layers including subgrades in case of the thin asphalt pavements. This may be mainly due to consolidation and lateral movement in component pavement layers. An earlier survey conducted by the American Association of State Highway and Transportation Officials Joint Task Force on Rutting indicated that 32 states in US identified base or subbase distress as a major cause of rutting (AASHTO 1995). In addition, from the various studies of field test, about 70 percent of permanent deformation occurred within the base and subgrade layers in conventional flexible pavements (Kenis and Wang 1997). Especially, deformation in the subgrade will be much severe on thin pavements. There are several factors that affect the permanent deformation of unbound pavement materials (Maree 1978; Lekarp 1997). These are stress condition and number of stress applications, rate of stress application, compaction, grading, plasticity of fines, geological origin of materials, strength of materials, particle shape or form, surface texture, moisture, and temperature.

The level of stress is one of the most important factors in the development of permanent deformation in pavements. Repetitive or cyclic loading may develop permanent deformation in unbound materials, subgrade soils causing more rapid deformation than monotonic loading. Several studies found that the permanent axial strain increases with decreasing confining pressure, and increasing deviatoric stress (Shackel 1973). An increase in stress

rotation also increases the permanent deformation (Momoya et al. 2005). Barksdale (1972) has reported that the accumulated plastic strain of base materials increased with an increase in the deviatoric stress or with a reduction in the confining pressure. The effect of the deviatoric stress in the accumulation of plastic strains was also found to be more pronounced for clay soils than granular materials (Shackel 1973; Li and Selig 1996). In addition, the accumulated permanent deformation is increased substantially with higher moisture contents primarily due to the loss of cohesion, particularly at moisture contents above optimum. There is also some interaction between the moisture content and the applied stress level. At high levels of deviatoric stress, an increase in moisture content will accumulate the development of permanent deformation more than at low levels of deviatoric stress.

3. Resilient Response Modeling

The strain resulting from traffic load on a typical pavement should be nearly completely recoverable and proportional to the applied load. Although there is some permanent deformation related to each load application, this strain is normally small and causes only long term deterioration of the pavement structure. The deformation can therefore be considered as elastic and this elastic or resilient modulus, M_r , is defined as the ratio of the repeated deviatoric stress to the recoverable part of the axial strain resulting from repeated load tests as described in Figure 1 and Equation 1.

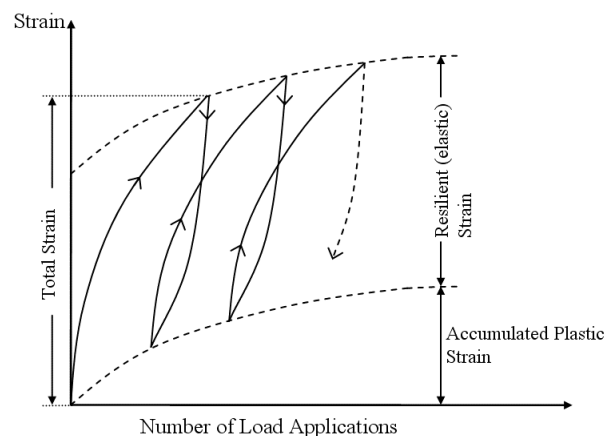


Fig. 1. Typical Resilient Response from Repeated Load Applications

$$M_r = \frac{\sigma_d}{\varepsilon_r} \quad (1)$$

where:

σ_d = the repeated deviatoric stress, and
 ε_r = the recoverable strains obtained from repeated load triaxial test.

Typically, the behavior of unbound pavement geomaterials is non-linear and stress-sensitive. In order to simulate this, the stress-dependent stiffness is calculated using nonlinear Universal Soil Model (Uzan 1992) which can consider the effect of octahedral shear stress with the confining stress simultaneously as shown by Equation 2.

$$M_r = K_1 P_a \left(\frac{I_1}{P_a} \right)^{K_2} \left(\frac{\tau_{oct}}{P_a} \right)^{K_3} \quad (2)$$

where:

M_r = resilient modulus for vertical direction,
 P_a = atmospheric pressure,
 I_1 = bulk stress,
 τ_{oct} = octahedral shear stress, and
 K_i = material constants ($i=1, 3$).

Depending on the level of stress, the bulk stress term considers the hardening response associated with higher modulus, while the octahedral shear stress term considers the softening response. In addition, Poisson's ratio of unbound geomaterials is also known to be stress-sensitive and should be considered simultaneously. For this, a relationship between Poisson's ratio and the resilient modulus can be established based on a thermodynamic constraint (Lade and Nelson 1987; Liu 1993). This relationship is established using the resilient property parameters as expressed in Equation 2 and the thermodynamic constraints to derive an expression that relates the state of stress and the rate of change of Poisson's ratio with the changing stress state as follows in Equation 3.

$$\frac{2}{3} \frac{\partial \nu}{\partial J_2} + \frac{1}{I_1} \frac{\partial \nu}{\partial I_1} = \nu \left[\frac{1}{3} \frac{K_3'}{J_2} + \frac{K_2}{I_1^2} \right] + \left[-\frac{1}{6} \frac{K_3'}{J_2} + \frac{K_2}{I_1^2} \right] \quad (3)$$

where:

ν = Poisson's ratio,
 $K_3' = K_3/2$,
 K_i = material parameters,
 I_1 = normalized first stress invariant, and
 J_2 = normalized second invariant of the deviatoric stress.

The stress-dependent Poisson's ratio can be determined using Equation 3. However, this analytical solution can be indeterminate for certain combinations of I_1 and J_2 conditions. Therefore, it can be solved numerically by simple substitutions of partial terms based on the backward difference method. These partial terms are shown in Equations 4 and 5.

$$\frac{\partial \nu}{\partial J_2} = \frac{\nu_j^i - \nu_{j-1}^i}{k} \quad (4)$$

$$\frac{\partial \nu}{\partial I_1} = \frac{\nu_j^i - \nu_{j-1}^i}{l} \quad (5)$$

where:

l, k = step sizes for increasing I_1 and J_2 , and
 i, j = counter for I_1 and J_2 .

By setting Equations 4 and 5 into Equation 3 and performing some algebraic manipulation, the iterative formula for estimating the Poisson's ratio for a given stress condition can be expressed as Equation 6.

$$\nu_j^i = \frac{\left[\left(\frac{2}{3k} \right) \times \nu_{j-1}^i + \left(\frac{1}{lI_1} \right) \times \nu_{j-1}^i - \frac{k_3'}{3J_2} + \frac{k_2}{I_1^2} \right]}{\left[\frac{2}{3k} + \frac{1}{lI_1} - 2 \frac{k_3'}{3J_2} - \frac{k_2}{I_1^2} \right]} \quad (6)$$

Equation 6 is solved by choosing a step size for increasing I_1 and J_2 and then increasing I_1 and J_2 from a fixed boundary condition for which the Poisson's ratio is known. Varying Poisson's ratio values are estimated iteratively until the specified convergence during each load increment is accomplished. More detailed information regarding resilient dilatancy approach can be found in elsewhere (Park and Lytton 2004).

4. Algorithm of Predicting Layer Deformation

Deformation in conventional flexible pavements is the direct result of the passage of loads over the pavement surface and the strain induced by the loads. This induced strain can be simplified as two components, the resilient strain and the permanent strain. It is suggested that the resilient strain remains fairly constant during the major part of the pavement's life, except for at a low number of load repetitions where the material undergoes conditioning and near failure (Uzan et al. 1988). Therefore, it can also be assumed that the elastic strain is constant throughout the pavement performance life and the plastic strain per load application is assumed to decrease with the number of load applications.

For the deformation calculation, uncoupled analysis by the simple layer strain approach is adopted with a finite element program. In this approach, the nonlinear stress-dependent finite element analysis is made using an incremental loading and an iterative solution technique for each load increment. From the results of stress-dependent finite element analysis, deformation at each layer is calculated by summing the products of the permanent strains and the corresponding difference in depths between the layers as described in the earlier paper by Park (2005).

The layer deformation is calculated by multiplying vertical strains at the center of each element by the layer thickness and by the plastic model properties of each layer. The VESYS model is used (Kenis and Wang 1997). This model states that the ratio of vertical plastic strain per cycle to the resilient strain is an exponential function of the number of load cycles as shown in below.

$$\frac{1}{\varepsilon_r} \frac{d\varepsilon_p}{dN} = \mu N^{-\alpha} \quad (7)$$

where:

- ε_p = permanent deformation,
- ε_r = elastic or/ resilient deformation,
- N = the number of load applications,
- μ = parameter representing the constant of proportionality of strains, and
- α = parameter indicating the rate of decrease.

Then, the total permanent deformation is calculated by Equation 8.

$$\delta_a(N) = \sum_{i=1}^n \left[\frac{\mu_i N^{1-\alpha_i}}{1-\alpha_i} \int_{d_{i-1}}^{d_i} \varepsilon_c(z) dz \right] \quad (8)$$

where:

- $\varepsilon_c(z)$ = compressive strain at depth z ,
- d_i = the depths of each layer in the pavement, and
- $\delta_a(N)$ = the total permanent deformation.

5. Determination of Layer Deformation Parameters

In order to evaluate deformation parameters under traffic loading, the repeated-load-permanent deformation test is necessary to conduct in the laboratory. Currently, the laboratory study of permanent deformation is less advanced than the resilient modulus test, and there is no standard test procedure for determining the permanent deformation of unbound materials. However, the VESYS procedure (Kenis 1978) has commonly been used for the repeated load-permanent deformation tests.

Each load cycle consisted of a 0.1-second loading time and a 0.9-second rest period. Initially, specimen is subjected to 200 cycles of preconditioning at vertical loads that were 10 percent of the deviatoric stress. The accumulated vertical and radial deformations are recorded throughout the test. Figure 2 provides a conceptual illustration of the data from a repeated load-permanent deformation test. In addition, the full deformation data covering the loading and unloading portions of a given

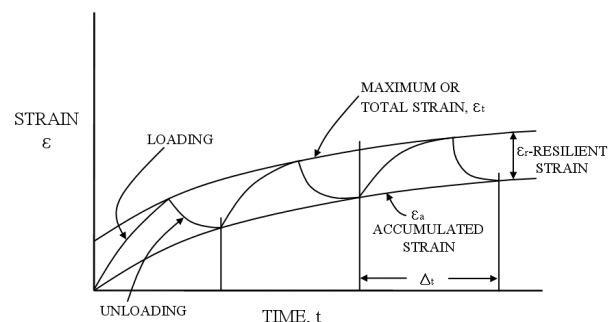


Fig. 2. Accumulated Strains due to Repeated-Load Deformation Test

cycle are recorded for the 199th, 200th, and 201st load cycles to determine the resilient strain at the 200th repetition. This quantity is needed to characterize the parameters, α and μ , of the VESYS rutting model.

The parameters, α and μ , of the VESYS rutting model can be determined using a simple relationship between the logarithm of the accumulated strain and the logarithm of the number of load cycles. This relationship between permanent strain and the repeated loads is assumed to be linear over a range of load applications. Two parameters are estimated using the y-intercept and the strain slope. Then, the corresponding rutting parameters can be estimated. If the α value is equal to zero, the rutting on unbound materials under repetitive loadings will be a constant rate. When the temperature increases and α will decrease, then the rutting potential becomes greater. In the case of a thin pavement with a clay subgrade, α will be negative when the clay warms up. Such a pavement will be subjected to more rutting.

6. Model Validation with Field Measurement

In order to validate the approach for layer deformation prediction, field measurement results from a full-scale loading test studies by Chen and Hugo (2001) and Zhou and Scullion (2002) were used. Based on the parameters in Table 1, the layer deformation on pavement foundations of each test was predicted and compared with the results from the literature. The equivalent of 8 years of traffic was applied. It is assumed that the traffic is equal for

Table 1. Moduli and rutting parameters for test sites (Chen and Hugo 2001; Zhou and Scullion 2002)

Site	Layer	Moduli (GPa)	α	μ
281N	AC	2.00	0.73	0.46
	Base	0.26	0.75	0.21
	Subgrade	0.06	0.75	0.02
281S	AC	4.01	0.74	0.21
	Base	0.26	0.73	0.07
	Subgrade	0.06	0.75	0.02
F5	AC	2.35	0.74	0.31
	Base	0.26	0.75	0.28
	Subgrade	0.06	0.75	0.02

all seasons and the initial set of resilient moduli for each season was used at the given traffic periods. The comparisons of layer deformation between the field measurements and the predictions are shown in Figures 3 through 5.

From Figure 3, it was found that the predicted rutting at the base and subgrade layers agrees well with the field measurements although predictions overestimate at an

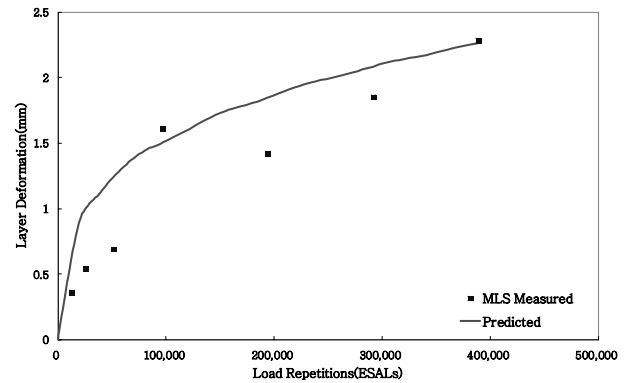


Fig. 3. Measured and Predicted Base and Subgrade Deformation in Site 281N

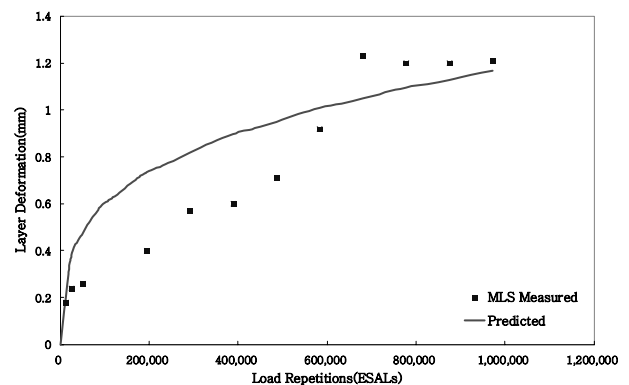


Fig. 4. Measured and Predicted Base and Subgrade Deformation in Site 281S

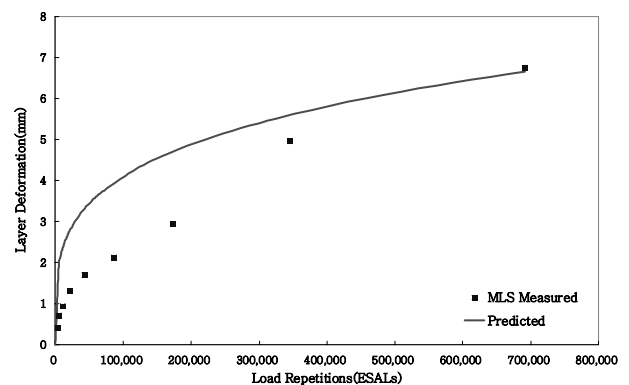


Fig. 5. Measured and Predicted Base and Subgrade Deformation in Site F5

early stage of trafficking. Figure 4 shows the comparison of the rutting for 281S1 test site. Still, the deformation at the base and subgrade layers is predicted fairly well. The comparisons of the F5 field measurements and predicted base and subgrade layer rutting are presented in Figure 5. It is found from these comparisons that predicted layer rutting on pavement foundations matches the field measurements results fairly well.

7. Effect of Stress Sensitivity on Deformation

A sensitivity analysis was conducted to identify the factors that have a significant influence on the development of layer permanent deformation in pavement foundations. For this purpose, each of the K1 to K3 resilient parameters was varied one at a time from its assumed base value, while the other parameters were held at their corresponding base values. The change in the predicted layer deformation due to a change in a given parameter was evaluated using the uncoupled finite element analysis program. Because of the unavailability of some of the material properties, typical values for the VESYS rutting parameters, α and μ , are assumed for each

layer in the analyses and were kept the same. To model the pavement response under the standard 80 kN single axle load, a single wheel load of 40.0 kN was applied over a circular area with a radius of 136 mm, which corresponds to a surface pressure of 689 kPa. Table 2 shows the base value used in the sensitivity analysis for the stress-dependent parameters respectively. Each parameter is determined from results of the laboratory study by Titus-Glover and Fernando (1995). In addition, each parameter was varied ± 30 percent from its base value except for the surface layer, k3, and the subgrade, k2, which were fixed at zero.

The results of predicted deformation from the variation in the resilient material properties are shown in Figures 6 through 12. These figures illustrate the layer deformation development on pavement foundations to changes in the resilient material parameters. Note that the base and subgrade k3 is negative, and an increase of 30 percent of the k3 means less negative and vice versa. In addition, the predicted layer rutting is summarized in Table 3.

Predicted deformation is most sensitive to the parameter k1. Figures 6, 8, and 11 show that the predicted deformation changes significantly whenever k1 for a given

Table 2. Base Levels of Resilient and Deformation Parameters Used in Sensitivity Analysis

Layer	Thickness (mm)	K ₁	K ₂	K ₃	α	μ
AC Surface	100	50,000	0.1	0.0	0.60	0.75
Granular Base	200	700	0.6	-0.3	0.84	0.53
Subgrade	2,300	400	0.0	-0.3	0.81	0.08

Table 3. Predicted Total and Layer Deformation to Changes in Resilient Parameters

Change Parameter	Deformationat	K ₁ (+30%)	K ₁ (-30%)	K ₂ (+30%)	K ₂ (-30%)	K ₃ (+30%)	K ₃ (-30%)
AC	Total	12.02	18.86	14.22	13.54	-	-
	AC	4.60	7.46	6.03	5.32	-	-
	Base	5.32	6.89	5.91	5.94	-	-
	Subgrade	2.10	2.52	2.28	2.28	-	-
Base	Total	12.87	17.21	14.70	13.16	14.48	13.34
	AC	5.46	7.04	5.79	5.52	5.76	5.56
	Base	5.46	7.80	6.60	5.40	6.44	5.51
	Subgrade	2.25	2.37	2.31	2.24	2.28	2.27
Subgrade	Total	13.39	14.73	-	-	14.16	13.61
	AC	5.54	5.85	-	-	5.73	5.59
	Base	5.96	5.99	-	-	5.93	5.94
	Subgrade	1.89	2.89	-	-	2.50	2.08

layer is varied. A higher increase in deformation is due to decreasing the AC k1 parameter, as shown in Figure 6. This is mainly due to higher induced strains resulting from a more flexible AC layer brought by a decrease in k1. It is also observed that major deformation occurs at both the AC and base layers. The lower the AC k1 value, the higher the strain in the base layer. This is due to the higher stresses predicted in the base because of the flexible AC surface. In addition, the effect of varying the AC k1 on the predicted deformation at the AC layer gives a higher percent change compared to the corresponding effect on the predicted deformation at the base layer, as shown in Table 3.

Figure 7 shows that predicted deformation is not very sensitive to changes in the AC k2 for the pavement considered. Even though an increase in deformation due to an increase in AC k2 is observed, the effects of the AC k2 on the predicted deformation of the AC layer are relatively smaller compared to the effects of k1. At the

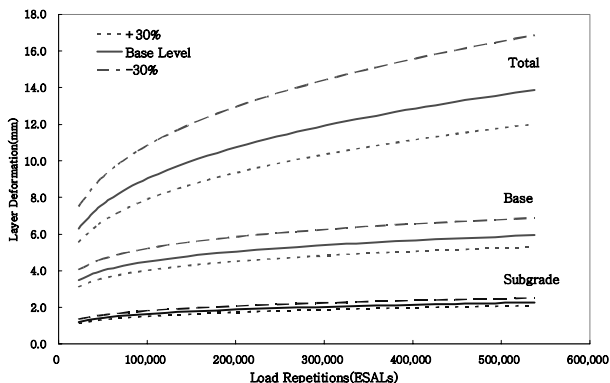


Fig. 6. Predicted Foundation Layer Deformation to Change in k1 Parameter of the AC

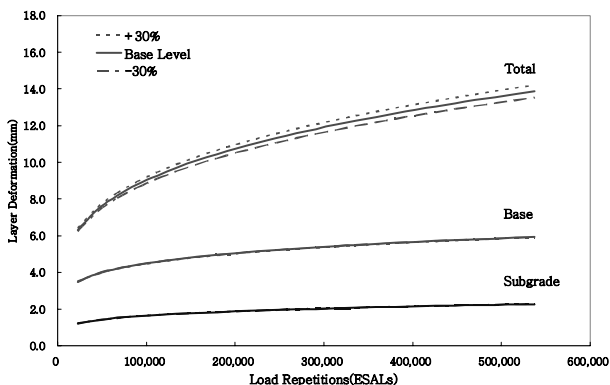


Fig. 7. Predicted Foundation Layer Deformation to Change in k2 Parameter of the AC

base and subgrade layers, the effects of the AC k2 are almost negligible. It would be expected that a higher k2 results in a higher modulus for that layer. However, in the case of the changes in the AC k2, the deformation predicted in the AC layer is slightly greater than that predicted in the case of the lower k2. It seems to indicate that a lower modulus in the AC layer is predicted by an increase in AC k2 because the higher AC k2 results in a lower modulus for base and subgrade layers due to the lower stress conditions for a given base and subgrade. Therefore, the ratio of modulus between the AC and base layer is increased when base k2 was increased by 30 percent. This may affect the stresses and strains in the bottom half of the AC layer and increase the resulting compressive strains.

Figures 8 through 10 show that the changes in the stress dependent behavior of the base layer led to significant changes in the predicted deformation. Figure 8 shows that increasing the base k1 led to a lower deformation in the AC and base layers, reflecting the reduction in the vertical strains in component layers due to the stronger support provided by the stiffer base. The deformations predicted in the AC and subgrade layers are not very sensitive to changes in the base k2 and k3 parameters, as shown in Figures 9 through 10. Only the base layer shows greater changes in deformation to the changes in the base k2, and k3 parameters. Again, this could be explained by the changes in the predicted stiffness ratio due to nonlinear stress dependency. When the base k2 is increased by 30 percent, the predicted deformation at the base is also

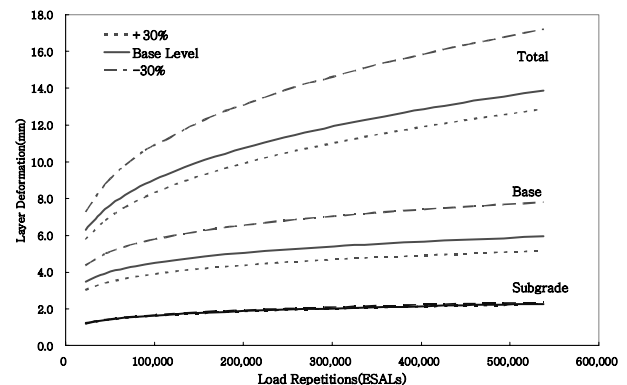


Fig. 8. Predicted Foundation Layer Deformation to Change in k1 Parameter of the Base

increased owing to the corresponding change in ratio of modulus between layers. Figure 10 shows that the less negative k_3 which is increased by 30 percent have a greater predicted deformation. The effects of the base k_3 parameter may be explained by the changes in the predicted base stiffness. Since the predicted values of the first stress invariant and the octahedral shear stress at the subgrade are less than atmospheric pressure, the stiffness of the base decreased when the base k_3 is increased by 30 percent.

Figure 11 shows that the subgrade k_1 increases the predicted deformation only in the subgrade layer. However, the predicted deformation in the AC and base layers are not sensitive to changes in the subgrade k_1 . Note that the subgrade k_3 is negative and the trends are the same as the base k_3 but have a lesser impact compared to the effects of base k_3 , as shown in Figure 12.

From the results, the variations of the deformation predicted in the AC and the base layers are far greater

than that of the subgrade. The greatest increase in deformation is observed when the base k_1 is decreased. Even when the base k_2 and k_3 were changed, minor changes are observed in the AC and base layers. As can be seen in Table 2, the parameters which relate to the nonlinear behavior, such as k_2 and k_3 , have a relatively smaller effect on the predicted deformation than did the k_1 parameter. The deformation predicted in the subgrade shows a lower change in most of the k_1 to k_3 parameters. For the base and subgrade layers, the high modulus ratio between the base and subgrade is seen as important because the vertical stresses and strains are major factors in deformation prediction. In some cases, the deformation is not very sensitive to changes in parameters due to the minor changes of the vertical compressive stresses. The effects of stress dependency on deformation prediction are affected by the applied load and pavement geometry due to the effects of the nonlinear parameters (k_2 and k_3). It is also noted that the boundary effects of the stress

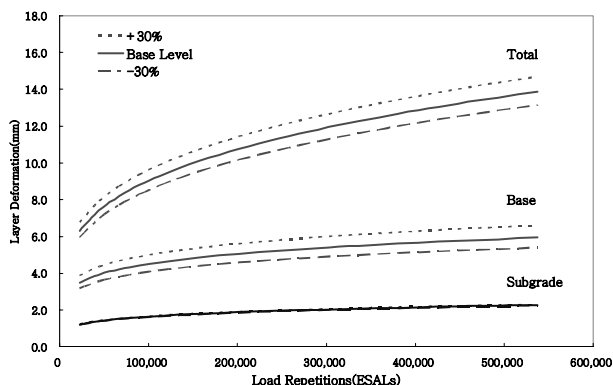


Fig. 9. Predicted Foundation Layer Deformation to Change in k_2 Parameter of the Base

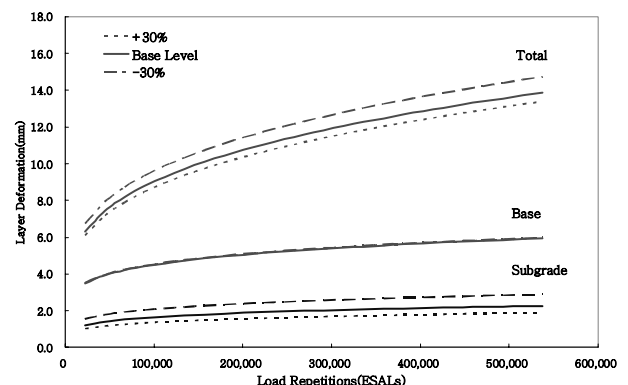


Fig. 11. Predicted Foundation Layer Deformation to Change in k_1 Parameter of the Subgrade

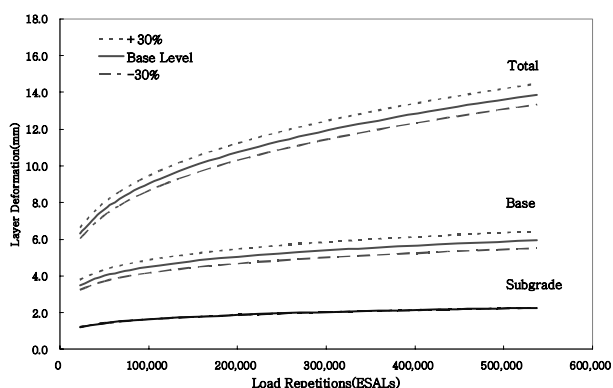


Fig. 10. Predicted Foundation Layer Deformation to Change in k_3 Parameter of the Base

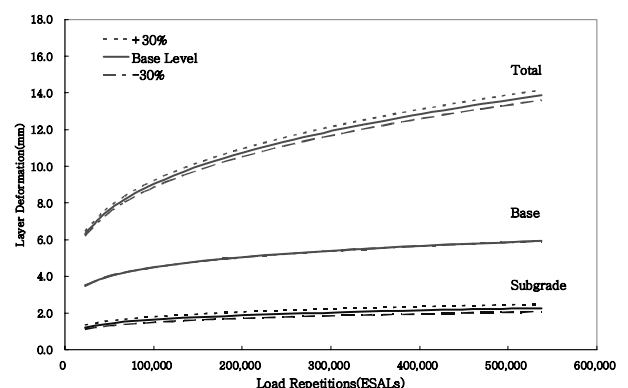


Fig. 12. Predicted Foundation Layer Deformation to Change in k_3 Parameter of the Subgrade

condition for the k_2 and k_3 terms used in stress dependent calculations may affect the deformation prediction and interact with pavement geometry.

As these results illustrate, it is apparent that both the stress dependent modulus and the Poisson's ratio vary considerably within the layers. This may significantly change the predicted deformation of unbound foundation layers. For a detailed study of the stress dependent behaviors on deformation, it is recognized that actual measurements from large-scale testing or in-field testing are needed.

8. Conclusions

A simplified layer deformation analysis on pavement foundation has been presented and discussed in which the layer strain method is incorporated in a nonlinear stress-dependent finite element analysis. Based on the analysis, the proposed approach adequately predicted the observed deformation on foundation layers. In addition, the following observations are noted.

- (1) Predicted deformation is most sensitive to the parameter k_1 . The effect of the higher k_1 is to increase the predicted deformation.
- (2) Largest Changes in predicted deformation occurred when AC k_1 was varied. Variations in base k_2 and k_3 parameters result in significant changes of the predicted deformation in base as well.
- (3) Because of the effects of the nonlinear characteristics of pavement materials, deformations are affected by the applied load, pavement geometry, and stress dependent parameters.
- (4) Good foundation support will mobilize resilient modulus and Poisson's ratio in unbound layers and reduce deformation in upper layers due to a lesser bending effect.

Although results indicated that it could predict deformation well, there is still a need to calibrate predicted deformation with the observed deformation data in fields. In particular, better estimation on deformation during the

early stages of traffic loadings and more full-scale trials are necessary to verify whether the results of the predictions are proved in practice.

Acknowledgements

The present research was conducted by the research fund of Dankook University in 2005. Their support was gratefully recognized.

References

1. AASHTO (1995), *Provisional Standards*. Am. Assn. of State Hwy. and Transportation Officials, Washington, DC, 10-93.
2. Barksdale, R. D. (1972), "Laboratory Evaluation of Rutting in Base Course Materials", *Proc. 3rd Int. Conf. on the Structural Design of Asphalt Pavements*, Vol.1, Ann Arbor, MI, 161-174.
3. Chen, D. and Hugo, F. (2001), "Comparison of two pavement rehabilitation strategies", *Journal of Transportation Engineering*, ASCE, 127(1), 47-59.
4. Kenis, W. and Wang, W. (1997), "Calibrating Mechanistic Flexible Pavement Rutting Models from Full Scale Accelerated Tests", *Proc. of the Eighth International Conference on Asphalt Pavements*, Seattle, Washington, 663-672.
5. Lade, P. V. and Nelson, R. D. (1987), "Modeling the Elastic Behavior of Granular Materials", *International Journal for Numerical and Analytical Methods in Geomechanics*, 11(5), 521-542.
6. Lekarp, F. (1997), "Permanent Deformation Behavior of Unbound Granular Materials", Licentiate Thesis, Royal Institute of Technology, Stockholm, Sweden.
7. Li, D., and Selig, E. T. (1996), "Cumulative Plastic Deformation for Fine-Grained Subgrade Soils", *Journal of Geotechnical Engineering*, ASCE, 122(12), 1006-1013.
8. Liu, M. (1993), *Numerical Prediction of Pavement Distress with Geotechnical Constitutive Laws*. Ph.D. Dissertation, Texas A&M University, College Station, TX.
9. Maree, J. H. (1978), *Design Parameters for Crushed Stone in Pavements*. MSc Thesis, University of Pretoria, Pretoria, South Africa.
10. Momoya, Y., Watanabe, K., Sekine, E., Tateyama, M., Shinoda, M., and Tatsuoka, F. (2005), "Effects of Continuous Principal Stress axis Rotation on the Deformation Characteristics of Sand under Traffic Loads", *Proc. of the 16th International Conference on Soil Mechanics and Geotechnical Engineering*, Vol.5, Osaka, Japan.
11. Park, S. and Lytton, R. (2004), "Effect of Stress-Dependent Modulus and Poisson's Ratio on Structural Responses in Thin Asphalt Pavements", *Journal of Transportation Engineering*, ASCE, 130(3), 387-394.
12. Park, S. (2005), "Prediction of Layer Rutting on Pavement Foundations Based on Stress Dependency", *Journal of Korean Geotechnical Society*, KGS, 21(7), 73-80.
13. Shackel, B. (1973), *Repeated Loading of Soils: A Review*. Australian Road Research, Kew, Victoria, Australia, 5(3), 22-49.
14. Titus-Glover, L. and Fernando, E. (1995), *Evaluation of Pavement*

- Base and Subgrade Material Properties and Test Procedures*. Research Report 1335-2, Texas Transportation Institute, College Station, TX.
15. Uzan, J. (1992), "Resilient Characterization of Pavement Materials", *International Journal for Numerical and Analytical Methods in Geomechanics*, 16(6), 435-459.
16. Uzan, J., Scullion, T., Michalek, C., Paredes, M., and Lytton, R. (1988), *A Microcomputer Based Procedure for Backcalculating Layer Moduli from FWD Data*. Research Report 1123-1, Texas Transportation Institute, College Station, TX.
17. Zhou, F. and Scullion, T. (2002), *VESYS5 Rutting Model Calibrations with Local Accelerated Pavement Test Data and Associated Implementation*. Research Report 1502-1, Texas Transportation Institute, College Station, TX.

(received on Jul. 7, 2006, accepted on Feb. 27, 2007)

Variation of Earth Pressure Acting on the Cut-and-Cover Tunnel Lining due to Geotextile Mat Reinforcement

지오텍스타일 매트 설치에 의한 개착식 터널 라이닝에 작용하는 토압의 변화

Bautista, F. E.¹ 펠디난드 이. 바우티스타 Park, Lee-Keun² 박 이 근
Im, Jong-Chul³ 임 중 철 Joo, In-Gon⁴ 주 인 곤

요 지

얕은 터널의 개착식 터널 라이닝에 발생하는 과잉토압은 라이닝의 변형과 손상을 유발하는 역학적 주요인자들 중의 하나이며(Kim, 2000), 과잉토압은 되메움토의 다짐불량, 자중에 의한 압밀, 강우의 침투에 의한 다짐, 차량에 의한 진동 등에 의해 발생할 수 있다(Komiya et al., 2000; Taylor et al., 1984; Yoo, 1997). 터널 라이닝에 발생하는 토압을 구하기 위한 많은 시험이 행해졌지만, 부등침하와 과잉토압을 줄일 수 있는 보강대책을 수립하기 위한 사례는 없다. 본 연구는 모래 지반에 1.0D~1.5D 깊이에 개착식으로 시공하는 원형의 강성 터널에 작용하는 토압에 관한 것으로 진동다짐의 영향을 모형실험에서 충분히 반영하기 위하여 100Hz의 진동주파수를 사용하였다. 본 연구에서는 개착식 터널 라이닝에 작용하는 부등침하와 과잉토압을 줄이기 위해서 지오텍스타일 매트를 설치하였다. 지오텍스타일 매트의 보강에 의한 부등침하와 토압의 감소효과를 확인하기 위해 실내모형실험을 수행하였다. 실내모형실험에서 토피, 매트 보강형태, 절취면의 거칠기 등을 달리하여 가장 효과적인 방법을 구하였다. 절취면의 거칠기 달리하기 위해 사면에 사포#100, 사포#400과 acetate 부착하였습니다. 무보강과 매트 보강에 대한 모형실험을 실시하여 구한 토압을 비교하여 매트 보강효과를 살펴보았으며, 사진분석법(Park, 2003)을 이용하여 지반의 변형을 분석하였다.

Abstract

Excessive earth pressure is one of the major mechanical factors in the deformation and damage of Cut-and-Cover Tunnel lining in shallow tunnels and portals of mountain tunnels (Kim, 2000). Excessive earth pressure may be attributed to insufficient compaction and consolidation of backfill material due to self-weight, precipitation and vibration caused by traffic (Komiya et al., 2000; Taylor et al., 1984; Yoo, 1997). Even though there were a lot of tests performed to determine the earth pressure acting on the tunnel lining, unfortunately there were almost no case histories of studies performed to determine remedial measures that reduce differential settlement and excessive earth pressure. In this study the installation of geotextile mat was selected to reduce the differential settlement and excessive earth pressure acting on the cut-and-cover tunnel lining. In order to determine settlement and earth pressure reduction effect (reinforcement effect) of geotextile mat reinforcement, laboratory tunnel model tests were performed. This study was limited to the modeling of rigid circular cut-and-cover tunnel constructed at a depth of 1.0D~1.5D in loose sandy ground and subjected to a vibration frequency of 100 Hz. Model tests with varying soil cover, mat reinforcement scheme and slope roughness were performed to determine the most effective mat reinforcement scheme. Slope roughness was adjusted by attaching sandpaper #100, #400 and acetate on the cut slope surface. Mat reinforcement effect of each mat reinforcement scheme were presented by the comparison of earth pressure obtained from the unreinforced and mat reinforced model tests. Soil settlement reduction was analyzed and presented using the Picture Analysis Method (Park, 2003).

Keywords : Cut-and-cover tunnel, Earth pressure, Geotextile, Tunnel lining, Tunnel model test

1 Member, Doctor Course-Pusan National Univ., Researcher of RIIT-PNU, denndenn@hotmail.com

2 Member, Ph.D., Post-Doc Researcher of BK21 Project, Pusan National Univ., theman4you@korea.com

3 Member, Ph.D., Prof., Dept. of Civil Engineering, Pusan National Univ., imjc@pusan.ac.kr

4 Member, Ph.D., Prof., School of Space Design, Busan College of Information Technology, igioo@bit.ac.kr

1. Introduction

Excessive surface settlement and excessive earth pressure are the two major problems encountered after the construction of cut-and-cover tunnels and mountain tunnel portals. These problems are caused by the consolidation of backfill material due to its self-weight or external forces in the form of precipitation and traffic vibration. At present there are several case studies regarding the earth pressure acting on cut-and-cover tunnel linings (Yoo, 1997; Kim, 1999) and tunnel lining behaviour (Lee et al., 1998; Kim, 2000). Unfortunately almost no case studies regarding the earth pressure reduction method are available.

Due to the increasing cases of tunnel lining cracks and damages due to excessive earth pressure and differential settlement of the restored soil cover, there is a need to find a simple, effective, and economical remedial measure that will solve both of these problems. The use of geotextile reinforcement method was considered since it is used to prevent differential settlement and to distribute loads in the construction of other engineering structures, especially in embankments (Venkatappa Rao et al., 1995; Koerner, 1986). In order to determine the feasibility of geotextile reinforcement in cut-and-cover tunnel construction, laboratory model test using a circular 1:20 scale rigid tunnel model was installed in a plane strain soil tank covered with $1.0D \sim 1.50D$ (D is the tunnel diameter) of loose sand with different geotextile mat reinforcement schemes. The plane strain soil tank was subjected to a vibration frequency of 100 Hz for a period of 10 minutes. Variation in soil cover, slope roughness and mat reinforcement schemes were applied. The soil settlement and earth pressure reduction of each mat reinforcement were

determined and the most efficient mat reinforcement scheme was recommended.

2. Tunnel Model Test Equipment and Testing Method

2.1 Test Equipment

The laboratory tunnel model tests with geotextile mat reinforcement were performed using the following equipments:

2.1.1 Plane Strain Soil Tank with Vibrating Motor

The plane strain soil tank with vibrating motor was the same as the soil tank used by Im et al. (2002) and Park (2003). In this study a vibration motor was installed beneath the soil tank with a control unit that controls the vibration frequency and vibration period. The vibration frequency used was 100 Hz and the vibration period was 10 minutes based on the preliminary test performed by Bautista et al. (2006). The vibration generated by the motor was used to consolidate the model soil in the soil tank. Photo 1 shows the plane strain soil tank used in this study.

2.1.2 Transverse Tunnel and Cut Slope Model

The transverse tunnel and cut slope model used in this study are shown in Photo 2. The transverse tunnel made of 8 aluminum segments with a bi-directional load cell was installed on the center of each segment (Park, 2003) while the cut slope model was made of plyboard installed at an angle of 45° on both sides of the tunnel at a distance (G) $1D$ from the center of the tunnel. The tunnel model

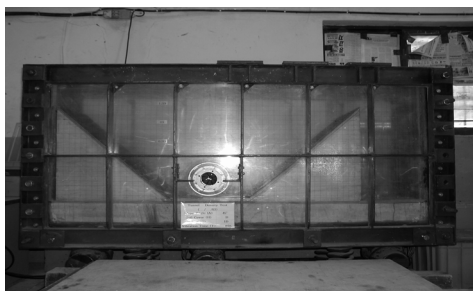


Photo 1. Plane Strain Soil Tank



Photo 2. Cut slope and tunnel model

was a 1:20 reduction of the actual tunnel size. The friction of transverse tunnel and cut slope were considered through the attachment of sand paper #100 for the tunnel and sand paper #100, #400 and acetate on the slope surface. Double sided adhesive tape was used to attach the sand paper and acetate to the model tunnel structure and slope surface. Sand paper #100 represents soil with sufficient slope roughness, sand paper #400 represents soil with medium slope surface roughness and acetate represents soil with almost no friction resistance.

2.1.3 Model Soil Laying Apparatus and Surface Leveling Device

Backfill soil was modeled using Sand Drop Method wherein the sand was dropped from a slot at a constant height and velocity. To ensure that the sand was layed at a uniform state close to minimum dry density (1.378 g/cm^3) of Jumunjin Standard Sand, a handheld slot with an opening of 3 mm was made of acrylic plates (Refer to Photo 3). Using this slot, loose sand with relative density of 38.9% was produced.

Surface leveling device or leveler was made of 2 acrylic plates connected by bolts and nuts (Refer to Photo 4). Holes were pre-drilled on the acrylic plate based on the depth of geotextile reinforcement location or surface level.

2.1.5 Deformation Monitoring Device

Due to the test condition of this study, the use of standard devices such as dial guage to determine the surface settlement and density cans to determine density was difficult. Instead, strings with weights attached on one end

were used to measure the initial and final surface settlement by lowering them from an aluminum channel placed longitudinally on the top of the soil tank (Refer to Photo 4). Markings made on the strings lowered from the aluminum channel indicate the surface level. The measured displacements were used in the calculation of the overall soil volume and density before and after the test.

Targets (Park, 2003) with a diameter of 1 cm installed at $2.5\text{ cm} \times 2.5\text{ cm}$ square interval on the front acrylic plate were covered with acetate (Refer to Photo 5). Pictures taken before, during and after the test were interpreted using Microstation. DALT Program (Park, 2003) was used on the interpreted values to determine the behaviour of soil around the tunnel.

2.2 Modelling Materials

2.2.1 Jumunjin Standard Sand

Jumunjin Standard Sand was used in the modelling of the soil material. The physical properties and particle size information of Jumunjin Standard Sand determined through laboratory tests were presented in Table 1 and Table 2, respectively.

Mechanical properties determined by using direct shear test, standard triaxial compression test and plane strain



Photo 3. Handheld Slot



Photo 4. Soil Leveler



Photo 4. Settlement monitoring apparatus



Photo 5. Target installed at a square interval

Table 1. Physical Properties

Physical Properties	Symbol	Unit	Value
Max. dry density	γ_{dmax}	g/cm ³	1.652
Min. dry density	γ_{dmin}	g/cm ³	1.378
Max. void ratio	e_{max}	–	0.923
Min. void ratio	e_{min}	–	0.604
Water content	w	%	0.300
Specific Gravity	G_s	–	2.650

Table 2. Particle Size Information

Physical Properties	Symbol	Unit	Value
Effective Diameter	D_{10}	mm	0.443
Average Diameter	D_{50}	mm	0.595
Maximum Diameter	D_{max}	mm	0.850
Curvature Coefficient	C_g	–	0.912
Uniformity Coefficient	C_u	–	1.402

compression test are shown in Table 3.

2.2.2 Geotextile Model Material

The geotextile mat reinforcements used in this experiment were polyester fabric screen and the properties are

presented in Table 4 based on the study performed by Joo (2000). The experiment was performed by varying the number of mat layers and installation location. During the installation, geotextile mat reinforcements were installed with a clear distance of 10 mm from the cut slope and model tunnel. The mat reinforcement used in this experiment is shown in Photo 6 and the installation is shown in Photo 7.

2.3 Earth Pressure Monitoring and Recording Device

8 bi-directional load cells were installed on each segment transverse tunnel model to monitor the earth pressure while UCAM-10A was used to record and print-out the monitored earth pressure. Even though there were 8 loadcells installed on the transverse tunnel, only 5 loadcells located on the crown, shoulder and sidewall portion were considered. The correction coefficient test was performed in order to determine whether there is coupling effect on the vertical and horizontal direction of the loadcell. The correction coefficients determined from the test were applied on the test results obtained from the tunnel model

Table 3. Mechanical Properties of Soil using Different Tests (Park, 2003)

Parameters	Test Types																	
	Direct Shear Test								Standard Triaxial Compression Test				Plane Strain Compression Test					
Number	1	2	3	4	5	6	7	8	1	2	3	4	1	2	3	4	5	6
γ_d (g/cm ³)	1.38	1.47	1.52	1.56	1.57	1.60	1.63	1.65	1.39	1.45	1.55	1.61	1.38	1.41	1.42	1.46	1.58	1.65
Dr (%)	0	36.9	57.0	70.7	74.4	84.3	93.8	98.2	6.9	29.9	66.9	86.9	0	11.6	15.8	31.9	77.1	98.5
ϕ_{TCT} (°)	31.2	33.0	35.0	33.7	38.0	39.2	41.1	42.0	31.2	33.4	36.5	41.3	36.4	35.8	36.8	39.6	46.1	51.1

Table 4. Properties of Mat Reinforcing Material (Joo, 2000)

Geotextile	Manufacture	Polymer Fiber	Tensile Strength (tf/m)	Tensile Strain (%)	Polymer Type
		Woven	Monofilament	0.278	26.46

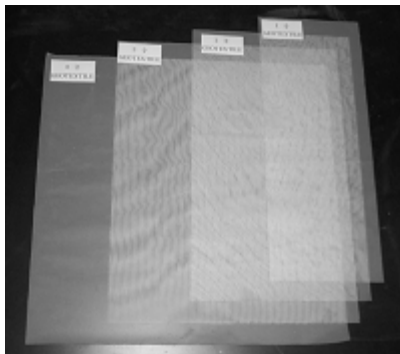


Photo 6. Geotextile reinforcements



Photo 7. Geotextile Installation

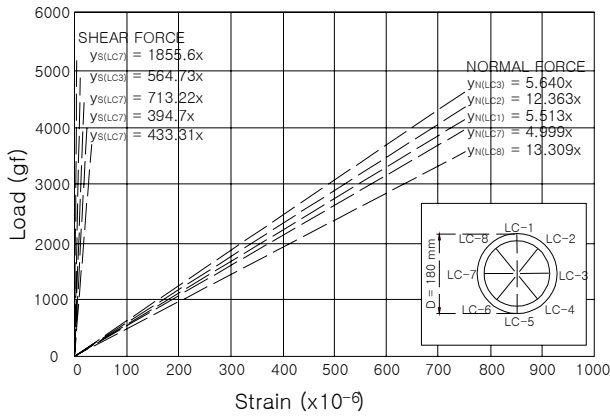


Fig. 1. Loadcell Installation Diagram and Calibration

test. The loadcell installation layout and calibration of the loadcell installed in the tunnel segment are shown in Fig. 1. The correction coefficient test showed that there was no coupling effect on the loadcells.

2.4 Test Method

In this study the earth pressure acting on an cut-and-cover tunnel with soil covers of 1.0D ~ 1.5D at a slope angle of 45° was determined through model tests. Earth pressure reduction of geotextile reinforcement (referred as mat reinforcement effect) for each reinforcement scheme was determined based on the comparison of measured earth pressure acting on the tunnel for unreinforced and reinforced model tests. Tests performed in this study can be divided into 3 major groups, namely:

- (1) Model Test with Varying Soil Cover
- (2) Model Test with Varying Mat Reinforcement
- (3) Model Test with Varying Slope Roughness

2.4.1 Types of Tests

The types of tests and its respective test conditions are shown in Table 4 and were graphically presented in Figure 2 to Figure 4. In this study, the tests were

Table 4. Test Types and Test Conditions

Test Designation	Soil Cover (H)	Reinforcement Type & Location	Slope Surface
1.0D-NR-100	1.0D	no reinforcement	Sandpaper #100
1.0D-1T-100		1 layer top reinforcement (0.5D from top of tunnel)	
1.0D-2T-100		2 layer top reinforcement (0.3D & 0.6D from top of tunnel)	
1.0D-2S-100		2 layer side reinforcement (0.5D & 1.0D from bottom of tunnel)	
1.0D-4S-100		4 layer side reinforcement (0.5D, 1.0D, 1.3D & 1.6D from bottom of tunnel)	
1.0D-2S2T-100		2 layer top & 2 layer side reinforcement (0.5D, 1.0D, 1.3D & 1.6D from bottom of tunnel)	
1.5D-NR-100	1.5D	no reinforcement	Sandpaper #100
1.5D-1T-100		1 layer top reinforcement (0.75D from top of tunnel)	
1.5D-2T-100		2 layer top reinforcement (0.5D & 1.0D from top of tunnel)	
1.5D-2S-100		2 layer side reinforcement (0.5D & 1.0D from bottom of tunnel)	
1.5D-4S-100		4 layer side reinforcement (0.5D, 1.0D, 1.5D & 2.0D from bottom of tunnel)	
1.5D-2S2T-100		2 layer top & 2 layer side reinforcement (0.5D, 1.0D, 1.3D & 1.6D from bottom of tunnel)	
1.5D-NR-400	1.5D	no reinforcement	Sandpaper #400
1.5D-2S2T-400		2 layer top & 2 layer side reinforcement (0.5D, 1.0D, 1.3D & 1.6D from bottom of tunnel)	
1.5D-NR-ACE		no reinforcement	Acetate
1.5D-2S2T-ACE		2 layer top & 2 layer side reinforcement (0.5D, 1.0D, 1.3D & 1.6D from bottom of tunnel)	

designated by a combination of numbers and letters as shown below:

$$\frac{1.5D}{\text{Soil Cover}} - \frac{2S2T}{\text{Reinforcement Type}} - \frac{100}{\text{Slope Material}}$$

The first two numbers represents the soil cover with respect to the diameter of the tunnel (D). The second set of numbers and letters represent the reinforcement type, the numbers representing the number of reinforcement and the letters representing the location. The letter “S” means that the inforcement is on the side of the tunnel and letter “T” meaning the reinforcement is on the top of the tunnel. “NR” is used in case there were “no reinforcements” used in the model test. The last portion of the test designation represents the type of material used on the cut slope. It can be “100” for Sandpaper #100, “400” for Sandpaper #400 or “ACE” for acetate.

2.4.1.1 Model Tests with Varying Soil Cover

Model tests representing the tunnel structure with varying soil cover were performed. The most conservative slope angle of 45° used in actual construction was selected for this study. The depth of soil cover is represented by the tunnel diameter (D). The test when it comes to soil cover is divided into 1.0D and 1.5D. The schematic diagram of the model test is presented in Fig. 2 and Fig. 3.

2.4.1.2 Model Tests with Varying Mat Reinforcement

In order to minimize excessive surface settlement and earth pressure, laboratory model test with different types of soil reinforcement method were performed. One un-reinforced test and five different mat reinforcement tests were performed (Refer to Fig. 4). In the figure, D is the

tunnel diameter, G is the distance between slope and tunnel, H is the soil cover, LC is the bi-directional loadcell and θ is the slope angle. The reinforcement effect was determined by comparing the surface settlement and earth pressure obtained from unreinforced and mat reinforced model tests.

2.4.1.3 Model Tests with Varying Slope Roughness

To determine the effect of slope roughness on the soil behaviour of soil, earth pressure and other geometric factors, 2 types of sandpaper (#100 and #400) and acetate were used to simulate the roughness of the slope surface. The smoothness of the material used to cover the cut slope surface represents the friction resistance. Generally, the cut slope possesses friction resistance which may depend on the soil material. In this test, general types of soil was model using sandpaper #100, and slope with little friction resistance was represented by sandpaper #400, while acetate represents soil with almost zero friction resistance.

2.4.2 Test Sequence

This study was performed based on the following sequence:

- a) Installation of cut slope and tunnel model
- b) Initialization of Load cell
- c) Laying of model soil using handheld slot and target installation on every 2.5 cm of model soil
- d) Installation of geotextile model for reinforced model test
- e) Surface leveling and monitoring of initial earth pressure and surface settlement
- f) Picture taking of the initial soil condition before vibration
- g) Vibration of soil tank at 100 Hz for 10 minutes

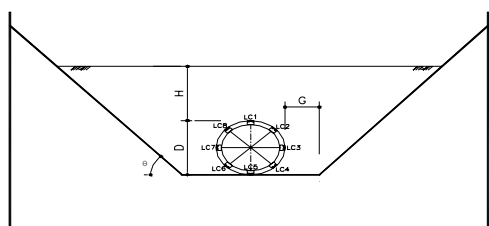


Fig. 2. Test Diagram for 1.0D Soil Cover

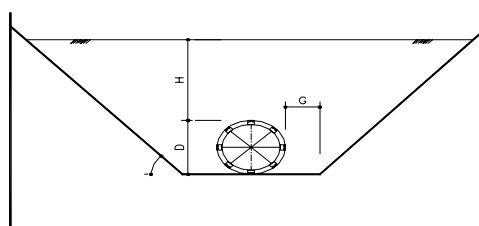


Fig. 3. Test Diagram for 1.5D Soil Cover

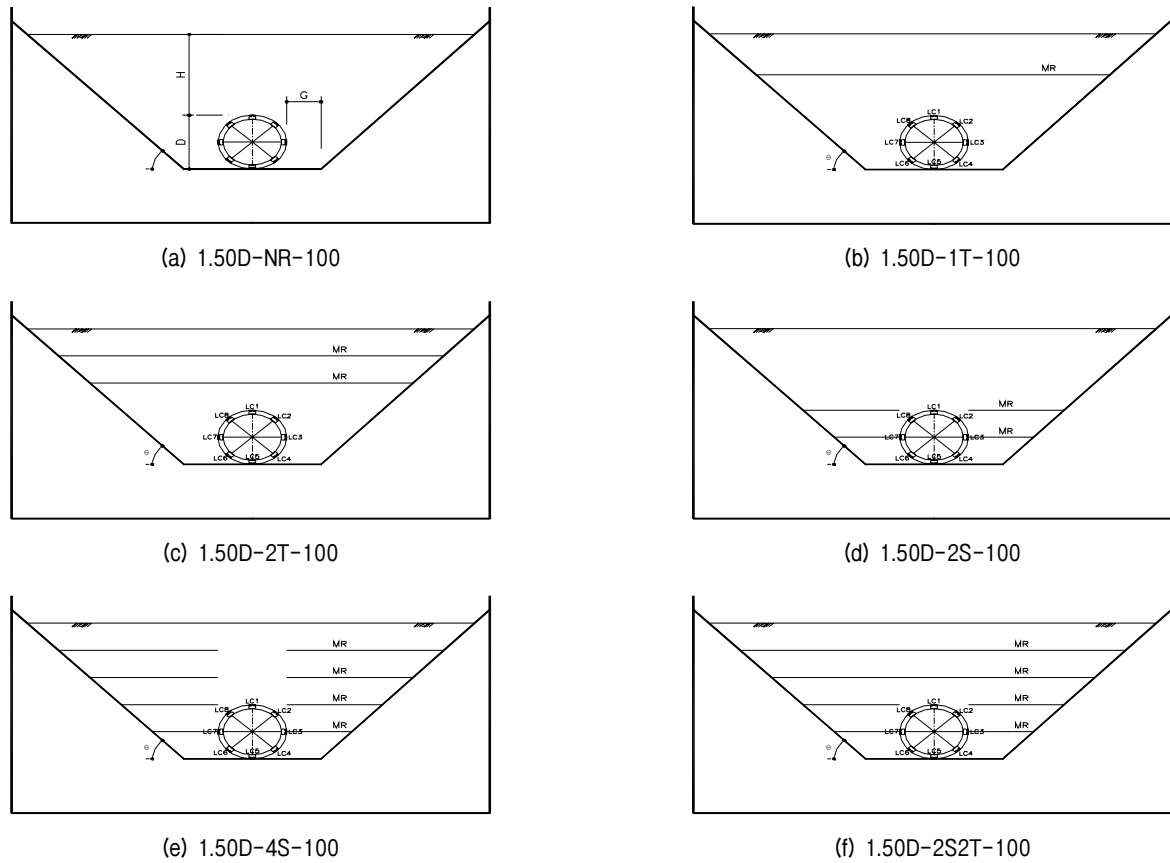


Fig. 4. Mat Reinforcement Scheme

- h) Picture taking of the final soil condition after vibration
- i) Monitoring of the final earth pressure and surface settlement
- j) Test data arrangement and analysis

3. Result of the Tunnel Model Test

After the soil tank was subjected to a vibration of 100 Hz for a period of 10 minutes an average dry density of 1.537 g/cm^3 and a relative density of 66.9% were

Table 5. Variation of Earth Pressure with 1.0D Soil Cover

Load Cell Location	Earth Pressure Before Vibration (gf/cm^2)						Earth Pressure After Vibration (gf/cm^2)						
	NR	1T	2T	2S	4S	2S2T	NR	1T	2T	2S	4S	2S2T	
Crown	41.110	35.765	34.532	33.504	30.421	33.093	57.142	54.676	56.937	55.087	55.909	51.593	
Shoulder	Right	15.924	16.332	15.720	16.332	14.290	14.903	19.394	22.661	22.252	23.477	22.252	22.456
	Left	18.578	19.394	23.477	23.273	24.090	26.744	25.723	23.477	24.294	24.294	19.803	20.823
Sidewall	Right	16.740	16.944	21.027	26.948	27.356	29.602	20.415	21.027	18.872	14.903	16.332	15.311
	Left	15.515	15.924	16.740	13.066	14.903	14.903	22.456	37.768	23.681	31.847	41.034	43.280

Table 6. Variation of Earth Pressure with 1.50D Soil Cover

Load Cell Location	Earth Pressure Before Vibration (gf/cm^2)						Earth Pressure After Vibration (gf/cm^2)						
	NR	1T	2T	2S	4S	2S2T	NR	1T	2T	2S	4S	2S2T	
Crown	50.770	49.126	46.659	50.976	49.537	47.687	96.608	90.852	89.002	96.197	80.896	79.753	
Shoulder	Right	24.702	23.886	24.702	26.131	20.415	22.661	30.418	34.705	34.297	36.135	36.339	33.889
	Left	21.232	21.640	21.844	23.477	39.809	30.214	30.214	31.031	34.501	34.501	30.010	32.256
Sidewall	Right	31.235	37.155	42.463	38.788	30.418	33.072	19.803	18.169	17.761	12.045	14.086	12.861
	Left	30.214	33.276	27.152	38.788	20.415	18.986	35.318	40.626	42.055	40.013	39.605	39.401

Table 7. Variation of Earth Pressure with Slope Roughness at 1.50D Soil Cover

Load Cell Location		Earth Pressure Before Vibration (gf/cm^2)						Earth Pressure After Vibration (gf/cm^2)					
		100		400		ACE		100		400		ACE	
		NR	2S2T	NR	2S2T	NR	2S2T	NR	2S2T	NR	2S2T	NR	2S2T
Crown		50.770	47.687	49.126	46.043	50.154	45.837	96.608	79.753	90.236	88.591	66.803	83.658
Shoulder	Right	24.702	22.661	22.456	21.232	22.252	23.273	30.418	33.889	33.072	38.993	37.972	41.034
	Left	21.232	30.214	20.619	19.598	20.007	21.232	30.214	32.256	32.664	35.930	33.276	33.685
Sidewall	Right	31.235	33.072	37.768	38.176	38.788	41.442	19.803	12.861	35.114	14.086	25.110	46.138
	Left	30.214	18.986	32.868	40.830	36.747	40.422	35.318	39.401	47.159	47.363	62.062	140.659

obtained. The measured earth pressures before and after vibration for model tests with 1.0D and 1.50D soil cover are shown in Table 5 and Table 6, respectively. The measured earth pressures for each model test with different slope roughness at 1.50D soil cover are shown in Table 7.

3.1 Analysis of Earth Pressure Reduction Around the Tunnel

Earth pressure reduction is determined by comparing the different reinforcement model tests with the unreinforced model test (NR). Difference in earth pressure and mat reinforcement effect due to the installation of geotextile reinforcement for each reinforcement scheme is presented below. In this test a negative value indicates increase in earth pressure and a positive value indicates reduction in earth pressure.

3.1.1 Model Test with Different Soil Cover

3.1.1.1 Model Test with 1.0D Soil Cover

Table 8 shows the difference in earth pressure and mat reinforcement effect of each mat reinforcement scheme after vibration with the earth pressure of the unreinforced test (NR) as the basis. Considering the reduction in earth pressure due to reinforcement type, it can be seen that there is a reduction in reinforcement effect as the mat reinforcement increase. This is visible in the comparison of the values of 1T and 2T and in the values of 2S and 4S. For 1D, the reinforcement effect is not only affected by the number of reinforcement but also by the location of mat reinforcement.

3.1.1.2 Model Test with 1.50D Soil Cover

Table 9 shows the reduction in earth pressure for each mat reinforcement scheme after vibration. For 1.5D, the mat reinforcement effect was influenced by 3 factors,

Table 8. Earth Pressure Reduction with Reinforcement Type (1.0D Soil Cover)

Load Cell Location		Earth Pressure in gf/cm^2 (Reinforcement Effect in %)				
		1T	2T	2S	4S	2S2T
Crown		2.47 (4.3)	0.21 (0.4)	2.06 (3.6)	1.23 (2.2)	5.55 (9.7)
Shoulder	Right	-3.27 (-16.8)	-2.86 (-14.7)	-4.08 (-21.1)	-2.86 (-14.7)	-3.06 (-15.8)
	Left	2.25 (8.7)	1.43 (5.6)	1.43 (5.6)	5.92 (23.0)	4.90 (19.0)
Sidewall	Right	-0.61 (-3.0)	1.54 (8.0)	5.51 (27.0)	4.08 (20.0)	5.10 (25.0)
	Left	-15.31 (-68.2)	-1.22 (-5.5)	-9.39 (-41.8)	-18.58 (-82.7)	-20.82 (-92.7)

Table 9. Earth Pressure Reduction w/ Reinforcement Type After Vibration(1.5D Soil Cover)

Load Cell Location		Earth Pressure in gf/cm^2 (Reinforcement Effect in %)				
		1T	2T	2S	4S	2S2T
Crown		5.76 (6.0)	7.61 (7.9)	0.41 (0.4)	15.72 (16.2)	16.86 (17.4)
Shoulder	Right	-4.29 (-14.1)	-3.88 (-12.8)	-5.72 (-18.8)	-5.92 (-19.5)	-3.47 (-11.4)
	Left	-0.82 (-2.7)	-4.29 (-14.2)	-4.29 (-14.2)	0.20 (0.7)	-2.04 (-6.8)
Sidewall	Right	1.63 (8.2)	2.04 (10.3)	7.76 (39.2)	5.72 (28.9)	6.94 (35.1)
	Left	-5.31 (-15.0)	-6.74 (-19.1)	-4.70 (-13.3)	- 4.29 (-12.1)	-4.08 (-11.6)

namely: (a) number of mat reinforcement, location of mat reinforcement and soil cover. The mat reinforcement effect has the tendency to increase with the increase in the number of mat reinforcement and soil cover. This phenomenon was visible in the comparison of the results of 1T and 2T, and 2S and 4S. Similar to 1.0D, the location of mat reinforcement was also a significant factor.

3.1.2 Model Test with Different Reinforcement Scheme

3.1.2.1 Model Test with Different Reinforcement Scheme at 1.0D Soil Cover

Based on Table 8, the earth pressure acting on the crown portion was reduced by 2~10% except for 2T wherein there was almost no reduction. By comparing the numerical values tabulated in Table 8 it can be seen that 2S2T reinforcement is the most efficient reinforcement scheme when it comes to the reduction of earth pressure

acting on the tunnel crown. On the shoulder portion, reduction of 5~23% was measured on the left side while there was an increase of 14~21% on the right side. If we were to consider the reduction of earth pressure, 4S and 2S2T are the most efficient reinforcement scheme with a reinforcement effect of 23% and 19%, respectively. For the left sidewall portion, there was 8~27% reduction in earth pressure for all reinforcement types except for 1T wherein there was a 3% increase. For the right sidewall portion, there was 5~92% increase in earth pressure for all reinforcement types. Considering only the reduction of earth pressure it can be seen that 2S and 2S2T are the most effective reinforcement schemes in the reduction of earth pressure acting on the tunnel sidewalls with a reinforcement effect of 27% and 25%. Considering the overall reduction on the earth pressure acting on the tunnel structure, 2S2T is the most effective reinforcement scheme

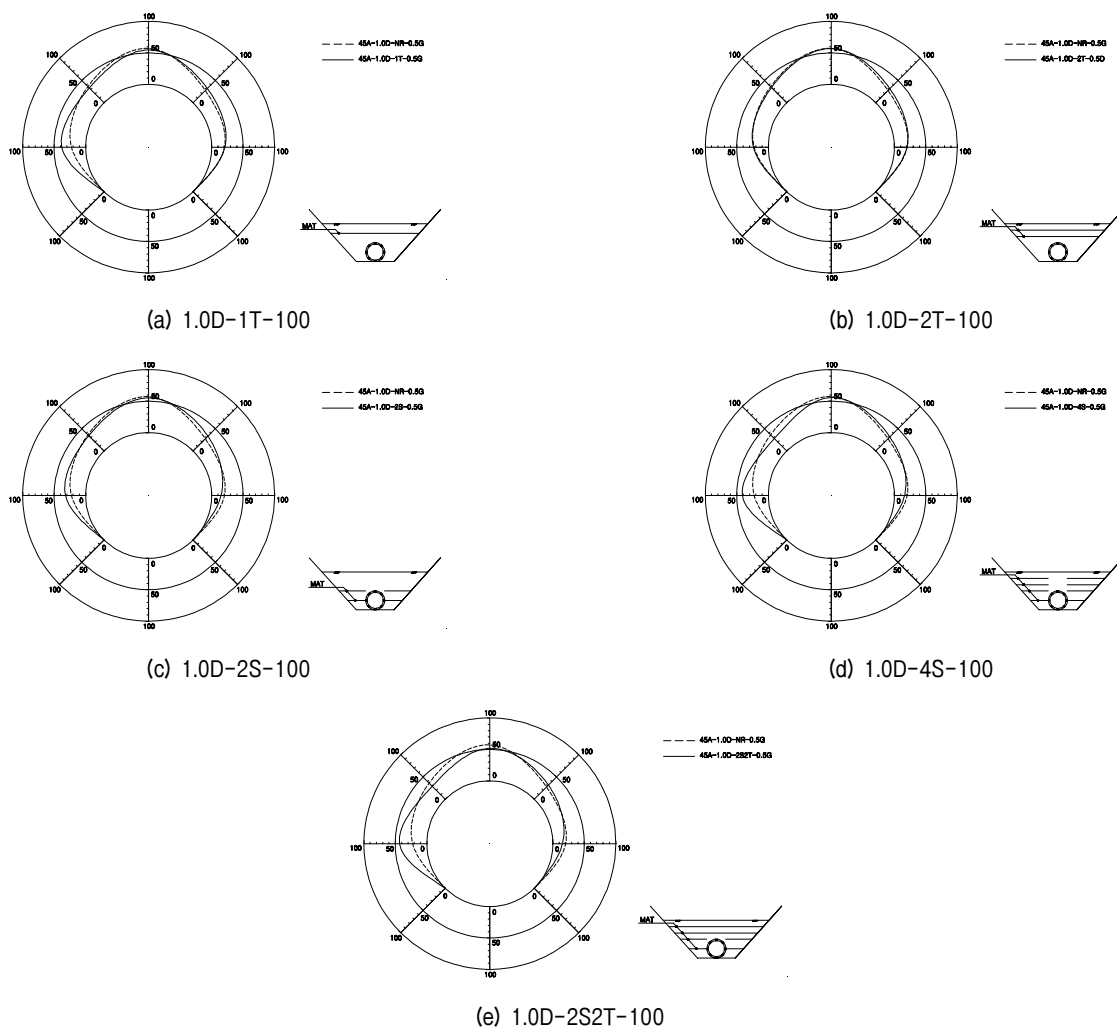


Fig. 5. Earth Pressure Reduction with Reinforcement Type (1.0D Soil Cover)

for soil model tests with 1.0D soil cover.

Fig. 5 shows the graphical representation of the mat reinforcement effect on the earth pressure acting on the tunnel structure for model tests with 1.0D soil cover. The broken line represents the earth pressure of the unreinforced soil acting on the tunnel structure while the solid lines represents the reduced earth pressure for each type of reinforcement.

3.1.2.2 Model Test with Different Reinforcement Scheme at 1.50D Soil Cover

Based on the examination of the numerical values presented in Table 9 and the plots shown in Fig. 6, it can be seen that 2S2T is the most effective reinforcement scheme in the reduction of earth pressure acting at the tunnel crown with a reinforcement effect of 17%. This was followed by 4S with 16%, 2T with 8%, 1T with 6% and 2S with 0.4% which has almost no reinforcement effect. For the shoulder portion, there was an overall increase in the earth pressure for all reinforcement. An increase of 2~18% was measured. When it comes to the sidewall portion, 2S and 2S2T are the most efficient reinforcement schemes when it comes to the earth pressure acting on the sidewalls with 39% and 35% earth pressure reduction.

Similar to what was obtained from the results of the model tests with 1.0D soil cover, 2S2T was the most effective reinforcement scheme in reducing the overall earth pressure acting on the tunnel structure. An increase in earth pressure for some portions of the tunnel was monitored.

3.1.2.3 Model Test with Varying Slope Roughness at 1.50D Soil Cover

Table 10 shows the earth pressure reduction effect of 2S2T with the slope roughness for tunnels with 1.50D soil cover. It can be seen in this table that 2S2T is very effective when it comes to 100, with 17% and 35% reduction on the crown and sidewalls, respectively. The mat reinforcement effect was not seen for 400 and ACE. For 400, there was only a 2% reduction at the crown portion while there was a 10~18% earth pressure increase at the shoulder portion. For ACE, 2S2T increased the earth pressure in all portions of the tunnel. This is due to the roughness of the cut slope. When there is low friction resistance (400) and zero resistance (ACE) excessive shear strain occurs between the boundary of the original soil and the backfill material (Refer to Fig. 12 (e) & (g)). The mat reinforcement fails to distribute the load and the load has the tendency to concentrate on the shoulder and sidewall portions of the tunnel.

3.1.3 Analysis of Results

The numerical and graphical results show considerable differences between the values monitored from the left side and the right side of the tunnel. Reduction in earth pressure occurred on the left side while an increase in earth pressure occurred on the right side of the tunnel. Since the soil tank was subjected to vibration in order to induce soil settlement, the difference in the result can be attributed to transmission of vibration influenced by several factors. These factors are: (a) rigidity of the soil structure, (b) soil tank structure and supporting elements and (c) location of vibrator (due to the frame of the soil tank the vibrator was installed slightly to the left of the tunnel).

Table 10. Earth Pressure Reduction w/ Slope Roughness After Vibration (1.5D Soil Cover)

Load Cell Location		Type of Reinforcement (Reinforcement Effect, %)		
		100-2S2T	400-2S2T	ACE-2S2T
Crown		16.86 (17.4)	1.65 (1.8)	-16.86 (-25.2)
Shoulder	Right	-3.47 (-11.4)	-5.92 (-17.9)	-3.06 (-8.1)
	Left	-2.04 (-6.8)	-3.27 (-10.0)	-0.41 (-1.2)
Sidewall	Right	6.94 (35.1)	21.03 (59.9)	-21.03 (-83.7)
	Left	-4.08 (-11.6)	-0.20 (-0.4)	-78.60 (-126.6)

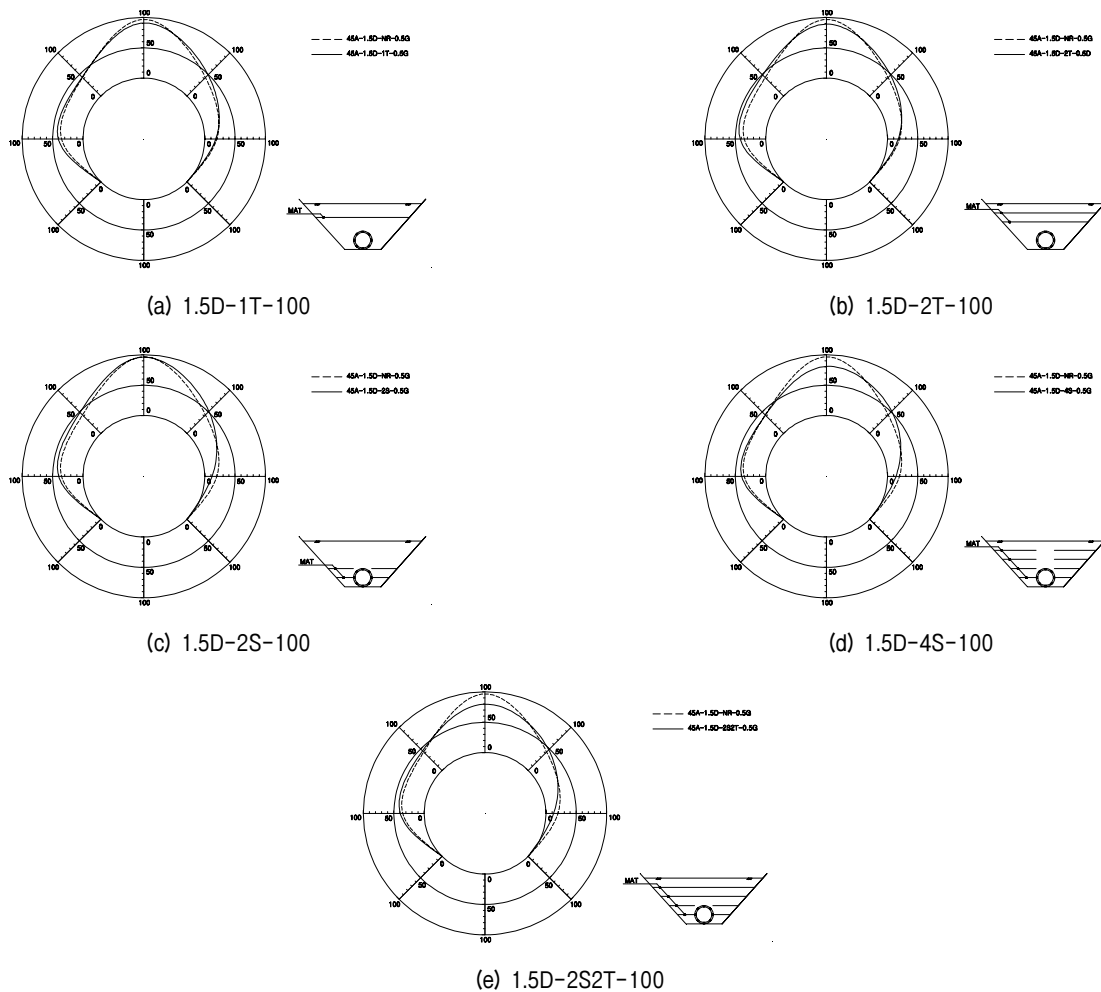


Fig. 6. Earth Pressure Reduction with Reinforcement Type (1.50D Soil Cover)

The numerical differences and the percentages were presented. In this test, the magnitude of earth pressure reduction or increase is not important. What is important is the fact that the installation of mat reinforcement effectively reduces the soil settlement and earth pressure acting on the tunnel lining.

3.2 Picture Analysis

Pictures of the model test were taken before, during and after the test to determine the behaviour of soil around the tunnel. Pictures were interpreted using Microstation and analyzed using DALT Program(Park, 2003). The results are presented below.

3.2.1 Behaviour of Soil around the Cut-and-Cover Tunnel

3.2.1.1 Model Test with 1.0D Soil Cover

Fig. 7 shows the mat reinforcement effect on the settlement of soil around the tunnel structure for model tests with 1.0D soil cover. When it comes to the reduction of soil settlement around the tunnel at 1.0D soil cover, 2T was the most effective as can be seen from the figures below, followed by 1T and 4S with similar soil settlement reduction and 2S2T with the less soil settlement reduction effect.

3.2.1.2 Model Test with 1.50D Soil Cover

Fig. 10 shows the mat reinforcement effect on the settlement of soil around the tunnel structure for model tests with 1.50D soil cover. For model tests with 1.50D soil cover, 1T, 2T and 2S can be considered the most

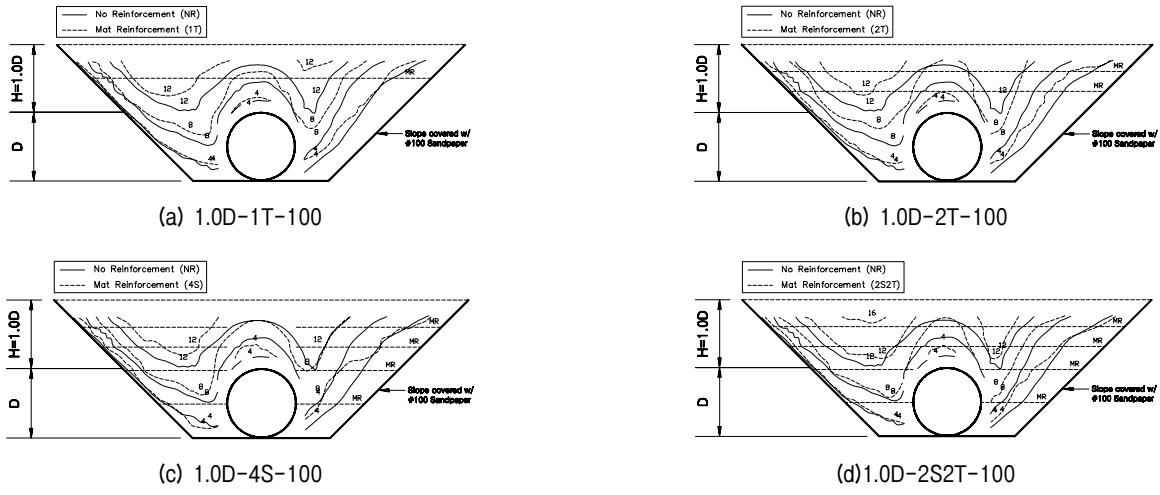


Fig. 7. Partial soil displacement contour at 1.0D Soil Cover

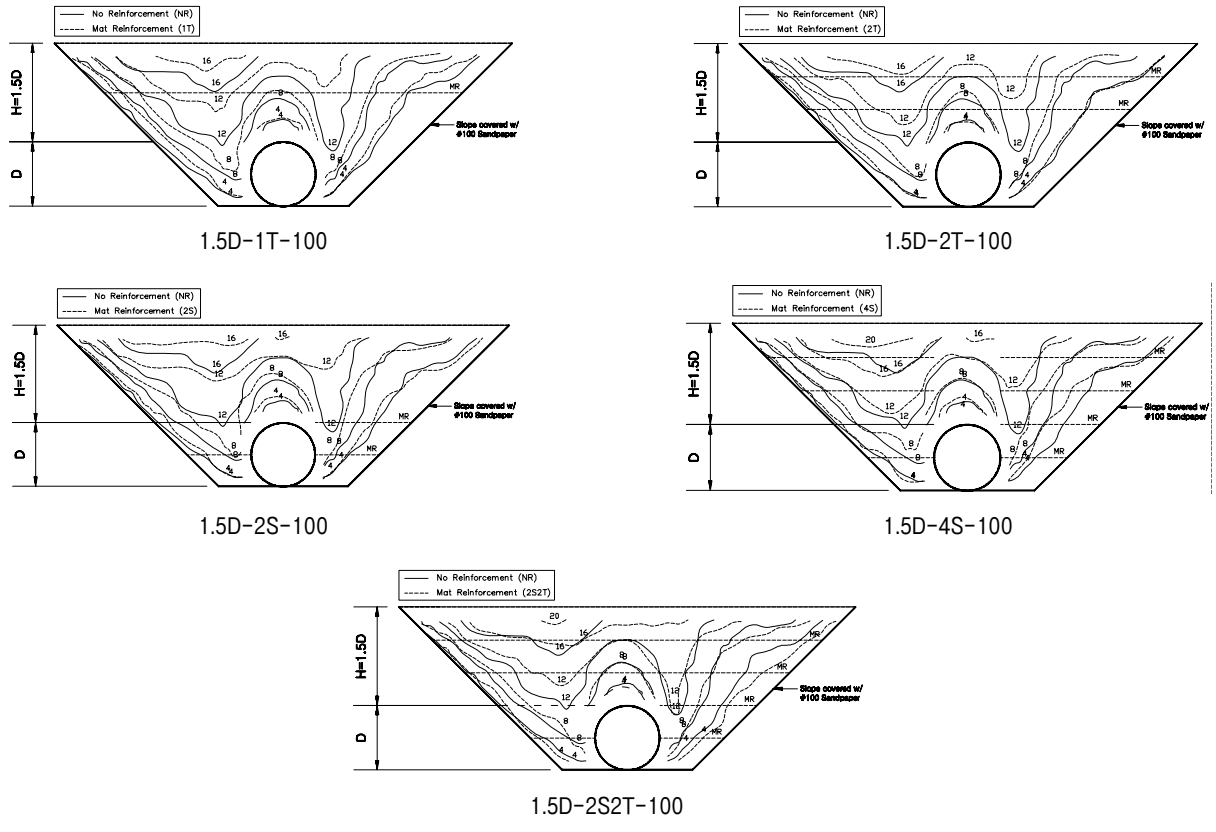


Fig. 8. Partial soil displacement contour at 1.50D Soil Cover

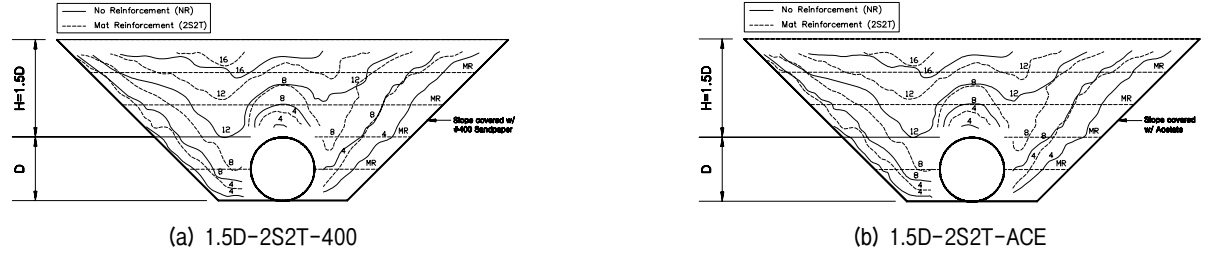


Fig. 9. Partial soil displacement contour at 1.50D Soil Cover

effective in the reduction of soil settlement around the tunnel as can be seen from the figures below, followed by 4S and 2S2T with similar soil settlement reduction. 2S2T was the most effective mat reinforcement scheme in the earth pressure reduction and it has the least soil settlement reduction effect around the tunnel.

3.2.1.3 Model Test with Varying Slope Roughness at 1.50D Soil Cover

Fig. 9 shows the mat reinforcement effect on the settlement of soil around the tunnel structure for model tests with varying slope roughness at 1.50D soil cover. The following figures show that there was less settlement for the mat reinforced soil (2S2T) as represented by the broken line compared to the unreinforced soil (NR) represented by the solid lines for both 400 and ACE.

Even though 2S2T was not effective in reducing the

earth pressure acting on the tunnel lining with varying slope roughness, it can be seen in the following figures that the mat reinforcement was effective in reducing the soil settlement around the tunnel.

3.2.2 Other Results

Results which include soil displacement contour diagram, soil displacement vector, zero extension direction and maximum shear strain contour diagram are presented in the figures below. For comparison purposes the unreinforced and reinforced model tests results are presented side by side. Fig. 10 shows the soil displacement contour diagram of the unreinforced test (NR) and most effective reinforcement scheme (2S2T). To clearly show the mat reinforcement effect, the soil behaviour around the tunnel was redrawn from the soil displacement contour and presented in Fig. 7. On the left side was drawn model

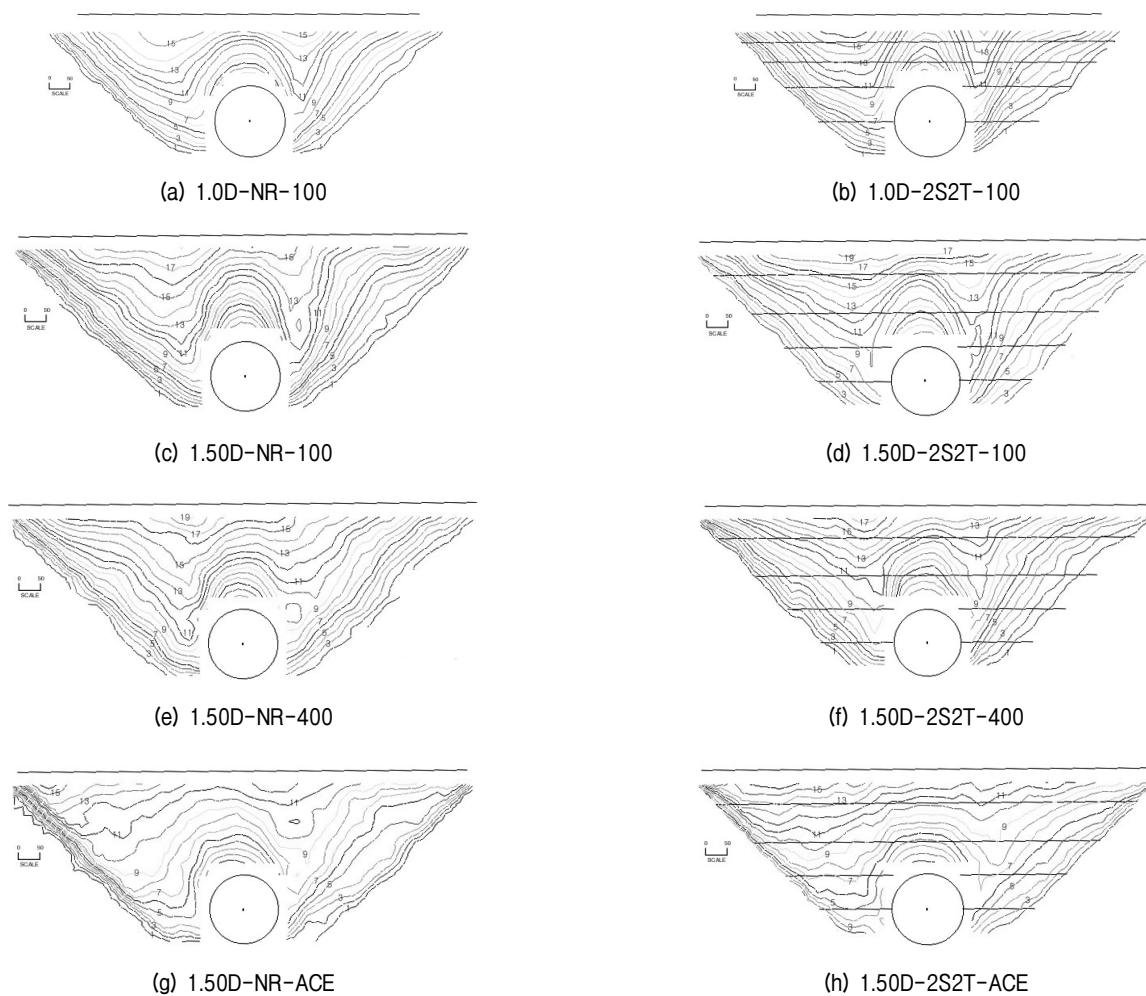


Fig. 10. Soil Displacement Contour Diagram

test with no reinforcement (NR) and model test with 2S2T reinforcement on the right side. It can be seen from the figures on the left that the mat installation has reduced the soil displacement. The mat reinforcement effect can be seen on the contour diagram on the right side. There was an overall reduction in soil displacement on all the tests performed.

Fig. 11 shows the zero extension direction diagram. Zero extension direction diagram shows the location of the failure plane. The point with a concentration of x represents the failure plane. In the case of this test the failure plane occurs between the original soil and backfill material. It can be seen that with installation of mat reinforcement the concentration of “x” was greatly reduced (Refer to Fig. 11 (b), (d), (f) & (h)). The installation of mat reinforcement prevents the occurrence of the failure surface.

Fig. 12 shows the maximum shear strain contour diagram. This diagram shows the concentration of shear strain location where failure will occur. Based on the zero extension direction and maximum shear strain contour diagram the location of failure surface can be determined. Comparing tests with different slope roughness at 1.50D soil cover shows excessive concentration shear strain along the slope with little friction resistance (400) and zero friction resistance (ACE). Diagrams in Fig. 12 (b), (d), (f) & (h) show a reduction of shear strain due to the installation of mat reinforcement.

Considering the zero extension direction and maximum shear strain contour diagram, it can be seen that failure surface occurs in the boundary between the original soil and backfill material. This can be seen in model tests with 1.0D and 1.5D soil cover. This phenomenon can be clearly seen in the 1.5D-ACE wherein the slope is covered with

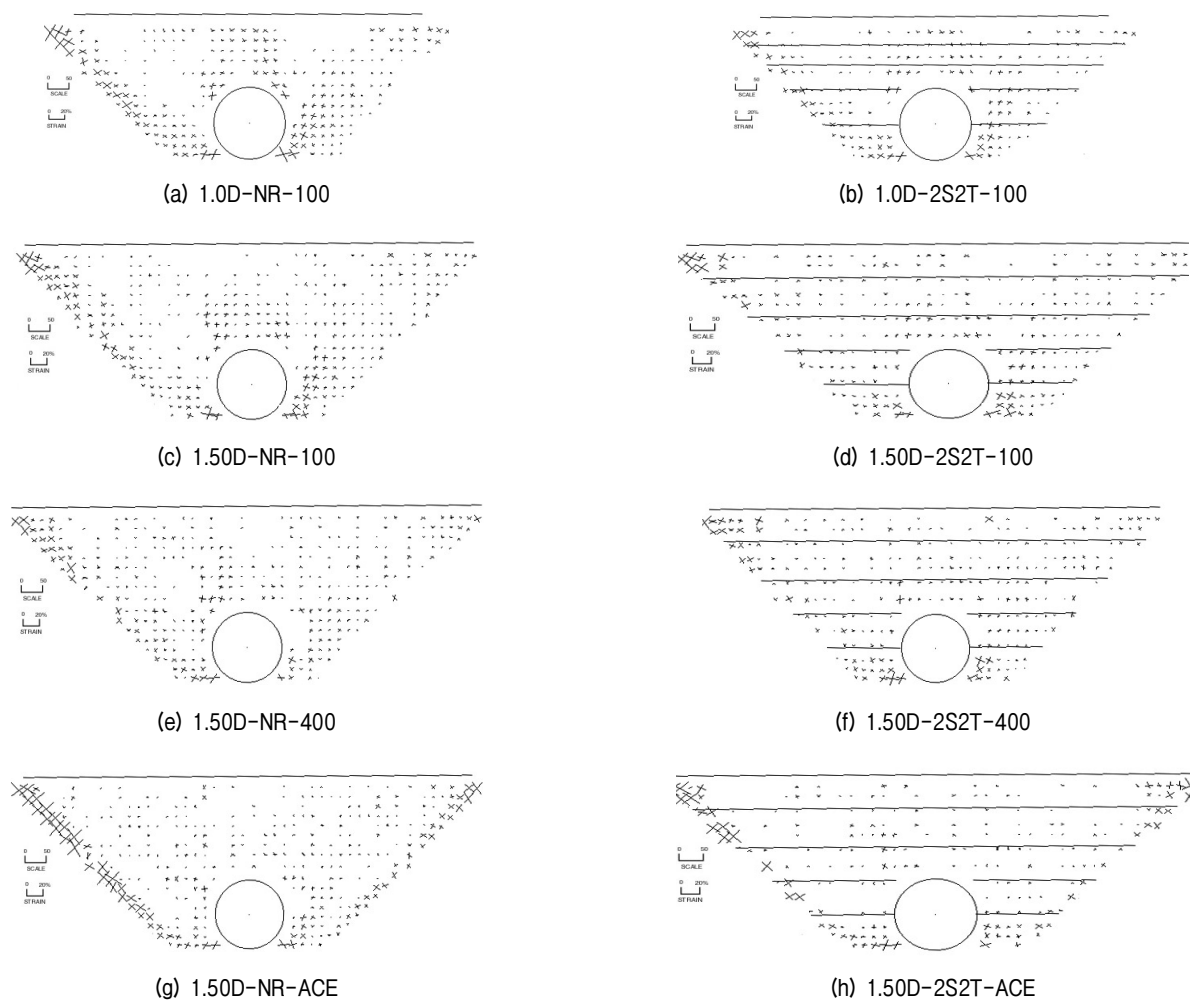


Fig. 11. Zero Extension Direction Diagram

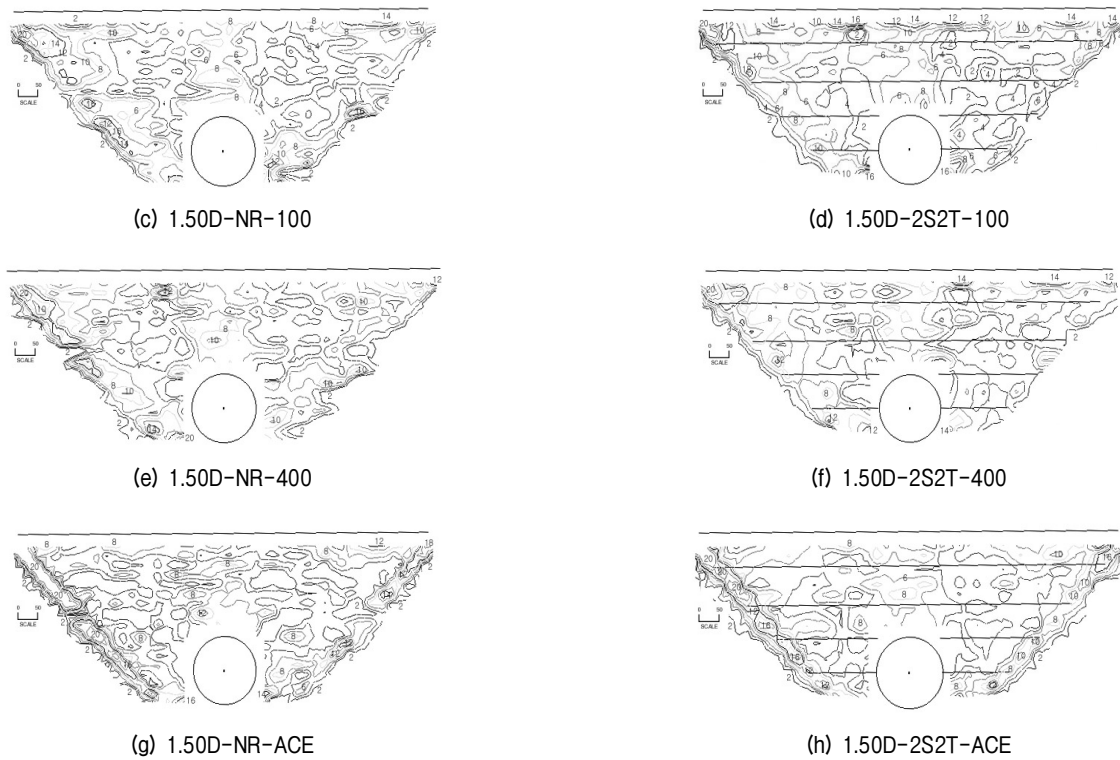


Fig. 12. Maximum Shear Strain Contour Diagram



Fig. 13. Maximum Shear Strain Contour Diagram

acetate.

4. Conclusion

Installation of geotextile mat reinforcement has been applied in other engineering construction like embankments and reclamations but there were no case histories wherein geotextile mat reinforcement was applied in cut-and-cover tunnel construction. In this study the application of geotextile mat reinforcement was recommended to reduce excessive surface settlement and earth pressure acting on the cut-and-cover tunnel lining through laboratory model test. In order to determine the feasibility of geotextile reinforcement in cut-and-cover tunnel construction, laboratory model test using a circular rigid 1:20 scale tunnel model was installed in a plane strain soil tank covered

with 1.0D~1.50D (D is the tunnel diameter) of loose sand with different geotextile mat reinforcement schemes. The plane strain soil tank was subjected to a vibration frequency of 100 Hz for a period of 10 minutes. Through the comparison of the results obtained from the unreinforced and reinforced model tests, the most effective mat reinforcement scheme for different soil cover and slope roughness was recommended. The following conclusion were obtained from this study:

- (1) Mat reinforcements installed above and beside the tunnel significantly reduced the earth pressure acting on the lining.
- (2) For tunnels with 1.0D soil covers, the mat reinforcement effect was affected by 2 major factors: namely, number of mat reinforcement and location of mat

reinforcement. Increase of mat reinforcement in the same location has the tendency to reduce the reinforcement effect as can be seen in the reduction in reinforcement effect between 1T and 2T, and 2S and 4S.

- (3) Among all the mat reinforcement schemes implemented, 2S2T was the most effective mat reinforcement scheme for tunnels with 1.0D soil covers.
- (4) For tunnels with 1.50D soil covers, the mat reinforcement effect has the tendency to increase with the number of mat reinforcement. Among all the reinforcement schemes 2S2T and 4S were the most effective. But when it comes to overall earth pressure reduction effect 2S2T was considered as the most effective.
- (5) For 2S2T, earth pressure reduction of as much as 10%, 19% and 25% on the crown, shoulder and sidewall portions was monitored for tunnels with 1.0D soil cover while earth pressure reduction of as much as 17% and 35% on the crown and sidewall portions was monitored for 1.50D.
- (6) 2S2T was not effective when it comes to slopes with model tests with varying slope roughness but it was very effective in reducing the settlement of soil around the tunnel.
- (7) Based on the zero extension direction diagram and maximum shear strain diagram, it was found that the failure surface occurred between the original soil and the backfill material.

References

1. Kim, Eun-Sup & Lee, Sang-Duk (1999), "An Experimental Study on the Earth Pressure on the Underground Box Structure", *Korean Geotechnical Society Journal*, Vol.15, No.6, pp.235-246.
2. Kim, Jong-Gyeong (2000), "A Study on the Measures and the Factors of Cracks Occurred at Tunnel Lining", Masteral Thesis, Pusan National University.
3. Bautista, Ferdinand E., Park, Lee-Ku, Im, Jung-Chul & Lee, Young-Nam (2006.6), "Variation of Earth Pressure on Cut-and-Cover Tunnel Lining with Settlement of Backfill", *Journal of Korean Geotechnical Society*, Vol.22, No.6, pp.27-40.
4. Park, Lee-Keun (2003), "A Study on the Characteristics of Ground Behaviour and Settlement Restraining Effect of Micropile during Shallow Tunnel Construction in Soft Ground", Doctorate Thesis, Pusan National University
5. Joo, In-Gon (2002), "A Study on the Behaviour & Bearing Capacity in Sandy Ground Reinforced by Geotextile", Doctorate Thesis, Pusan National University
6. Yoo, Gun-Son (1997), "A Study on the Earth Pressure Around Cut-and-Cover Tunnel and the Structural Behaviour of Tunnel Lining by Experimental and Numerical Analyses", Doctorate Thesis, Seoul National University
7. Lee, Dae-Hyuk, Kim, Young-Geun & Lee, Ki-Keun (1998), "Mechanical Behaviour and Cracking Characteristics of Tunnel Lining by Model Experiment", *Journal of Korean Society of Rock Mechanics, Tunnel & Underground*, Vol.8, pp.53-66.
8. Im, Jung-Chul, et al. (2002), "A Laboratory Model Test on the Reduction of Structure Settlement due to the Excavation of Earth NATM Tunnel", *Samsung Corporation & Pusan National University-Research Institute of Industrial Technology Joint Research*, pp.19-23.
9. Koerner, R. M. (1986), *Design with Geosynthetics*, Prentice and Hall, New Jersey, pp.1-61.
10. Komiya, K., Shimizu, E., Watanabe, T. & Kodama, N. (2000), "Earth pressure exerted on tunnels due to the subsidence of sandy ground", *Geotechnical Aspect of Underground Construction in Soft Ground*, Balkema, Rotterdam, pp.397-402.
11. Taylor, R. K. & Atterwell, P. B. (1984), *Ground Movements and their effects on structures*, Surrey University Press, USA.
12. Venkatappa Rao, G. & Suryanarayana Raju, G.V.S. (1995), *Engineering with Geosynthetics*, Tata McGraw-Hill Publishing Co. Ltd., pp.1-70.

(received on Jul. 13, 2006, accepted on Mar. 15, 2007)

Characteristics of Shear Behavior of Remolded Nak-dong River Sandy Silt

재성형된 낙동강 모래질 실트의 전단거동 특성

Kim, Young-Su¹ 김 영 수
Tint, Khin Swe² 탄킨스웨
Kim, Dae-Man³ 김 대 만

요 지

본 논문에서는 실트 함유율이 높은 모래에 대한 정규압밀 등방배수 및 비배수 삼축압축시험(NCIU 및 NCID) 결과를 나타내었다. 유효구속응력 100~400kpa하에서 실트 함유율이 63%인 낙동강 모래 시료를 사용하여 실험을 실시하였다. 실험결과, 모래질 실트는 초기에는 압축이 되지만 전체적인 응력-변형률 곡선에서 최종적으로 체적팽창반응을 보였다. 모래질 실트의 거동은 낮은 소성 특성으로 인하여 점토와 모래보다 비하여 그 특성을 묘사하기가 어려웠다. 특히, 시료는 파괴 후 전단과정에서 팽창현상을 보였다. 모래질 실트의 전단거동과 전단강도정수는 응력-변형률 거동과 Mohr-Coulomb 파괴규준에 의하여 결정되는데, 전단거동은 파괴 후 변형률 연화 경향과 같이 체적변화가 증가하는 것으로 관찰되었다. 본 논문에서 모래질 실트의 전단과정 동안에 발생하는 팽창거동은 모래 함유율 뿐만 아니라 저점착력을 가진 세립자의 함유율에 의해서도 달라졌다.

Abstract

The results from normally consolidated isotropic drained and undrained triaxial compression tests (NCIU and NCID) on sand with high silt content were presented in this paper. The experiments were performed on specimens of Nak-dong River sand with 63% silt content under effective confined pressures, 100 kPa to 400 kPa. From test results, Sandy silt became initially compressive but eventually appeared to provide dilatancy response throughout the entire stress-strain curve. The behavior of sandy silt was more difficult to characterize than that of clay and sand due to lower plastic characteristic. Especially, the samples exhibited dilatancy development during shear after failure. The shear behavior and shear strength parameters of sandy silt can be determined as stress-strain behaviors are described by the Mohr-Coulomb failure criterion. The shear behaviors were observed increasing dilatancy volume change tendency with strain-softening tendency after failure. In this paper, the behavior of dilatancy depends on not only sand content but also fine content with low-cohesion during shear in the samples of sandy silt.

Keywords : Critical state line, Sandy silt, Shear strength, Stress-strain response, Triaxial tests

1 Member, Ph.D., Prof., Dept. of Civil Engrg., Kyungpook National Univ., Korea

2 Doctor Course, Dept. of Civil Engrg., Kyungpook National Univ., Korea, khinswetint@yahoo.com, Corresponding Author

3 Member, Ph.D., Lecturer, Dept. of Civil Engrg., Jinju National Univ., Korea

1. Introduction

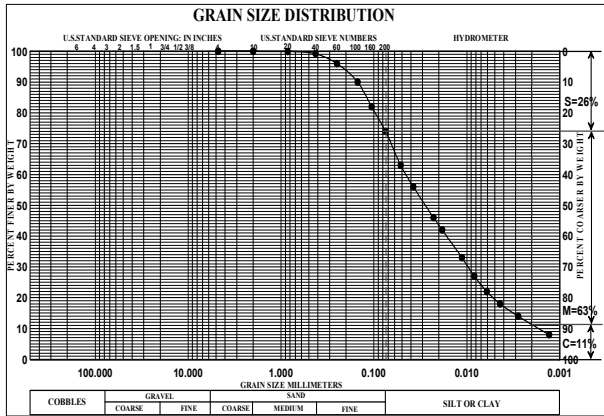
The sandy silt is more difficult to characterize than the behavior of clay or sand because of its tendency to dilate during shear and establish a consistent and practically useful failure criterion (Yamamoto 2001). When granular soils contain a certain amount of fines, the characteristics of shear strength vary with fines content. The shear strength parameters of soil for foundation designs essentially require the shear strength of the soil to check the stability and settlements of soil. From the experiment results, the appropriate shear strength parameters that can be used to foundation design are important. The stress-strain curve is significant for safety structure limitation and the development of soil failure depends on the range of stress-strain response obtained from triaxial compression tests. Preparing sandy silt samples for triaxial and consolidation testing without sampling disturbance is very difficult. Disturbance influences the measured shear strength in triaxial tests and obscures the past consolidation pressure in consolidation tests. Sandy silts tend to dilate during shear, and changes in pore water pressure decrease due to strains increase. In this paper, to study the normally consolidated isotropic drained and undrained shear strength behaviors of Nak-dong River sandy silt, series of standard triaxial tests were performed on the soil specimens which isotropically consolidated in the remolded conditions. From the test results, the stress-strain relationship is nonlinear and peak shear strength develops at intermediated axial strain and critical-state shear strength (corresponding to no volume change during shearing) develops with large axial strains after failure. If the pore pressures decrease to values below the vapor pressure of water, cavitations occur and bubbles of air are liberated from the pore water (Brandon 2006). When this happens, shear does not occur at constant volume but the specimens were exhibited with no volume change at critical state in shearing under loading. Normally consolidated tests were carried out for various confining pressures. The soil specimens used in this paper consisted of silt-sand mixtures that include fine-grained surface soils which is defined as ML (sandy silts) according to Unified Classification System (Yilmaz

2004). The samples were sheared to failure under static loading to investigate the strength and deformation response in triaxial compression test. Remolded soils had a significant effect on the stress-strain and pore water pressure behavior under undrained condition. The increment of undrained strength was a result of the reduction in water content that occurred when the remolded sample was consolidated. The strength values in laboratory are higher than the field strength (Fleming 1990). An increase of dilatancy with fines content is related to the greater fines content (Salgado 2000). When granular soils contain a certain amount of fines, the characteristics of shear strength vary with fines content. The focus of the laboratory testing program was to develop shear strength parameters and shear behaviors of drained and undrained consolidated (CD and CU triaxial tests) on Nak-dong River sandy silt. Shear strength parameters and shear behaviors can be determined as the Mohr-Coulomb failure criterion is commonly used to describe shear failure in soils and stress-strain responses. Moreover, the laboratory tests included soil classification, primary consolidation, unit weight, Atterberg limit, saturation and consolidation in triaxial tests.

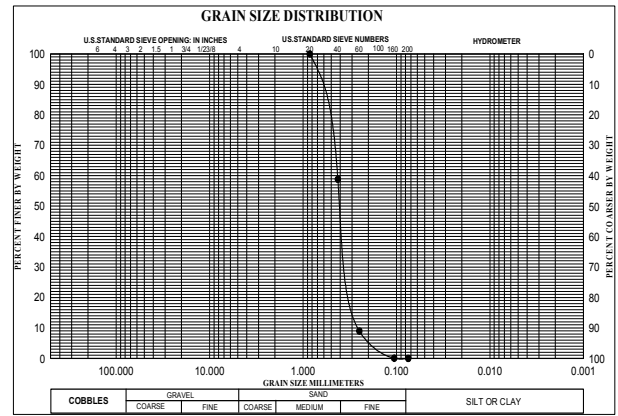
2. Experimental Methods

2.1 Physical Properties

Atterberg limits tests were performed on the sandy silt to classify the soils and to establish their geotechnical engineering properties after remolding. Laboratory tests in this paper included physical properties and two types of triaxial tests (Consolidated drained and undrained tests). The soil materials were obtained from Nak-dong River in Gumi. The soil was prepared with sieve No.40 and remolded before preconsolidation test. The physical properties of Nak-dong River sandy silt and loose sand are presented in Tables 1 and 2. The soil classifications based on grain-size distribution curve of Nak-dong River sandy silt and loose sand are shown in Figs. 1 (a) and (b). The soil was graded between No.10 and 200 sieve sizes.



(a)



(b)

Fig. 1. Grain size distribution of (a) Nak-dong River sandy silt and (b) loose sand

Table 1. Physical properties of Nak-dong River sandy silt

G_s	D_{60} (mm)	D_{30} (mm)	D_{10} (mm)	C_u	C_z	e_{max}	e_{min}	LL (%)	PI (%)	Sand (%)	Silt (%)	Clay (%)	USCS
2.64	0.045	0.01	0.0018	25	1.235	0.713	0.631	25	6	26	63	11	ML

Table 2. Physical properties and grain sizes of Nak-dong River loose sand

G_s	D_{60} (mm)	D_{30} (mm)	D_{10} (mm)	C_u	C_z	e_{max}	e_{min}	Sand (%)	Silt (%)	Clay (%)	USCS
2.676	0.43	0.37	0.27	1.593	1.179	1.137	0.765	100	0	0	SP

2.2 Primary Consolidation Test

The cylindrical preconsolidation apparatus in diameter 28 cm and height 50 cm is shown in Fig. 2. The sandy silt was provided as a bulk sample which is mixed with water and remolded before testing. The soil slurry was applied to by preconsolidated pressures, 7.5, 15, 30 and 60 kPa respectively during one month. The settlements of preconsolidation test results by using primary pressures



Fig. 2. Preconsolidation test

step by step are shown in Fig. 3. The primary consolidation test is conducted on a remolded sample of sandy silt. After the sample of sandy silt is set up and an initial small load 7.5 kPa is applied to it, the amount of compression that the soil undergoes is measured over time. Firstly the samples will be compressed rapidly under initial preconsolidation pressure 7.5 kPa as the water flows out of the sample and grains shift position to decrease the size of the voids. Therefore the settlements of samples are very large in the beginning of pressure. Eventually the rate of consolidation will slow and the settlements are not as large as initial stage because the samples start to consolidate under increasing preconsolidation pressure. The height of sample decreased and the settlement happened continuously until constant value of settlement due to consolidation under preconsolidation pressures as shown in Fig. 3. If the settlement is constant under each of preconsolidation pressures, the current consolidation step is ended and the preconsolidation pressure is increased to next step. The total settlements of samples are 14 cm in about one month. The water content is calculated after maximum load was exposed to the soil.

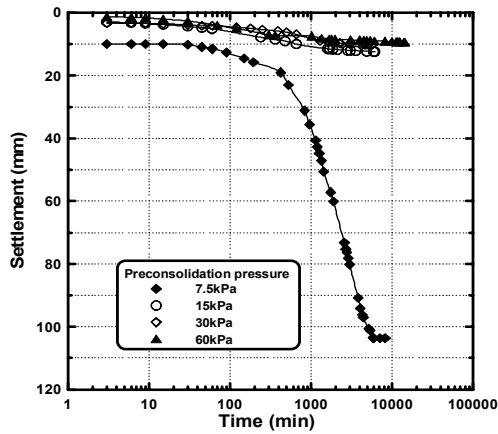


Fig. 3. Settlement and time (log t)

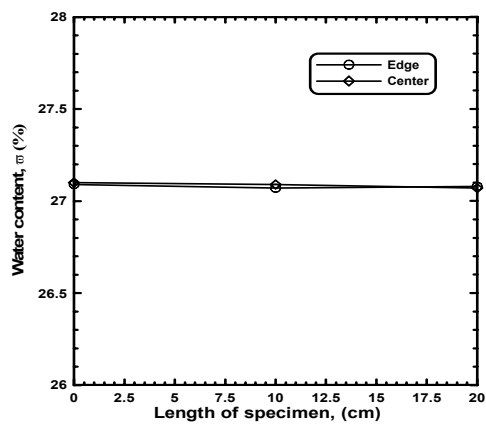


Fig. 4. Water content and length of specimen

Thus some of the soils have been taken from top, middle and bottom layers of center and edge of the preconsolidation sample for checking of water content after preconsolidation test. The values of water content for samples are approximately the same and the soil is approximately homogenous as shown in Fig. 4. The water content was 27.1% and the unit weight of dry density, γ_d is 15.11 kN/m³ after preconsolidation test. The water

content, ω was 74% before preconsolidation test. The sample were extruded and coated with wax prior to triaxial testing.

2.3 Preparation for Specimen and Shear Test

Normally consolidated isotropic drained and undrained triaxial compression tests were performed on cylindrical specimens measuring 50 mm in diameter by 100 mm in height as shown in Fig. 5. The specimens were trimmed as a necessary cylindrical shape before triaxial testing. The void ratio of the test specimens ranged from 0.713 (initial stage) to 0.631 (before shear). The undrained shear strength significantly depends on the initial void ratio and water content of the each sample due to the changing of excess pore water pressure. Water content is little different from among the specimens after preconsolidation test because of taking the setting time for the triaxial test. The saturation of sample was performed by cell pressure, 50 kPa and back pressure, 45 kPa at the beginning and gradually increased during saturation stage until B-value is at least 0.95. A back pressure was used to prevent cavitations of the pore water and to ensure full saturation in all tests (Yamamuro 2004). The effects of membrane penetration and filter paper were not considered significant during shear test because for soft and very soft soil the membrane effect can form an appreciable proportion of the measured strength and for soils of high strength, the effect of the membrane restraint is insignificant and is usually neglected. After saturation stage, the specimens were consolidated under isotropic effective confining pressures, 100, 200, 300 and 400 kPa respectively.

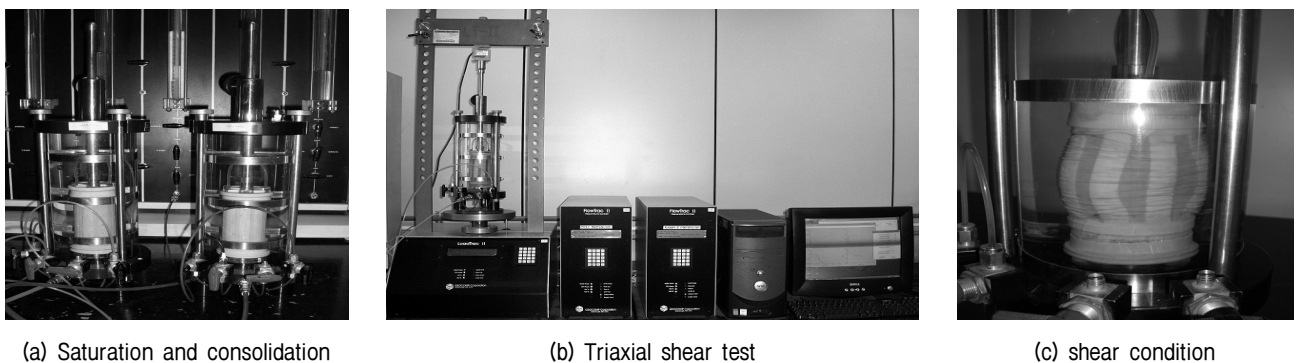


Fig. 5. Normally consolidated isotropic drained and undrained triaxial test of Nak-dong River sandy silt

Table 3. Normally consolidated isotropic triaxial test

Sample	Conditons	Final effective consolidated stress (kPa)
Sandy silt	NCIU NCID	100
		200
		300
		400

Significant volume changes of specimen may occur particularly during the consolidation. The following Table 3 is presented for normally consolidated isotropic condition of triaxial compression test. Shear strength tests were conducted on the remolded samples of sandy silt after consolidation phase. Normally consolidated undrained and drained tests were performed in strain rate 0.1% per minute and 0.05% per minute under shear condition because the maximum rate of strain to be applied is equal to ϵ_f/t_f % per minute. The value of t_f which is the time from the start of compression to failure is obtained from $1.8t_{100}$ minutes for CU test and $14t_{100}$ for CD test with side drains (the use of filter paper).

3. Test Results

3.1 Normally Consolidated Isotropic Undrained Tests (NCIU)

In a series of undrained triaxial compression tests, the strength didn't increase with further straining and dilatency because deviator stresses exhibited softening tendency after the specimen statically collapsed. The typical behavior of normally consolidated isotropic undrained triaxial test for Nak-dong river sandy silt is shown in Fig. 6. The deviator stress and axial strain responses are presented in Fig. 6 (a). A stress-strain curve can be delineated into three regions: initial elastic region, hardening region and softening region. The peak of deviator stress is smooth in higher confining pressure and is not presented in lower confining pressure due to the dilatency during undrained shearing. The following distinguishing features are: (1) the peak and the ultimate points of the deviator stresses are one and the same; (2) pore- water pressure buildup is positive; (3) the effective stress path from mean effective

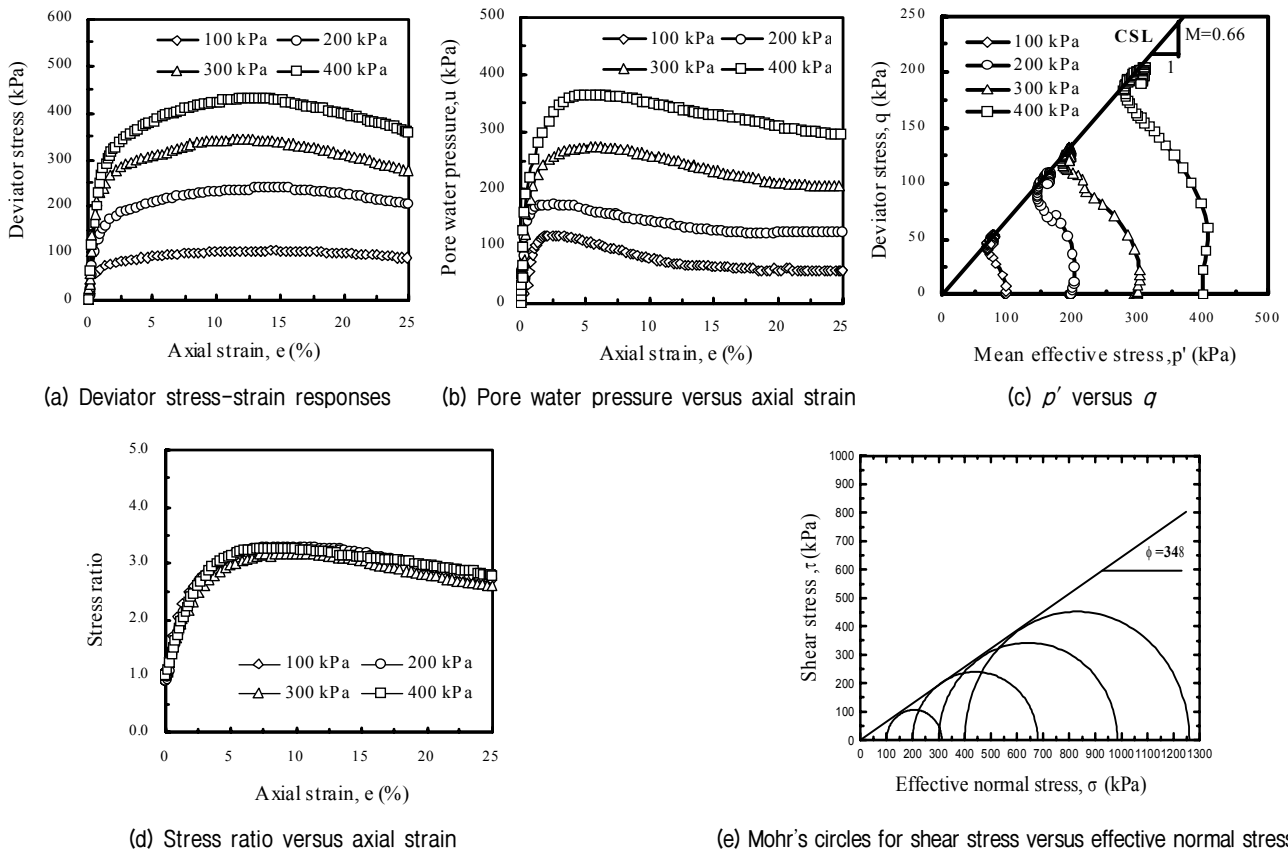


Fig. 6. Results of normally consolidated isotropic undrained triaxial tests for Nak-dong River sandy silt

stress, $p'=100, 200, 300$ and 400 kPa are approximately geometrically similar; and (4) the failure points lie on a line (the critical state line, CSL) that passes through the origin of the $p'-q$ space (Anandarajah 2000) as shown in Fig. 6 (c). The maximum deviator stresses between $\sigma'_3=100$ and 400 kPa are 81.65 kPa (14.56% failure strain), 330.31 kPa (13.01% failure strain) as shown in Fig. 6 (a). Moreover, the plots of deviator stresses are constant under effective confining pressure, $\sigma'_3=100$ kPa and showed the softening tendency under $\sigma'_3=200, 300$ and 400 kPa after peak deviator stress.

When the deviator stresses increase, the effective vertical stress, σ'_1 decreases and total vertical stress, σ'_1 , effective confining pressure, σ'_3 and pore water pressure, u increase and total confining stresses are constant before failure. The pore water pressures decrease and then the void ratio of the samples increase due to dilatant behavior beyond failure during shearing as shown in Fig. 6 (b). All of peak pore water pressures exist between 120 kPa ($\sigma'_3=100$ kPa) and 360 kPa ($\sigma'_3=400$ kPa) in 2 to 5% failure strain. The maximum pore water pressure is exhibited in small strain and decreased as axial strain increase after critical state. Due to the dilatancy, the bonding tendency among the soil particles is destroyed and happened with no interlocking at failure state. The peak strength of sandy silts is insignificantly influenced by interlocking because the undrained stress paths are different from the drained stress paths that converged toward the right side of each mean effective stress, p' to the critical state line since the excess pore water pressure development is positive (Horpibulsuk 2004). The effective confining stress has major influence in changing the behavior of sandy silt from contractive to dilative. M is a critical state frictional constant, (the slope of the critical state line on a $q-p'$ plot at failure condition) which is a function of ϕ'_{cs} (from $M = 6\sin\phi/(3-\sin\phi)$) and essential for critical state model in Fig. 6 (c). The parameter, $M(q_f/p'_f)$ is 0.66 . The sample is sheared with constant pore water pressure at the steady or critical state. The effective stress ratios and axial strain are shown in Fig. 6 (d). All of stress ratios declined slightly that the sample exhibited dilatancy after the peak values of stress ratio.

The limiting stress ratio suggests that the true frictional angle should not be changed throughout the stress-strain history. Peak undrained strength followed a lower stress ratio for the critical state condition (Been 2004). According to the normally consolidated undrained triaxial tests, the shear strength increases with the amount of greater silt content owing to higher dilatancy by Salgado (2004). The angle of internal friction, ϕ is 34° and the failure deviator stresses in Mohr's circle are shown in Fig. 6 (e). The shear strength increases due to increasing shear stress with higher effective normal stress in Fig. 6 (e).

3.2 Normally Consolidated Isotropic Drained Tests (NCID)

In four drained triaxial compression tests, there are no distinct peak deviator stress and smooth curve under effective confining pressure, 300 and 400 kPa and then the peak deviator stresses do not appear under effective pressure, 100 and 200 kPa as shown in Fig. 7 (a). The deviator stresses at σ'_3 kPa decreased slightly but these at $\sigma'_3 = 100$ to 300 kPa decreased smoothly and showed softening tendency after the peak value of deviator stress in Fig. 7 (a). The peak deviator stresses are between 200 kPa (15% axial strain) at $\sigma'_3 = 100$ kPa and 750 kPa (16.25% axial strain) at $\sigma'_3 = 400$ kPa. The volumetric strain at $\sigma'_3 = 100$ kPa decreased to negative value (i.e. swelling) after failure. The behavior of specimens showed the first strain hardening character at $\sigma'_3 = 200$ to 400 kPa because of the (positive) compressive volumetric strains, (i.e. contraction of volume) before failure and the second strain showed a strain-softening tendency due to the expansive volumetric strains (i.e. dilation of volume) after failure in Fig. 7 (b). Based on the test results, the specimens exhibited the decrement of volume under higher confining pressure before failure. The minimum and maximum values of volumetric strains at $\sigma'_3 = 100$ kPa and 400 kPa are between 0.05% (4% failure strain) and 0.12% (7.6% failure strain) as shown in Fig. 7 (b).

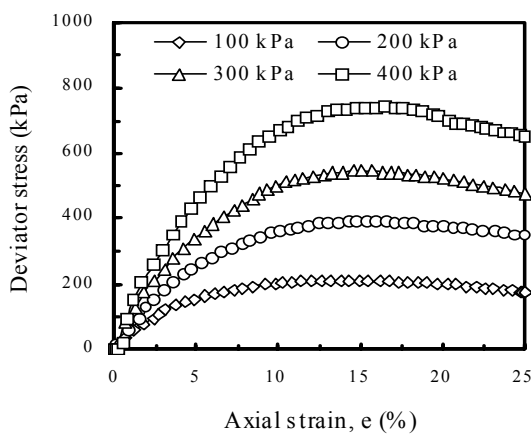
The results indicated that the failure stress levels, overall trends of the stress-strain behavior and the volume change behavior are significantly influenced by the presence

of silt (Shapiro and Yamamuro 2003). For tests conducted with 100 kPa, the samples at the end of testing were distinctly dilatant and hence critical state had not been approached in volumetric strains. For $\sigma'_3 = 400$ kPa, the samples at failure (or the end of test) were closed to constant volume.

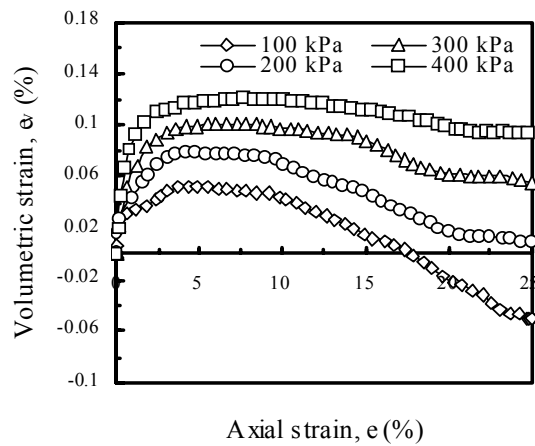
Failure deviator stresses exist on a unique line which is a critical state line (CSL) as shown in Fig. 7 (c). The stress paths are similar and converged to the right side of the each mean effective stress towards a critical state line and then all of the failure points terminated at the critical state line in the stress paths diagram. Furthermore, the mean effective stresses and deviator stresses were increased to CSL. The slope of critical state line in the stress paths is denoted by M , a material parameter which is 0.49. When the specimen of soil reaches a critical state, the sample is sheared continuously and causes failure as constant shear stress and no volume change tendency with

increasing shear strain (Boukpeti 2000). The frictional angle ϕ is 29° as shown in Fig. 7 (d).

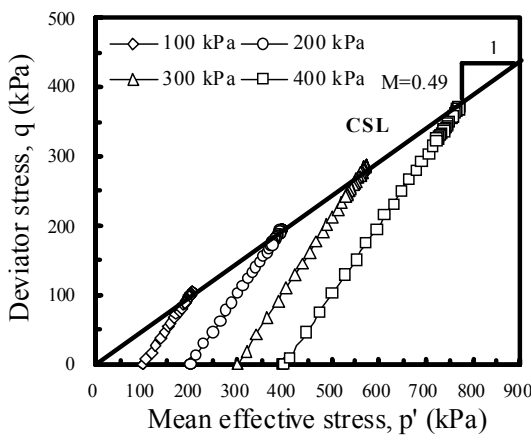
It is possible to trace the stress paths of the specimens during shearing in the tests to determine if the stress paths would eventually reach the extended Mohr-Coulomb failure envelope which is significant for the shear strength of specimens (Rahardjo 2004). According to the analysis of test results, the volume of sample tends to decrease because the void ratio is smaller with higher confining pressures and the strength increases as the effective normal stress increases before critical state. When the deviator stresses hardened, the effective vertical stress, σ'_1 and total vertical stress, σ'_1 , also increased and then the effective confining pressure, σ'_3 , total confining stress, σ_3 are constant with increasing axial strain before failure. When the deviator stresses softened, the effective vertical stress, σ'_1 and the total vertical stress, σ'_1 , decrease after



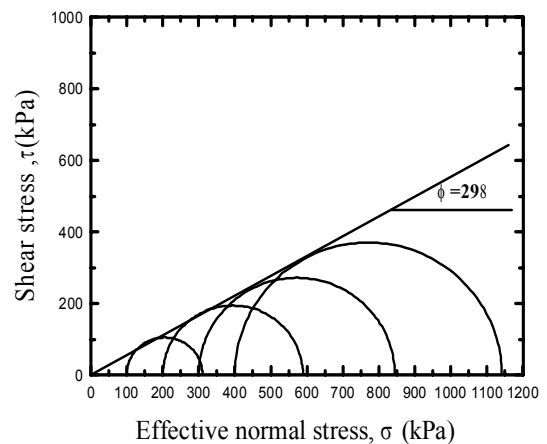
(a) Deviator stress-strain response



(b) Volumetric strain versus axial strain



(c) p' versus q



(d) Mohr's circles

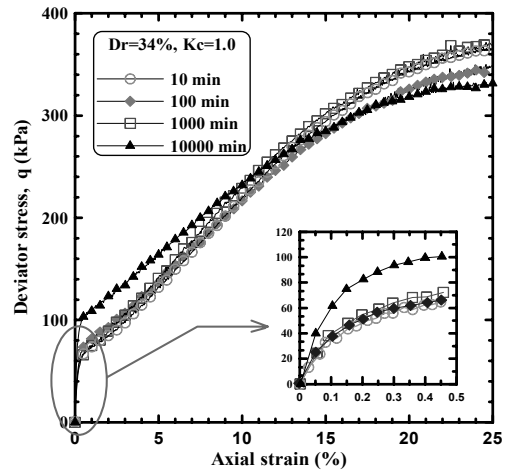
Fig. 7. Normally consolidated isotropic drained triaxial tests results of Nak-dong River sandy silt

failure condition during shearing. From these results, tests were conducted for compression at lower confining stress during the initial stage of shearing before failure.

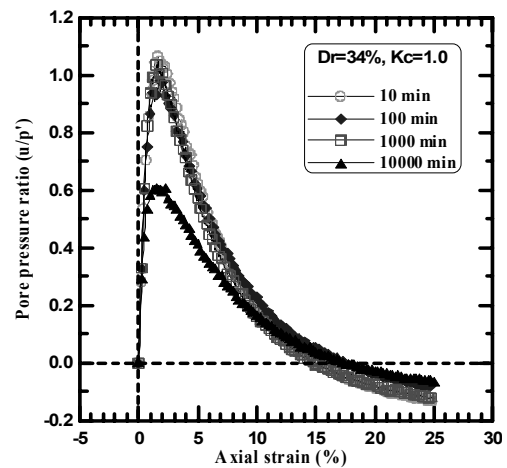
4. Comparison of Undrained Nak-Dong River Sandy Silt with Loose Sand

According to the undrained test results of shear strength of loose sand as shown in Fig. 8, the framework of understanding is stress-dilatancy theory because the pore water pressure showed negative value after maximum pore water pressure. The samples of saturated loose sand were sheared to failure and showed only a hardening tendency and a significant decrease in pore water pressure due to the increment of effective stress and strength and then deviator stresses of sandy silt showed softening tendency after failure in stress-strain response. The loose sands do not increase in volume to failure (Been 2004) and tend to dilate due to development of the negative pore water pressure (i.e. swelling of volume) after critical state (Pestana 2002). The sandy silts exhibited only positive value of pore water pressure which decreased slowly after failure and showed a little dilation behavior. In stress-strain behavior of sand and sandy silt, the critical state is the same as the failure state in sand because there is no peak deviator stress. However, the peak deviator stress of sandy silt appears under higher confining pressure and then the critical state is the same as the failure state at lower confining pressure similar to loose sand behavior. In sand, critical state typically occurs after effective stress failure at large strains. At the critical state, all samples remain constant values of pore water pressure and effective stresses at large strains (Yamamuro 1998). Deviator stresses of sand are more than those of sandy silt at $\sigma'_3 = 100$ to 300 kPa except 400 kPa. Moreover, the deviator stress of sand hardened at small strain within 0.5% and that of sandy silt increased stiffly at large strain within 2.5% at the beginning condition. The maximum failure strain of pore water pressures of sandy silt is 5% and 2% in loose sand. The pore water pressure of sand has more softening tendency than that of sandy silt which showed only positive value but pore pressure of sand happened to be

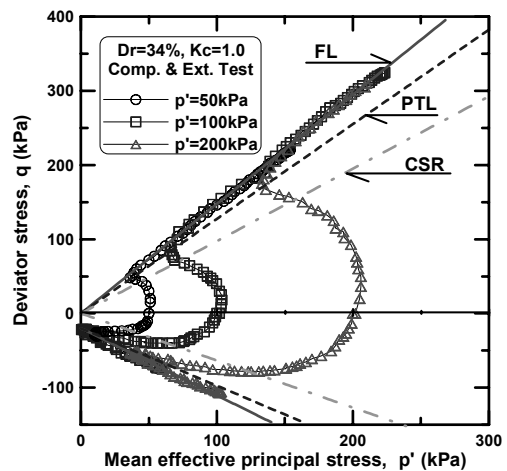
negative values after failure. The failure deviator stresses, q of sandy silt are shorter length than these of sand on the critical state line. The peak values of q with maximum



(a) Deviator stress versus axial strain



(b) Pore water pressure versus axial strain



(c) Stress paths

Fig. 8. Results of laboratory tests using Nak-dong River loose sand (Kim Young-Su, 2004)

effective confining pressures are 200 kPa of sandy silt and 400 kPa of sand on the failure line in stress paths. All of failure deviator stresses followed to a critical state line (CSL) when specimens of sandy silt and loose sand are sheared. From analysis of results, deviator stress of normally consolidated sandy silt is failure at 12.5% strain but loose sands didn't exhibit the failure exactly.

5. Conclusions

Analysis of the experimental study on Nak-dong River sand with high silt content was conducted. From the laboratory test results of normally consolidated isotropic undrained of sandy silt, the deviator stress increased to peak value as a strain-hardening tendency until failure and showed strain-softening tendency after failure. Peak deviator stresses are not distinct and smooth under increasing effective confining pressure and not appeared under lower effective confining pressure. Pore water pressure decreased and exhibited as the dilative behavior of the samples after failure during shearing. Stress paths converged to the left side of the each mean effective stress towards the critical state line. Stress ratios decreased and presented a unique line and dilatancy of sample with increasing axial strain after failure. Shear stresses increase under higher effective confining pressure. Undrained shear behavior of sandy silt showed dilatancy and the shear strength increased with higher effective normal stress.

Normally consolidated drained triaxial compression tests of Nak-dong River sandy silt also indicated that deviator stresses at failure were constant for $\sigma'_3 = 100$ kPa hence the sample approached to the critical state. However, for tests conducted with $\sigma'_3 = 100, 200$ and 300 kPa, the deviator stresses were softened at the end of testing so that the critical state had not been approached after failure. The initial strain before failure hardened up to peak value and exhibited compression volumetric strains and then the final strain after failure softened and presented expansive volumetric strains under various effective confining pressures after failure condition. Stress paths converged to the right side of the each mean effective stress towards the critical state line. Drained shear behavior of sandy

silt exhibited more dilatancy with lower effective confining pressure and the shear strength increased with shear stress and the effective normal stress.

Nak-dong River sandy silt and sand have different behaviors in normally consolidated isotropic undrained tests. The deviator stress of sand with small strain and sandy silt with large strain increased stiffly at the initial condition during shear.

From analysis of these results, the deviator stress of sandy silt showed strain-softening tendency after failure but loose sand exhibited a strain-hardening tendency until the end of test. There are no peak deviator stresses in sand but the peak deviator stresses of sandy silt appeared smoothly under high confining pressure until failure. The pore water pressure of sandy silt showed only positive value but pore pressure of sand was exhibited by decreasing to negative after failure. The failure deviator stresses of sandy silt are shorter than that of sand along the critical state line. All of the stress paths are similar in each test and all failure deviator stresses followed to a unique line which is a critical state line (CSL) or steady state line in stress path diagram.

The axial strain for peak strength of the interlocked structure of soil specimens increases with confining pressure. The strength derived from the interlocking increases with increasing confining pressure. If we consider soil properties in terms of effective stress, the most marked feature of which the failure criterion must take account is the increment of strength as the effective stress increases. The pore water pressure build-up is reduced under undrained loading and undrained strength increase in stress paths diagram. The dilation component contributes to a portion of total strength whereas for the higher effective confining stress, the strength after the peak is dominated by dilation with lower plasticity.

References

1. Anandarajah, A. (2000), "Triaxial behavior of kaolinite in different pore fluids", *J. Geotech. Eng.*, ASCE, Vol.126, No.2, pp.148-156.
2. Been Ken and Jefferies Michael (2004), "Stress-dilatancy in very loose sand", *Can. Geotech. J.*, Vol.41, pp.972-989.
3. Boukpeti, N. (2000), "Triaxial behavior of refined Superior sand

- model”, *Computer and Geotechnics. J.*, Vol.26, pp.65-81.
4. Brandon Thomas L., Rose Andrew T. (2006), “Drained and undrained strength interpretation for low-Plasticity silts”, *J. Geotech. Engrg.*, ASCE, Vol.132, No.2, pp.250-257.
 5. Fleming Lorraine N. (1990), “Stress-deformation characteristics of Alaskan silt”, *J. Geotech. Eng.*, ASCE, Vol.116, No.3, pp.377-393.
 6. Horpibulsuk Suksun (2004), “Undrained shear behavior of cement admixed clay at high water content”, Vol.130, No.10, pp.1096-1105.
 7. Lee Junhwan, Salgado Rodrigo (2004) “Stiffness degradation and shear strength of silty sands”, *Can. Geotech. J.*, Vol.4, pp.831-843.
 8. Lo S.R. and Wardani S.P.R. (2002) “Strength and dilatancy of a silt stabilization by a cement and fly ash mixture”, *Can. Geotech. J.*, Vol.39, pp.77-89.
 9. Pestana Juan M. (2002), “Evaluation of a constitutive model for clays and sands : Part I-sand behavior”, *Int. J. Numer. Anal. Meth. Geomech.*, Vol.26, pp.1097-1121.
 10. Rahardjo, H. (2004), “Shear strength of a compacted residual soil from consolidated drained and constant water content triaxial tests”, *Can. Geotech. J.*, Vol.41, pp.421-435.
 11. Salgado, R. (2000), “Shear strength and stiffness of silty sand”, *J. Geotech. Eng.*, ASCE, Vol.126, No.5, pp.451-462.
 12. Shapiro Saul (2003) “Effect of silt on three-dimensional stress-strain behavior of loose sand”, *J.Geotech. Engrg.*, ASCE, Vol.129, No.1, pp.1-11.
 13. Yamamuro Jerry A., Kelly M. Covert (2001), “Monotonic and cyclic liquefaction of very loose sands with high silt content”, *J. Geotech. Eng.*, ASCE, Vol.127, No.4, pp.314-324.
 14. Yamamuro Jerry A. and Lade Poul V. (1998), “Steady-state concepts and static liquefaction of silty sands”, *J.Geotech. Engrg.*, ASCE, Vol.124, No.9, pp.868-877.
 15. Yamamuro Jerry A., Wood Fletcher M. (2004), “Effect of depositional method on the undrained behavior and microstructure of sand with silt”, *Soil dynamics and Earthquake Eng.*, Vol.24, pp.751-760.
 16. Yilmaz, M.T. (2004), “Undrained cyclic shear and deformation behavior of silt-clay mixtures of Adapazari, Turkey”, *Soil dynamics and Earthquake Eng.*, Vol.24, pp.497-507.
 17. Young-Su Kim, Dae-Man Kim (2004), “Characteristics of Undrained static Shear Behavior for Sand Due to ageing effect”, *J. Geotech. Eng.*, KGS, Vol.20, No.6, pp.137-150.

(received on Sep. 28, 2006, accepted on Jan. 31, 2007)

Reliability Analysis of Slope Stability with Sampling Related Uncertainty

통계오차를 고려한 사면안정 신뢰성 해석

Kim, Jin-Man¹

김진만

요 지

다양한 불확실성을 체계적으로 반영하는 신뢰성 기반 해석기법을 사면안정 해석의 한 형식으로 제시한다. 통계오차, 공간 변동성, 그리고 공간 평균의 효과를 고려할 수 있는 지반특성 표현식이 사용되었다. 여러 가지 형식의 지반특성 표현식을 이용하여 사면안정 신뢰성 해석을 수행한 결과 통계오차, 공간적 상관성, 그리고 조건부 해석기법을 사용할 경우가 기존의 단순 확률변수 기법에 비해 상당히 작은 파괴확률을 제시한다는 사실이 밝혀졌다. 이 결과는 사면안정 해석에서 공간적 변동성과 통계오차가 합리적으로 고려되어야 한다는 점을 제시한다.

Abstract

A reliability-based approach that can systematically model various sources of uncertainty is presented in the context of slope stability. Expressions for characterization of soil properties are developed in order to incorporate sampling errors, spatial variability and its effect of spatial averaging. Reliability analyses of slope stability with different statistical representations of soil properties show that the incorporation of sampling error, spatial correlation, and conditional simulation leads to significantly lower probability of failure than that obtained by using simple random variable approach. The results strongly suggest that the spatial variability and sampling error have to be properly incorporated in slope stability analysis.

Keywords : Conditional approach, Random field, Reliability, Slope stability, Spatial averaging

1. Introduction

The estimation of key soil properties and subsequent quantitative assessment of the associated uncertainties has always been an important issue in geotechnical engineering. The most common reliability-based approach has been to assume that soil properties could be modeled as simple random variables (e.g., Christian et al. 1994; Christian and Urzua 1998; Duncan 2000). This approach implicitly assumes that a given soil property is perfectly correlated with the seemingly homogeneous segment of

soil profile, and is the same at all locations within that segment. It is, however, known that the assumption of perfect correlation can lead to an overestimate of the failure probability of a geotechnical structure, since it usually overestimates the level of uncertainty. In general, the stochastic nature of spatially varying soil properties can be treated in the framework of a random field (e.g. Vanmarcke, 1977a). Since in typical applications the whole domain of interest is discretized into smaller elements, the random field property has to be represented by a suitable spatial average of each element. Over the

¹ Member, Assistant Prof., Dept. of Civil Engrg., Pusan National Univ., jmkim@pusan.ac.kr

last couple of decades various spatial averaging methods have been proposed for slope stability analysis (Vanmarcke 1977a, 1977b; Li and White 1987a, 1987b; Li and Lumb 1987).

Kim (2003) reported the importance of geotechnical variability in the analysis of earthquake-induced slope deformations. This paper reports a follow-up analytical study that investigated the influence of inherent variability and sampling errors in the analysis of static slope stability. Kim (2003) briefly described some of the findings from that study and this paper reports all the remaining findings in details. In this work, the author is particularly interested in the development of the statistics of the local average of the material property of a certain portion of the space, since soils generally exhibit plastic behavior and the stability of a soil slope tends to be controlled by the averaged soil properties rather than the properties at a particular location along the potential slip surface (i.e., Li and White 1987a, Tang et al. 1976, Vanmarcke 1977b). In this regard the author extends the previous applications of the spatial averaging method presented by Vanmarcke (1977a, 1977b) and Li and White (1987a, 1987b) by accounting for the sampling errors and the locations of measurements. Both unconditional and conditional simulation approaches are described and illustrated. Reliability-based computational techniques are then used to obtain a probability of slope failure. The results are compared with the conventional random variable approach to illustrate the influence of the various assumptions on the computed probability of failure.

2. Statistical Spatial Averaged Soil Properties

A random field is defined as a family of random variables at points with coordinates $\mathbf{x} = (x_1, \dots, x_n)$ in an n -dimensional parameter space (Vanmarcke 1983). If the random field is Gaussian, then the random field $v(\mathbf{x})$ can be completely described by its mean function $\mu(\mathbf{x})$, variance function $\sigma^2(\mathbf{x})$, and the correlation $\rho(\mathbf{x}, \mathbf{x}')$. Non-Gaussian random fields, in general, need more information beyond second moment statistics to completely describe them. One special case is when the random fields

are defined by the Nataf multivariate distribution (Liu and Der Kiureghian 1986), which is adopted in this study when modeling non-Gaussian random fields.

The spatial average \bar{v} of a random soil property $v(\mathbf{x})$ of the certain element Ω_e (i.e., discretized zone of interest) can be defined as the stochastic integral (Vanmarcke 1983). For the sake of simplicity the author will first consider that the (sample) data are error free as:

$$\bar{v} = \frac{1}{V} \int_{\Omega_e} v(\mathbf{x}) d\mathbf{x} \quad ; \quad V = \int_{\Omega_e} d\mathbf{x} \quad ; \quad \mathbf{x} \in \Omega_e \quad (1)$$

where Ω_e is an elementary volume, area or line in the three-, two- and one-dimensional cases, respectively.

The first and second moment statistics (i.e., mean, variance, and covariance) of spatial average \bar{v} can then be manipulated in terms of the statistics of point random property $v(\mathbf{x})$ as:

$$E[\bar{v}] = E\left[\frac{1}{V} \int_{\Omega_e} v(\mathbf{x}) d\mathbf{x}\right] = \frac{1}{V} \int_{\Omega_e} \mu(\mathbf{x}) d\mathbf{x} \quad (2)$$

$$\text{var}[\bar{v}] = E\left\{\left[\bar{v} - E(\bar{v})\right]^2\right\} = \frac{1}{V^2} \iint_{\Omega_e} \sigma(\mathbf{x})\sigma(\mathbf{x}')\rho(\mathbf{x}, \mathbf{x}') d\mathbf{x}d\mathbf{x}' \quad (3)$$

where the random property can be described with trend and random components such that $v(\mathbf{x}) = \mu(\mathbf{x}) + \varepsilon(\mathbf{x})$. Similarly, covariance of the spatial average \bar{v} between Ω_e and $\Omega_{e'}$ is given as:

$$\begin{aligned} \text{cov}[\bar{v}, \bar{v}'] &= E\left\{[\bar{v} - E(\bar{v})][\bar{v}' - E(\bar{v}')]\right\} \\ &= \frac{1}{VV'} \int_{\Omega_e} \int_{\Omega_{e'}} \sigma(\mathbf{x})\sigma(\mathbf{x}')\rho(\mathbf{x}, \mathbf{x}') d\mathbf{x}d\mathbf{x}' \end{aligned} \quad (4)$$

If the field is a weakly stationary field, $\sigma^2(\mathbf{x})\sigma^2(\mathbf{x}')$ and $\rho(\mathbf{x}, \mathbf{x}')$ can be replaced by σ^2 and $\rho(\mathbf{r})$ respectively, where \mathbf{r} is a lag distance vector between the \mathbf{x} and \mathbf{x}' such as $\mathbf{r} = (x_1 - x_1', x_2 - x_2', \dots, x_n - x_n')$. Then the variation and covariance of the spatial average can further be simplified as:

$$\text{var}[\bar{v}] = \sigma^2 \cdot \gamma(\Omega_e) \quad (5)$$

Where $\gamma(\Omega_e) = \frac{1}{V^2} \iint_{\Omega_e} \rho(\mathbf{r}) d\mathbf{x}d\mathbf{x}'$ and $\mathbf{r} = \mathbf{x} - \mathbf{x}'$. Similarly,

$$\text{cov}[\bar{v}, \bar{v}'] = \sigma^2 \cdot \gamma(\Omega_e, \Omega_e') \quad (6)$$

$$\text{Where } \gamma(\Omega_e, \Omega_e') = \frac{1}{VV'} \int_{\Omega_e} \int_{\Omega_e'} \rho(\mathbf{r}) d\mathbf{x}d\mathbf{x}'$$

In the above formulations, $\gamma(\Omega_e)$ and $\gamma(\Omega_e, \Omega_e')$ may be called the variance and covariance reduction factors, respectively (Vanmarcke 1983). It should be noted that the reduction factors are dependent only on the correlation function (i.e., scale of fluctuation, etc.) and geometry of the domain of interest and independent of the magnitude of the point variance. The variance reduction factor is bounded by 0 to 1 since the correlation coefficient is always equal or less than unity. Therefore, the variability of local average is always less than that of the point value and further decreases as the size of the averaged domain increases.

The first and second moment statistics of the spatial averages can be obtained once the variance and covariance reduction factors are determined. Detailed derivations of statistics of the linear and areal averages for specific geometries can be found in Vanmarcke (1977a, 1983) and Li and White (1987a).

3. Conditional and Unconditional Approach

Uncertainty in the determination of soil properties comes from various sources. One obvious source of uncertainty is the inherent randomness of the natural phenomena. Other sources of uncertainty include the inaccuracies in the estimation of the parameters and in the choice of the distribution representing the randomness, due to limited observational data. The following derivations are based on a (weakly) homogeneous random field. The author begins with the unconditional approach that does not account for the location of measurements.

3.1 Unconditional Approach

Suppose that random soil properties $v(\mathbf{x})$ have been observed at N points (or areas) inside the homogeneous zone of interest. Each measurement v_i^* may be regarded as a realization of random properties $v(\mathbf{x})$ and statistics

of random properties $v(\mathbf{x})$ can be estimated from the measured values. Let us assume, for the moment, that the observations are made at sufficiently large distance from each other so that correlation between samples can be neglected for practical purpose (statistically independent). Unbiased sample moments may be used as point estimates of the corresponding moments of population such as (e.g., Ang and Tang 1975):

$$\mu \approx \hat{\mu} = \frac{1}{N} \sum_{i=1}^N v_i^* \quad (7)$$

$$\text{var}[v] \approx \sigma^{*2} \quad (8)$$

The above estimates, however, do not convey information on the degree of accuracy of those estimates of parameters, which depends mainly on the number of the observations. The observational data v_i^* can be conceived to be realizations of a set of independent sample random variables $V_i^*; i=1, 2, \dots, N$ among the population and then the sample mean $\hat{\mu}$ can be regarded a random variable, given as:

$$\hat{\mu} = \frac{1}{N} \sum_{i=1}^N V_i^* \quad (9)$$

Its mean value is given as:

$$E[\hat{\mu}] = \frac{1}{N} \sum_{i=1}^N E(V_i^*) = \frac{1}{N} \cdot N\mu = \mu \quad (10)$$

and its variance is:

$$\text{var}[\hat{\mu}] = \frac{1}{N^2} \sum_{i=1}^N \text{var}[V_i^*] = \frac{\sigma^{*2}}{N} \quad (11)$$

Thus, the sample mean $\hat{\mu}$ has a mean value μ (i.e., unbiased estimator) and standard deviation (or error) σ^*/\sqrt{N} .

Now, the first two moments of spatial average can be estimated based on the observational data, accounting for not only point estimates but also the degree of accuracy of those estimations. Here we first define the spatial average over the element domain Ω_e in the same way as

we did in the previous sections.

$$\begin{aligned}\bar{v} &= \frac{1}{V} \int_{\Omega_e} v(\mathbf{x}) d\mathbf{x} \\ &= \frac{1}{V} \int_{\Omega_e} [\mu(\mathbf{x}) + \varepsilon(\mathbf{x})] d\mathbf{x} ; V = \int_{\Omega_e} d\mathbf{x} ; \mathbf{x} \in \Omega_e \quad (12)\end{aligned}$$

For a homogeneous random field, $\mu(\mathbf{x}) = \mu$ and $E[\varepsilon(\mathbf{x})\varepsilon(\mathbf{x}')] = \sigma^2 \rho(\mathbf{r})$. The expected value of the spatial average can be evaluated by replacing μ with sample mean $\hat{\mu}$ as:

$$E[\bar{v}] \approx E\left[\frac{1}{V} \int_{\Omega_e} (\hat{\mu} + \varepsilon(\mathbf{x})) d\mathbf{x}\right] = E[\hat{\mu} + \varepsilon(\mathbf{x})] = \mu \quad (13)$$

Similarly, the variance of the spatial average is estimated (see the Appendix for the derivation):

$$\text{var}[\bar{v}] \approx \frac{\sigma^{*2}}{N} + \sigma^2 \gamma(\Omega_e) \quad (14)$$

Finally, the covariance between two spatial averages is given (see the Appendix for the derivation):

$$\text{cov}[\bar{v}, \bar{v}'] \approx \frac{\sigma^{*2}}{N} + \sigma^2 \gamma(\Omega_e, \Omega_e') \quad (15)$$

The first term in the above two solutions (Equations 14 and 15) represents sampling errors (i.e., uncertainties in the estimation of the sample mean) while the second term is the reduced inherent variance due to the spatial average. It should be noted that the equations explicitly separate spatial correlation and sampling-related uncertainty. In the special case of $\text{var}(\hat{\mu}) = 0$, which happens when $N \rightarrow \infty$, the above two solutions (Equations 14 and 15) become identical with Equations 5 and 6. Ang and Tang (1984) and Tang (1984) reported a relationship that is similar to Equation 14. Their proposed formula combines various individual sources of uncertainties in determining the c.o.v. (i.e., σ / μ) of the spatial average soil property. Their formula, however, is based on the first order approximation of various sources of uncertainties that are factored (i.e., in a multiplicative form), and therefore may not be applicable to a problem with sources of large uncertainty. Li and White (1987a) also reported similar relationships.

Although the above formulation provides a simple and yet systematic tool to quantify the absolute and relative uncertainty in the determination of soil properties, in some situations as described in the following section, more general approach may be necessary to consider the correlation between the measurements.

3.2 Conditional Approach

An important and highly desirable characteristic of a random field simulation is that the random field simulation reproduces the observed values at their respective sampling locations. Conditional simulation has this very desirable property and it has been extensively used in many different applications, particularly mineral exploration (see e.g. Krige 1966; Matheron 1967; Journel 1989).

When a prior estimate of the mean value of a property is not available, as is usually the case in most field exploration problems, a linear estimator may be expressed as a weighted linear combination of the observed values in the form:

$$\hat{v}_a = \hat{v}(\mathbf{x}_a) = \sum_{j=1}^N w_{aj} v_j^* \quad (16)$$

Requirements that the estimator be unbiased and the expected value of its squared error be minimal yield the following conditions for weights w_{aj} :

$$\sum_{j=1}^N w_{aj} = 1 \quad (17)$$

$$\sum_{j=1}^N w_{aj} \sigma_{jk} - \lambda_a = \sigma_{ak}; \quad k = 1, 2, \dots, N \quad (18)$$

where λ_a is a Lagrange multiplier. The above two equations are a system of $N+1$ linear equations with N unknowns w_{aj} and λ_a . A measure of the error in the estimation can be given in terms of the expected value of the squared error at the minimum condition (sometimes called ‘‘ordinary kriging variance’’):

$$\sigma_{OK,a}^2 = E[(\hat{v}_a - v_a)^2] = \sigma_a^2 - \sum_{j=1}^N w_{aj} \sigma_{ja} + \lambda_a \quad (19)$$

The second term in the right hand side of Equation 19 represents the reduction in the variance of the estimator from the ensemble (or point) variance as a result of spatial correlation. If all of the observation points and the point to be estimated are separated far enough to be $\sigma_{ja} \approx 0$; $\sigma_{ij} \approx 0$ for $i \neq j$, the estimate may equal to the arithmetic mean, and the ordinary kriging variance may reduce to:

$$\sigma_{OK,a}^2 \approx \sigma_a^2 + \lambda_a \approx \sigma^2 \gamma(\Omega_a) + \frac{\sigma^{*2}}{N} \quad (20)$$

because $w_{aj}\sigma_{jj} \approx w_{aj} \text{var}[v_j^*] = w_{aj}\sigma^{*2} \approx \lambda_a$; $w_{aj} \approx \frac{1}{N}$ from Equations 17 and 18.

Similarly, the covariance between two values \hat{v}_a and \hat{v}_b is given by:

$$\sigma_{OK,ab} = E[(\hat{v}_a - v_a)(\hat{v}_b - v_b)] = \sigma_{ab} - \sum_{k=1}^N w_{ak} \sigma_{kb} + \lambda_a \quad (21)$$

alternatively,

$$\sigma_{OK,ab} = E[(\hat{v}_a - v_a)(\hat{v}_b - v_b)] = \sigma_{ab} - \sum_{k=1}^N w_{bk} \sigma_{ka} + \lambda_b \quad (22)$$

Again when $\sigma_{ja} \approx 0$; $\sigma_{ij} \approx 0$ for $i \neq j$, the ordinary kriging covariance reduces to:

$$\sigma_{OK,ab} \approx \sigma_{ab} + \lambda_a \approx \sigma^2 \gamma(\Omega_a, \Omega_b) + \frac{\sigma^{*2}}{N} \quad (23)$$

It should be noted that uncertainties arising from the sampling errors are implicitly included in Equations 19 and 21, because the mean value needs to be estimated based on observations. Also, Equations 20 and 23 are identical to Equations 14 and 15 (based on the unconditional evaluation) as they should be.

4. Probability of Failure

Conceptually, the performance of a structure can be described by a limit state function $g(\mathbf{x})$ such that failure is defined whenever the condition of $g(\mathbf{x}) \leq 0$ is satisfied, where \mathbf{x} is the vector of model variables. The probability of failure is then given by:

$$p_f = P(g(\mathbf{x}) \leq 0) = \int_{g(\mathbf{x}) \leq 0} f(\mathbf{x}) d\mathbf{x} \quad (24)$$

where $f(\mathbf{x})$ is the joint probability density function (PDF) of \mathbf{x} .

During last four decades, a number of computational methods have been developed to efficiently solve the problem. These include the mean-value first order second moment (MVFOSM or often simply FOSM) (Cornell 1969) and the first- and second-order reliability methods (FORM and SORM) (Ang and Tang 1984; Madsen et al. 1986). A variety of other computation methods, including simulation methods (Rubinstein 1981; Shinozuka 1983) and response surface methods (Faravelli 1989) are also available.

5. Example Analyses

The purpose of the example analyses is to illustrate the influence of the various assumptions on the estimated soil properties and the resulting probabilities of failure

5.1 Influence of Spatial Correlation and Averaging

The author is interested in evaluating the risk of failure of a hyperthetic cohesive slope shown in Figure 1. Three vertical borings are carried out and 10 soil samples are taken at the specific locations shown in Figure 1. Subsequent tests yield a sample mean $\hat{\mu}_c = 45 \text{ kN/m}^2$ and a sample standard deviation $s_c (= \sigma_c^*) = 13.5 \text{ kN/m}^2$ for undrained shear strength, and $\hat{\mu}_\gamma = 18 \text{ kN/m}^3$ and $s_\gamma = 0.9 \text{ kN/m}^3$ for soil density. For practical purpose, these values can be considered as point statistics (e.g., Vanmarcke

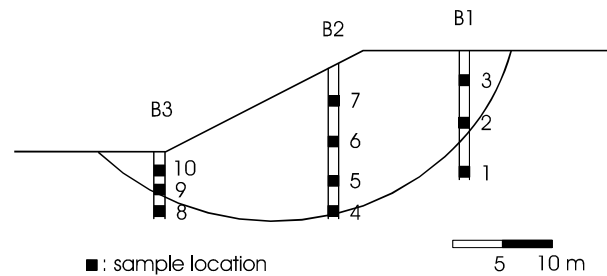
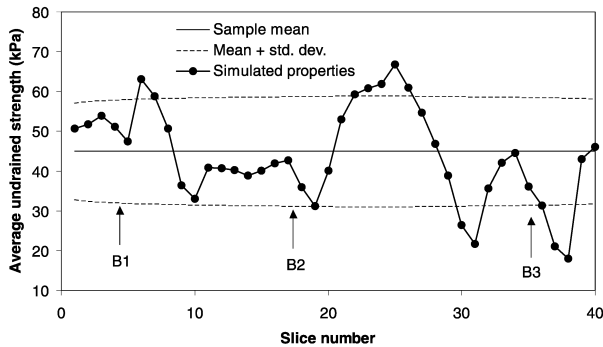


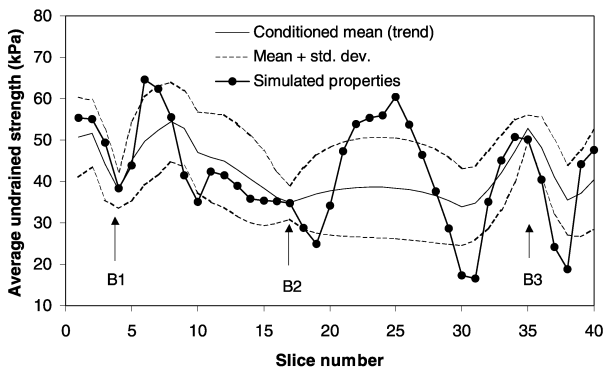
Fig. 1. Geometry and Sample Location of a Circular Slip Surface

1977a). Previous experience with local geology indicates that the soil can be modeled as a homogeneous random field, and scales of fluctuation are taken as $\delta_x = 5m$ and $\delta_y = 1m$ respectively. A separable 2-D exponential auto-correlation function is employed to model the correlation (i.e., Vanmarcke 1983; Li and White 1987a). It is known that the computed statistics of the local average is generally not sensitive to the type of autocorrelation function (i.e., Vanmarcke 1977a).

For limit equilibrium analyses, the author is interested in simulating the random soil properties that represent the spatial averages of the vertical soil slices and thus we need to compute the statistics of averaged soil properties for each slice. Figures 2a and 2b show samples of simulated shear strengths over the 40 slices of the slip surface for both unconditional and conditional cases, assuming a Gaussian distribution. Scales of fluctuation used in those figures, however, are not $\delta_x = 5m$, $\delta_y = 1m$ but $\delta_x = 25m$, $\delta_y = 5m$ just for clear illustrative purpose. The undrained strengths generated by the conditional method (Figure 2b) show that the conditional mean (trend)



(a) Unconditional Simulation (With Sampling Errors Considered)



(b) Conditional Simulation

Fig. 2. Simulation of Average Undrained Shear Strengths

is no longer stationary, but deviates from the sample mean and is influenced by the measured values nearby. The conditional standard deviation becomes smaller near the measurement points and gradually increases with increasing distance, ultimately reaching the value of the unconditional standard deviation. Hence the conditional approach leads to increasing variance reduction with increasing number of measurements as would be expected.

The correlation between the average shear strengths over the soil slices (Figure 3) shows that sampling error increases the correlation between the random quantities. It is interesting to observe that the conditional correlation does not decrease monotonically with distance but it even increases with increase of distance from the measurement points. That is because the conditional correlation depends not only on the lag distance between the random quantities of interest, but also depends on the distance from the sampling points to the point (or area) of interest.

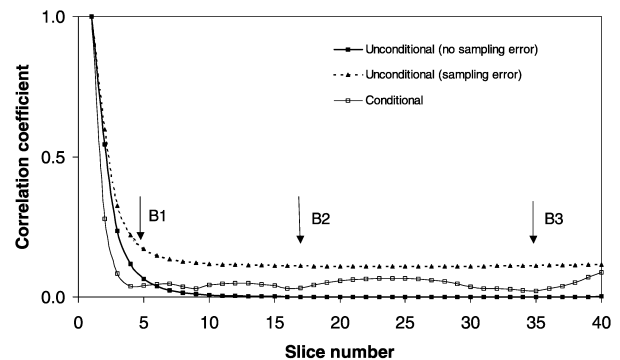


Fig. 3. Correlation Between the Line Averages with Respect to the Average of the First Slice

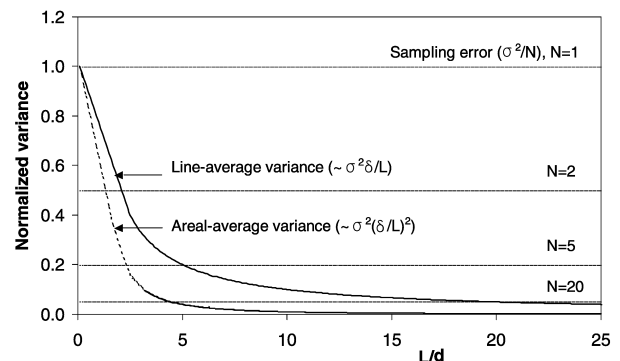


Fig. 4. Comparison of the Uncertainty Magnitudes Between the Spatial Variation (Inherent Uncertainty) and Sampling error (Statistical Uncertainty); N is the Number of Tests, L is the Scale of Averaging, and δ is the Scale of Fluctuation (Kim, 2003)

Figure 4 shows the comparison of magnitude of uncertainty between the spatial variation and sampling error. Unlike the inherent uncertainty, errors from the insufficient data and imperfect measurement do not decrease by averaging over the area of space, but depend on the number of samples.

5.2 Reliability Analysis of Slope Stability

The potential sliding mass was divided into 40 vertical soil slices of equal width for stability analyses using the Simplified Bishop method. Deterministic analyses of the static slope stability, with the mean soil properties, yielded a factor of safety 1.52. Analyses with more adverse soil properties ($\mu - \sigma$ for the shear strengths and $\mu + \sigma$ for soil density) resulted in a factor of safety 1.02.

The limit-state function for the reliability analyses was defined as:

$$g(\mathbf{x}) = FS(\mathbf{x}) - 1$$

which defined the slope to be safe for factor of safety $FS(\cdot)$ greater than one. The reliability computations were carried out with the aid of CALREL, a general-purpose structural reliability analysis program developed by Liu et al. (1989), linked to user-defined subroutine programs for static slope stability analyses including STAGLEM and GLEM developed by Kim (2001). The undrained strength of soil was modeled with both normal and lognormal distributions in order to examine the influence of uncertainty of distribution forms on the risk level of the problem. The soil properties were modeled using the same parameters as used in the previously discussed statistical analyses.

The computed distributions (densities) of the factors of safety are shown in Figure 5. The mean is essentially the same for all the cases but the shape of the distribution for the case of the sampling error added (both conditional and unconditional cases) is more dispersed due to the added uncertainty and, consequently, resulted in a higher probability of failure. It should be noted that the area underneath the density function with the factor of safety FS less than one is the probability of failure. Reflecting

the variance reduction from the spatial averaging, the density of the unconditional approach (without sampling error) is relatively narrower than that of the conventional random value approach. In this particular example problem, the differences between the unconditional and conditional cases are relatively small because the additional variance reduction by conditioning is small due to the relatively small scale of fluctuation ($\delta_x = 5m$ and $\delta_y = 1m$).

The results in Table 1 also show that the risk of failure is sensitive to the choice of the distribution model of random soil properties (i.e., an order of magnitude difference in P_f). In this particular case, the analyses with soil properties assumed to have normal distributions consistently yield higher probability of failure than with lognormal distributions. That may be mainly because the normal distribution has more density (or weight) in smaller values than the lognormal distribution with the same mean and standard deviation, since the lognormal is non-negative. Thus, if the distribution form is uncertain, it may be worth examining distributions other than normal distribution.

The scale of fluctuation has significant effect on the reliability of the slope stability, especially for the unconditional approach without sampling errors (Figure 6). As expected, risk of failure significantly increases with increase

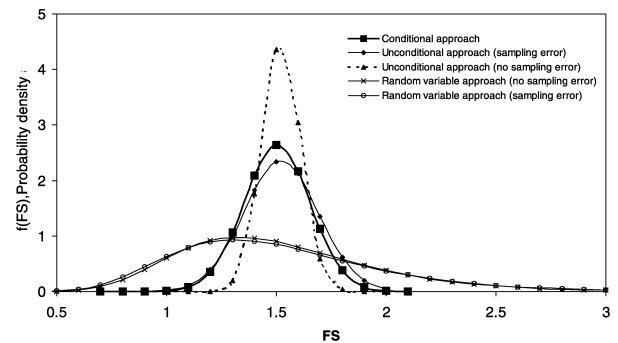


Fig. 5. Probability Distributions of Factors of Safety ($\delta_x = 5m$ and $\delta_y = 1m$) with Soil Properties Normally Distributed

Table 1. Probabilities of failure (P_f) for three different approaches with normal and lognormal distributions

Source of uncertainty	Normal	Lognormal
Spatial variation only	2.1×10^{-9}	1.2×10^{-12}
Sampling error added	1.4×10^{-3}	2.2×10^{-4}
Conditional approach	4.2×10^{-4}	6.1×10^{-5}

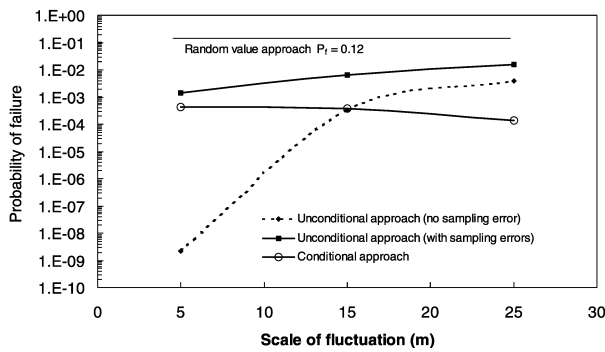


Fig. 6. Effects of the Scale of Fluctuation on the Failure Probability of the Slope

of the scale of fluctuation, since the variance reduction decreases. Uncertainty arising from sampling errors substantially contributes to the risk of failure, thus illustrating the importance of the sampling errors in the assessment of slope stability problem. In contrast, the results of the unconditional approach with sampling errors and conditional approach are relatively insensitive to the scale of fluctuation. That is partly due to the fact that with the increasing scale of fluctuation the increase in variance reduction by conditioning is offset by a decrease in the variance reduction as a result of spatial averaging. The fact that these approaches are less sensitive to the scale of fluctuation can be potentially important implication, since accurate determination of the scale of fluctuation has been problematic and requires an additional effort beyond that needed to obtain the mean and standard deviation. This example also shows that significant variance reduction can be achieved by spatial averaging, and illustrates the importance of spatial correlation with the soil property determination. The results suggest that if the size of the averaging domain is sufficiently large, the variance associated with inherent uncertainty may be practically neglected, thus allowing us to focus on the statistical uncertainty and measurement errors

6. Conclusions

The results of analyses confirm that the variability of the local average is always less than that of the point value and that it decreases with increase of the size of the averaging domain. Another important outcome of the

stochastic treatment is that the variability of the local average always decreases as the dimension of a domain increases. The variance reduction due to averaging of an area or a volume can be more significant than line averaging. Thus, the uncertainty of the area or volume-averaged soil properties is consequently often far less than that of the point properties.

Unlike the inherent uncertainty, sampling-related uncertainty does not decrease by averaging of the area or space, but depends on only the number of samples.

The results suggest that if the size of the averaging domain is sufficiently large, relative to the scale of fluctuation, the variance associated with inherent uncertainty may be practically neglected, thus allowing us to focus on the sampling-related uncertainty such as the statistical uncertainty.

The conditional approach, while computationally more intensive, offers the advantage of honoring the data at the respective sampling points and it is particularly well suited in situations with large numbers of samples in a highly correlated random field.

Estimates of probability of failure obtained from reliability analyses show that the conditional approach, which accounts for the inherent spatial variability of the soil deposit and sampling errors, leads to significantly lower estimates of the probability of failure than that obtained by using simple random variable (perfectly correlated soil) approach. The proposed unconditional approach that accounts for sampling-related uncertainty also results in a good approximation to the results of more general conditional approach.

Finally, the analyses strongly suggest that the spatial variability and sampling error have to be properly incorporated in slope stability analysis.

Acknowledgements

This work was supported for two years by Pusan National University Research Grant. The author thanks professor Sitar of University of California at Berkeley for reviewing the manuscript.

Appendix

The following derivations may help the reader understand the developed equations.

$$\begin{aligned}\text{var}[\hat{\mu}] &= \text{var}\left[\frac{1}{N} \sum_{i=1}^N V_i^*\right] \\ &= \frac{1}{N^2} \left[\sum_{i=1}^N \text{var}(V_i^*) \right] \\ &= \frac{\sigma^{*2}}{N}\end{aligned}\quad \text{Equation (11)}$$

$$\begin{aligned}\text{var}[\bar{v}] &= E[(\bar{v} - \mu)^2] \approx E\left\{\left[\frac{1}{V} \int_{\Omega_e} (\hat{\mu} - \mu) dx + \frac{1}{V} \int_{\Omega_e} \varepsilon(\mathbf{x}) dx\right]^2\right\} \\ &= \frac{1}{V^2} \int_{\Omega_e} \int_{\Omega_e} E[(\hat{\mu} - \mu)(\hat{\mu}' - \mu)] dx dx' + \frac{1}{V^2} \int_{\Omega_e} \int_{\Omega_e} E[\varepsilon(\mathbf{x})\varepsilon(\mathbf{x}')] dx dx' \\ &= \frac{1}{V^2} \int_{\Omega_e} \int_{\Omega_e} \text{var}(\hat{\mu}) dx dx' + \frac{1}{V^2} \int_{\Omega_e} \int_{\Omega_e} \sigma^2 \rho(\mathbf{r}) dx dx' \\ &= \frac{\sigma^{*2}}{N} + \sigma^2 \gamma(\Omega_e)\end{aligned}\quad \text{Equation (14)}$$

$$\begin{aligned}\text{cov}[\bar{v}, \bar{v}'] &= E[(\bar{v} - \mu)(\bar{v}' - \mu)] \\ &\approx E\left\{\left[\frac{1}{V} \int_{\Omega_e} (\hat{\mu} - \mu) dx + \frac{1}{V} \int_{\Omega_e} \varepsilon(\mathbf{x}) dx\right] \left[\frac{1}{V'} \int_{\Omega_e'} (\hat{\mu}' - \mu) dx' + \frac{1}{V'} \int_{\Omega_e'} \varepsilon(\mathbf{x}') dx'\right]\right\} \\ &= \frac{1}{VV'} \int_{\Omega_e} \int_{\Omega_e'} E[(\hat{\mu} - \mu)(\hat{\mu}' - \mu)] dx dx' + \frac{1}{VV'} \int_{\Omega_e} \int_{\Omega_e'} E[\varepsilon(\mathbf{x})\varepsilon(\mathbf{x}')] dx dx' \\ &= \frac{1}{VV'} \int_{\Omega_e} \int_{\Omega_e'} \text{var}(\hat{\mu}) dx dx' + \frac{1}{VV'} \int_{\Omega_e} \int_{\Omega_e'} \sigma^2 \rho(\mathbf{r}) dx dx' \\ &= \frac{\sigma^{*2}}{N} + \sigma^2 \gamma(\Omega_e, \Omega_e')\end{aligned}\quad \text{Equation (15)}$$

References

- Ang, A. H. S., and Tang, W. H. (1984), *Probability Concepts in Engineering Planning and Design, Volume II-Decision, Risk, and Reliability*, John Wiley & Sons, New York.
- Ang, A. H. S., and Tang, W. H. (1975), *Probability Concepts in Engineering Planning and Design, Volume I-Basic Principles*, John Wiley & Sons, New York.
- Christian, J. T., Ladd, C. C., and Baecher, G. B. (1994), "Reliability Applied to Slope Stability Analysis", *Journal of Geotechnical Engineering*, ASCE, Vol.120, No.12, pp.2180-2207.
- Christian, J. T., and Urzua, A. (1998), "Probabilistic Evaluation of Earthquake-Induced Slope Failure", *Journal of Geotechnical and Geoenvironmental Engineering*, ASCE, Vol.124, No.11, pp.1140-1143.
- Cornell, C. A. (1969), "Structural Safety Specification Based on Second-Moment Reliability", *Symposium, International Association of Bridge and Structural Engineers*, London.
- Duncan, J. M. (2000), "Factors of Safety and Reliability in Geotechnical Engineering", *Journal of Geotechnical and Geoenvironmental Engineering*, ASCE, Vol.126, No.4, pp.307-316.
- Faravelli, L. (1989), "Response Surface Approach for Reliability Analysis", *Journal of Engineering Mechanics*, ASCE, Vol.115, No.12, pp.2763-2781.
- Journel, A. G. (1989), *Fundamentals of Geostatistics in Five Lessons*, American Geophysical Union.
- Kim, J. (2001), *Probabilistic Approach to Evaluation of Earthquake-Induced Permanent Deformation of Slopes*, Ph.D. Dissertation, Dept. of Civil and Env. Engineering, University of California at Berkeley.
- Kim, J. (2003), "The Importance of Geotechnical Variability in the Analysis of Earthquake-Induced Slope Deformations", *Journal of Korean Geotechnical Society*, Vol.19, No.2, pp.123-133
- Krige, D. G. (1966), "Two-Dimensional Weighted Moving Averaging Trend Surfaces for Ore Evaluation", *Proceedings of Symposium on Mathematical Statistics and Computer Applications for Ore Evaluation*, Johannesburg, S. A., pp.13-38.
- Li, K. S., and Lumb, P. (1987), "Probabilistic Design of Slopes", *Canadian Geotechnical Journal*, Vol.24, pp.520-535.
- Li, K. S., and White, W. (1987a), *Probabilistic Characterization of Soil Profiles*, Research Report No.19, Department of Civil Engineering, University College, The University of New South Wales, Canberra, Australia.
- Li, K. S., and White, W. (1987b), *Probabilistic Approaches to Slope Design*, Research Report No. 20, Department of Civil Engineering, University College, The University of New South Wales, Canberra, Australia.
- Liu, P. L., and Der Kiureghian, A. (1986), "Multivariate Distribution Models with Prescribed Marginals and Covariances", *Probabilistic Engineering Mechanics*, Vol.1, No.2, pp.105-112.
- Liu, P. L., Lin, H. Z., and Der Kiureghian, A. (1989), *CALREL User Manual*, Report No. UCB/SEMM-89/18, Department of Civil Engineering, University of California at Berkeley, USA.
- Madsen, H. O., Krenk, S., and Lind, N. C. (1986), *Methods of Structural Safety*, Prentice-Hall, Englewood Cliffs, NJ.
- Matheron, G. (1967), "Kriging or Polynomial Interpolation Procedures", *Canadian Institute of Mining Bulletin*, Vol.60, pp.1041.
- Rubinstein, R. Y. (1981), *Simulation and the Monte Carlo method*, John Wiley & Sons, New York.
- Shinozuka, M. (1983), "Basic Analysis of Structural Safety", *Journal of Structural Engineering*, ASCE, Vol.109, No.3, pp.721-740.
- Tang, W. H. (1984), "Principles of Probabilistic Characterization of Soil Properties", *Proceedings of the Symposium on Probabilistic Characterization of Soil Properties*, Atlanta, Georgia, pp.74-89.
- Tang, W. H., Yucemen, M. S., and Ang, A. H. S. (1976), "Probability-Based Short Term Design of Soil Slope", *Canadian Geotechnical Journal*, Vol.13, pp.201-215.
- Vanmarcke, E. (1983), *Random Fields: Analysis and Synthesis*, The MIT Press, Cambridge, Massachusetts.
- Vanmarcke, E. H. (1977a), "Probabilistic Modeling of Soil Profiles", *Journal of Geotechnical Engineering Division*, ASCE, Vol.103 (GT11), pp.1227-1246.
- Vanmarcke, E. H. (1977b), "Reliability of Earth Slopes", *Journal of Geotechnical Engineering Division*, ASCE, Vol.103 (GT11), pp.1247-1265.

(received on Jan. 8, 2007, accepted on Mar. 19, 2007)

Comparative Study between Design Methods and Pile Load Tests for Bearing Capacity of Driven PHC Piles in the Nakdong River Delta

낙동강 삼각주에 향타된 PHC말뚝의 지지력을 위한 재하시험과 지지력 공식의 비교연구

Dung, N. T.¹

Chung, S. G.²

정 성 교

Kim, S. R.³

김 성 렬

Chung, J. G.⁴

정 진 교

요 지

우리나라에서는 암반 및 자갈층과 같은 단단한 층 내에 깊은 기초를 매입하는 것이 일반적이다. 그러나 Chaophraya(Bangkok)와 Mississippi강 삼각주에서 실시되고 있는 것과 같이, 대심도 낙동강 삼각주 퇴적토에서도 말뚝의 지지층으로써 중간 깊이에 위치하는 모래 및 모래질 자갈층을 고려할 필요가 있다. 이 연구는 이 지역에서 PHC 말뚝을 요구하는 깊이까지 향타할 때, 말뚝의 지지력을 위한 적절한 평가법을 찾고자 하였다. 지반조사는 두 현장의 5개소에서 실시되었다. 말뚝의 지지력은 지반조사 결과를 이용하고 CPT에 근거한 평가법과 여러 다른 해석법을 적용하여 계산되었으며, 상호 비교가 이루어 졌다. 향타된 5개의 말뚝에 대해 매입된 전 깊이에 걸쳐 잘 알려진 PDA시험이 체계적으로 수행되었다. 여러 평가법에 의하여 계산된 지지력은 PDA 및 정재하 시험결과와 함께 비교되었다. 그 결과, 주면마찰력은 set-up 효과에 따라 지배적으로 영향을 받으며, 장시간 경과 후에는 β 법에 의한 결과와 좋은 일치를 보였다. 선단 지지력은 과소평가되는 PDA시험 보다는 정재하시험결과에 근거하여 적절한 평가법을 선정하였다. 최종적으로, CPT결과를 이용하여 이 지역에 적합한 지지력의 평가법을 도출하였다.

Abstract

Deep foundations have been popularly installed in hard stratum such as gravels or rocks in Korea. However, it is necessary to consider sand or sandy gravel layers that locate at the mid-depths as the bearing stratum of piles in the thick Nakdong River deltaic deposits, as done in the Chaophraya (Bangkok) and Mississippi River deltas. This study was focused on the finding of suitable methods for estimating bearing capacity when driving prestressed high-strength concrete (PHC) piles to a required depth in the deltaic area. Ground investigation was performed at five locations of two sites in the deltaic area. Bearing capacity of the driven piles has been computed using a number of proposed methods such as CPT-based and other analytical methods, based on the ground investigation and comparison one another. Five PDA (pile driving analyzer) tests were systematically carried out at the whole depths of embedded piles, which is a well-known useful technique for the purposes. As the results, the bearing capacities calculated by various methods were compared with the PDA and static load testing results. It was found that the shaft resistance is significantly governed by set-up effects and then the long-term value agrees well with that of the β method. Also, the design methods for toe resistance were determined based on the SLT result, rather than PDA results that led to underestimation. Moreover, using the CPT results, appropriate methods were proposed for calculating the bearing capacity of the piles in the area.

Keywords : Bearing capacity, PHC pile, Drivability, CPT, PDA, Sand

1 Member, PhD Student, Dong-A Univ., School of Civil Engrg., Busan, Korea

2 Member, Prof., Dong-A Univ., School of Civil Engrg., Busan, Korea, sgchung@dau.ac.kr, Corresponding Author

3 Member, Assistant Prof., Dong-A Univ., School of Civil Engrg., Busan, Korea

4 Member, Associate Prof., Pusan Information Technology College, Dept. of Civil Engrg., Busan, Korea

1. Introduction

In the west marginal lands of Busan city and its vicinity, which are located in the mouth of the Nakdong River, reclamation works have been started to develop industrial and residential complexes, since early 1990s. Although the new development was complete, most of the developed lands have been lying vacant for a long time. As unusually soft and thick clay was deposited in the area, the high construction cost for deep foundations was a problem for the housing development. The costly foundations come from long piles (e.g. steel pipe piles) founded on rocks and/or gravel layer, sometimes from bitumen coating.

Case histories of friction pile in the other deltaic areas, such as Chaophraya river delta (Phien-wej, 2006) and Mississippi River deltas (Blessey, 1976), are interesting to be observed. These deltas are well-known as unusually deep deposits where bedrock exists at the depths of 400-500 m and 1-2 km respectively. And also, deep foundations have mostly been installed into the medium or dense sand layers in both areas. Therefore, it is necessary to consider whether friction piles in sand layer is possible to be applied in the Nakdong River estuary.

The aim of this study is to examine bearing capacities of piles at various depths in the sand layers of the Nakdong River deltaic deposit. For this, two locations were chosen in two different sites. A comprehensive geotechnical investigation was performed to determine soil parameters for pile design, using high-capacity CPT equipment, BST (borehole shear test) etc. A number of CPT-based design and other analytical methods were applied to calculate the bearing capacity and then the calculated results were compared with PDA analysis and static loading test (SLT) results. Unlike the steel pipe piles that are usually used in the area, the PHC piles of 600 mm in diameter were chosen and driven up to gravelly sand layer overlying the lower sand layer or to the sand layer. PDA (pile driving analyzer) tests were systematically performed for every blow during pile driving. Based on the results of PDA tests, the bearing capacity (resistance) as well as the drivability was analyzed. Finally, by

comparing the measured and calculated bearing capacities, appropriate design methods are proposed to evaluate the proper bearing capacity in the area.

2. Study Sites and Ground Conditions

The study sites were Myeongji (MJ) and Shinho (SH) areas in the Nakdong River estuary, as shown in Fig. 1. Ground investigation for pile design was performed in the MJ and SH sites and the soil profiles are shown in Fig. 2. The fill of about 5 m thick was placed on the original ground surface and followed by loose silty sand (upper sand), soft clayey silt (upper clay), dense sand (lower sand) and sandy gravel on bed rock. Thin clayey silt mostly is sandwiched in the lower sand layer.

The geotechnical profiles for both the sites are shown in Figs. 3 and 4, in which the presented soil parameters were adopted for pile design. The soil parameters of the sand were determined based on CPTU data: The unit weight was obtained based on the soil classification system proposed by Robertson et al. (1986); the effective friction angle was obtained from the chart of the relationship between effective stress and cone tip resistance proposed by Robertson & Campanella (1983a). However, most of the soil parameters of the clay were determined from laboratory tests. The undrained shear strength, S_u , was determined from both laboratory (CIU) and field (CPT and Field vane) tests. The corrected vane strength by the method of Aas et al. (1986) is close to $0.22\sigma'_{v0}$,

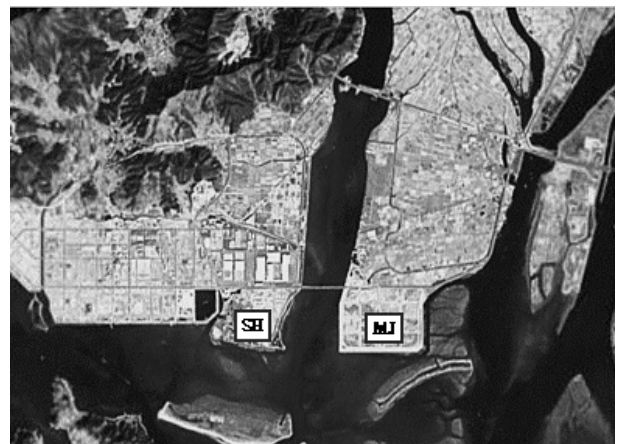


Fig. 1 Locations of study sites

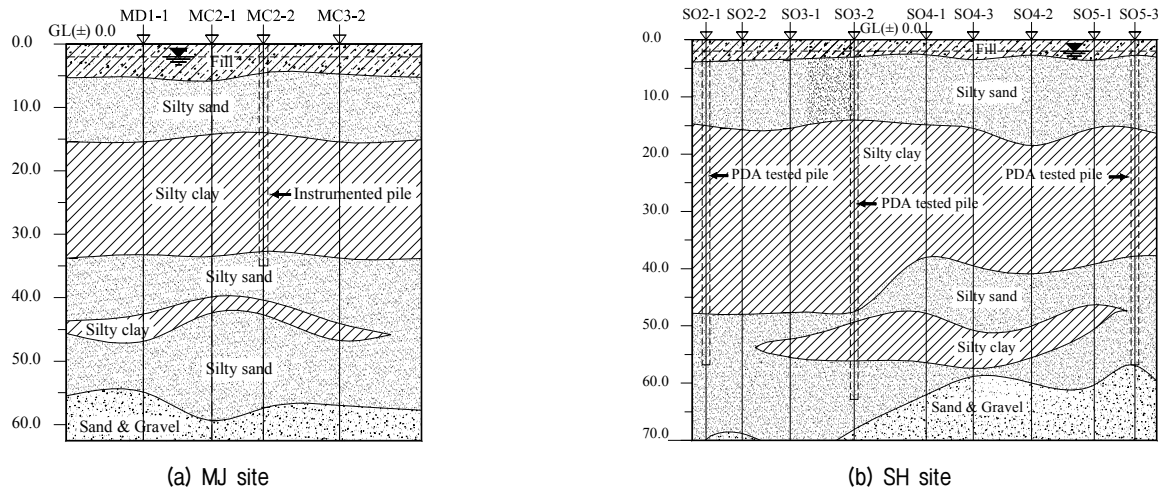


Fig. 2. Boring logs and soil profile

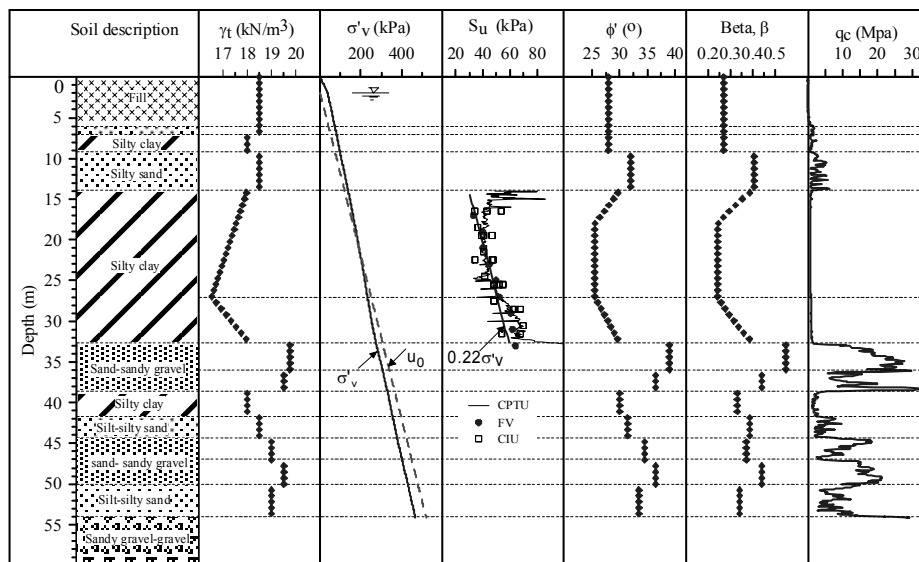


Fig. 3. Geotechnical profile at MC2-2

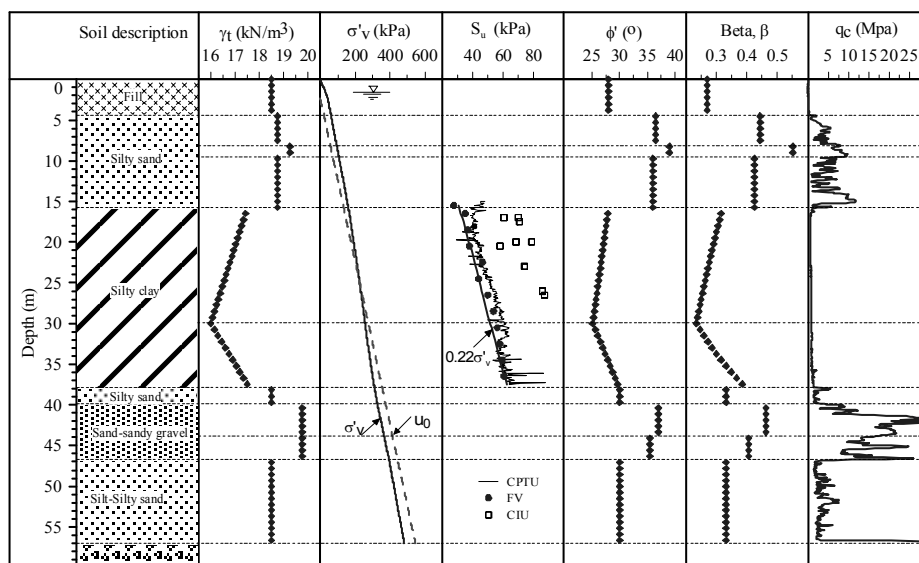


Fig. 4. Geotechnical profile at SO5-3

as indicated by Chung et al. (2006). Due to the recent fill, the maximum excess pore pressure of about 20 kPa existed at the middle of the upper clay in both sites.

3. Evaluation Methods for Pile Bearing Capacity

A number of pile design methods have been developed

to calculate bearing capacity by using CPT or CPTU data (named as CPT-based design methods), which are summarized in Table 1. In the table, r_s and r_t are unit shaft and toe resistances and other parameters such as f_s , q_c , q_t , and q_E are shaft, cone tip, corrected cone tip and effective cone tip resistances respectively. The details of each

Table 1. CPT-based design methods

Method	Unit shaft resistance	Unit toe resistance
Schmertmann (1975)	$r_s = Kf_s$ Clay: $(0.25 \leq K \leq 1.25)$ Sand: $(0.25 \leq K \leq 1.25)$	$r_t = C_{OCR} q_{ca}$ Influence zone: 8D above, 4D below pile toe
European (1979) (DeRuiter and Beringen, 1979)	Clay: $r_s = \alpha S_u = 0.05 \alpha q_c$ $\alpha = 1$ (NC clay), 0.5 (OC clay) Sand: $r_s = \min(f_s, q_c/300)$	Sand $r_t = C_{OCR} q_{ca}$ (Smert. method) Clay: $r_t = N_c S_u$ $r_t = 15$ MPa)
French (1982) (Bustamente and Gianceselli, 1982)	$r_s = K q_c \leq J$ K, J are given in table from original paper	$r_t = C q_{ca}$ Infl. Zone (1.5D, 1.5D) Clay: $0.45 \leq C \leq 0.55$ Sand: $0.40 \leq C \leq 0.50$
Mayerhof (1976,1983)	$r_s = K_f f_s$ ($K = 1$) [*] $r_s = C_c q_c$ ($C_c = 0.5$)	$r_t = C_1 C_2 q_{ca}$ Influence zone: 4D above, 1D below pile toe. C_1, C_2 are function of diameter, embedded depth into bearing stratum
Tumay & Fakhroo (1981)	$r_s = K f_s$ $K = 0.5 + 9.5e^{-90f_s}$ (f_s in MPa)	$r_t = C_{OCR} q_{ca}$ (Schmert. method) Influence zone: 8D above, 4D below pile toe
Eslami–Fellenius (1997) (E–F method)	$r_s = C_s q_E$ ($q_E = q_t - U_2$) $C_s = 0.004 - 0.08$ depends on soil type	$r_t = C_t q_{Eg}$ q_{Eg} = geometric average of q_E over infl. zone of 8D above, 4D below. $C_t = 1/(3D)$ if $D \geq 400$ mm
Prince and Wardle (1982)	$r_s = \alpha f_s$ ($\alpha = 0.53$ driven pile)	$r_t = k_{t2} q_{ca}$ $k_{b2} = 0.35$ (driven pile) q_{ca} arithmetic average over an infl. zone of 4D above and 4D below pile toe
Aoki and De Alencar (1975)	$r_s = \alpha_1 q_{ca} / F_{s2}$ ($r_s \leq 120$ kPa) $\alpha_1 = 1.4 - 6\%$ depends on soil type, $F_{s2} = 3.5$ (selected from given table)	$r_t = q_{ca} / F_b$ ($r_t \leq 15$ MPa) $F_b = 1.75$ (concrete pile, from given table). q_{ca} = arithmetic average over infl. zone of 4D above and 4D below pile toe
Philipponnat (1980)	$r_s = \alpha q_{ca} / F_s$ ($\alpha = 1.25$ driven pile) $F_s = 50 - 200$ depends on soil type	$r_t = k_t q_{ca}$ ($k_b = 0.35 - 0.5$ depends on soil type). Infl. zone 3D and 3D
Jardine et al. (2005) (ICP method)	Sand: $r_s = \sigma'_{rf} \tan \delta_{cv}$ Clay: $r_s = \sigma'_{rf} \tan \delta_f$ Details are given in reference	$r_t = q_c \left[1 - 0.51 \log \left(\frac{D}{D_{CPT}} \right) \right]$ D: pile diameter, D_{CPT} = cone diameter

* The method will be used for comparison with the PDA analysis.

Table 2. Analytical design methods

Resistance	Method	Unit resistances	Soil type	Reference
Shaft resistance (β methods)	Burland	$r_s = (K \tan \delta) \sigma'_v$	clay–sand	Burland (1973)
	Fellenius	$r_s = \beta \sigma'_v$ ^{**}	clay–sand	Fellenius (1991)
Toe resistance	Janbu	$r_t = c N_c^* + q^* N_q^*$	clay–sand	Janbu (1976)
	Vesic	$r_t = c N_c^* + \sigma'_0 N_\sigma^*$	clay–sand	Vesic (1977)
	Kulhawy	$r_t = B \gamma N_\gamma^* + \sigma'_{zD} N_q^*$	clay–sand	Kulhawy et al. (1983)
	Fellenius	$r_t = N_t \sigma'_{z=D}$	clay–sand	Fellenius (1991)

**The method will be used for comparison with the PDA analysis and modification of the Eslami–Fellenius (1997) method (which will be mentioned as the β method in the late sections).

method can be referred to the listed references.

A number of other analytical methods have also been developed and widely applied to estimate pile bearing capacity. In this paper, all available methods could not be mentioned in detail, however, some common methods used for this study are briefly described in Table 2.

4. Calculation of Bearing Capacity Based on Evaluation Methods

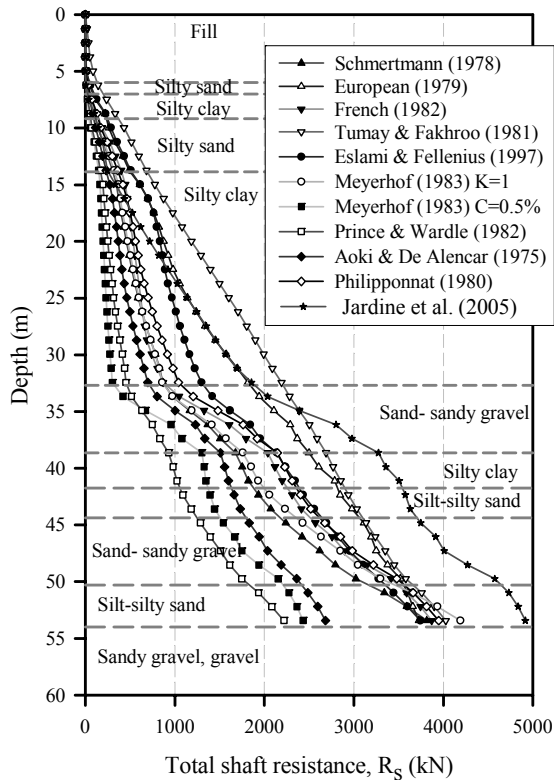
Bearing capacity was calculated under the following conditions: (a) Concrete cylinder pile with diameter of 600mm; (b) Soil classification was performed based on borehole logs data and CPTU data (by Eslami-Fellenius (1997) method); (c) The clays and sands are assumed as normally consolidated (NC) soils (Chung et al. 2002) and therefore parameters were taken for NC soils; and (d) An arithmetic average of cone tip resistance in the influence zone, q_{ca} , was used for all methods except the Eslami-Fellenius (1997) method which adopts geometric average of q_E .

The coefficient, $\beta = K \cdot \tan \delta$ that was proposed by Burland (1973) can be expressed as Eq. (1):

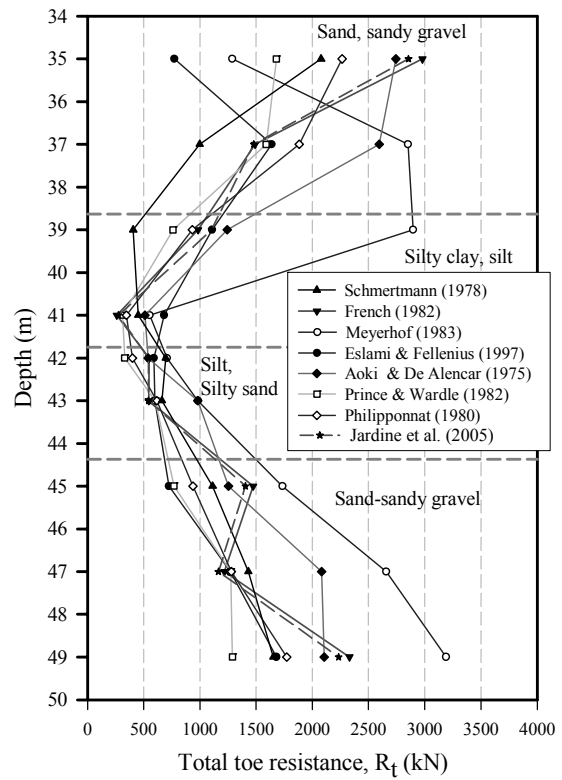
$$\beta = \left(\frac{K}{K_0} \right) K_0 \tan \delta = \left(\frac{K}{K_0} \right) (1 - \sin \phi') \tan(0.8\phi') \quad (1)$$

The average ratio, K/K_0 , was taken averagely as 1.60 for driven piles (large displacement piles) and the friction angle, δ , between pile and soil was taken as $0.8\phi'$, which is the average value of $\delta = (2/3 \sim 1) \phi'$. The values of β and N_t (toe bearing capacity coefficient) were linearly interpolated from an approximate range of β and N_t (Fellenius, 1991).

Figs. 5 and 6 show calculated results from the CPT-based methods for MC2-2 and SO5-3 locations. It is noted that the results significantly vary due to differences in the methods, rather than differences in the soil properties at the sites. In Figs. 5 (a) and 6 (a), the Jardine et al. (2005) and Prince and Wardle (1982) methods usually give largest and smallest shaft resistance values, respectively. The different magnitude increases significantly when the

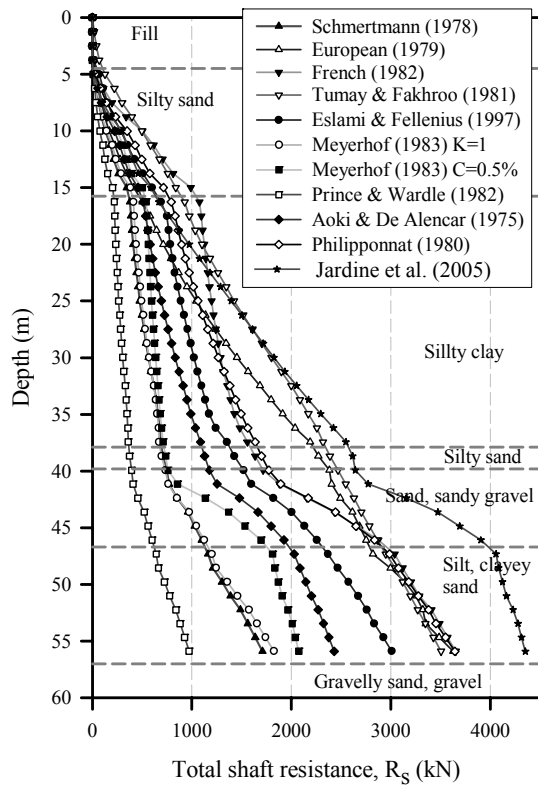


(a) shaft resistance

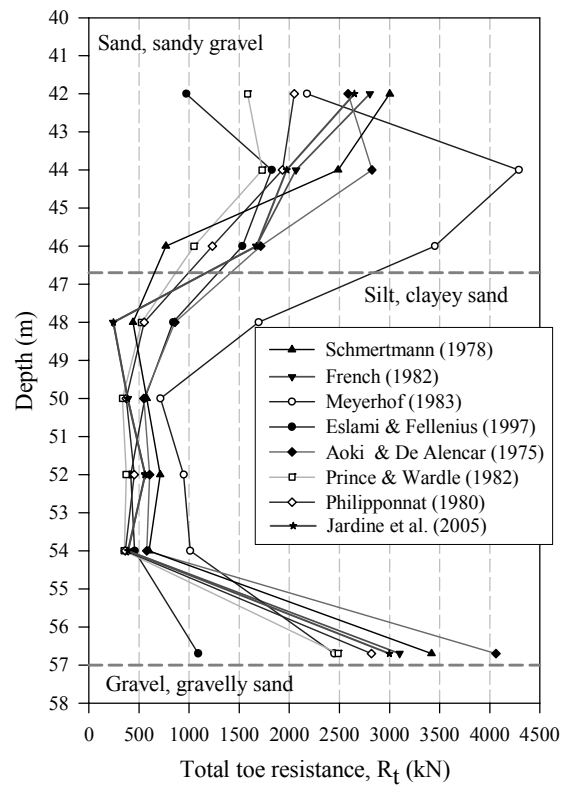


(b) toe resistance

Fig. 5. CPT-based total shaft and toe resistances at the MC2-2

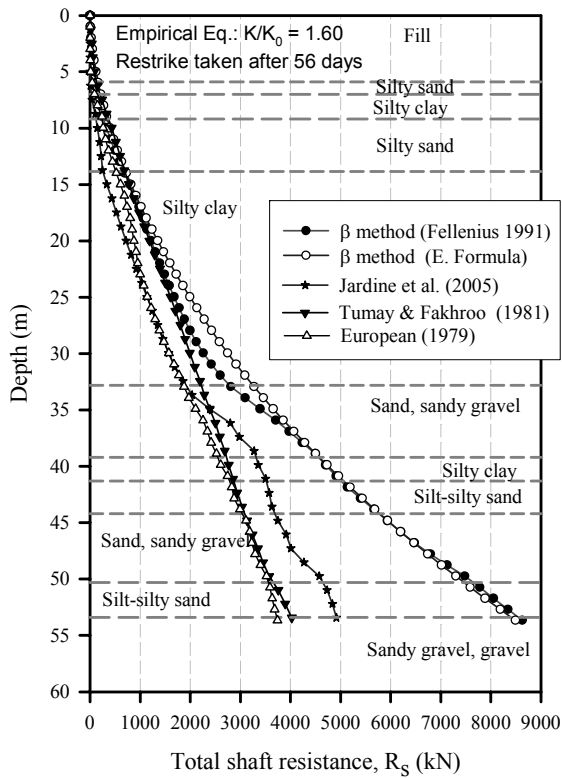


(a) shaft resistance

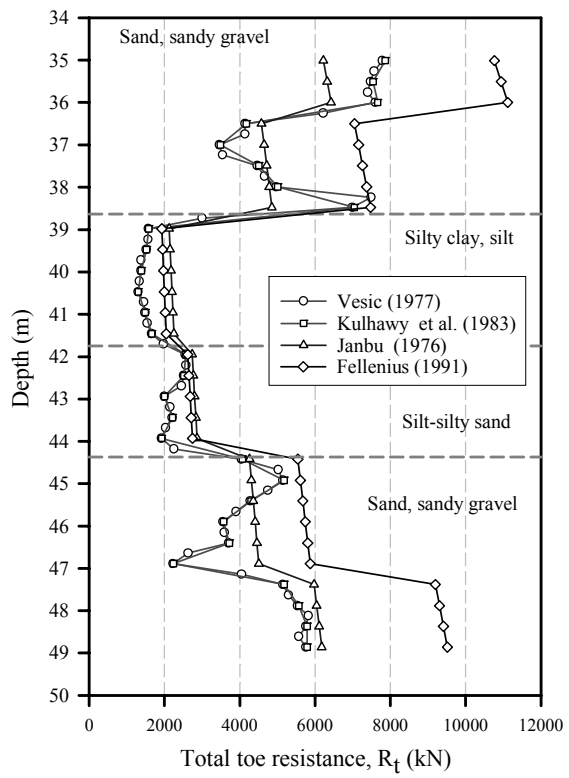


(b) toe resistance

Fig. 6. CPT-based total shaft and toe resistances at the SO5-3



(a) shaft resistance



(b) toe resistance

Fig. 7. Shaft and toe resistances from the analytical methods at the MC2-2

pile goes deeper into the sand layers and the maximum difference is up to 2500 kN at the study locations.

In Figs. 5 (b) and 6 (b), the calculated toe resistances have a similar trend to that from the cone tip resistance except the Meyerhof (1983) method. The toe resistances vary significantly when pile toe is located in the sand layers and the values tend to be much closer when pile toe is located in the silty clay or silt layers. As the soil is coarser, the difference in the toe resistance generally becomes larger. Figs. 5 (b) and 6 (b) show that there is no distinctive difference but a constant trend of the toe resistance between the methods; however, the Eslami-Fellenius (1997) method usually gives smallest values while the Meyerhof (1983) method the largest values for both sites. The maximum difference in the toe resistances is approximately 2000 kN in dense sand layers.

Figs. 7 and 8 show the shaft and toe resistances calculated by the analytical methods for both sites. The shaft resistances from the analytical methods were compared with those of the European (DeRuiter and Beringen, 1979), Tumay and Fakhroo (1981) and Jardine

et al. (2005) that gave largest values in the CPT-based methods. It is shown from Figs. 7 (a) and 8 (a) that the shaft resistance obtained from the β methods is significantly larger than the largest resistances obtained from the CPT-based methods. Considering that the β values were statistically derived from ultimate bearing capacity of static loading tests for friction piles (Fellenius, 2006a), the other methods lead to the underestimation. In addition, the shaft resistance from the β methods significantly increases with depth, compared to the others, when the pile goes deeper into the sand layers. It is because the β values are directly interpolated from the effective friction angle which is usually high in sand layers. Figs. 7 (b) and 8 (b) show that the toe resistances obtained from the methods of Janbu (1976), Vesic (1977) and Kulhawy et al (1983) are quite similar to one another, while the Fellenius (1991) method gives the largest values. In general, toe resistances obtained from these methods are usually 2 to 3 times larger than those obtained from the CPT-based methods.

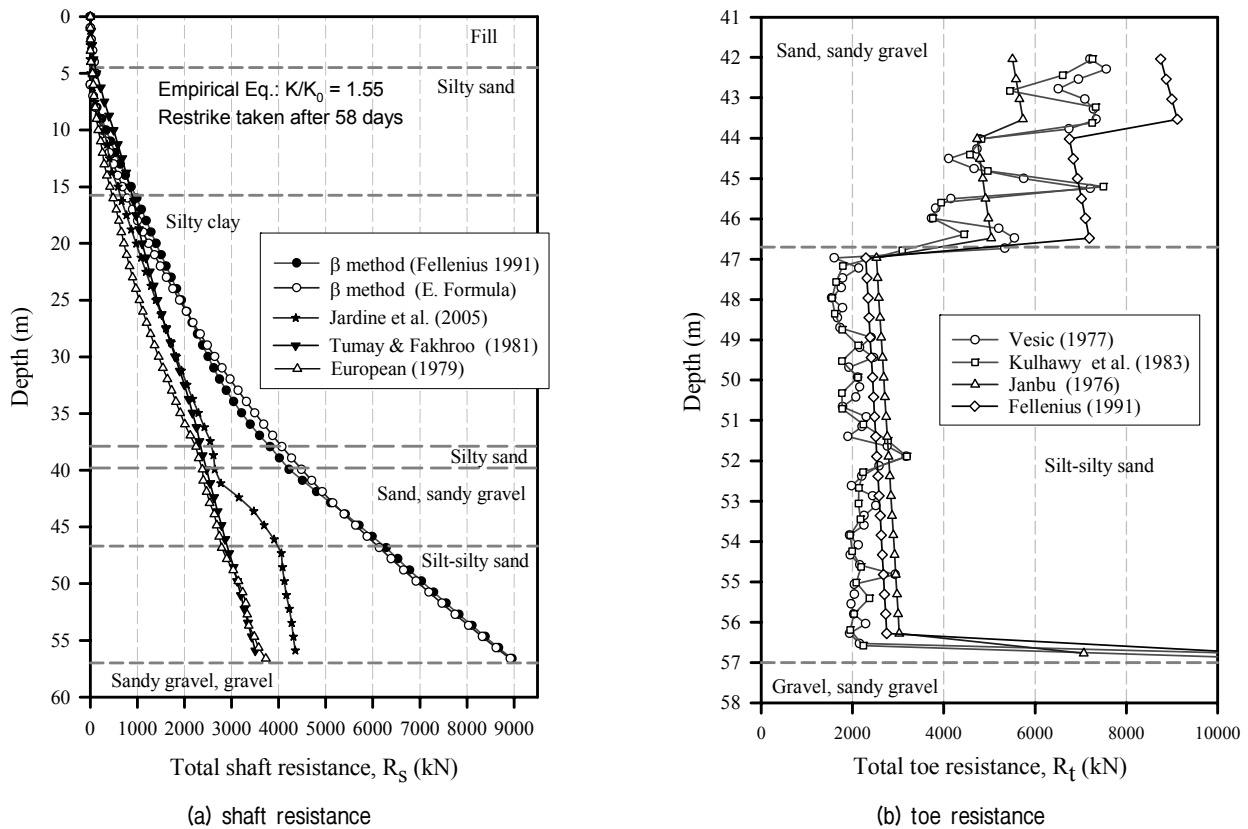


Fig. 8. Shaft and toe resistances from the analytical methods at the SO5-3

5. Pile Driving Analyzer (PDA) Test

5.1 Methodology

Five PHC piles (600 mm outer diameter, B-type) were driven to evaluate bearing capacity and drivability of long PHC piles at the sites: two piles that called MJ-2 at the borehole MC2-2 and three piles that called SH-2, SH-3, and SH-5 at the boreholes SO2-1, SO3-2, and SO5-3, respectively. The PDA tests were performed through the driving process, starting from the first stroke until the last meter depth. The piles were closed-end, driven by a hydraulic impact hammer having a weight of 16 ton. All the piles were driven successfully up to designed depths.

5.2 Drivability Analysis

A summary of pile drivability from the sites is given in Table 3. Figs. 9 and 10 show typically the results obtained from PDA tests on the two piles. It is very

interesting to note that the tendency of the stress and capacity curves (CSX, RMX) matched well with the cone tip resistance curves shown in Figs. 2 and 3. The allowable compressive and tensile stresses of the piles are 0.48 t/m^2 and 0.102 t/m^2 , respectively. As shown in Table 3, the maximum stresses (CSX, CSB and TSX) of the piles induced from driving process are all less than the allowable ones.

The quake value, which is the movement between the pile and the soil required to mobilize fully plastic resistance, is important to analyze the drivability of the pile. It was observed that the maximum quake values (Q) at the MJ and SH sites were 3.5 mm (0.58% of the pile diameter) and 6.9 mm (1.15% of the pile diameter), respectively. The quake value at the pile toe is known to be related to pile diameter and it is usually within the range of 1% of the pile diameter (Fellenius, 2006a). It could therefore be stated that the piles were driven within the range of reasonable values.

Table 3. Summary of drivability

Location	Monitored Depth (m)	Ram height (m)	F.P (mm)	Q (mm)	CSX (t/cm^2)	CSB (t/cm^2)	TSX (t/cm^2)	EMX (t-m)	ETR (%)	RMX (ton)	BTA
MJ-2*	14.0-35.0	0.2-0.8	3	2.54	0.29	0.23	0.031	7.89	62	320	88
MJ-2	14.0-49.4	0.2-0.8	4	3.50	0.31	0.27	0.065	10.4	81	370	86
SH-5	14.0-56.7	0.2-0.8	3	6.90	0.33	0.26	0.071	10.0	78	430	81
SH-3	14.0-63.7	0.2-0.8	5	2.60	0.34	0.25	0.061	10.1	79	300	79
SH-2	13.7-57.1	0.2-0.8	2	2.54	0.26	0.24	0.096	10.3	80	406	91

* The instrumented pile for static loading test.

Where F.P = Final penetration (mm/impact); Q = Quake value at final depth; CSX and CSB = maximum compressive stress at pile head and pile toe, respectively; TSX = maximum tensile stress along the pile; EMX = maximum driving energy measured at pile head; ETR = Energy translation ratio; RMX = Total resistance by the Case method; BTA = Integrity of pile material.

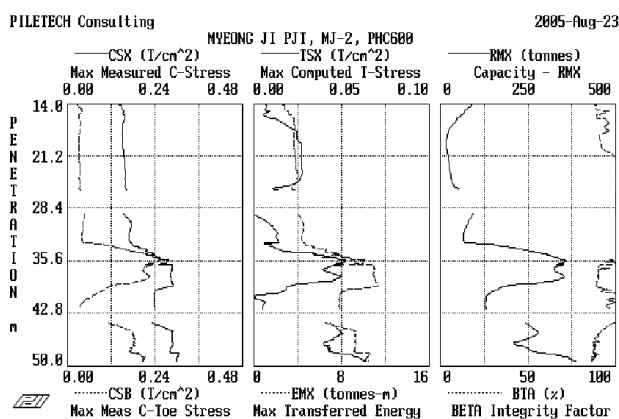


Fig. 9. PDA diagrams at the MC2-2

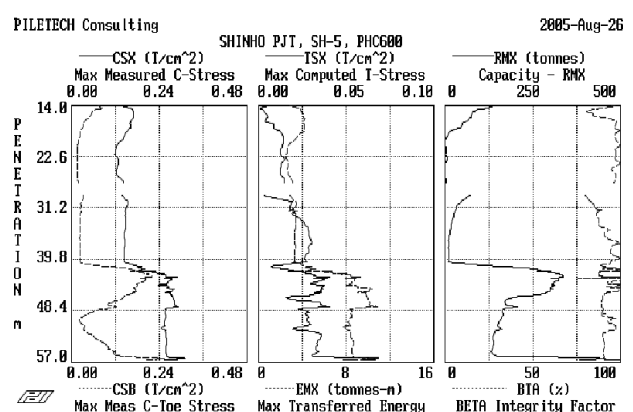


Fig. 10. PDA diagrams at the SO5-3

It is noted from Figs. 9 and 10 that the tensile stress induced along the piles in clay layers increased with depths. High tensile stress was developed in clay layers even under the ram height of about 0.2-0.3 m, while normal ram height of about 0.5-0.8 m was applied in the sand layers. The maximum energy translation ratios (ETR) from the pile are 80% in average, except the instrumented pile which was driven very carefully to avoid any damage of strain gages. An average BTA value of 85% was recorded, indicating that the piles were driven in high integrity. Conclusively, the parameters have proved that without damages, the PHC piles are able to be driven up to desirable depths in the area.

5.3 Bearing Capacity Estimated from PDA Test

In order to verify the reliability of the CPT-based and the analytical methods, bearing capacity at 17 depths in the sand layers was obtained from CAPWAP analysis. Fig. 11 shows results from CAPWAP analysis, in which the EOID and restrrike shaft resistances for all the depths are shown in Fig. 11 (a). It is noted that the CAPWAP shaft resistances shown in Fig. 11 (a) have a very similar trend with that from the CPT-based methods shown in Figs. 5 (a) and 6 (a). The shaft resistance increases

significantly as the piles penetrate deeply into the lower dense sand layers (Fig. 11 (a)), however, the toe resistance sensitively changed depending on the density of sand (Fig. 11 (c)). Consequently, it is shown that the total resistances roughly increase with depth (Fig. 11 (d)), which means that the shaft resistance considerably governs the total resistance.

6. Comparison between the Experimental and Calculation Methods

6.1 Comparison between CAPWAP and Calculated Resistances

It is known that bearing capacity obtained from CAPWAP analysis is reliable before a static loading test is performed. Therefore, in order to estimate the applicability of the calculation methods in the sites, CAPWAP resistances obtained from the PDA tests were compared with the calculated resistances. The ratios of calculated resistances to the CAPWAP resistances are shown in Fig. 12, where the ratios of $R_s/R_{s,PDA}$, $R_t/R_{t,PDA}$, and $R_u/R_{u,PDA}$ indicate the shaft (Fig. 12 (a)), the toe (Fig. 12 (b)), and the total resistances (Fig. 12 (c)), respectively.

As shown in Fig. 12 (a), the shaft resistance ratios from

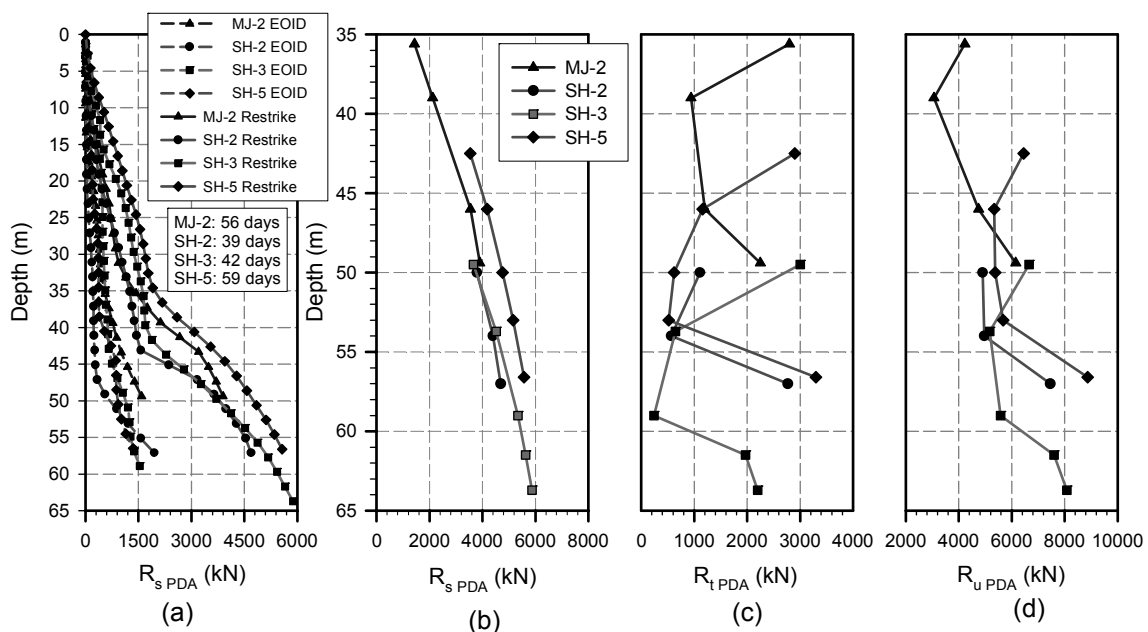


Fig. 11. CAPWAP analysis results of the piles

the CPT-based methods are almost less than unity, whereas only the β method gives the ratio of 1.5 to 2. It implies that though the shaft resistance of the pile was not fully mobilized for the entire depths (Kim et al, 2006), most of the CPT-based methods underestimate the shaft resistance compared with the CAPWAP results. Among them, the Prince & Wardle (1982) and β methods usually give the smallest and largest ratios, respectively.

Fig. 12 (b) shows that the toe resistance ratios are so scattered, ranging from 0.5 to 2 for the CPT-based methods and from 2.5 to 4.5 for the other analytical methods. The results of Eslami-Fellenius (1997) and Fellenius (1991) usually give the smallest and largest ratios, respectively.

Fig. 12 (c) shows that the total resistance ratios from the CPT-based methods are almost in the range of 0.5 to 1. It could be stated from Fig. 12 (c) that the CPT-based methods usually underestimate pile bearing capacity at the study locations. The bearing capacity would be more underestimated if the shaft resistance were fully mobilized due to soil set-up effect. In general, the methods of Prince & Wardle (1982) and Jardine et al. (2005) give the smallest and largest total resistance ratios, respectively. However, it should be noted that the CAPWAP results significantly depend not only on restrike time after the

end of driving but also on the soil profile conditions.

6.2 Comparison of the CAPWAP, Static Loading Test, and Calculated Results

It is worthwhile that the bearing capacity indicated previously is compared with the result of the static loading test (SLT) which was performed at MJ-2 location. Fig. 13 presents a comparison of shaft resistances between the previous results and the SLT result. It is recognized from Fig. 13 that the shaft resistance from the SLT considerably agrees with that of the β methods, rather than the results of CAPWAP and Jardine et al. (2005). The shaft resistance from the β methods is a little smaller up to 13 m and then larger than that of the SLT at the lower depths. If the shaft resistance at the lower part were fully mobilized (in fact, the lower part of the pile was not fully mobilized (Kim et al, 2006)), the agreement between them would become better. Though the method of Jardine et al (2005) showed the best agreement with the CAPWAP (restrike data), it still underestimates shaft resistance compared with the SLT data.

Fig. 14 presents a simulated toe resistance-movement (t-z) curve for the instrumented pile at the MJ-2, associated with toe resistances from the CPT-based and the analytical

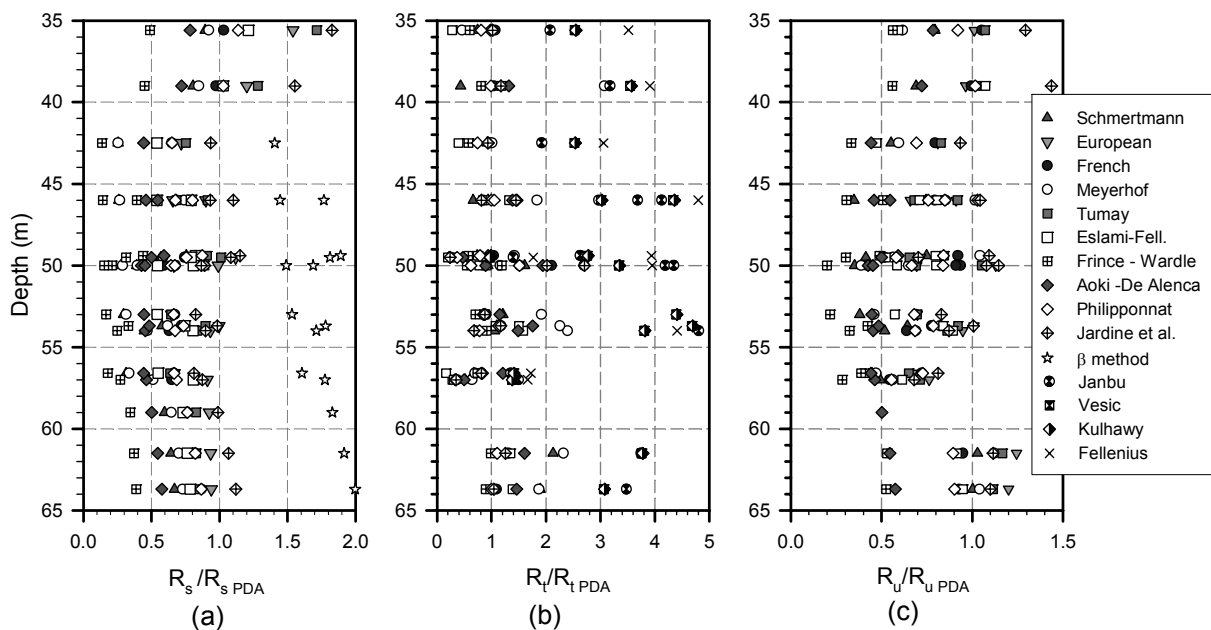


Fig. 12. Resistance ratios of the piles

methods given in Tables 1 and 2 (Kim et al. 2006). It is featured that there is no particular yield (failure) point on the curve that could be considered as ultimate toe resistance, but the toe resistance increases with increasing of toe movement. Therefore, the ultimate toe resistance from the SLT could be obtained from the curve at a toe movement value of 10 mm, as Fellenius' recommendation (2006a) for the design purposes. Because the PDA final stroke from the EOID was about 2-3 mm, it could be explained that the toe resistance obtained from the

CAPWAP analysis is smaller than that from the SLT ($R_{PDA} = 2800 \text{ kN} < R_{SLT} = 4370 \text{ kN}$). It is also shown that if the pile toe movement were taken at about 2-3 mm, then toe resistance would be about 3000 kPa and it would be quite similar to that from the CAPWAP result. A group of three methods, i.e., Aoki and De Alenca (1981), French (1982) and Jardine et al. (2005) give similar toe resistances to the CAPWAP result.

Fig. 15 presents a comparison of total resistance among the CAPWAP, SLT, and Jardine et al (2005) methods. In addition, the toe resistance from the method of Aoki and De Alenca (1975) that agreed well with the CAPWAP result is also plotted. The predicted total resistances from CAPWAP analysis and the calculation methods are less than the SLT result. It can be recognized that the discrepancy is attributed to the difference in toe resistances. If the toe resistance is appropriately predicted and the β method (Fellenius, 1991) is adopted, then the total resistance could be determined without any difficulty in this case. Considering the safety for the design purpose, the toe resistance from the methods of Aoki and De

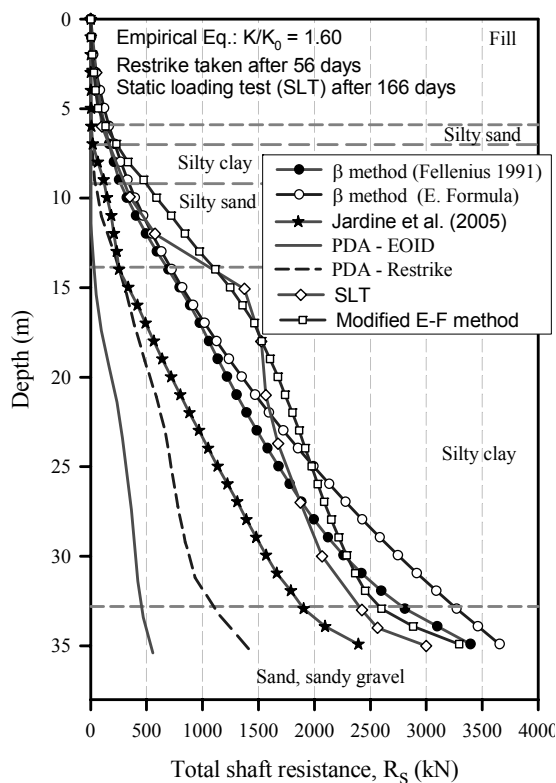


Fig. 13. Comparison of shaft resistances for the pile MJ-2

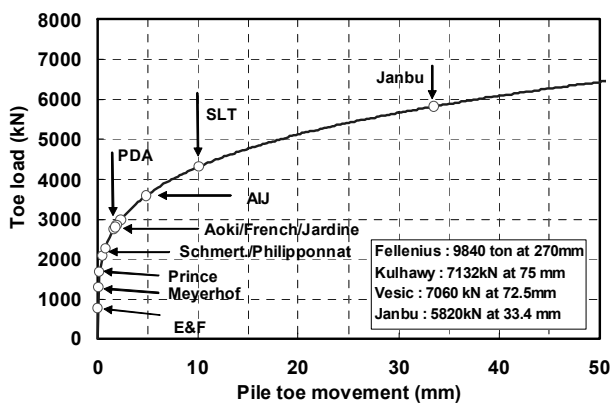


Fig. 14. Comparison of toe resistances between the SLT and the calculated methods (Data from Kim et al, 2006)

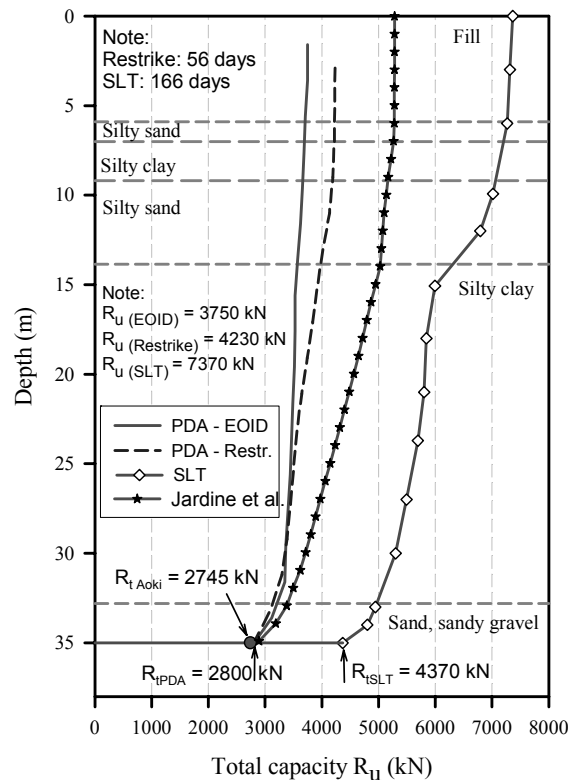


Fig. 15. Comparison of total bearing capacity for the pile MJ-2 (Data from Kim et al, 2006)

Alenca (1975), French (1982), Jardine et al. (2005) and AIJ (2001) and the shaft resistance from the β method would be reasonable.

7. Modification of Eslami-Fellenius Method (1997) for Shaft Resistance

It was previously shown that though the CPT has an advantage to obtain a continuous soil profile, the CPT-based methods underestimated shaft resistance at the study sites. It would be useful to modify a CPT-based method for estimating shaft resistance. Among the number of CPT-based methods, only Eslami-Fellenius (1997) developed the unit shaft resistance based on CPTU as follows:

$$r_s = C_s \cdot q_E \quad (2)$$

where C_s is shaft correlation coefficient, which depends on soil type obtained by their soil classification chart; $q_E = q_t - u_2$. However, the method also underestimated pile bearing capacity at the study sites. In order to correlate with the β values (Fellenius, 1991) that agreed well with

shaft resistance from the SLT as above, a modified shaft coefficient C'_s was proposed for the study sites by the following equation:

$$C'_s = \beta \cdot \frac{\sigma'_v}{q_E} \quad (3)$$

Table 4 shows the coefficients C_s and C'_s for each soil type identified by the Eslami-Fellenius (1997)'s classification. Fig. 16 shows a comparison of shaft resistances for the methods of β (Fellenius, 1991), Eslami-Fellenius (1997) and modified Eslami-Fellenius (1997) for 7 locations in the study sites. Though the shaft resistances obtained from the Eslami-Fellenius (1997) method were usually equal to 50% of that obtained from the β method or the SLT, the modified shaft resistances match quite well with that obtained from the β method. It would be proper to use the modified shaft coefficients for practical design at the study sites when CPTU data are available.

8. Discussions

The importance of soil set-up effect was previously

Table 4. Shaft coefficients from the methods

β method	β	Eslami-Fellenius (1997)	C_s	C'_s
Clay	0.23-0.40	Soft sensitive soils	0.080	0.120
		Clay	0.050	0.080
Silt	0.27-0.50	Silty clay, stiff clay and silt	0.025	0.040
		Sandy silt and silt	0.015	0.035
sand	0.30-0.80	Fine sand or silty sand	0.010	0.045
		Sand to sandy gravel	0.004	0.010

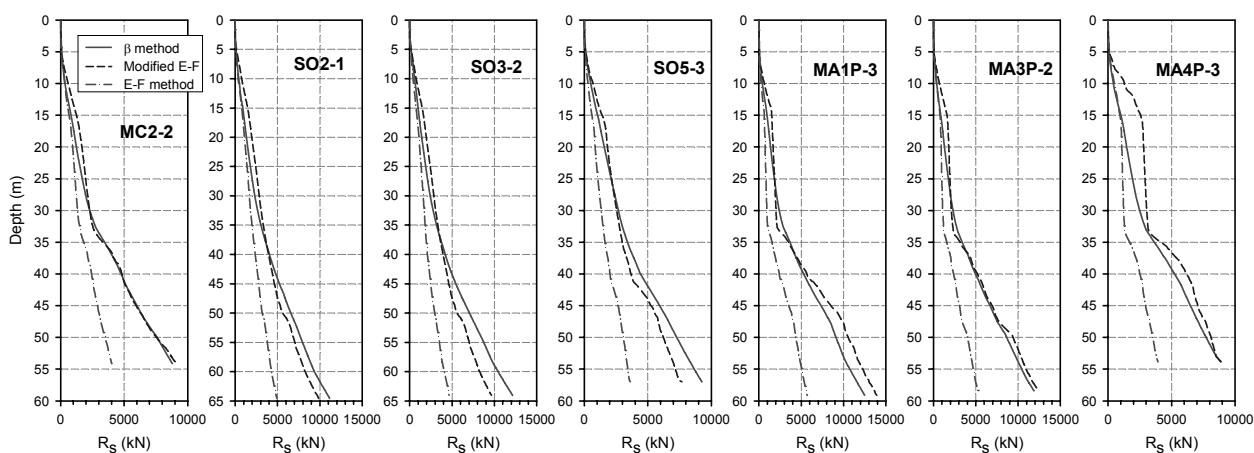


Fig. 16. Comparison of shaft resistances between the β , E-F and modified E-F methods

described in bearing capacity on piles. Therefore, it is meaningful to observe a few interesting testing results on piles. According to the study of Fellenius (2002) for a pile of 19 m long in sand deposit, the shaft resistance induced from long-term soil set-up could be continuously increased during 143 days after driving, which was shown in a series of CAPWAP analysis. The toe resistance of the pile from the soil set-up effect was also found increased simultaneously. It is also meaningful to mention about the recent study of Fellenius (2006b), which has the results on several full-scale, long-term tests performed since the 1960s through the 1990s, in several countries. The load transfer is governed by effective stress and very small movement results in mobilization of ultimate shaft resistance. And also, the pile toe resistance is determined by downdrag of the pile and the resulting pile toe penetration. Based on this study, it is difficult to say which method is appropriate for the toe resistance. In other words, the toe resistance is just the value depending on the toe movement, unlike the shaft resistance.

On the other hand, Murad and Titi (2004) evaluated the applicability of methods for bearing capacity using the static load test results of 35 PPC (precast prestressed concrete piles) driven piles. The piles had different sizes and lengths, and were failed during the SLT in the altered layers by sand and clay. According to the evaluated results, the European (1979) and French (1982) methods showed the best agreement with the SLT results. It is shown that the total shaft resistance from the SLT in the Louisiana area is much different from those evaluated previously in the Nakdong River delta. We can infer that this result did not consider the long-term effects and hence the shaft resistance must be underestimated.

Kim et al. (2006) also presented a persuasive evidence of pile bearing capacity influenced significantly from soil set-up effect in the Nakdong River delta. Especially, the significance was also emphasized where the soil profiles involve unusually thick and soft clay layers and the ongoing consolidation process was being taken place during the period until the restrike.

Herein, it would be worthwhile to remind Fellenius' valuable experiences (Fellenius, 2006a). There are many

factors which cause various bearing capacity among the methods as well as from site to site, however, a number of key factors could be: (1) each method was usually developed based on a number of static loading tests in a local area or a number of places which can not be representative for all kinds of soils in the world; (2) the methods might have been developed from different procedures of static loading test (for example: slow or quick test) and interpreted from different failure criteria; (3) the residual load concept might not be considered properly among the methods. In addition, fully mobilized shaft resistance during soil set-up duration might not be considered or properly calculated so that many of the CPT-based methods underestimate shaft resistance compared with the SLT data; (4) the length of the influent zone above and below pile toe is not unified among the CPT-based methods. This factor could significantly make variant toe resistances among the methods in strongly layered soil profiles as the MJ and SH sites; (5) The CPT-based methods which were developed before the piezocone came in general use (all the CPT-based methods except the method of Eslami-Fellenius, 1997). They do not consider the more accurate measurement achievable with the piezocone.

Consequently, it can be said that the bearing capacity analyzed from PDA test is a reference value at any testing time, because it depends on soil set-up effect. Considering that the bearing capacity from a few CPT-based methods agreed well with those from the EOID values of PDA test, it would be inferred that most of the CPT-based methods are appropriate for the bearing capacity when piles are just driven. Because the drag load is important in a thick soft deposit, the empirical methods for shaft resistance should be better to be applied for the MJ and SH sites. The toe resistance increased with increasing the toe displacement (see Fig. 14), so that the methods equivalent to the displacement of 10 mm as usual should be proper to be chosen.

9. Conclusions

Several PHC piles were driven well up to 60 m depth

at the MJ and SH sites in the Nakdong River deltaic area where pile toe is located at the top of middle dense sand and lower sand layers, followed by loose sand and soft clay layers. The PDA test was performed during the driving and restriking after a long duration. Using the PDA testing results, the drivability and bearing capacity were analyzed. A number of calculation methods for bearing capacity, which were developed based on CPT and experiments, were adopted. The computed results were compared with those from CAPWAP analysis and SLT data for an instrumented pile installed at the MJ site. The following conclusions and recommendations can be drawn from the study.

- (1) The soil set-up effect was important on bearing capacity in the thick soft clay deposit. The PDA tests performed during a short duration after pile driving gave a good agreement with the shaft resistance calculated by the methods of Jardine et al (2005), French (1982) and Tumay and Fakhroo (1981). However, the shaft resistance from the β method agreed well with the SLT result that was performed long after pile driving and was much larger than the previous results.
- (2) According to the SLT result, the t-z curve (Fig. 14) was governed by an exponential function. The toe resistance from the PDA tests (the restriking result) underestimated more than the SLT value at the toe movement of 10 mm. It was because the PDA results were taken from the toe movement of less than 5 mm. The methods of Aoki and De Alenca (1975), French (1982) and Jardine et al. (2005) gave better agreement with the PDA data. However, the analytical methods such as Fellenius (1991), Janbu (1976) Vesic (1977), Kulhawy et al (1983) overestimated (2~3) times the toe resistance from the PDA results. It would be very risky if we consider these methods for practical design.
- (3) A modified method for shaft resistance was newly proposed based on the β method and Eslami-Fellenius method (1997), which has an advantage of easily calculating a continuous shaft resistance profile using the CPTU data. This method, as well as the β method, would be applicable to the drag loads that are critical in the thick deltaic deposit.

Acknowledgement

This work was supported from Korea Institute of Construction & Transportation Technology Evaluation and Planning (KITTEP) and Youngjo Engineering & Construction Co. Ltd, Seoul Korea.

References

1. Architectural Institute of Japan (AIJ) (2001), "Recommendations for design of building foundation", 483p.
2. Aoki, N. and de Alencar, D. (1975), "An approximate method to estimate the bearing capacity of piles", *Proceeding, the 5th Pan-American Conference of Soil Mechanics and Foundation Engineering*, Buenos Aires, Vol.1, pp.367-376.
3. Aas G., Lacasse, S., Lunne, T. and Hoeg, K. (1986), "Use of in situ tests for foundation design on clay", *Use of In Situ Tests in Geotechnical Engineering*, ASCE, GSP No. 6, pp.1-30.
4. Blessey, W. E. (1976), "Pile foundation in the Mississippi River deltaic plain", *Analysis and Design of Building Foundations*, Edited by H.Y. Fang, Envo Publishing Co: pp.799-834.
5. Bustamante, M. and Ganeselli, L. (1982), "Pile bearing capacity predictions by means of static penetrometer CPT", *Proceeding of the 2nd European Symposium on Penetration Testing*, ESOPT-2, Amsterdam, Vol.2, pp.493-500.
6. Burland, J. (1973), "Shaft friction of piles in clay-A simple fundamental approach", *Ground Engineering*, Vol.6, No.3, pp.30-42.
7. Chung, S. G., Giao, P. H., Kim, G. J. and Leroueil, S. (2002), "Geotechnical properties of Pusan clays", *Canadian Geotechnical Journal*, Vol.39, No.5, pp.1050-1060.
8. Chung, S. G., Kim, S. K., Kang, Y. J., Im, J. C. and Prasad, K. N. (2006), "Failure of a breakwater founded on a thick normally consolidated clay", *Geotechnique*, Vol.56 No.6, pp.393-409.
9. DeRuiter, J. and Beringen, F. L. (1979), "Pile foundation for large North sea structures", *Marine Geotechnology*, Vol.3, No.3, pp.267-314.
10. Eslami, A. and Fellenius, B. H. (1997), "Pile capacity by direct CPT and CPTU method applied to 102 Case Histories", *Canadian Geotechnical Journal*, Vol.34, No.6, pp.880-898.
11. Fellenius, B. H. (1991), "Chapter 13: Pile foundation", *Foundation Engineering Handbook*. 2nd edition. H.S. Fang, editor, New York, pp.511-536.
12. Fellenius, B. H. (2002), "Determining the true distributions of load on instrumented pile", *Geotechnical Special Publication No. 116*, ASCE, Vol.2, pp.1455-1470.
13. Fellenius, B. H. (2006a), "Chapter 7-8-9: Basic of Foundation design", *E-book*, 2nd edition.
14. Fellenius, B.H. (2006b), "Results from long-term measurement in piles of drag load and downdrag", *Canadian Geotechnical Journal*, Vol.43 No.4, pp.409-430.
15. Janbu, N. (1976), "Static bearing capacity of friction piles", *Proceeding of the 6th European Conference on Soil Mechanics and Foundation Engineering*, Vol.1, pp.479-482.
16. Jardine et al. (2005), "ICP design method for driven piles in sands and clays", Thomas Telford Publishing, London, 105p.

17. Kim, S. R., Chung, S. G. and Dzung, N. T. (2006), "Determination of true resistance from load transfer test performed on a PHC pile", *Journal of the Korean Geotechnical Society*, Vol.22, No.11, pp. 113-122, (in Korean).
18. Kulhawy et al. (1983), "Transmission line structure foundation for uplift-compression loading", Report No.EL-2870, *Electric Power Research Institute*, Palo Alto, CA.
19. Meyerhof, G. G. (1976), "Bearing capacity and settlement of pile foundations", *Journal of Geotechnical Engineering*, The Eleventh Terzaghi Lecture, ASCE, Vol.102, GT3, pp.195-228.
20. Meyerhof, G. G. (1983), "Scale effects of pile capacity", *Journal of Geotechnical Engineering*, ASCE, Vol.108, GT3, pp.195-228.
21. Murad, Y. A-F. and Hani, H. T. (2004), "Assessment of direct cone penetration test methods for predicting the ultimate capacity of friction driven piles", *Journal of Geotechnical and Geoenvironmental Engineering*, ASCE, Vol.130, No.9, pp.935-944.
22. Prince, G. and Wardle, I. F. (1982), "A comparison between cone penetration test results and the performance of small diameter instrumented piles in stiff clay", *Proceeding of the 2nd European Symposium on Penetration testing*, Amsterdam, Vol.2, pp.775-780.
23. Philipponnat, G. (1980), "Methode pratique de calcul d'un pieu isole a l'aide du penetrometre statique", *Revue Francaise de Geotechnique*, pp.55-64.
24. Phien-wej, N., Giao, P. H. and Nutalaya, P. (2006), "Land subsidence in Bangkok, Thailand", *Engineering Geology*, Vol.82, No.4, pp.187-201.
25. Robertson et al. (1986), "Use of piezometer data", *Proceeding of the ASCE Specialty Conference In Situ '86: Use of In Situ Tests in Geotechnical Engineering*, Blacksburg, pp.1263-1280.
26. Robertson, P. K. and Campanella, R. G. (1983), "Interpretation of cone penetration tests, Part I: Sand". *Canadian Geotechnical Journal*, Vol.20, No.4, pp.718-733.
27. Schmertmann, J. H. (1978), "Guidelines for Contest, Performance, and Design", *Federal Highway Administration*, Report FHWA-TS-78209, Washington, 145p.
28. Tumay, M. T. and Fakhroo, M. (1981), "Pile capacity in soft clays using electric QCPT data", ASCE, *Cone Penetration Testing and Experience*, St. Louis, pp.434-455.
29. Vesic, A. S. (1977), "Design of pile foundation", *Synthesis of Highway*, No. 42, National Cooperative Highway Research Program Transportation Research Board, National Research Council, Washington.

(received on Jan. 12, 2007, accepted on Mar. 26, 2007)

Elastic-plastic Micromechanics Modeling of Cross-anisotropic Granular Soils: I. Formulation

직교 이방적 사질토의 미시역학적 탄소성 모델링: I. 정식화

Jung, Young-Hoon¹ 정 영 훈
Chung, Choong-Ki² 정 충 기

요 지

본 연구에서는 사질토의 탄성 및 탄소성 거동을 모사하기 위한 미시역학 기반의 구성 모델을 개발하였다. 개발 모델은 접촉 방향의 공간 분포를 통계적으로 처리한 조직 이방성, 응력비에 따른 조직 이방성의 변화, 간극비 변화에 따른 접촉점 수의 변화, 그리고 미시적 탄성-탄소성 접촉 강성을 고려하였다. 금속 재료에 대한 시험결과를 이용하여 미시적 탄소성 접촉 강성 모델을 수직 접촉력과 입자의 항복 접촉력에 대한 거듭제곱 함수의 형태로 유도하였다. 모델 변수를 정량적으로 평가하기 위해 직교 이방 탄성 계수의 근사식을 유도하였다.

Abstract

A micromechanics-based model to simulate the elastic and elastic-plastic behavior of granular soils is developed. The model accounts for the fabric anisotropy represented by the statistical parameter of the spatial distribution of contact normals, the evolution of fabric anisotropy as a function of stress ratio, the continuous change of the co-ordination number relating to the void ratio, and the elastic and elastic-plastic microscopic contact stiffness. Using the experimental data for metallic materials, the elastic-plastic contact stiffness is derived as a power function of the normal contact force as well as the contact force initiating the yielding of contact bodies. To quantitatively assess microscopic model parameters, approximate solutions of cross-anisotropic elastic moduli are derived in terms of the micromechanical parameters.

Keywords : Constitutive modeling, Elastic-plastic behavior, Granular soils, Micromechanics

1. Introduction

Recently, a number of sophisticated constitutive models (e.g. Einav and Puzrin 2004; Pestana et al. 2002; Stallebrass and Taylor 1997) based on the traditional continuum mechanics have been developed to incorporate plenty of new information on soil behavior. Data showing

severe nonlinearity in stress-strain responses force a new elastic-plastic model into employing a number of yield surfaces as well as increasing the number of model parameters. Even in the so-called simplified pseudo-elastic model (e.g. Jung et al. 2004; Puzrin and Burland 2000), higher-order nonlinear equations are inevitable to match its simulation with realistic soil responses. Unfortunately,

¹ Member, Post-doctoral fellow, Dept. of Civil and Env. Engrg., Northwestern Univ., 2145 Sheridan Rd. Rm. AG 50, Evanston, IL 60208, U.S.A., j-young-hoon@northwestern.edu, Corresponding Author

² Member, Prof., School of Civil and Environment Engrg., Seoul National Univ., San 56-1, Shillim-dong, Kwanak-gu, Seoul 151-742, Korea

such great effort based on the continuum mechanics does not guarantee that one can simulate a realistic nonlinear response of soils in the whole range of deformation. Obviously, a simple reason contributes to unsatisfactory performance of the conventional continuum-based soil models: soil is not a continuum material but a particulate material.

Micromechanics theory, in which the interaction among contacts of particles at the micro scale is being scaled up to calculate the macroscopic deformation, is a viable alternative to the traditional continuum mechanics in soil modeling. For the last two decades, two different types of micromechanics approaches—discrete element method and microstructural continuum mechanics—have been used to simulate the nonlinear behavior, especially of granular soils. The discrete element method (Cundall and Strack 1979), in which the interaction between two particles is computed explicitly to retrieve the macroscopic stress-strain data, usually requires a new workspace in computation and interpretation, whereas the microstructural continuum mechanics incorporates a conventional form of incremental stress-strain relationships in the calculation. Currently, significant efforts in the microstructural continuum mechanics (hereinafter called the micromechanics) have been devoted to the interpretation and simulation of various aspects of nonlinear responses in granular soils. Theoretical micromechanics analysis on the soil elasticity has made progress beyond the classical studies on regular packing structures. By using homogenization techniques, Chang et al. (1995) and Liao et al. (2000) proposed the analytical solutions of elastic moduli for a random packing assembly with the anisotropic fabric and the nonlinear contact stiffness, respectively.

The primary focus of this paper is to develop the micromechanics-based elastic-plastic constitutive model to simulate the nonlinear cross-anisotropic behavior of granular soils. The model accounts for the fabric anisotropy represented by the statistical parameter of the spatial distribution of contact normals, the evolution of fabric anisotropy as a function of stress ratio, the continuous change of the co-ordination number relating to the void ratio, and the elastic and elastic-plastic microscopic contact

stiffness. The microscopic behavior in a single contact point is thoroughly examined for the various states of contact geometries to find the best expression of the microscopic contact stiffness accounting for the naturally generated heterogeneity of the contact surface of granules. In addition, the approximate analytical solutions of cross-anisotropic elastic moduli and the simple linear relationship between the degree of fabric anisotropy and the stress ratio are provided to finely calibrate the microscopic parameters in the model.

2. Micromechanics Formulation

The computational scales of the micromechanics approach can be categorized into three different levels: (i) the macroscopic level in which for an assembly of particles the boundary stresses and strains are related by integrating all the information from the lower levels, (ii) the inter-contact level in which the contact density and the orientation of each contact are statistically described, and (iii) the microscopic level in which a law relating the force acting on a particular orientation of the contact plane to the corresponding displacement is established.

2.1 Notation and Main Assumptions

As shown in Fig. 1, two different reference frames—the global ($x_1 - x_2 - x_3$) and local ($s - t - n$) reference frames—

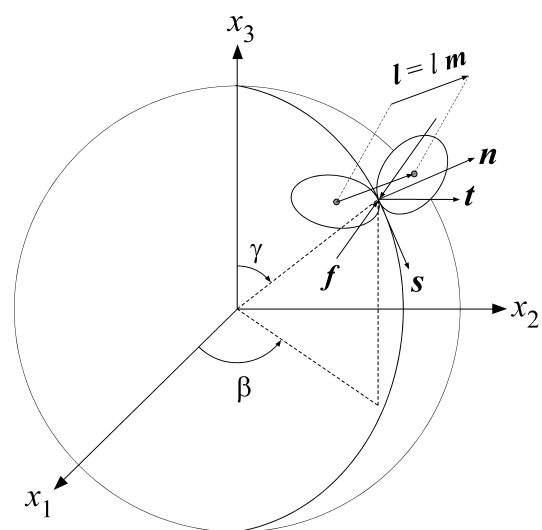


Fig. 1. Global and local coordinate systems in the unit sphere

are used to describe the macroscopic and microscopic behaviors in a separate way. Any nonscalar quantity describing the microscopic response at a single contact point is denoted by ${}^s\mathbf{A}$ in the local reference frame and \mathbf{A} in the global reference frame. The transformation of the quantity from the local reference frame to the global frame can be done by defining the rotation matrix, \mathbf{R} , as:

$$\mathbf{R} = \begin{bmatrix} s_1 & t_1 & n_1 \\ s_2 & t_2 & n_2 \\ s_3 & t_3 & n_3 \end{bmatrix} = \begin{bmatrix} \cos\gamma \cos\beta & -\sin\beta & \sin\gamma \cos\beta \\ \cos\gamma \sin\beta & \cos\beta & \sin\gamma \sin\beta \\ -\sin\gamma & 0 & \cos\gamma \end{bmatrix} \quad (1)$$

where γ and β represents the angles in the global reference frame as indicated in Fig. 1, and n_i , s_i , and t_i denote the component of the unit vectors, \mathbf{n} , \mathbf{s} , and \mathbf{t} corresponding to the orthogonal axes of the local reference frame, respectively. Thus, a quantity \mathbf{A} in the global reference frame will be transformed by ${}^s\mathbf{A} = \mathbf{R}^T \mathbf{A}$ in the local reference frame.

As shown in Fig. 1, the branch vector, \mathbf{l} , represents the vector connecting the centroids of two contacting granules. The branch vector for the c -th contact point can be expressed by

$$\mathbf{l}^c = l^c \mathbf{m}^c \quad (2)$$

where l and \mathbf{m} are the branch length and unit branch vector, respectively. For the finite number N of contacts within the assembly, a fabric tensor, F_{ij} , is given by (Oda et al. 1982),

$$F_{ij} = \frac{1}{V} \sum_{c=1}^N l_i^c m_j^c \quad (3)$$

where N is the total number of contacts, V is the volume of the particle assembly. A transition to continuously distributed branch vectors can be achieved by introducing an orientation distribution function (ODF), $E(\mathbf{m})$, which gives the relative density of the branches whose vectors have the same orientation (γ, β) in the unit sphere, Ω . Assuming that the distribution of branch lengths is continuous and also uncorrelated with that of branch vectors, the fabric tensor can be rewritten as,

$$F_{ij} = \frac{N}{V} \int_{\Omega} l_i m_j E(\mathbf{m}) d\Omega = \frac{N}{V} \bar{l} \int_{\Omega} m_i m_j E(\mathbf{m}) d\Omega = \frac{N}{V} \bar{l} \langle m_i m_j \rangle \quad (4)$$

where \bar{l} is the overall average of branch lengths. It is noted that the use of the mean value of branch length distribution, in principle, resorts to the assumption on an ideal assembly with equal-sized spheres. For further simplification, it is assumed that (i) the shape of particles is spherical, thus replacing the branch vector, \mathbf{m} , with the contact normal, \mathbf{n} , and (ii) the distribution of branch lengths are represented by \bar{l} which is equal to the mean diameter of particles, d_g , for the assembly of equal-sized spherical particles. Detailed discussion on the fabric tensor of the polydisperse granular materials can be found in Madadi et al. (2004).

The angle brackets in the last term of Eq. (4) denotes the weighted average operator using the continuous function of $E(\mathbf{m})$. Thus, a quantity within the angle brackets represents the microscopic quantity at the contacts with the same direction of \mathbf{m} prior to considering the relative contact density with its orientation. It is also worth noting that herein the term ‘microscopic’ means the averaged micro-directional response over the contacts sharing a given direction of the contact normal, rather than the individual response at each contact point.

The orientation distribution function, $E(\mathbf{n})$, expressed by the angle γ and β , needs to satisfy

$$\int_{\Omega} E(\mathbf{n}) d\Omega = \frac{1}{4\pi} \int_0^{2\pi} \int_0^{\pi} E(\gamma, \beta) \sin\gamma d\gamma d\beta = 1 \quad (5)$$

where $E(\gamma, \beta) \sin\gamma$ is the relative number of contacts with orientation (γ, β) . According to Chang et al. (1989), the function of $E(\mathbf{n})$ for the cross-anisotropic material can be expressed by the second-order spherical harmonics with the symmetry of the vertical axis in the global reference frame, x_3 , (i.e. the function of γ), as:

$$E(\mathbf{n}) = E(\gamma) = \frac{3(1+a \cos 2\gamma)}{(3-a)} \quad (6)$$

where a is the so-called ‘degree of fabric anisotropy’ ($-1 < a < 1$) which controls the shape of the angular distribution of contact normals.

The contact density, ρ_c , which denotes the average number of contacts per unit volume, can relate to the void ratio for the assembly of equal-sized particles by adopting the published empirical relationship (Chang et al. 1991; Mehrabadi et al. 1982) as:

$$\rho_c = \frac{N}{V} = \frac{3c_n}{\pi d_g^3(1+e)} = \frac{3(13.28-8e)}{\pi d_g^3(1+e)} \quad (7)$$

where c_n is the co-ordination number indicating the mean number of contacts per particle, d_g is the mean diameter of particles, and e is the void ratio. As noted by Nicot and Darve (2006), a single relationship between the void ratio and the co-ordination number used in Eq. (7) may not be valid after the failure peak for dense materials where the dilatancy induces the major change in the void ratio without changing the co-ordination number. Herein, we limit our discussion to the non-dilative deformation of granular soils. This is also necessary for interpreting the experimental data because the empirical correlation between macroscopic elastic moduli and principal stresses, which is essential to describe the experimental soil elasticity in this research, no longer apply when the dilatancy of the specimen occurs (Kuwano and Jardine 2002; Yu and Richart 1984). As the void ratio changes during loading, the value of co-ordination number keeps updated in the incremental formulation of the micromechanics constitutive model.

2.2 Relationship Between Microscopic and Macroscopic Quantities

Following the well-established average procedure based on principle of virtual work (Chang et al. 1989; Christoffersen et al. 1981; Love 1927; Mehrabadi et al. 1982), the macroscopic stress tensor, σ_{ij} , can be expressed in terms of the microscopic contact forces, f_j , as:

$$\sigma_{ij} = \rho_c d_g \int_{\Omega} f_i n_j E(\mathbf{n}) d\Omega \quad (8)$$

Instead of the kinematic assumption of the uniform deformation field, the average macroscopic strain tensor, ε_{ij} , derived from a least square minimization of the mean

displacement field (Emeriault and Chang 1997; Liao et al. 1997), is employed. The expression of ε_{ij} in terms of the contact displacement, δ_i , is given by,

$$\varepsilon_{ij} = \rho_c \int_{\Omega} \delta_i n_k F_{jk}^{-1} E(\mathbf{n}) d\Omega \quad (9)$$

where F_{ij}^{-1} is the inverse of the fabric tensor, F_{ij} , in Eq. (4).

The macroscopic stress-strain relationship can be derived in either of two different approaches: one is the kinematic hypothesis where the stress-strain relationship is derived from the average stress in Eq. (8) along with the assumption of the uniform deformation field, given by

$$\delta_i = \varepsilon_{ji} l_j = \varepsilon_{ji} d_g n_j \quad (10)$$

Another approach is the static hypothesis where the derivation of the stress-strain relationship starts from the average strain definition in Eq. (9), followed by the static hypothesis equation (Chang et al. 1995; Chang and Gao 1996; Liao et al. 2000; Liao et al. 1997) defining the mean contact force on a given contact orientation as:

$$f_i = \sigma_{ij} n_k F_{jk}^{-1} \quad (11)$$

Herein, the static hypothesis approach is used because the static hypothesis equation accounts for the effect of strain fluctuation in a granular material (Liao et al. 1997) and provides the local magnitude of the contact force directly to the microscopic contact stiffness. In order to match the empirical correlation of the elastic moduli, the incremental form of the elastic constitutive equation is derived.

Differentiation of Eq. (9) yields the incremental macroscopic strain as

$$\begin{aligned} \dot{\varepsilon}_{ij} = & \rho_c \int_{\Omega} \dot{\delta}_i n_k F_{jk}^{-1} E(\mathbf{n}) d\Omega + \rho_c \int_{\Omega} \delta_i \dot{n}_k F_{jk}^{-1} E(\mathbf{n}) d\Omega \\ & + \rho_c \int_{\Omega} \delta_i n_k \dot{F}_{jk}^{-1} E(\mathbf{n}) d\Omega + \rho_c \int_{\Omega} \delta_i n_k F_{jk} \dot{E}(\mathbf{n}) d\Omega \end{aligned} \quad (12)$$

As inferred by Eq. (12), a full description of the macroscopic responses requires the proper formulations including (i) the elastic and plastic micro-macro responses

for the condition of the fixed packing structure (i.e. first term in Eq. (12)), and (ii) the change of packing structure or the fabric evolution (i.e. terms for \dot{n}_i , \dot{F}_{ij}^{-1} , and $\dot{E}(\mathbf{n})$). The elastic-plastic micro-macro response can be taken into account by extending the local contact stiffness to the elastic-plastic model. However, the rigorous formulations related to the change of packing structure may be difficult to derive because \dot{n}_i , \dot{F}_{ij}^{-1} and $\dot{E}(\mathbf{n})$ correlate to each other in the static hypothesis formulation and, in principle, results from the particle rotation and spin as well as the tangential elastic-plastic displacement in the contact planes. Within the kinematic assumption of the uniform deformation field, Darve and Nicot (2005) and Nicot and Darve (2006) provided the in-depth platform for the incrementally nonlinear formulation of the complete micromechanics model considering the fabric evolution. In an alternative way, the change of packing structure, $\dot{E}(\mathbf{n})$, can be investigated exclusively by tracing possible differences between the elastic moduli measured in the experiment and the micromechanics-based elastic stiffness during loading. Herein, we employed the alternative method to measure the evolution of fabric as will be shown in the subsequent paper. Therefore, the further formulation in the micromechanics model will focus on the incremental formulation of stress-strain relationship via the elastic-plastic contact stiffness. It is assumed that the state of the fabric in an increment is constant; however, the state of soil fabric expressed by $E(\mathbf{n})$ keeps updated as the stress changes during loading.

For a given state of the fabric, Eq. (12) yields the incremental strains as

$$\dot{\epsilon}_{ij} = \rho_c \int_{\Omega} \dot{\delta}_i n_k F_{jk}^{-1} E(\mathbf{n}) d\Omega \quad (13)$$

Replacing $\dot{\delta}_i$ with the incremental contact force, \dot{f}_i , yields

$$\dot{\epsilon}_{ij} = \rho_c \int_{\Omega} (K_{ip}^{ep})^{-1} \dot{f}_p n_k F_{jk}^{-1} E(\mathbf{n}) d\Omega \quad (14)$$

where K_{ip}^{ep} represents the elastic-plastic contact stiffness tensor, which relates the incremental contact force to the

incremental contact displacement as:

$$\dot{f}_i = K_{ij}^{ep} \dot{\delta}_j \quad (15)$$

By substituting the incremental form of Eq. (11) for the fixed packing structure into Eq. (14), the macroscopic compliance tensor, C_{ijkl}^{el} , can be formulated as:

$$\dot{\epsilon}_{ij} = C_{ijkl}^{el} \dot{\sigma}_{kl} = \left[\rho_c \int_{\Omega} (n_m F_{lm}^{-1}) (K_{ik}^{ep})^{-1} (n_n F_{jn}^{-1}) E(\mathbf{n}) d\Omega \right] \dot{\sigma}_{kl} \quad (16)$$

Adopting the conventional notion of elastic-plastic strain decomposition, the elastic strain-stress relationship can be derived by

$$\epsilon_{ij}^{el} = C_{ijkl}^{el} \dot{\sigma}_{kl} = \left[\rho_c \int_{\Omega} (n_m F_{lm}^{-1}) (K_{ik}^{el})^{-1} (n_n F_{jn}^{-1}) E(\mathbf{n}) d\Omega \right] \dot{\sigma}_{kl} \quad (17)$$

where ϵ_{ij}^{el} is the elastic strain increment, C_{ijkl}^{el} is the macroscopic elastic compliance tensor, and K_{ip}^{ep} is the microscopic elastic contact stiffness. A simple numerical integration method is used to approximate the integral in Eq. (17), while some researchers (e.g. Bazant et al. 2000; Fang 2003; Hicher and Chang 2005) have introduced the optimal Gaussian formula to reduce computational time.

3. Nonlinear Contact Stiffness Model

The contact stiffness model in the microscopic level defines the relationship between the contact force and contact displacement. Assuming no coupling effect between the elastic responses in the normal and that in the tangential directions on a contact plane, the elastic contact stiffness in the global reference frame, K_{ij} , can be related to that in the local reference frame, ${}^gK_{ij}$, as follows:

$$K_{ij} = {}^gK_{11} s_i s_j + {}^gK_{22} t_i t_j + {}^gK_{33} n_i n_j = {}^gk_n n_i n_j + {}^gk_r (s_i s_j + t_i t_j) \quad (18)$$

where gK_n and gK_r are the normal and tangential contact stiffnesses in the local reference frame, respectively.

3.1 Geometry of Contact Surfaces

The area of contact under an incipient contact force

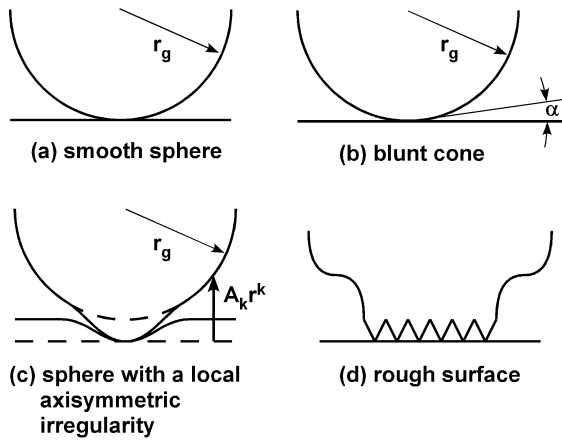


Fig. 2. Geometry of contact surface

and the distribution of the pressure acting on the contact area determine the contact stiffness. Soil particle, generally, has a significant order of irregularity on its geometry of surfaces. Thus, the severe idealization of the geometry of contact surface is inevitable to measure the area of contact and the distribution of contact pressure.

In the theory of tribology, the idealized geometry for the axisymmetric contact surface can be categorized as: (i) smooth sphere, (ii) blunt cone, (iii) sphere with a local axisymmetric irregularity, and (iv) rough surface with the numerous irregularities, as illustrated in Fig. 2. While the assumption of smooth sphere leads to severe restriction to simulate the real contact phenomena, the expressions established for this geometry such as the Hertzian contact (Hertz 1882) serve as a basic formulation for the contact force-displacement relationship for the other contact geometries. For the contact problems of the granular soils, it may be reasonable that the geometry of contact surfaces is idealized as the rough surface for the larger particles or the sphere with a local axisymmetric irregularity for the smaller particles.

3.2 Elastic Contact Stiffness

The normal elastic contact stiffness is formulated as a general form based on the classical Hertz theory for the contact between two smooth spheres, as:

$${}^g k_n^{el} = c_n ({}^g f_n / f_{ref})^{\alpha_n^{el}} \quad (19)$$

where ${}^g f_n$ is the normal contact force in the local reference frame, f_{ref} is the reference force (1 kN), used as a normalizing constant, c_n^{el} and α_n^{el} are the material constants which relate to the geometry of contact and material properties. For instance, the Hertz's model yields

$$c_n^{el} = [3r_c G_g^2 / (1 - \nu_g)^2]^{1/3} \quad \text{and} \quad \alpha_n^{el} = 1/3 \quad (20)$$

where r_c is the radius of curvature of the contact surface, G_g and ν_g are the elastic shear modulus and the Poisson's ratio of particles, respectively. The general form of the normal contact stiffness given in Eq. (19) can be adopted for various contact conditions, which do not obey the ideal condition in the Hertz's theory, such as the contact of a blunt cone on the plane (Goddard 1990) and the contact between the rough surfaces (Yimsiri and Soga 2000). For the contact in the spheres with a local axisymmetric irregularity, which closely simulates the realistic contact behavior in the granular soils, Jäger (1999) shows that the exponent in the equation of the normal contact stiffness (e.g. α_n^{el} in Eq. (19)) is greater than 0.5 when the surface has an acute peak and this value decreases as the irregularity becomes flatter as shown in Fig. 3.

The tangential elastic contact stiffness is also formulated as a general form based on the Mindlin's model without partial slippages (Johnson 1985; Mindlin 1949), given by

$${}^g k_r^{el} = c_r^{el} {}^g k_n^{el} \quad (21)$$

where c_r^{el} denotes the proportional factor, which relates to the bulk elastic distortion. Herein, the Mindlin's tangential contact stiffness model is adopted, thus leading to

$$c_r^{el} = 2(1 - \nu_g) / (2 - \nu_g) \quad (22)$$

In summary, the contact stiffness model in Eqs. (19) and (21) requires three parameters of c_n^{el} , α_n^{el} , and c_r^{el} . By referring to published values of the Poisson's ratio for a specific mineral type of particles, one can easily determine c_r^{el} based on Eq. (22). However, determination of c_n^{el} and α_n^{el} is not straightforward because these parameters relate not only to mechanical properties of

particles but also to geometries of the contacts.

3.3 Elastic-plastic Contact Stiffness

The solutions for the contact in the elastic bodies remain valid until the applied load is sufficiently large so as to initiate plastic deformation. When the internal stress at a specific point within the contact body reaches the yield strength of material, the yielding will be initiated. However, the plastic zone at the initial yielding stage is very small and fully contained by the material which remains elastic. In this circumstance, the material displaced by the indenter is accommodated by an elastic expansion of the surrounding elastic solid. Thus, the elasticity of material plays an important part in the early stage of the plastic indentation process. As the indentation becomes more severe, the plastic zone breaks out to the free surface and the material reaches a fully plastic state.

The three ranges of loading: purely elastic, elastic-plastic and fully plastic are the common feature of most engineering materials. The early two stages of contact loading (i.e. purely elastic and elastic-plastic stages) are likely to appear in the perfect plastic or brittle materials including the granular soils. For the strain-hardening material such as steel and bronze, the plastic flow or straining continuously occurs in the fully plastic state with the increasing contact pressure. However, the additional resisting of the strain-hardening material at the fully plastic stage cannot be expected in the brittle material. A sudden drop of stiffness or an unlimited plastic flow will occur and the brittle particles will be crushed.

If the contact force acting on a single contact point is below a specific value which yields the crushing or fully plastic failure of the particle, it could be postulated that the elastic-plastic contact behavior of granular soils exhibits the same response in the metallic materials. It is also expected that the response of granular soils at the elastic-plastic stage involves the irrecoverable volumetric compression associated with progressive crushing of the materials. If this hypothesis is correct, one can formulate the elastic-plastic contact stiffness of granular soils using the experimental data on the force-displacement relations

at the elastic-plastic stage of metallic materials.

Johnson (1985) summarized the experimental data on the normalized force-displacement relationship in the metallic material for the case of penetration of a spherical indenter into an elastic-plastic half-space, as shown in Fig. 4. According to Adams and Nosonovsky (2000), both the Tresca and the von Mises theories predict the onset of yielding induced by the spherical indenter when

$$f_Y = \frac{\pi r_c^2 (1 - \nu_g)^2}{8G_g^2} Y^3 \quad \text{and} \quad \delta_Y = \frac{\pi r_c (1 - \nu_g)^2}{4G_g^2} Y^2 \quad (23)$$

where f_Y represents the maximum contact force to initiate yielding of the contact, δ_Y is the corresponding displacement at the onset of yielding, r_c is the radius of curvature at the contact point, and Y is the yield stress of material. Johnson (1985) reported that the material reaches the fully plastic stage when $f_n = 400f_Y$ for the metallic materials. Accordingly, the experimental data on the limited range of $1 \leq f_n / f_Y \leq 400$ can be used to formulate the elastic-plastic contact stiffness.

In this study, it is assumed that the normalized force-displacement relationship at the elastic-plastic stage can be expressed by an exponential function similar to the elastic case, given by

$$\frac{{}^g f_n}{f_Y} = \left(\frac{{}^g \delta_n}{\delta_Y} \right)^\theta \quad \text{and} \quad \frac{{}^g \delta_n}{\delta_Y} = \left(\frac{{}^g f_n}{f_Y} \right)^{1/\theta} \quad (24)$$

where θ is the material constant governing the power

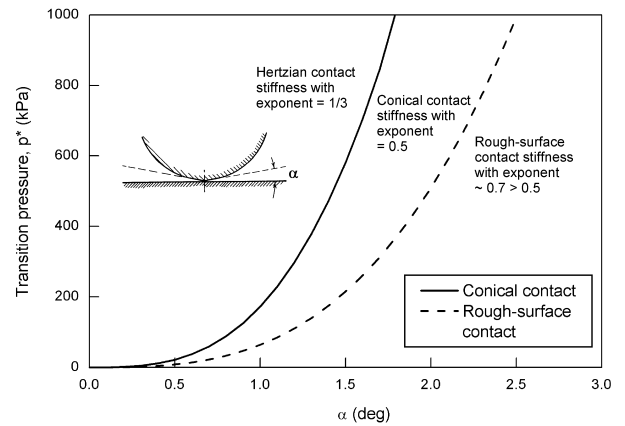


Fig. 3. Transition pressure plotted against α for the FCC packing of quartz

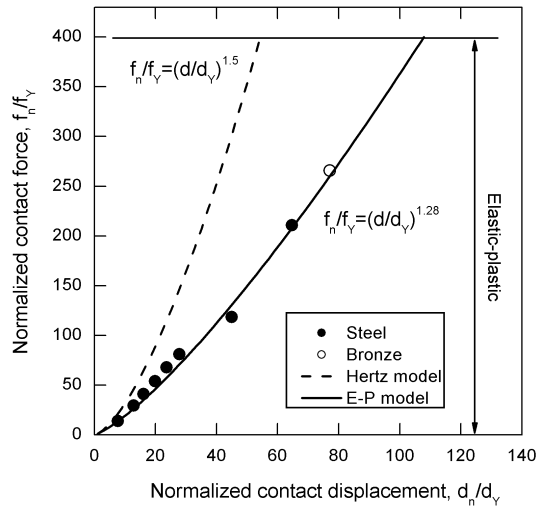


Fig. 4. Normalized force-displacement relationship at the elastic-plastic stage

relationship in the elastic-plastic contact deformation. The interpolation over the experimental data given in Fig. 4 indicates that the value of exponent $\theta = 1.28$. By differentiating Eq. (24), the elastic-plastic contact stiffness can be expressed as

$${}^g k_n^{el} = \frac{d {}^g f_n}{d {}^g \delta_n} = \theta \frac{f_Y}{\delta_Y} \left(\frac{{}^g f_n}{f_Y} \right)^{(\theta-1)/\theta} = \frac{\theta (f_Y)^{1/\theta}}{\delta_Y} ({}^g f_n)^{(\theta-1)/\theta} \quad (25)$$

For $\theta = 1.28$, the exponent of elastic-plastic contact stiffness $(\theta - 1)/\theta = 0.22$. In the elastic-plastic contact, the pressure distribution of plastic indentation spreads over larger area than that in the Hertz contact model. The response in the elastic-plastic contact of spherical indenter could represent the responses for other contact geometries based on the observation of Samuels and Mulhearn (1956) and Mulhearn (1959), who reported that the subsurface displacements produced by any blunt indenter (cone, sphere or pyramid) are approximately radial from the point of first contact, with roughly hemi-spherical contour of the equal strains. Herein, the generalized elastic-plastic contact stiffness is used given by

$${}^g k_n^{ep} = c_n^{ep} ({}^g f_n / f_{ref})^{\alpha_n^{ep}} \quad (26)$$

where c_n^{ep} is the material constant relating to f_Y , δ_Y , and θ as introduced in Eq. (25), and α_n^{ep} is the exponent with the value of 0.22 based on the experimental data for the

metallic materials, and f_{ref} is the normalizing constant (1 kN).

Considering the origin of friction induced by plastic deformation of contact, Mindlin's model including micro-slip could be regarded as one of the idealized formulations of the tangential contact stiffness of elastic-plastic bodies. Herein, we employ a function that approximates the expressions of Mindlin and Deresiewicz (1953) for the tangential contact stiffness as follows:

$${}^g k_r^{ep} = {}^g k_r^0 \left(1 - \frac{{}^g f_r}{{}^g f_n \tan \phi_m} \right)^{\alpha_r^{ep}} = c_r^{ep} {}^g k_n^{ep} \left(1 - \frac{{}^g f_r}{{}^g f_n \tan \phi_m} \right)^{\alpha_r^{ep}} \quad (27)$$

where ${}^g k_r^0$ is the initial tangential stiffness, and α_r^{ep} is a fixed parameter usually set to 1/3 to agree with Mindlin's theory. The parameter c_r^{ep} represents the distortion during tangential loading on the elastic-plastic bodies, which is certainly similar to c_r^{el} because most part of contact bodies still deform elastically even under the plastic indentation and the tangential loading. Thus, it is assumed that the value of c_r^{el} is the same as that of c_r^{ep} .

For the general case of contact geometry, the value of α_r^{ep} is different from 1/3. Walton and Braun (1986) reported that experimental measurements of initial displacements of frictional forces acting between metals in contact of non-spherical bodies produce force deflection curves with a more gradual change in slope, as would be produced with a larger value for the exponent α_r^{ep} . However, specific ranges of the exponent have not been reported yet in the literature. Thus, one can only expect that in the contact with the irregular surface of granular soils the value of α_r^{ep} would be greater than 1/3.

4. Approximate Solutions of Cross-anisotropic Elastic Moduli

A constitutive equation based on the micromechanics theory requires a relatively small number of model parameters. However, the determination of such parameters, especially for the microscopic contact stiffness, is not straightforward. One of the reasonable ways to determine such parameters is to compare the closed-form solutions

of macroscopic elastic moduli expressed by these parameters to the experimental data obtained in the macroscopic scale. However, rigorous solutions accounting both for the nonlinear contact stiffness and the anisotropic fabric cannot be derived (Emeriault and Cambou 1996). Herein, instead of developing a rigorous form of equations, the approximate approach to obtain closed-form solutions is attempted.

If a soil assembly consisting of the spherical particles with the symmetric distribution of contact orientations is subject to the isotropic stress of σ_0 , Eq. (11) becomes

$$f_1 = \sigma_0 n_1 F_{11}^{-1}, \quad f_2 = \sigma_0 n_2 F_{22}^{-1}, \quad \text{and} \quad f_3 = \sigma_0 n_3 F_{33}^{-1} \quad (28)$$

The contact forces in the local reference frame can be obtained from Eq. (28) via the transformation rule:

$$\begin{aligned} {}^g f_n &= \sigma_0 [F_{11}^{-1} n_1 n_1 + F_{22}^{-1} n_2 n_2 + F_{33}^{-1} n_3 n_3] \\ {}^g f_s &= \sigma_0 [F_{11}^{-1} n_1 s_1 + F_{22}^{-1} n_2 s_2 + F_{33}^{-1} n_3 s_3] \\ {}^g f_t &= \sigma_0 [F_{11}^{-1} n_1 t_1 + F_{22}^{-1} n_2 t_2 + F_{33}^{-1} n_3 t_3] \end{aligned} \quad (29)$$

where ${}^g f_n$ is the local contact force along the contact normal (i.e. \mathbf{n} -direction), and ${}^g f_s$ and ${}^g f_t$ are the tangential contact forces in two tangential directions (i.e. \mathbf{s} - and \mathbf{t} -directions). The inverse of the fabric tensor, F_{ij}^{-1} , can be decomposed into two parts:

$$F_{ij}^{-1} = \bar{F}_a \begin{bmatrix} 1 & 0 & 0 \\ 0 & 1 & 0 \\ 0 & 0 & 1 \end{bmatrix} + \bar{F}_b \begin{bmatrix} 0 & 0 & 0 \\ 0 & 0 & 0 \\ 0 & 0 & 1 \end{bmatrix} \quad (30)$$

where $\bar{F}_a = 5(3 - a_0) / \rho_c d_g (5 - 3a_0)$, $\bar{F}_b = -20a_0(3 - a_0) / \rho_c d_g (5 - 3a_0)(5 + a_0)$, and a_0 is the degree of fabric anisotropy in the isotropic stress condition. By substituting Eqs. (1) and (30) into (29), the local contact forces can be expressed as:

$$\begin{aligned} {}^g f_n &= \bar{F}_a \sigma_0 + \bar{F}_b \sigma_0 \cos^2 \gamma \\ {}^g f_s &= -\bar{F}_b \sigma_0 \cos \gamma \sin \gamma \\ {}^g f_t &= 0 \end{aligned} \quad (31)$$

Thus, the normal elastic contact stiffness in Eq. (19) becomes

$${}^g k_n^{el} = c_n^{el} (\bar{F}_a \sigma_0 / f_{ref})^{\alpha_n^{el}} \left(1 + (\bar{F}_b / \bar{F}_a) \cos^2 \gamma \right)^{\alpha_n^{el}} \quad (32)$$

Assuming that the term of $(\bar{F}_b / \bar{F}_a) \cos^2 \gamma$ can be ignored, the local contact stiffnesses can be simplified as:

$${}^g k_n^{el} = c_n^{el} (\bar{F}_a \sigma_0 / f_{ref})^{\alpha_n^{el}} \quad \text{and} \quad {}^g k_r^{el} = c_r^{el} {}^g k_n^{el} \quad (33)$$

The elastic contact stiffness matrix in the global coordinate is given by

$$\begin{aligned} K_{ij}^{el} &= {}^g k_n^{el} n_i n_j + {}^g k_r^{el} (s_i s_j + t_i t_j) \\ &= c_n^{el} (\bar{F}_a \sigma_0 / f_{ref})^{\alpha_n^{el}} [n_i n_j + c_r^{el} (s_i s_j + t_i t_j)] \end{aligned} \quad (34)$$

Substituting Eq. (34) into (17), the approximate solutions of the cross-anisotropic elastic moduli and Poisson's ratios in the isotropic stress condition can be derived as follows:

$$E_v^{el} = c_n^{el} c_r^{el} \left[\frac{7d_g^2 \rho_c (5 + a_0)^2}{5(3 - a_0) \{14 - 2a_0 + c_r^{el} (21 + 9a_0)\}} \right] \left[\frac{5(3 - a_0)}{\rho_c d_g f_{ref} (5 - 3a_0)} \right]^{\alpha_n^{el}} (\sigma_0)^{\alpha_n^{el}} \quad (35a)$$

$$E_h^{el} = c_n^{el} c_r^{el} \left[\frac{7d_g^2 \rho_c (5 - 3a_0)^2}{5(3 - a_0) \{14 - 6a_0 + c_r^{el} (21 - 15a_0)\}} \right] \left[\frac{5(3 - a_0)}{\rho_c d_g f_{ref} (5 - 3a_0)} \right]^{\alpha_n^{el}} (\sigma_0)^{\alpha_n^{el}} \quad (35b)$$

$$G_{vh}^{el} = c_n^{el} c_r^{el} \left[\frac{7d_g^2 \rho_c (5 - 3a_0)^2 (5 + a_0)^2}{10(5 - a_0) \{3 - a_0\} \left\{ \begin{array}{l} 105 - 46a_0 - 23a_0^2 \\ + c_r^{el} (70 - 24a_0 + 2a_0^2) \end{array} \right\}} \right] \left[\frac{5(3 - a_0)}{\rho_c d_g f_{ref} (5 - 3a_0)} \right]^{\alpha_n^{el}} (\sigma_0)^{\alpha_n^{el}} \quad (35c)$$

$$G_{hh}^{el} = c_n^{el} c_r^{el} \left[\frac{7d_g^2 \rho_c (5 - 3a_0)^2}{10(3 - a_0) \{21 - 11a_0 + c_r^{el} (14 - 10a_0)\}} \right] \left[\frac{5(3 - a_0)}{\rho_c d_g f_{ref} (5 - 3a_0)} \right]^{\alpha_n^{el}} (\sigma_0)^{\alpha_n^{el}} \quad (35d)$$

$$\nu_{vh}^{el} = \frac{(7 - a_0)(5 + a_0)(1 - c_r^{el})}{(5 - 3a_0) \{14 - 2a_0 + c_r^{el} (21 + 9a_0)\}} \quad (35e)$$

$$\nu_{hv}^{el} = \frac{(7 - a_0)(5 - 3a_0)(1 - c_r^{el})}{(5 + a_0) \{14 - 6a_0 + c_r^{el} (21 - 15a_0)\}} \quad (35f)$$

$$\nu_{hh}^{el} = \frac{(7 - 5a_0)(1 - c_r^{el})}{\{14 - 6a_0 + c_r^{el} (21 - 15a_0)\}} \quad (35g)$$

It should be noted that the error in the approximate solutions depends on the magnitude of a_0 because we ignored the term, $\bar{F}_b / \bar{F}_a = -4a_0 / (5 + a_0)$, to produce the normal contact force which is not correlated to the contact orientation. For the case that $\alpha_n^{el} = 0.5$ and $c_r^{el} = 0.824$ (i.e. $c_r^{el} = 2(1 - \nu_g) / (2 - \nu_g)$ with $\nu_g = 0.3$ for quartz), the ratios between the elastic moduli from approximate solutions and those from Eq. (17) are plotted against the magnitude

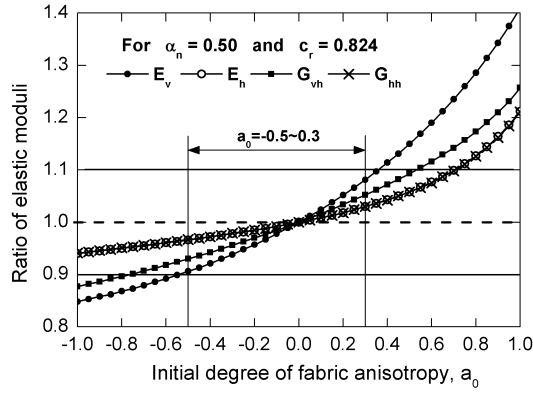


Fig. 5. Variation of $|n - \alpha|$ for the various values of a_1

of a_0 in Fig. 5. As can be seen in Fig. 5, the ratio of elastic moduli ranges between 0.9 and 1.1 for the values of a_0 in between -0.5 and 0.3. When considering the low degree of anisotropy in the isotropic stress and the level of accuracy of measurement in the experiments, such magnitude of errors in the approximate solutions is practically acceptable in the determination of model parameters.

5. Evolution of Contact Orientations

The fabric tensor is manifested in the anisotropic elastic responses in the macroscopic scale. The contact force can be resolved into the component, f^n in the contact normal direction, n_i , and f^r in the tangential direction of the contact plane, r_i , along which the maximum shear contact force applies. In a particular case of the symmetry in the cross-anisotropic material and the triaxial macroscopic stresses, the direction of r_i coincides with the unit vector, s_i so that $f_i = f^n n_i + f^r s_i$. Thus, Eq. (8) can alternatively be expressed as:

$$\sigma_{ij} = \rho_c d_g \langle f^n n_i n_j \rangle + \rho_c d_g \langle f^r s_i n_j \rangle \quad (36)$$

By taking the average of normal and tangential contact forces, Eq. (36) becomes,

$$\sigma_{ij} = \rho_c d_g \hat{f}^n \langle n_i n_j \rangle + \rho_c d_g \hat{f}^r \langle s_i n_j \rangle = \hat{f}^n F_{ij} \quad (37)$$

where \hat{f}^n and \hat{f}^r are the overall average magnitude of normal and tangential contact forces. Note that

$\langle s_i n_j \rangle = \int_{\Omega} s_i n_j E(\mathbf{n}) d\Omega = 0$. Consequently, in this limited condition, the macroscopic stress tensor can be proportional to the fabric tensor. Eqs. (4) and (6) allow the explicit relationship between the macroscopic stress and fabric tensor from Eq. (37) such that

$$\begin{bmatrix} \sigma_r & 0 & 0 \\ 0 & \sigma_r & 0 \\ 0 & 0 & \sigma_a \end{bmatrix} = \rho_c d_g \hat{f}^n \begin{bmatrix} \frac{5-3a}{5(3-a)} & 0 & 0 \\ 0 & \frac{5-3a}{5(3-a)} & 0 \\ 0 & 0 & \frac{5+a}{5(3-a)} \end{bmatrix} \quad (38)$$

where $\sigma_r (= \sigma_{11} = \sigma_{22})$ and $\sigma_a (= \sigma_{33})$ denote the radial and axial stresses in the triaxial stress condition, respectively. Furthermore, the mean normal stress, p , and the deviator stress, q , in the triaxial stress condition can be expressed as,

$$p = \frac{\sigma_a + 2\sigma_r}{3} = \frac{\rho_c d_g \hat{f}^n}{3} \quad \text{and} \quad q = \sigma_a - \sigma_r = \frac{4a\rho_c d_g \hat{f}^n}{5(3-a)} \quad (39)$$

Thus, the degree of fabric anisotropy, a , has a unique relationship with the stress ratio, q/p , as:

$$a = \frac{15(q/p)}{12 + 5(q/p)} \quad (40)$$

Despite its mathematical simplicity, Eq. (40) hides some critical points: (i) in general, taking the average of contact forces, especially in the tangential contact direction, is not sufficient to describe the directional variation of the contact force and (ii) Eq. (40) does not allow the anisotropic state of the fabric in the isotropic stress condition. With respect to the directional variation of the contact forces, one can find the enhanced expressions of the stress-contact force-fabric relationship in Mehrabadi et al. (1982) and Ouadfel and Rothenburg (2001). To account for the possible fabric anisotropy in the isotropic stress condition within the simple format of Eq. (40), we modify Eq. (40) as a linear equation:

$$a = a_0 + a_1(q/p) \quad (41)$$

where a_0 is the magnitude of a in the isotropic stress condition, and a_1 is, in general, the function of contact

Table 1. Required parameters for the micromechanics modeling

Category	Input parameter		Relevant formulation
Contact Stiffness	c_n^{el} and α_n^{el}	Elasticcontact stiffness	${}^g k_n^{el} = c_n^{el} ({}^g f_n / f_{ref})^{\alpha_n^{el}}$
	c_r^{el}		${}^g k_r^{el} = c_r^{el} {}^g k_n^{el}$
	c_n^{ep} and α_n^{ep}	Elastic–plastic contact stiffness	${}^g k_n^{ep} = c_n^{ep} ({}^g f_n / f_{ref})^{\alpha_n^{ep}}$
	c_r^{ep} and α_r^{ep}		${}^g k_r = {}^g c_r^{ep} {}^g k_n^{ep} \left(1 - \frac{{}^g f_r}{{}^g f_n \tan \phi_m} \right)^{\alpha_r^{ep}}$
	ϕ_m		
Contact density	e_0	Initial void ratio	
	d_g	Mean diameter of particles	
Contact orientation	a_0	Initial degree of fabric anisotropy	
	a_1	Evolution of fabric anisotropy	$a = a_0 + a_1(q/p)$

forces and their directional distribution. The parameter, a_1 , relates implicitly to the evolution of contact forces as does the contact force relate to the macroscopic stress in the simplest case of Eq. (40). Herein, a_1 is regarded as a material constant.

6. Conclusions

A micromechanics-based model to simulate the elastic and elastic-plastic behavior of granular soils is developed. The model accounts for the fabric anisotropy represented by the statistical parameter of the spatial distribution of contact normals, the evolution of fabric anisotropy as a function of stress ratio, the continuous change of the co-ordination number relating to the void ratio, and the elastic and elastic-plastic microscopic contact stiffness. The microscopic behavior in a single contact point is thoroughly examined for the various states of contact geometries, which reveals that regardless of contact geometry the normal contact stiffness can be expressed by a power function of the normal contact force. The elastic-plastic contact stiffness is newly derived based on the experimental data for the metallic materials. The elastic-plastic contact stiffness can also be expressed by the power function of the normal contact force as well as the contact force initiating the yielding of contact

bodies. To quantitatively assess the microscopic model parameters, the approximate solutions of cross-anisotropic elastic moduli are derived in terms of the micromechanics parameters. The possible errors in the approximation are estimated for the reasonable ranges of the degree of fabric anisotropy. Without the rigorous formulation to describe the evolution of fabric anisotropy, a simple linear relationship between the degree of fabric anisotropy and the stress ratio is provided.

The elastic and elastic-plastic responses in the micromechanical modeling for the nonlinear deformation are meticulously investigated in the companion paper.

Acknowledgements

Financial support for this work was provided by Korea Research Foundation Grant No. KRF-2005-214-D00166. The support of Engineering Research Institute at Seoul National University is greatly appreciated.

References

1. Adams, G. G., and Nosonovsky, M. (2000), "Contact modeling - forces", *Tribology international*, 33, 431-442.
2. Bazant, Z. P., Caner, F. C., Carol, I., Adley, M. D., and Akers, S. A. (2000), "Microplane model M4 for concrete. I: Formulation with work-conjugate deviatoric stress", *Journal of Engineering Mechanics-ASCE*, 126(9), 944-953.

3. Chang, C. S., Chao, S. J., and Chang, Y. (1995), "Estimates of Elastic-Moduli for Granular Material with Anisotropic Random Packing Structure", *International Journal of Solids and Structures*, 32(14), 1989-2008.
4. Chang, C. S., and Gao, J. (1996), "Kinematic and static hypotheses for constitutive modelling of granulates considering particle rotation", *Acta Mechanica*, 115(1-4), 213-229.
5. Chang, C. S., Misra, A., and Sundaram, S. S. (1991), "Properties of granular packings under low amplitude cyclic loading", *Soil Dynamics and Earthquake Engineering*, 10(4), 201-211.
6. Chang, C. S., Sundaram, S. S., and Misra, A. (1989), "Initial Moduli of Particulated Mass with Frictional Contacts", *International Journal for Numerical and Analytical Methods in Geomechanics*, 13(6), 629-644.
7. Christoffersen, J., Mehrabadi, M. M., and Nematnasser, S. (1981), "A Micromechanical Description of Granular Material Behavior", *Journal of Applied Mechanics-Transactions of the Asme*, 48(2), 339-344.
8. Cundall, P. A., and Strack, O. D. L. (1979), "Discrete Numerical-Model for Granular Assemblies", *Geotechnique*, 29(1), 47-65.
9. Darve, F., and Nicot, F. (2005), "On incremental non-linearity in granular media: phenomenological and multi-scale views (Part I)", *International Journal for Numerical and Analytical Methods in Geomechanics*, 29(14), 1387-1409.
10. Einav, I., and Puzrin, A. M. (2004), "Continuous hyperplastic critical state (CHCS) model Derivation", *International Journal of Solids and Structures*, 41(1), 199-226.
11. Emeriault, F., and Cambou, B. (1996), "Micromechanical modelling of anisotropic non-linear elasticity of granular medium", *International Journal of Solids and Structures*, 33(18), 2591-2607.
12. Emeriault, F., and Chang, C. S. (1997), "Interparticle forces and displacements in granular materials", *Computers and Geotechnics*, 20(3-4), 223-244.
13. Fang, H. L. (2003), "A state-dependent multi-mechanism model for sands", *Geotechnique*, 53(4), 407-420.
14. Goddard, J. D. (1990), "Nonlinear Elasticity and Pressure-Dependent Wave Speeds in Granular Media", *Proceedings of the Royal Society of London Series a-Mathematical Physical and Engineering Sciences*, 430(1878), 105-131.
15. Hertz, H. (1882), "Über die Berührung fester elastischer Körper (On the contact of elastic solids)", *Journal of reine und angewandte mathematik*, 92, 156-171.
16. Hicher, P. Y., and Chang, C. S. (2005), "Evaluation of two homogenization techniques for modeling the elastic behavior of granular materials", *Journal of Engineering Mechanics-ASCE*, 131(11), 1184-1194.
17. Jager, J. (1999), "Uniaxial deformation of a random packing of particles", *Archive of Applied Mechanics*, 69(3), 181-203.
18. Johnson, K. L. (1985), *Contact mechanics*, Cambridge University Press, Cambridge.
19. Jung, Y. H., Chung, C. K., and Finno, R. J. (2004), "Development of nonlinear cross-anisotropic model for the pre-failure deformation of geomaterials", *Computers and Geotechnics*, 31(2), 89-102.
20. Kuwano, R., and Jardine, R. J. (2002), "On the applicability of cross-anisotropic elasticity to granular materials at very small strains", *Geotechnique*, 52(10), 727-749.
21. Liao, C. L., Chan, T. C., Suiker, A. S. J., and Chang, C. S. (2000), "Pressure-dependent elastic moduli of granular assemblies", *International Journal for Numerical and Analytical Methods in Geomechanics*, 24(3), 265-279.
22. Liao, C. L., Chang, T. P., Young, D. H., and Chang, C. S. (1997), "Stress-strain relationship for granular materials based on the hypothesis of best fit", *International Journal of Solids and Structures*, 34(31-32), 4087-4100.
23. Love, A. E. H. (1927), *A Treatise of the mathematical theory of elasticity*, Cambridge university press, Cambridge, U.K.
24. Madadi, M., Tsoungui, O., Latzel, M., and Luding, S. (2004), "On the fabric tensor of polydisperse granular materials in 2D", *International Journal of Solids and Structures*, 41(9-10), 2563-2580.
25. Mehrabadi, M. M., Nematnasser, S., and Oda, M. (1982), "On Statistical Description of Stress and Fabric in Granular-Materials", *International Journal for Numerical and Analytical Methods in Geomechanics*, 6(1), 95-108.
26. Mindlin, R. D. (1949), "Compliance of elastic bodies in contact", *Journal of applied mechanics*, 16, 259-270.
27. Mindlin, R. D., and Deresiewicz, H. (1953), "Elastic spheres in contact under varying oblique forces", *Journal of applied mechanics*, ASME, 20(3), 327-344.
28. Mulhearn, T. O. (1959), "Deformation of metals by Vickers-type pyramidal indenters", *J. Mech. Physics Solids*, 7, 85-92.
29. Nicot, F., and Darve, F. (2006), "Micro-mechanical investigation of material instability in granular assemblies", *International Journal of Solids and Structures*, 43(11-12), 3569-3595.
30. Oda, M., Nematnasser, S., and Mehrabadi, M. M. (1982), "A Statistical Study of Fabric in a Random Assembly of Spherical Granules", *International Journal for Numerical and Analytical Methods in Geomechanics*, 6(1), 77-94.
31. Ouadfel, H., and Rothenburg, L. (2001), "'Stress-force-fabric' relationship for assemblies of ellipsoids", *Mechanics of Materials*, 33(4), 201-221.
32. Pestana, J. M., Whittle, A. J., and Salvati, L. A. (2002), "Evaluation of a constitutive model for clays and sands: Part I - sand behaviour", *International Journal for Numerical and Analytical Methods in Geomechanics*, 26(11), 1097-1121.
33. Puzrin, A. M., and Burland, J. B. (2000), "Kinematic hardening plasticity formulation of small strain behaviour of soils", *International Journal for Numerical and Analytical Methods in Geomechanics*, 24(9), 753-781.
34. Samuels, L. E., and Mulhearn, T. O. (1956), "The deformation zone associated with indentation hardness impressions", *J. Mech. Physics Solids*, 5, 125-130.
35. Stallebrass, S. E., and Taylor, R. N. (1997), "The development and evaluation of a constitutive model for the prediction of ground movements in overconsolidated clay", *Geotechnique*, 47(2), 235-253.
36. Walton, O. R., and Braun, R. L. (1986), "Viscosity, granular-temperature, and stress calculations for shearing assemblies of inelastic, friction disks", *Journal of rheology*, 30(5), 949-980.
37. Yimsiri, S., and Soga, K. (2000), "Micromechanics-based stress-strain behaviour of soils at small strains", *Geotechnique*, 50(5), 559-571.
38. Yu, P., and Richart, F. E., Jr. (1984), "Stress ratio effects on shear modulus of dry sands", *Journal of Geotechnical Engineering*, 110(3), 331-345.

(received on Jan. 12, 2007, accepted on Mar. 26, 2007)

Elastic-plastic Micromechanics Modeling of Cross-anisotropic Granular Soils: II. Micromechanics Analysis

직교 이방적 사질토의 미시역학적 탄소성 모델링: II. 미시역학적 해석

Jung, Young-Hoon¹ 정 영 훈
Chung, Choong-Ki² 정 충 기

요 지

본 논문과 함께 제출한 논문에서는 미시역학 기반의 새로운 탄소성 모델의 정식화에 대해 설명하였다. 본 논문에서는 사질토 변형의 탄성 및 탄소성 거동을 미시역학에 근거하여 자세히 분석하였다. 모델에 필요한 변수 평가를 위한 과정을 제시하였다. 등방 및 삼축 압축 시험에서 나타난 사질토의 탄성 거동을 분석한 결과, 직교 이방 탄성계수의 응력 종속성은 미시적 수직 강성에서 나타난 수직 접촉력의 거듭제곱 함수 형태가 반영되어 나타나며, 삼축 압축 응력 상태에서는 조직 이방성의 변화가 응력 종속성에 영향을 미침을 알 수 있었다. 미시역학적 해석을 통해 소성 변형이 매우 낮은 변형률 수준에서도 발견되며, 변형 중 사질토 강성의 비선형적 감소는 접촉점에서의 접선 방향 소성 변형에 의해 나타남을 밝혔다.

Abstract

In the companion paper, we provided the novel elastic-plastic constitutive model based on the micromechanics theory. Herein, the elastic and elastic-plastic deformation of granular soils is meticulously analyzed. To guarantee high accuracy of the microscopic parameter, the systematic procedure to evaluate the parameters is provided. The analysis of the elastic response during the isotropic and triaxial compression shows that the stress-level dependency of cross-anisotropic elastic moduli is induced by the power relationship of the contact force in the normal contact stiffness, while the evolution of fabric anisotropy is more pronounced during triaxial compression. The micromechanical analysis indicates that the plastic strains are likely to occur at very small strains. The plastic deformation of tangential contacts has an important role in the reduction of soil stiffness during axial loading.

Keywords : Constitutive modeling, Elastic-plastic behavior, Granular soils, Micromechanics

1. Introduction

It is not questionable whether the behavior of the granular soil is the essential topic in the geotechnical area that a geotechnical professional should understand. The

stress-strain behavior of granular soils has been understood within the notion of the elasticity as well as the elastic-plastic theory of the solid, which inevitably ignores the particulate feature of soils. Even though the existing framework of the finite element method, which is

¹ Member, Post-doctoral fellow, Dept. of Civil and Env. Engrg., Northwestern Univ., 2145 Sheridan Rd. Rm. AG 50, Evanston, IL 60208, U.S.A., j-young-hoon@northwestern.edu, Corresponding Author

² Member, Prof., School of Civil and Environment Engrg., Seoul National Univ., San 56-1, Shillim-dong, Kwanak-gu, Seoul 151-742, Korea

commonly employed in the geotechnical designs, is not likely to be abandoned without the presence of an ultimate theory to compensate for every single defect in the finite element method and its continuum-based constitutive model, it is quite necessary to expand our knowledge on the fundamental mechanisms of soil behavior, especially in the microscopic level of soil deformation.

The nonlinearity and anisotropy of the stress-strain responses in the granular soils are key features one needs to address to elevate the accuracy of the prediction in the geotechnical problems. Recalling the particulate nature of granular soils, one can suspect that both the nonlinearity and the anisotropy of soil deformation originate from the microscopic nonlinear anisotropic responses. In the companion paper, we derived the micromechanics-based elastic-plastic constitutive model, which includes a number of microscopic features the particles can possess. It was theoretically examined that the contacts in the particle assembly are nonlinearly deformed regardless of the elastic or elastic-plastic contacts.

In this paper, it will be shown that the macroscopic nonlinearity in the stress-strain responses relates to various microscopic features such as the nonlinear elastic and elastic-plastic contact stiffnesses. The elastic and plastic strains are decomposed into the strains induced by the normal and tangential contact deformations as well as the elastic and elastic-plastic contact deformation. The contributions of microscopic mechanisms are quantitatively examined, from which authors are to provide the theoretical basis to extend the understanding of the nonlinear cross-anisotropic deformation of the granular soils.

2. Summary of Micromechanics Formulations

The detailed derivation of the micromechanics-based elastic-plastic model was explained in the companion paper. Herein, the essential formulations in the model are summarized.

To characterize the heterogeneity of the contact distribution, the fabric tensor, F_{ij} , is introduced, given by

$$F_{ij} = \frac{Nd_g}{V} \int_{\Omega} n_i n_j E(\mathbf{n}) d\Omega \quad (1)$$

where N is the number of contacts in an particle assembly, V is the total volume of the assembly, d_g is the mean diameter of particles within an assembly, n_i is the direction of the contact normal, $E(\mathbf{n})$ is the distribution function of the contact normals, and Ω is the unit sphere. The orientation distribution function, $E(\mathbf{n})$, is formulated based on the spherical harmonics with the symmetry of the vertical axis, as

$$E(\mathbf{n}) = E(\gamma) = \frac{3(1 + a \cos 2\gamma)}{(3 - a)} \quad (2)$$

where γ is the angle between the vertical axis in the global coordinate system and the contact normal, and a is the degree of fabric anisotropy.

Assuming the static hypothesis in defining the strains, the incremental compliance tensor, C_{ijkl} , is expressed by

$$\dot{\epsilon}_{ij} = C_{ijkl} \dot{\sigma}_{kl} = \left[\rho_c \int_{\Omega} (n_m F_{im}^{-1}) (K_{ik})^{-1} (n_n F_{jn}^{-1}) E(\mathbf{n}) d\Omega \right] \dot{\sigma}_{kl} \quad (3)$$

where $\dot{\sigma}_{ij}$ and $\dot{\epsilon}_{ij}$ are incremental stresses and strains, K_{ij} is the microscopic contact stiffness, F_{ij}^{-1} is the inverse of the fabric tensor, and ρ_c is the contact density relating to the void ratio, e , and co-ordination number, c_n , such that

$$\rho_c = \frac{N}{V} = \frac{3c_n}{\pi d_g^3 (1 + e)} = \frac{3(13.28 - 8e)}{\pi d_g^3 (1 + e)} \quad (4)$$

The microscopic contact stiffness, K_{ij} , in the global coordinate system is related to the normal contact stiffness, ${}^g k_n$, and the tangential contact stiffness, ${}^g k_r$, in the local coordinate system as

$$K_{ij} = {}^g k_n n_i n_j + {}^g k_r (s_i s_j + t_i t_j) \quad (5)$$

where n_i , s_i , and t_i denote the unit vectors corresponding the axes of the local coordinate system so that

As a general form, the elastic normal and tangential contact stiffnesses, ${}^g k_n^{el}$ and ${}^g k_r^{el}$, is expressed by

$${}^g k_n^{el} = c_n^{el} ({}^g f_n / f_{ref})^{\alpha_n^{el}} \quad (6)$$

$${}^g k_r^{el} = c_r^{el} {}^g k_n^{el} \quad (7)$$

where f_{ref} is the normalizing constant (1 kN), c_n^{el} and c_r^{el} are the material constants relating to the geometry of the contact surface and the elastic modulus and Poisson's ratio of the particle, and $^g f_n$ is the normal contact force in the local coordinate system. The elastic-plastic normal contact stiffness, $^g k_n^{ep}$, which will be scaled up to the macroscopic elastic-plastic response, is defined by

$$^g k_n^{ep} = c_n^{ep} ({}^g f_n / f_{ref})^{\alpha_n^{ep}} = \frac{\theta (f_Y)^{1/\theta}}{\delta_Y} ({}^g f_n)^{(\theta-1)/\theta} \quad (8)$$

where c_n^{ep} is the material constant, θ ($=1.28$) is the exponent which governs the power relationship of elastic-plastic contact behavior, and f_Y and δ_Y are the contact force and displacement initiating the yielding of the contact. The elastic-plastic tangential contact stiffness, $^g k_r^{ep}$, is defined by

$$^g k_r^{ep} = c_r^{ep} {}^g k_n^{ep} \left(1 - \frac{{}^g f_r}{{}^g f_n \tan \phi_m} \right)^{\alpha_r^{ep}} \quad (9)$$

where c_r^{ep} is the material constant which is practically the same as c_r^{el} , ϕ_m is the friction angle of the particle, α_r^{ep} is the exponent defining the magnitude of nonlinearity induced by the frictional responses. To take the fabric evolution into account, the linear relationship between the degree of fabric anisotropy, a , and the macroscopic stress ratio, q/p , is employed, given by

$$a = a_0 + a_1 (q/p) \quad (10)$$

where a_0 is the degree of anisotropy in the isotropic stress condition, and a_1 is the slope of a for the increase of the stress ratio.

The approximate analytical solutions of cross-anisotropic elastic moduli in the isotropic stress condition are derived

in terms of the micromechanical parameters, given by

$$E_v^{el} = c_n^{el} c_r^{el} \left[\frac{7d_g^2 \rho_c (5+a_0)^2}{5(3-a_0)\{14-2a_0+c_r^{el}(21+9a_0)\}} \right] \left[\frac{5(3-a_0)}{\rho_c d_g f_{ref} (5-3a_0)} \right]^{\alpha_n^{el}} (\sigma_0)^{\alpha_n^{el}} \quad (11a)$$

$$E_h^{el} = c_n^{el} c_r^{el} \left[\frac{7d_g^2 \rho_c (5-3a_0)^2}{5(3-a_0)\{14-6a_0+c_r^{el}(21-15a_0)\}} \right] \left[\frac{5(3-a_0)}{\rho_c d_g f_{ref} (5-3a_0)} \right]^{\alpha_n^{el}} (\sigma_0)^{\alpha_n^{el}} \quad (11b)$$

$$G_{vh}^{el} = c_n^{el} c_r^{el} \left[\frac{7d_g^2 \rho_c (5-3a_0)^2 (5+a_0)^2}{10(5-a_0)(3-a_0) \left\{ \frac{105-46a_0-23a_0^2}{+c_r^{el}(70-24a_0+2a_0^2)} \right\}} \right] \left[\frac{5(3-a_0)}{\rho_c d_g f_{ref} (5-3a_0)} \right]^{\alpha_n^{el}} (\sigma_0)^{\alpha_n^{el}} \quad (11c)$$

$$G_{hh}^{el} = c_n^{el} c_r^{el} \left[\frac{7d_g^2 \rho_c (5-3a_0)^2}{10(3-a_0)\{21-11a_0+c_r^{el}(14-10a_0)\}} \right] \left[\frac{5(3-a_0)}{\rho_c d_g f_{ref} (5-3a_0)} \right]^{\alpha_n^{el}} (\sigma_0)^{\alpha_n^{el}} \quad (11d)$$

where σ_0 is the macroscopic isotropic stress.

3. Identification of Micromechanics Parameters

The data obtained from a series of triaxial tests performed by Kuwano and Jardine (2002) were used to evaluate the model parameters. The soil was the Ham River sand with physical properties as summarized in Table 1. Complete details of the experiments are given by Kuwano (1999). To measure the elastic properties of the tested material, both small unload/reload cyclic tests and shear wave measurements using bender elements were conducted.

Basically, the model parameters involved with the elastic contact stiffness are determined by simply matching the approximate solutions of elastic moduli given in Eq. (11) to the empirical expressions of elastic moduli (1963) in the isotropic stress condition. The void ratio and mean diameter of particles were previously determined based on the physical properties for a specific sample. In the matching process, elastic Poisson's ratios are not considered particularly because the experimental measurement of the elastic Poisson's ratios is relatively inaccurate.

For the isotropic stress of σ_0 , the empirical expressions of the cross-anisotropic elastic moduli are given by

Table 1. Physical properties of tested material (after Kuwano and Jardine, 2002)

Mineralogy	Specific gravity	Limit void ratio		Particle distribution		Particle shape
		e_{max}	e_{min}	D_{50}	U_c	
Quartz	2.66	0.849	0.547	0.27 mm	1.67	Sub-angular

U_c = Uniformity coefficient, D_{50} = Mean particle size, e_{max} = maximum void ratio, e_{min} = minimum void ratio. Maximum and minimum void ratios were determined following BS 1377.

$$E_v^{el} = A_v f(e) p_a^{-n_v} (\sigma_0)^{n_v} \quad (12a)$$

$$E_h^{el} = A_h f(e) p_a^{-n_h} (\sigma_0)^{n_h} \quad (12b)$$

$$G_{vh}^{el} = A_{vh} f(e) p_a^{-n_{vh}} (\sigma_0)^{n_{vh}} \quad (12c)$$

$$G_{hh}^{el} = A_{hh} f(e) p_a^{-n_{hh}} (\sigma_0)^{n_{hh}} \quad (12d)$$

where A_v , A_h , A_{vh} , and A_{hh} are the material constants, n_v , n_h , n_{vh} , and n_{hh} are the exponents indicating the stress-level dependence of experimental elastic moduli, and p_a is the atmospheric pressure (101.3 kPa), normalizing the macroscopic isotropic stress. The void ratio function, $f(e) = (2.17-e)^2/(1+e)$, used here is provided by Hardin and Richart (1963).

The value of α_n^{el} can be easily determined by comparing the exponents in Eqs. (11) and (12). The average of the experimentally determined values of n_v , n_h , n_{vh} , and n_{hh} , is taken as the value of α_n^{el} , while the values of A_v , A_h , A_{vh} , and A_{hh} are also adjusted to compensate for the change of the exponents in the empirical expressions. Table 2 summarizes the measured values of A and n , and their adjustments for the further use.

The degree of fabric anisotropy in the isotropic stress condition, a_0 , and the proportional factor, c_r^{el} , can be determined by matching the moduli ratios, E_h/E_v and G_{hh}/G_{vh} , from the approximate solutions of Eq. (11) to those from the empirical expressions as:

$$\frac{E_h^{el}}{E_v^{el}} = \frac{A_h}{A_v} = \frac{(5-3a_0)^2}{(5+a_0)^2} \left[\frac{14-2a_0+c_r^{el}(21+9a_0)}{14-6a_0+c_r^{el}(21-15a_0)} \right] \quad (13a)$$

$$\frac{G_{hh}^{el}}{G_{vh}^{el}} = \frac{A_{hh}}{A_{vh}} = \frac{(5-a_0)}{(5+a_0)^2} \left[\frac{105-46a_0-23a_0^2+c_r^{el}(70-24a_0+2a_0^2)}{21-11a_0+c_r^{el}(14-10a_0)} \right] \quad (13b)$$

With the given values of A_h/A_v and A_{hh}/A_{vh} , the solution of Eqs. (13a) and (13b) yields the values of a_0 and c_r^{el} , as summarized in Table 3. As can be seen in Table 3, however, these estimations are unreasonable when considering the possible range of c_r^{el} , which should be positive and less than 1.0 based on the Mindlin's equation. To avoid such anomalous results, the values of a_0 are evaluated by employing either Eq. (13a) or Eq. (13b) with a fixed value of $c_r^{el} = 0.824$ based on the Poisson's ratio of 0.3 for the quartz. The remaining parameter, c_n^{el} , can be evaluated by substituting all the pre-determined values of α_n^{el} , c_r^{el} , a_0 , e , and d_g into Eq. (11) and matching these to the empirical expressions in Eq. (12), thereby yielding four different values of c_n^{el} for each test. The average of four values is chosen as the representative value of c_n^{el} .

The sign of a_0 from Eq. (13a) is different from that from Eq. (13b), which is physically inadmissible in an identical sample. This contradictory result may come from the particular assumption to estimate the elastic moduli: Kuwano and Jardine (2002) assumed that the elastic properties obtained from small-cyclic triaxial tests are compatible with those from bender element tests to obtain a complete set of cross-anisotropic elastic moduli. As reported by Chaudhary et al. (2004) and Yimsiri and Soga (2002), such discrepancy in the value of a_0 was found in other experimental data but has not been clearly explained yet. Herein either set of parameters based on Eq. (13a) or (13b) is selectively adopted. For instance, the set of parameters based on Eq. (13a) is used to compute the Young's moduli such as E_v^{el} and E_h^{el} , while

Table 2. Material constants for empirical expressions of cross-anisotropic elastic stiffnesses (adjusted values are in parentheses)

Elastic Modulus	A (MPa)	Exponent			Relevant Expression ($P_a = 101.3\text{kPa}$)
		a	b	a+b	
E_v^{el}	$A_v = 204(204)$	0.52(0.52)	–	0.52(0.52)	$E_v^{el} = A_v f(e) (\sigma_v / p_a)^{a_v}$
E_h^{el}	$A_h = 174(176)$	–	0.53(0.52)	0.53(0.52)	$E_h^{el} = A_h f(e) (\sigma_h / p_a)^{b_h}$
G_{vh}^{el}	$A_{vh} = 72(72)$	0.32(0.32)	0.20(0.20)	0.52(0.52)	$G_{vh}^{el} = A_{vh} f(e) \left(\frac{\sigma_v}{p_a} \right)^{a_{vh}} \left(\frac{\sigma_h}{p_a} \right)^{b_{vh}}$
G_{hh}^{el}	$A_{hh} = 81(82)$	-0.04(-0.03)	0.53(0.55)	0.50(0.52)	$G_{hh}^{el} = A_{hh} f(e) \left(\frac{\sigma_v}{p_a} \right)^{a_{hh}} \left(\frac{\sigma_h}{p_a} \right)^{b_{hh}}$

another set based on Eq. (13b) is chosen to compute the elastic shear moduli such as G_{vh}^{el} and G_{hh}^{el} .

If the contact force to initiate the elastic-plastic deformation of a single particle is f_Y , the magnitudes of elastic contact stiffness and elastic-plastic contact stiffness are approximately the same when $f_n = f_Y$:

$$C_n^{ep}(f_Y)^{\alpha_n^{ep}} = C_n^{el}(f_Y)^{\alpha_n^{el}} \quad \text{and} \quad C_n^{ep} = C_n^{el}(f_Y)^{\alpha_n^{el} - \alpha_n^{ep}} \quad (14)$$

In Eq. (14), the values of C_n^{el} and α_n^{el} were already evaluated. The value of α_n^{ep} is assumed to be 0.22 as described in the companion paper so that the determination of f_Y is important to find the value of C_n^{ep} . If the yielding is initiated in the conical contact, f_Y can be estimated by the following equation:

$$f_Y = \frac{\pi r_c^2}{8} \frac{(1 - \nu_g)^2}{G_g^2} Y^3 \quad (15)$$

For the granular soils, the definite value of yield stress, Y , is difficult to find, because the yielding or failure point of brittle material is not well defined and affected by the

size of specimen and the confining pressure. However, the yield stress can be estimated using the relation between Vickers diamond pyramid hardness parameter, H_V , and the yield stress, Y , (Johnson 1985), given by

$$H_V \approx 2.8Y \quad (16)$$

For quartz, with a hardness of about 10 GPa (Brace 1963), the value of Y is the order of 3 GPa. The approximate value of r_c can be obtained from the relation between the shape of particle and the ‘roundness’ parameter which is estimated by comparing the curvature of different surface features in the particle to the lowest curvature that can be assigned to the particle (e.g., the radius of the largest sphere that can be inscribed in the particle). For the ‘sub-angular’ particle, the value of r_c is about $3.4 \sim 4.7 \times 10^{-2}$ mm (Jung 2004). For the selected material of quartz, with $G_g = 29$ GPa, $\nu_g = 0.31$, $Y = 3$ GPa, and $r_c = 3 \times 10^{-2}$ mm, the value of f_Y is 5×10^{-6} kN. Using Eq. (14), the value of C_n^{ep} can be evaluated as summarized in Table 3. The parametric studies are needed to evaluate the remaining parameters, a_1 and α_r^{ep} .

Table 3. Summary of the evaluated parameters

Material parameters		Values	Note
Void ratio	e_0	0.658	initial void ratio
Mean diameter	d_g (mm)	0.27	D_{50}
Elastic contact stiffness	C_n^{el} (kN/m)	19775	using Eq. (13a); for E_v^{el} and E_h^{el}
		17599	using Eq. (13b); for G_{vh}^{el} and G_{hh}^{el}
	C_r^{el}	-0.982	using Eq. (13a) and (13b); not used
		0.824	$2(1 - \nu_g)/(2 - \nu_g)$ for $\nu_g = 0.3$
α_n^{el}	0.52	based on the experimental data	
Elastic-plastic contact stiffness	C_n^{ep} (kN/m)	513.6	$C_n^{ep} = C_n^{el}(f_Y)^{\alpha_n^{el} - \alpha_n^{ep}}$; $f_Y = 5 \times 10^{-6}$ kN for quartz
		451.7	
	α_n^{ep}	0.22	$\theta = 1.28$
	C_r^{ep}	0.824	$C_r^{ep} = C_r^{el}$
	α_r^{ep}	3.0	based on the parametric study
ϕ_m (deg)	26	referring to published data	
Evolution of fabric anisotropy	a_0	-0.103	using Eq. (13a) and (13b); not used
		0.171	using Eq. (13a); for E_v^{el} and E_h^{el}
		-0.244	using Eq. (13b); for G_{vh}^{el} and G_{hh}^{el}
	a_1	0.34	based on the parametric study

4. Micromechanics Analysis of Granular Soils

4.1 Elastic Behavior

The main experimental features of macroscopic responses in granular soils are summarized as: (i) the elastic responses exhibit the cross-anisotropic elasticity, and (ii) the magnitude of each elastic modulus depends on the stress level in the form of the power function. These two features are manifested as the empirical correlations of the elastic moduli, thus the value of elastic modulus in any stress state can be estimated from the empirical expressions such as Eq. (12). From the viewpoint of the micromechanics theory, it is supposed that the cross-anisotropy of soil elasticity relates to the fabric tensor and the stress-level dependency of elastic moduli relates to the nonlinear contact stiffness depending on the level of contact forces, respectively.

The problem arises in the quantitative assessment of each role of two micro-mechanisms. In the previous section, except for a_1 , the required parameters for the micromechanics analysis were precisely evaluated. Using these parameters, the elastic moduli are computed along two different stress paths—the isotropic compression and the triaxial compression, as shown in Fig. 1.

Fig. 2 compares the computed values of the Young's moduli and elastic shear moduli for the isotropic compression

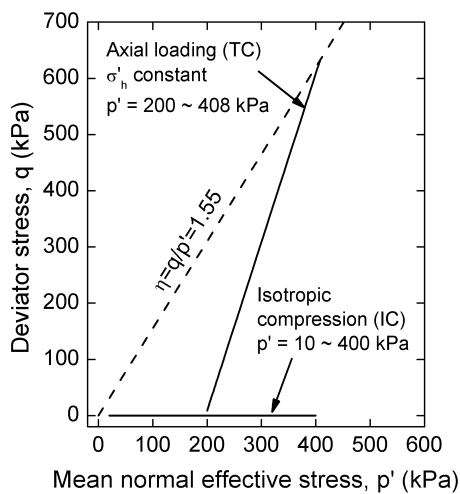


Fig. 1. Stress paths for the numerical simulation

(IC) to the experimental data of each test. The value of a_1 , which relates the variation of a to the stress ratio, is set to zero for the isotropic compression. As can be seen in Fig. 2 (a), the computed and measured data are practically identical, indicating that a certain degree of errors in the approximation of the closed-form solutions does not affect the reliability of prediction, partly due to relatively low degrees of fabric anisotropy. Moreover, this result confirms that the ignorance of the fabric evolution by setting a_1 to zero does not affect the accuracy of

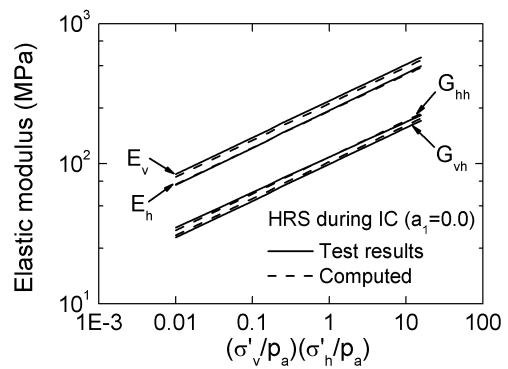


Fig. 2 (a) Variation of elastic moduli (for the constant a in the isotropic compression)

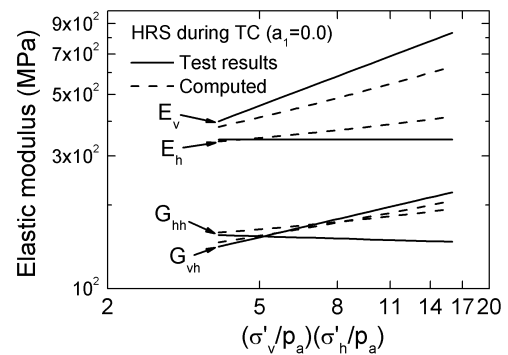


Fig. 2 (b) Variation of elastic moduli (for the constant a in the triaxial compression)

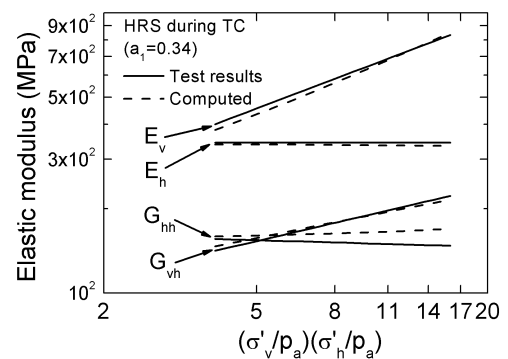


Fig. 2 (c) Variation of elastic moduli (for the varying a in the triaxial compression)

prediction. This also implies that the soil fabric remains constant when the samples are subject to the isotropic stress. In the isotropic stress condition, therefore, the stress-level dependency of cross-anisotropic elastic behavior is fully explained based on the nonlinear contact stiffness in the constant fabric condition. The exponent of the power function in the normal contact stiffness manifests itself as the exponent in the empirical expression of cross-anisotropic elastic modulus in the isotropic stress condition.

Fig. 2 (b) shows the computed and testing data during the triaxial compression (TC). In this case the value of a_1 is equal to zero, thus leading to the constant fabric condition as it was in the isotropic compression. As shown in Fig. 2 (b), even though the computed values of elastic moduli keep increasing during loading, the computed trend lines significantly differ from the experimental trend in elastic moduli. This discrepancy implies that in the anisotropic stress condition, the nonlinear contact stiffness at the constant fabric is not sufficient to explain the stress-level dependency of elastic moduli, and thus the remaining micromechanical feature—the evolution of fabric anisotropy—must be taken into account.

Within the framework of this research, the evolution of fabric anisotropy can be taken into account via a single parameter a_1 in Eq. (10). As noted previously, the value of a_1 implicitly includes the directional evolution of contact forces during loading. To choose a proper value of a_1 , a parametric study is conducted. In the parametric study, the exponent of n in the empirical expression of test data is compared to the exponent of α obtained by the regression fitting on the computed elastic moduli of E_v^{el} , E_h^{el} , G_{vh}^{el} , and G_{hh}^{el} versus the applied stresses in the triaxial compression. The average of four different values of $|n - \alpha|$ for E_v^{el} , E_h^{el} , G_{vh}^{el} , and G_{hh}^{el} is taken to plot against the variation of a_1 , as shown in Fig. 3. The results show that the value of $|n - \alpha|$ gradually decreases as a_1 increase, and minimized when $a_1 = 0.34$. Hence, the optimum expression to describe the evolution of fabric anisotropy for the triaxial compression, is given by

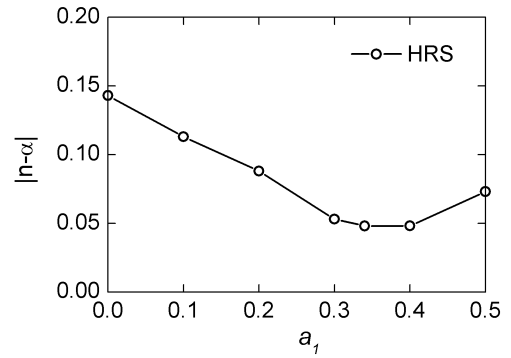


Fig. 3. Variation of $|n - \alpha|$ for the various values of a_1

$$a = a_0 + 0.34(q/p) \quad (17)$$

A similar research on the variation of a_1 via the discrete element method (Jung et al. 2006) also confirms that a simple linear relationship between a and q/p is valid for lower value of the stress ratio in the compression tests. Using the value of a from Eq. (17) for a given q/p , the elastic moduli are re-computed and compared to the experimental data in Fig. 2 (c). As can be seen in Fig. 2 (c), all the trends of computed elastic moduli match up with those of experimental trends.

The stress-level dependency of cross-anisotropic elastic moduli can be completely explained only if one can fully account for the evolution of fabric anisotropy in the anisotropic stress condition, together with the nonlinearity of the contact stiffness which is pronounced in the isotropic stress condition. The evolution of fabric anisotropy can quantitatively be expressed as the linear function of the stress ratio, q/p , at least for the triaxial compression, while the further calibration of Eq. (17) would be necessary for the general loading conditions. The numerical results show that as the stress ratio, q/p , changes, the state of fabric needs to be changed along with the applied anisotropic stresses to reproduce the experimental elastic response for the given stress condition. As mentioned previously, the evolution of fabric originates from the inelastic strains and particle rotations in the microscopic level so that the evolution equation of Eq. (17) indicates the magnitude of effect of the inelastic behavior on the elastic responses. To develop a complete micromechanics model aiming on the simulation of overall elastic-plastic stress-strain behavior

of granular soils, the change of fabric—loss and creation of contacts followed by the change of contact directions—should be taken into account in its formulation. The feasibility of such formulation on the fabric evolution could be examined based on the evolution equation such as Eq. (17), which is independently derived from the observation of experimental elastic responses.

4.2 Elastic-plastic Behavior

In the drained triaxial compression test (TC), the simulation results obtained from the micromechanical analysis with the elastic-plastic contact models were compared with the experimental data. During TC, the actual measurements related to the elastic-plastic behaviour are taken on the vertical (axial) stresses, the vertical (axial) strains and the horizontal (radial) strains. Thus, the physical quantities directly obtained from the measurements are the vertical Young's modulus, E_v^{ep} , and the Poisson's ratio, ν_{vh}^{ep} . The arbitrary assumptions are usually accompanied to obtain the other quantities such as E_h^{ep} , ν_{hh}^{ep} and ν_{hv}^{ep} . Herein, the quantitative comparisons between the computed and the measured data will be limited to E_v^{el} and ν_{vh}^{ep} .

In the micromechanics analysis, it is assumed that the degree of fabric anisotropy continuously changes with the stress ratio. The inclination of the linear $a - \eta$ curve, a_1 is set to 0.34 which gives the best-fitting results for the stress-level-dependent behavior of the elastic moduli. The initial value of the degree of fabric anisotropy, a_0 , however, is still uncertain because the inconsistency in the value of a_0 is not resolved. Thus, the possible values of a_0 between 0.171 from Eq. (13a) and -0.224 from Eq. (13b) are applied and the different responses of elastic-plastic modulus, E_v^{ep} , are examined. In addition, as discussed in the previous section, the parameter α_r^{ep} for the tangential contact stiffness is not defined. Herein, the value of α_r^{ep} is set to 3.0 based on the parametric study conducted by Jung (2004). Fig. 4 summarizes the results of the simulation for $\alpha_r^{ep} = 3.0$. It is noted that the scattering of measured tangent modulus in Fig. 4 (a) is inevitable due to the limitation of measurement of the stresses and strains at small strains. The scatters of tangent modulus do not

appear in the variation of secant modulus as shown in Fig. 4 (b).

The numerical results in Fig. 4 provide useful information on the elastic-plastic behavior during the axial compression. Fig. 5 shows the stress-strain curves in the vertical direction for various strain levels. The numerical findings for the elastic-plastic behavior during triaxial compression are:

- (1) The plastic strains are likely to occur even at very small strains. The linear response of the stress-strain curve at very small strains does not indicate the pure elastic response of soils. Combination of the increasing elastic modulus with the increasing vertical stress and the plastic strains degrading the slope of stress-strain curve produces the apparent linearity in the initial part of the stress-strain curve.
- (2) At very small strains, the effect of plastic straining on the degradation of elastic-plastic modulus is minimized when the initial state of soil is under the isotropic

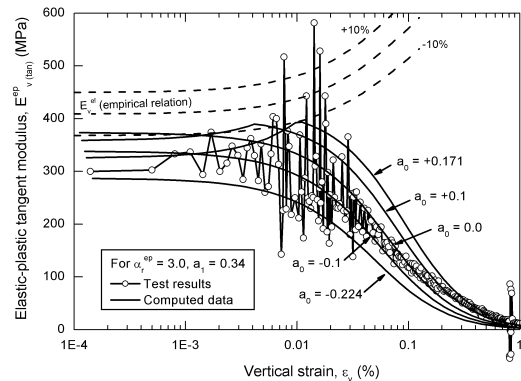


Fig. 4 (a) Variation of E_v^{ep} with the different a_0 during triaxial compression (tangent modulus)

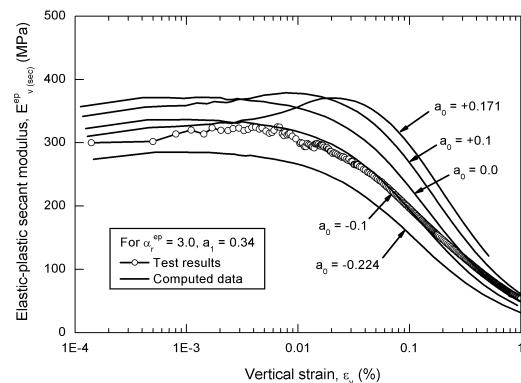


Fig. 4 (b) Variation of E_v^{ep} with the different a_0 during triaxial compression (secant modulus)

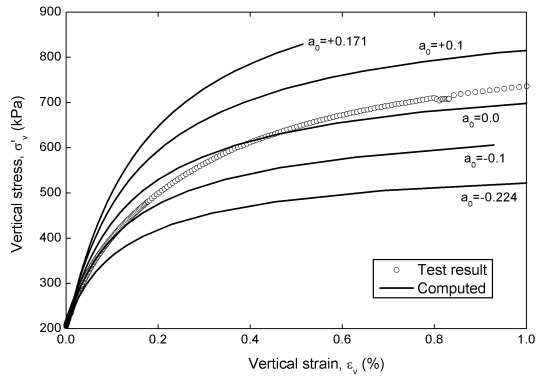


Fig. 5 (a) Stress-strain curves in the vertical direction (up to 1%)

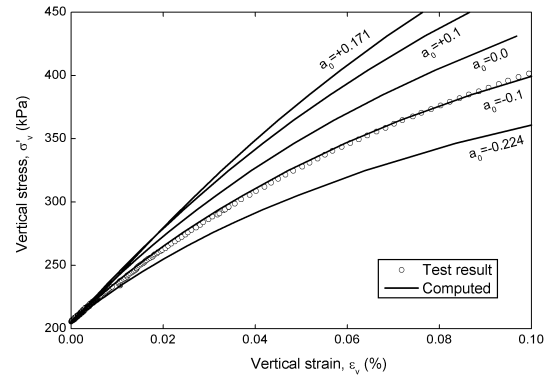


Fig. 5 (b) Stress-strain curves in the vertical direction (up to 0.1%)

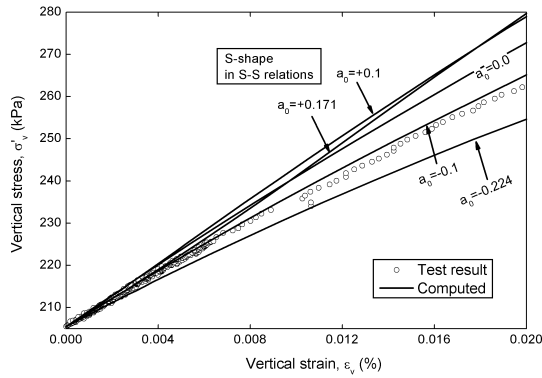


Fig. 5 (c) Stress-strain curves in the vertical direction (up to 0.02%)

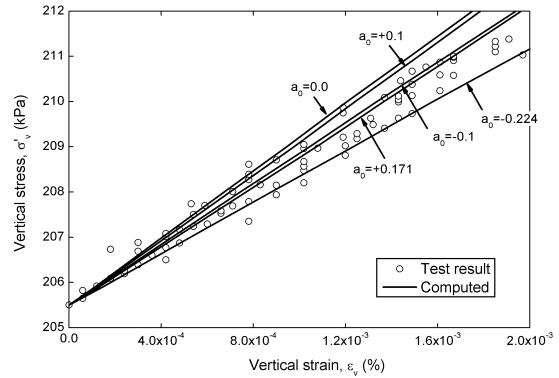


Fig. 5 (d) Stress-strain curves in the vertical direction (up to 0.002%)

fabric condition (i.e. $a_0 = 0.0$). The larger a_0 deviates from the isotropic value of 0.0, the larger decrease of initial modulus takes place.

- (3) When $a_0 > 0$, the increasing pattern of E_v^{ep} appears at small strains. Due to the increasing modulus, the apparent linear range in the stress-strain relations increased up to about $\epsilon_v = 0.01\%$ (see Fig. 5(c)). When a_0 is less than or equal to zero, however, E_v^{ep} continuously decreased with the axial strains. If the increase of E_v^{ep} can be regarded as the linear elastic response, the size of elastic region increases as the value of a_0 increases.

- (4) For a specific value of α_r^{ep} , the magnitude of E_v^{ep} for the higher value of a_0 is larger than that for the lower value of a_0 after the axial strain exceed 0.01%.

It is interesting that the values of E_v^{ep} increase in the small strain range and the corresponding ‘S-shaped’ stress-strain relationship appears when $a_0 > 0.0$. The similar pattern of increasing E_v^{ep} can be found in the other experimental results reported by Kohata et al. (1997). They observed that the increasing E_v^{ep} and the ‘S-shaped’

stress-strain relationships in the cyclic pre-stained specimens in which the larger number of cycles was applied to the specimen, the higher increase of E_v^{ep} took place. This experimental phenomena are very similar to the numerical results for $a_0 > 0$ in Figs. 4 and 5. In terms of micromechanics, it can be thought that the process of the cyclic pre-straining increases the number of contacts in the vertical (axial) direction. The maximum value of E_v^{ep} for $a_0 = +0.171$ is larger than that for $a_0 = +0.1$. Based on the above discussion, one can conclude that the increase of E_v^{ep} during compression is the distinctive feature of the stress-strain response for the initial fabric condition with $a_0 > 0$. It is noted that the experimental data of stress-strain curves in Fig. 5 does not show the particular ‘S-shaped’ pattern during compression. This may imply that the initial state of fabric anisotropy is close to the condition with $a_0 < 0$. There is a possibility that $a_0 < 0.0$ obtained from Eq. (13b) represents the real state of the initial condition of specimen more closely.

Fig. 6 shows the contribution of elastic and plastic strains to the total strains in the vertical direction. For

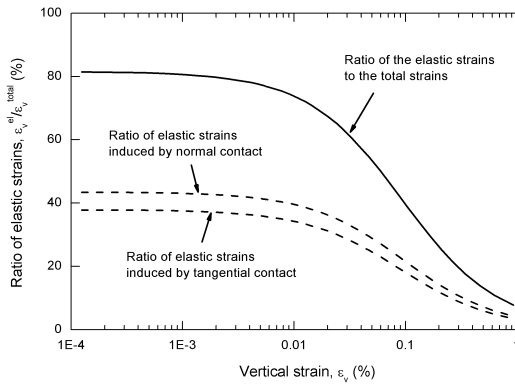


Fig. 6 (a) Strains developed in the vertical direction (elastic and total strains)

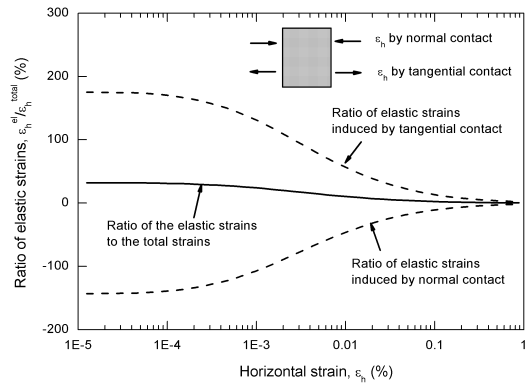


Fig. 7 (a) Strains developed in the horizontal direction (elastic and total strains)

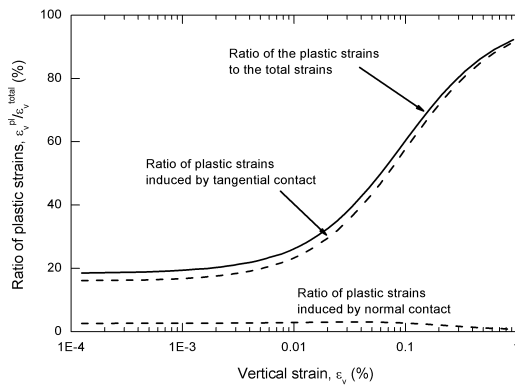


Fig. 6 (b) Strains developed in the vertical direction (plastic and total strains)

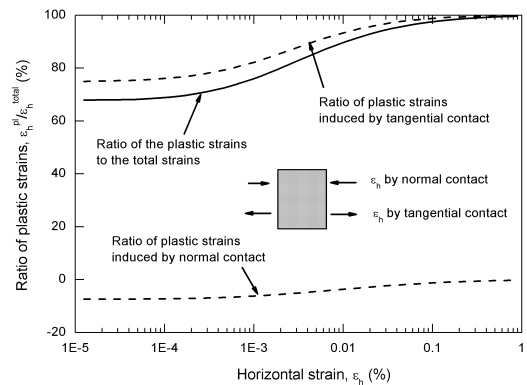


Fig. 7 (b) Strains developed in the horizontal direction (plastic and total strains)

convenience, the numerical results for $a_0 = -0.1$, which closely matched the experimental relationship between E_v^{ep} and ε_v , are analyzed. The strains are decomposed into the components induced by normal and tangential contact displacements to investigate the effect of contact stiffnesses on the overall behavior of elastic-plastic straining.

Fig. 6 shows that the contribution of elastic strains, which initially occupies about 80% of total strains, continuously reduces during axial compression. The elastic strains induced by the tangential contacts have a considerable portion of total elastic strains compared with those induced by the normal contacts. However, in case of the plastic strains, the different pattern of the contribution of strains induced by the normal and the tangential contacts takes place. The ratio of plastic strains induced by the normal contacts is very small in the overall strain range. The plastic strains induced by the tangential contacts occupy most of the plastic strains. Thus, one may conclude that the plastic strains, which reduce the stiffness in the vertical

direction, are mainly controlled by the properties of tangential contact stiffness. The contributions of elastic and plastic strains in the total horizontal strains, however, are quite different from those in the vertical strains. Fig. 7 shows the ratio of elastic and plastic strains to the total strains in the horizontal direction. The differences between the responses in the vertical and horizontal strains can be summarized as follows:

- (1) While both of the elastic strains induced by the normal contact and the elastic strains induced by the tangential contact are in compression in the vertical direction, the direction of horizontal strains induced by the normal contact are opposite to that by the tangential contact. The elastic strains induced by the normal contacts are developed in the compression side of the horizontal direction, but the elastic strains induced by the tangential contacts are in the extension. The same pattern of the plastic straining takes place.
- (2) In the horizontal strains, the ratio of elastic strain to

total strain is only about 20–40% even at the very small strains. The horizontal strains induced by the plastic deformation or slippage induced by the tangential contacts occupy most of the horizontal strains during axial loading. Similar to the pattern of the vertical strains, the plastic strains induced by the normal contacts occupy the small portion of the total plastic strains in the overall horizontal strains.

The cross-anisotropic Poisson’s ratios are also affected by the magnitude of the horizontal strains. Fig. 8 shows the variation of cross-anisotropic Poisson’s ratios during triaxial compression. In the triaxial compression, the value of $\nu_{vh}^{ep} = -\delta\epsilon_h^{ep} / \delta\epsilon_v^{ep}$ can be measured during test. The pattern of variation in the computed values of ν_{vh}^{ep} is similar to that in the test data. For the elastic-plastic values of Poisson’s ratios, ν_{vh}^{ep} is generally higher than ν_{hv}^{ep} and ν_{hh}^{ep} because the magnitude of ν_{vh}^{ep} is significantly affected by the magnitude of ϵ_h^{ep} . In the overall strains, ν_{hh}^{ep} ranging from 0.1 to 0.35 is lower than the other two Poisson’s ratios. It should be noted that the elastic Poisson’s ratios are nearly zero and do not exceed 0.1. The value of ν_{vh}^{ep} increases with the axial strains from the values close to ν_{vh}^{el} to the values of $\nu_{vh}^{pl} = -\delta\epsilon_h^{pl} / \delta\epsilon_v^{pl}$. Hayano and Tatsuoka (1997) reported the similar behavior of ν_{vh}^{el} , ν_{vh}^{pl} and ν_{vh}^{ep} from a drained triaxial compression test, from which it may be considered that values of ν_{vh}^{ep} exceeding 0.1 at the very small strains in the drained compression test indicate the generation of the plastic strains primarily induced by tangential contacts.

The above analysis results ascribed the overall deg-

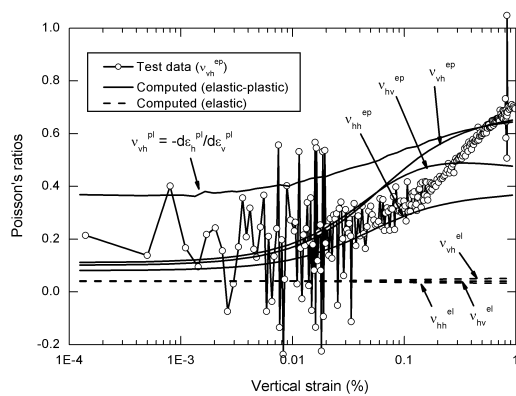


Fig. 8. Cross-anisotropic Poisson’s ratios during triaxial compression

radation of soil stiffness mainly to the plastic strains induced by the tangential contacts. However, the shear failure of particulate materials after dilation seems not to be massive as much as the micromechanics model predicts. Even before failure, the groups of particles, in general, move together in ‘wedges’. Eventually, neighboring wedges become kinematically locked, they shear, and a new subsystem of wedges is formed. In many cases, deformations continue localizing in narrow shear bands. Once such mechanism is formed, the blocks bound by the slip plane move as rigid bodies and deformation localizes within the slip planes producing progressive failure. The internal energy exerted on the tangential contacts at the early stage of shearing is transferred to the localized slip plane generating two sliding ‘wedges’ at the large strains. The micromechanics approach with homogenization technique adopted in this study cannot simulate such a localization of the particulate structure experiencing large strains. Consequently, there is a possibility to underestimate the stiffnesses of soils subjected to the large deviator stress. The plastic strain in every single contact in the homogenization technique leads to the excessive volumetric expansion at the early stage of shearing. Fig. 9 compares the volumetric strains in the test data and the numerical results in the large strain range. While the computed stress-strain relationship shows the good agreement before the deviator stress reaches a stress point at the onset of marked dilation, significant discrepancy between the test and computed data appears after the apparent dilation takes place. Different method such as the bifurcation

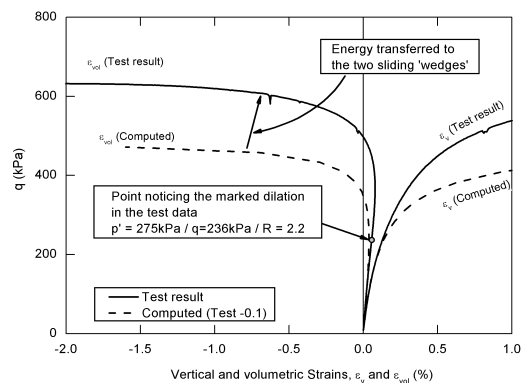


Fig. 9. Vertical and volumetric strains during shearing in test data and simulations

analysis would be useful to predict the stress-strain behavior after a particulate material shows the dilation.

5. Conclusions

In terms of the micromechanics theory, the elastic and elastic-plastic responses of deformation of granular soils are meticulously analyzed. To guarantee the high accuracy of the microscopic parameter, the systematic procedure to evaluate the parameters is provided. The parameters involved with the elastic contact stiffness are mainly evaluated by the direct comparison between the empirical expression of cross-anisotropic elastic moduli and the micromechanics-based analytical solutions. The parameters to formulate the elastic-plastic contact stiffness are determined based on the published experimental data for the metallic materials as well as the material references.

The analysis of the elastic response during the isotropic and triaxial compression shows that the stress-level dependency of cross-anisotropic elastic moduli is induced by the power relationship of the contact force in the normal contact stiffness, while the evolution of fabric anisotropy is more pronounced during triaxial compression. The evolution of fabric anisotropy is quantitatively evaluated by observing the difference between the experimental data and the micromechanical predictions.

In the light of the micromechanics theory, the elastic-plastic responses of soil deformation are thoroughly scrutinized. The micromechanical analysis indicates that the plastic strains are likely to occur at the very small strains. The linear response of the stress-strain curve at the very small strains does not represent the pure elastic response of soils. The combination of the stress-level-dependent elastic modulus and the plastic straining generates the apparent linearity in the initial part of the stress-strain curve. The magnitude of the elastic strains induced by the tangential contacts is comparable to the strains induced by the normal contacts. However, in the case of the plastic

strains, the pattern of contribution between the normal and the tangential contacts is different from the elastic case. The ratio of plastic strains induced by the normal contacts to the total plastic strains is very small in the overall strain range. The plastic strains induced by the tangential contacts occupy most of the plastic strains. The plastic deformation of tangential contacts has an important role in the reduction of soil stiffness during axial loading.

Acknowledgements

Financial support for this work was provided by Korea Research Foundation Grant No. KRF-2005-214-D00166. The support of Engineering Research Institute at Seoul National University is greatly appreciated.

References

1. Brace, W. F. (1963), "Behavior of quartz during indentation", *Journal of geology*, 71(5), 581-595.
2. Chaudhary, S. K., Kuwano, J., and Hayano, Y. (2004), "Measurement of quasi-elastic stiffness parameters of dense Toyoura sand in hollow cylinder apparatus and triaxial apparatus with bender elements", *Geotechnical Testing Journal*, 27(1), 23-35.
3. Hardin, B. O., and Richart, F. E. J. (1963), "Elastic wave velocities in granular soils", *Journal of Soil Mechanics and Foundation Engineering, ASCE*, 89(SM1), 33-65.
4. Johnson, K. L. (1985), *Contact mechanics*, Cambridge University Press, Cambridge.
5. Jung, Y.-H., Lee, J.-H., and Chung, C.-K. (2006), "Evolution of Fabric Anisotropy in Granular Soils under Triaxial Loadings", *Proc. Geot congress 2006*, Atlanta, Georgia.
6. Jung, Y. H. (2004), "Modeling of nonlinear anisotropic deformation of granular soils in pre-failure condition by numerical approach", Seoul National University, Seoul, Korea.
7. Kohata, Y., Tatsuoka, F., Wang, L., Jiang, G. L., Hoque, E., and Kodaka, T. (1997), "Modelling the non-linear deformation properties of stiff geomaterials", *Geotechnique*, 47(3), 563-580.
8. Kuwano, R. (1999), "The stiffness and yielding anisotropy of sand", Ph.D. thesis, Imperial college, University of London, London.
9. Kuwano, R., and Jardine, R. J. (2002), "On the applicability of cross-anisotropic elasticity to granular materials at very small strains", *Geotechnique*, 52(10), 727-749.
10. Yimsiri, S., and Soga, K. (2002), "Application of micromechanics model to study anisotropy of soils at small strains", *Soils and Foundations*, 42(5), 15-26.

(received on Jan. 12, 2007, accepted on Mar. 26, 2007)

Effect of Fines on the Stability of Unsaturated Soil Slopes

불포화 사면안정에 미치는 세립분의 영향분석

Lee, Kyu-Hyun¹ 이 규 현
Jeong, Sang-Seom² 정 상 섬
Kim, Tae-Hyung³ 김 태 형

요 지

국내 풍화토사면의 경우 순수 균질 사면보다는 대부분 점토 및 세립분이 섞인 비균질 상태로 존재하며 이러한 함유비율은 풍화도 및 지역에 따라 다르다. 따라서 세립분함량 변화에 따른 불포화사면의 분석을 위해, 화강풍화토(SW)에 일정비율의 세립분(CH)을 섞어 성형한 시료를 통해 GCTS pressure plates을 이용한 함수특성곡선 실험을 수행하였다. 실험 및 침투해석결과 강우지속시간에 따른 포화깊이의 증가율은 세립분이 증가할수록 또한 상대밀도가 증가할수록 작아졌다. 또한 침투해석과 포화 및 불포화강도정수를 이용한 사면 안정성 해석결과(SLOPE/W), 전반적으로 세립분함량 10~15%의 범위까지는 침투깊이 증가에 따른 흡수력 변화가 안전율에 지대한 영향을 미치는 반면 이를 초과하는 경우(>15%)에는 오히려 세립분함량 증가에 따른 강도정수의 변화가 크게 영향을 미침을 알 수 있었다.

Abstract

In South Korea, many weathered soil slopes are composed of soil mixtures with certain amount of clay fractions in natural soil deposits. Accordingly, it is very important to analyze that effect of the fines on the stability of unsaturated soil slopes. In this study, five different soil types classified by mixture portion of fines were used and experiment on the soil-water characteristic curve tests (SWCC) using GCTS (Geotechnical Consulting and Testing Systems) pressure plate were performed in order to analyze the stability of unsaturated soil slopes. Based on the infiltration analysis which contains SWCC test result by the SEEP/W, it is shown that the increasing rate of the wetting band depth was decreased as the fines content and the relative density were increased. According to the stability analysis result of the unsaturated soil slopes through the SLOPE/W, it is found that the transition from the wetting band depth to the variation of strength parameters which affect the stability of unsaturated soil slopes appears to occur around 10~15% of clay contents in the mixtures.

Keywords : GCTS pressure plate, Infiltration analysis, Strength parameters, SWCC, Wetting band depth

1. Introduction

Effective factors of rock slopes stability due to rainfall are the value of water pressure in vertical joint or in

tension-cracks and up-lift water pressures on sliding plane (s). On the other hand, in case of the stability analysis on unsaturated soil slopes, the wetting band depth due to rainfall is the main reason of unsaturated soil slope

1 Researcher, Civil Research & Eng. Team, Technology Research Institute, Daelim Industrial Co., Ltd.

2 Member, Prof., Dept. of Civil Eng., Yonsei Univ., soj9081@yonsei.ac.kr

3 Graduate Student, Dept. of Civil Eng., Yonsei Univ., tvnimph@hotmail.com

failure. Accordingly, it is very important to analyze the wetting band depth due to rainfall for unsaturated soil slopes.

Most of the land area of Korean peninsula are composed of soils formed from the in situ weathering of granite and genesis. Many slope failures in these weathered failure of these weathered soils are triggered by heavy rainfall. These failures are characterized by relatively shallow failure surfaces that develop parallel to the original slope. These failures may be attributed to the deepening of a wetting front into the slope due to rainfall infiltration which results in an increase in moisture content, a decrease in soil matric suction and a decrease in shear strength on the potential failure surface (Ng and Shi, 1998; Fourie et al., 1999; Lee et al., 2002; Kim et al., 2004). It is generally said that the unsaturated soil slope failures due to rainfall are mainly caused by the decrease in suction of unsaturated soil with the increase of the water content and wetting band depth.

In South Korea, many weathered soils can be classified as SW or SM according to the Unified Soil Classification System (USCS). These soils consist of soil mixture with certain amount of clay fractions in natural soil deposits. This paper describes the results of a series of soil-water characteristic curve tests and numerical analyses aimed

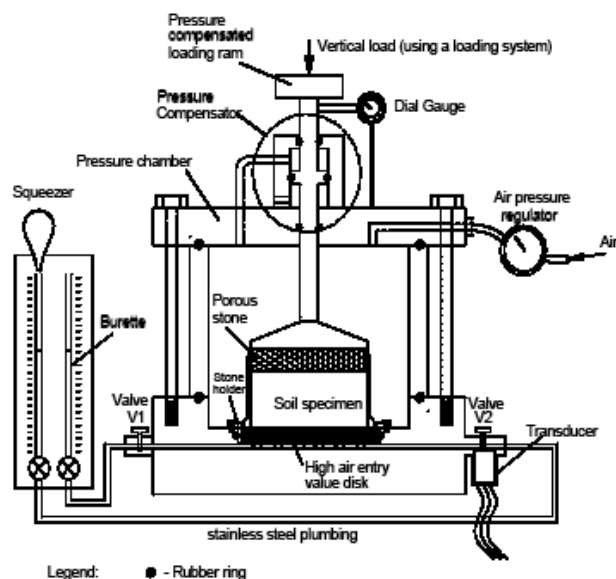
at clarifying the effect of the magnitude of wetting band depth on unsaturated soil slopes. Special attention is given to the prediction of approximate limit of clay content which influences the magnitude of wetting band depth in soil mixtures.

2. Soil-Water Characteristic Curve Testing

The soil suction, generally called ‘total suction’, consists of matric and osmotic suctions. Soil suction is commonly referred to as the free energy state of soil water. For groundwater flow through an unsaturated soil, the coefficient of permeability is not a constant but a function of soil suction. Therefore, it is necessary to determine the soil-water characteristic curve (SWCC) that defines the relationship between the suction and the volumetric water content of the soil. This curve can be used to derive permeability functions for use in unsaturated groundwater flow problems (Fredlund and Rahardjo, 1993). It is also possible to use SWCC to establish unsaturated shear strength parameters (Vanapalli et al., 1996).

2.1 Description of the Apparatus

The GCTS pressure plate was developed by Fredlund in 2005. The GCTS pressure plate uses the axis-translation



(a) Schematic of the GCTS pressure plate



(b) Photo of the GCTS pressure plate measuring for SWCC

Fig. 1. The GCTS pressure plate

technique to control matric suction in the soil specimen (Fredlund and Rahardjo, 1993). The GCTS pressure plate consists of two main parts (Fig. 1) which are a pressure chamber and a loading system. The pressure chamber was designed for measuring soil-water characteristic curves. The pressure chamber is stainless steel and can be subjected to extremely high air pressure. The soil specimen is rammed into a stainless steel ring and placed on top of the high air entry ceramic stone. Different high air entry ceramic stones can be inserted into the base of the apparatus and used for different soil types. It is also possible to use a range of ceramic stone on one soil that is tested over a wide range of matric suction (i.e., 1 bar, 3 bars, 5 bars and 15 bars). The apparatus is capable of testing the soil specimen over a wide range of matric suction from 1 kPa to 1000 kPa. At a low soil suction (i.e., from 1 kPa to 10 kPa), a hanging burette can be attached to provide an accurate value of soil suction to the soil specimen. At higher soil suctions (i.e., from 3 kPa to 1000 kPa) the axis-translation technique is used. Dual pressure gauge (i.e., a high pressure gauge and a low pressure gauge) and regulators are designed to accurately control the applied soil suction over the entire range.

The bottom of the pressure chamber (i.e., below the ceramic stone) is connected to two burettes. The amount of water drained out (i.e., drying process) or absorbed into the soil specimen (i.e., wetting process) can be measured using the two burettes. The burettes can be connected to a squeezer that is used to flush diffused air from the bottom of the pressure chamber.

2.2 Materials

The soils used in this study are weathered soil (SW) and clay soil (CH) in Korea. The grain-size distribution curves of weathered soil (SW) are shown in Fig. 2 and the plasticity chart of clay soil (CH) is shown in Fig. 3. The weathered soil had a liquid limit, $LL = 28.7$, plastic limit, $PL = 21.35$, specific gravity, $G_s = 2.683$. The clay soil had a liquid limit, $LL = 63$, plastic limit, $PL = 29.3$, specific gravity, $G_s = 2.604$.

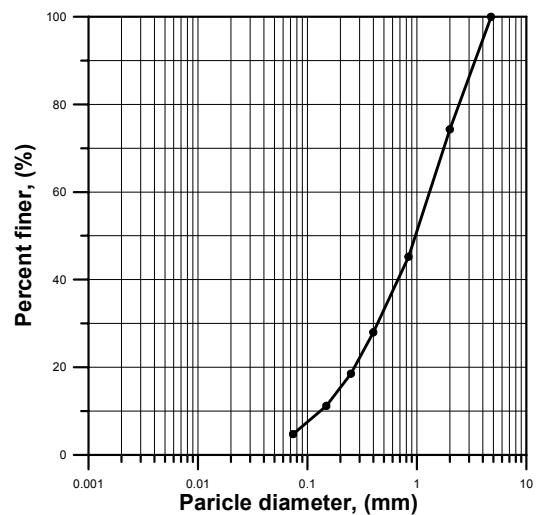


Fig. 2. Grain-size distribution curves (SW)

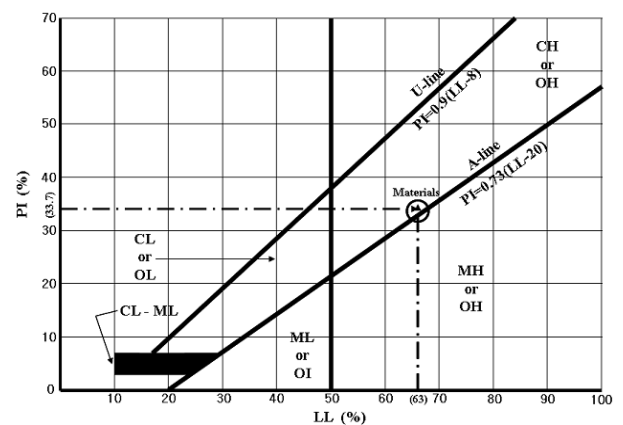


Fig. 3. Plasticity chart (CH)

For measuring soil-water characteristic curves, sample with different clay contents of 0%, 5%, 10%, 15%, and 20% were formed. The soil-water characteristic curve and coefficient of permeability were measured for different densities ($D_r = 70, 90\%$). In case of the 70% densities, all of the clay contents were used and in case of the 90% densities, 3 clay contents (i.e., 10%, 15%, 20%) were used.

2.3 Testing Procedures

A solid stainless steel with diameter of 60 mm and a height of 30 mm was substituted for soil specimen. It was assumed that the solid stainless steel was rigid and did not deform (i.e., a K_0 condition). The amount of water in the burettes was recorded under various soil suctions.

In order to measure the soil-water characteristic curve

of the soil specimens in the GCTS pressure plate, specimens were compacted by the ramming. The following procedures were used to prepare a soil specimen : (1) Calculate the γ_{min} and γ_{max} , (2) Decide the weight of soil by the relative densities of 70% and 90%, (3) Compact the soil mixtures in the solid stainless steel by the ramming (Fig. 4), (4) Submerge (saturate) the soil specimen (Fig. 5).

The saturated soil specimen is placed on a saturated ceramic disk and mounted on the bottom plate. The ceramic disk acts like a semi-permeable medium and allows water, but not air, to pass through the disk up to



Fig. 4. Compaction of the soil mixtures

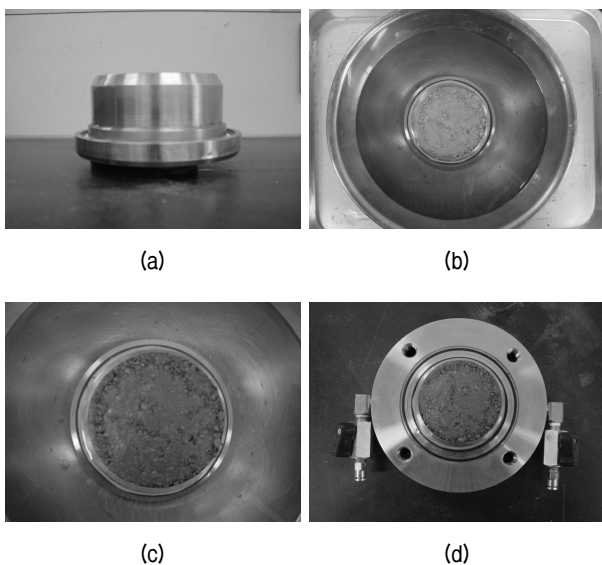


Fig. 5. Preparation of the soil specimen

a rated air pressure value (i.e., air-entry value of the ceramic). The bottom of the ceramic disk is maintained more or less at atmospheric pressure by connecting the drain holes to two tubes filled with water. The applied air pressure represents the applied matric suction. In response to the applied suction the water moves out of the soil specimen and drains through the ceramic disk until the equilibrium is established. The magnitude of the applied matric suction is the same for each soil specimen (i.e., 4, 10, 20, 40, 100, 200 and 400 kPa).

2.4 Discussion on the Test Results for Soil-Water Characteristic Curve

The GCTS pressure plate was used for defining the SWCC for each soil mixtures. The values of a , m and n used in the Fredlund & Xing's SWCC equation (1994) (Eq. 1) are given in Table 1.

$$\theta = C(\psi) \frac{\theta_s}{\ln[e + (\psi/a)^n]^m} \quad (1)$$

where $C(\psi)$ is the correction function, θ is the volumetric water content, θ_s is the saturated volumetric water content, e is the natural number (2.71828), ψ is the negative pore-water pressure (suction), and a , n and m are curve fitting parameters

The results of the soil-water characteristic curve tests are shown Fig. 6. It is difficult to compare the results of the SWCC tests for each soil mixtures, because the saturated volumetric water content at saturation is different according to each soil mixture to compare the results of the SWCC test for each soil mixtures, the volumetric water content was normalized by the initial volumetric water content. As you see the Fig. 6, the volumetric water content decrement was decreased as the fines content of each soil mixture was increased. And the volumetric water content had critical differences between SW100% and other soil mixture (SW95%+CH5%, SW90%+CH10%, SW85%+CH15%, SW80%+CH20%). However, there were no notable distinctions on soils that were mixed with some fines.

Table 1. Curve-fitting parameters for the SWCC

	$D_r=70\%$					$D_r=90\%$		
	SW100	SW95	SW90	SW85	SW80	SW90	SW85	SW80
a	4.811	8.819	5.452	7.827	8.368	9.283	8.164	9.477
n	2.536	8.637	1.690	1.305	1.849	2.515	2.366	1.51
m	0.637	0.151	0.27	0.302	0.221	0.294	0.226	0.217

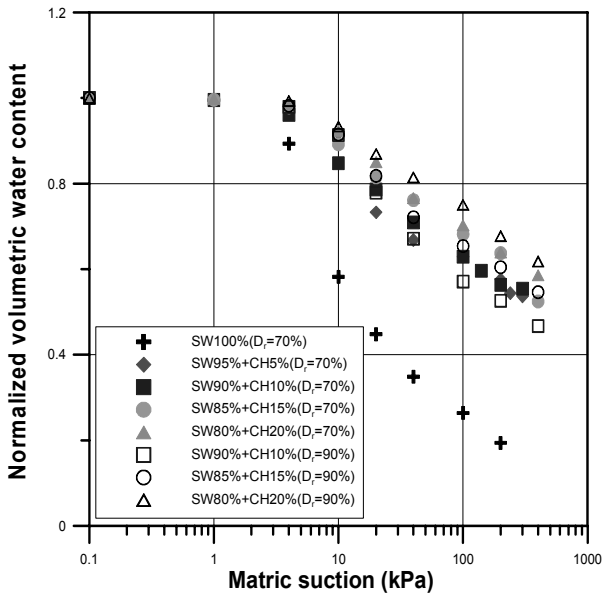


Fig. 6. Test results of the SWCC

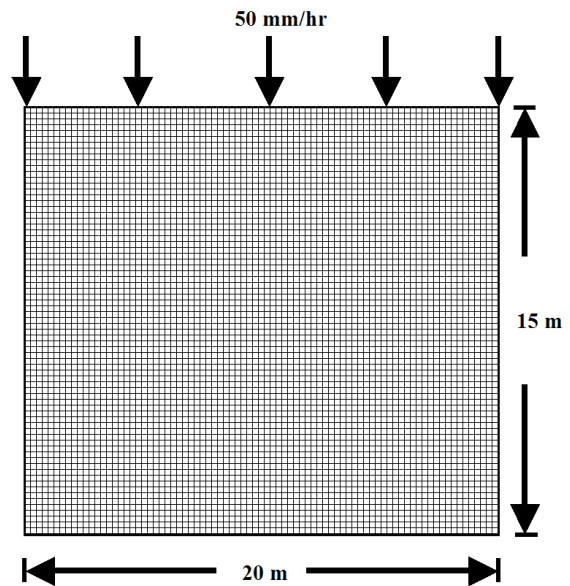


Fig. 7. Finite element mesh (seepage analysis)

3. Transient Finite Element Seepage and Theoretical Analysis

Transient seepage analyses of rainfall infiltration were carried out by means of the two-dimensional finite element program SEEP/W (Geo-Slope, 2004). The finite element mesh used in these analyses is shown in Fig. 7. The groundwater table is located at the bedrock-weathered soil interface. The top boundary is subjected to a rainfall intensity that is equal to the saturated permeability of the weathered soil to ensure downward infiltration into the weathered soil layer. Actually measuring the hydraulic conductivity function is a time-consuming and expansive procedure, but the function which was used by SEEP/W can be readily developed using measured volumetric water

content function (i.e., SWCC) and the saturated hydraulic conductivity (Table 2). The results of hydraulic conductivity which were used in seepage analysis are shown in Fig. 8.

The total duration of rainfall is 96 hours. It was divided into 11 time stages (0.1, 0.5, 1, 2, 3, 5, 10, 24, 48, 72 and 96 hours) and wetting band depth was obtained for each of these stages. For simplicity, the intensity of rainfall was kept constant for the entire duration of rainfall. Similarly, the wetting band depth from a transient seepage analysis is calculated as the normal distance from the surface of the mesh at which a contour of -0.2 m pressure head is located. The contour for -0.2 m pressure head is chosen based on the observation from slope stability analysis that normal distance between the critical

Table 2. Coefficient of permeability at saturation (m/s)

	$D_r=70\%$					$D_r=90\%$		
	SW100	SW95	SW90	SW85	SW80	SW90	SW85	SW80
K_{sat} (m/s)	$5.05 \times E-6$	$1.13 \times E-6$	$7.84 \times E-7$	$5.87 \times E-7$	$2.58 \times E-7$	$2.94 \times E-7$	$7.84 \times E-8$	$3.45 \times E-8$

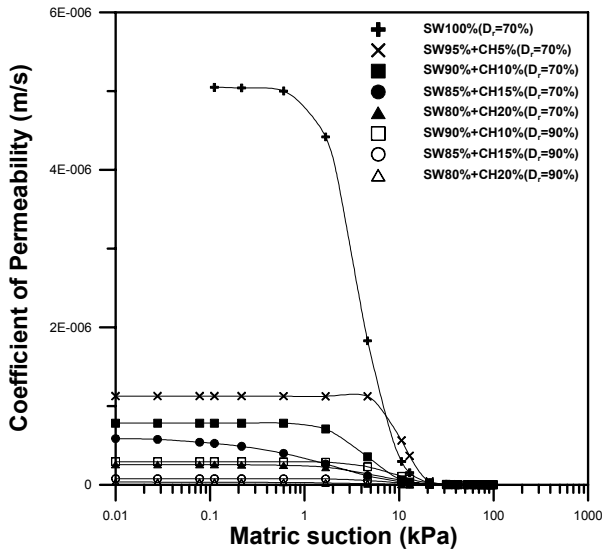


Fig. 8. K vs. matric suction

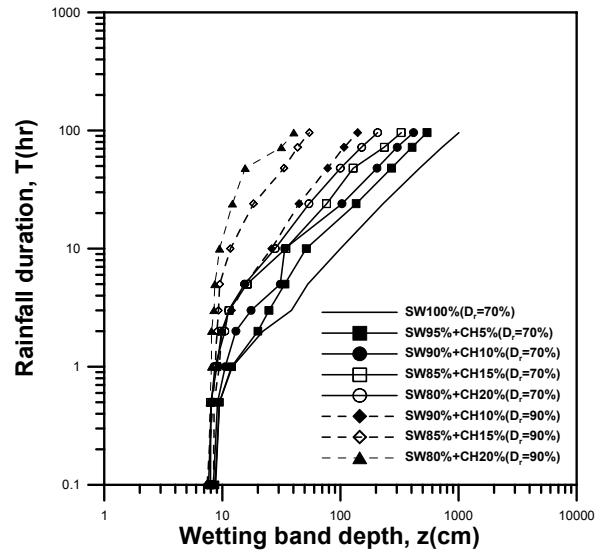


Fig. 9. Wetting band depth vs. rainfall duration

failure plane and the surface of the slope was always equal to normal distance between this contour and the surface of the slope (Kim et al., 2006).

It is shown that increase of the fines content affects the decrease of the infiltration rate for all soil mixtures (Fig. 9). And the increasing rate of wetting band depth was decreased as the fines contents in the mixtures and the relative densities were increased. These results come from the decrease of coefficient of permeability and the increase of the soil suction (Fig. 8).

4. An Internal Friction Angle Associated with Matric Suction(ϕ^b)

Generally, an internal friction angle associated with matric suction which is called the ϕ^b is obtained by the unsaturated soil triaxial test. However, establishing the triaxial test on unsaturated soils needs lots of time and has some difficulties in operation. For an alternative solution, it has been investigated in different ways in order to define ϕ^b . Fortunately, Vanapalli et al. (1996) already defined the relationship between internal friction angle

and internal friction angle of unsaturated soils (i.e., ϕ^b). For the friction angle of unsaturated soils, Eq. 2 (Vanapalli et al., 1996) in this study is used.

$$\tan(\phi^b) = \tan(\phi') \left(\frac{\theta - \theta_r}{\theta_s - \theta_r} \right) \quad (2)$$

where ϕ' is the angle of internal friction, θ is the volumetric water content, θ_r is the residual volumetric water content (Table 3), θ_s is the saturated volumetric water content and ϕ^b is the angle indicating the rate of increase in shear strength to the matric suction.

Because the volumetric water content was decreased as the matric suction was increased, the internal frictional angle associated with matric suction was decreased as the matric suction was increased (Fig. 10).

5. Numerical Analysis of the Stability of Unsaturated Soil Slopes

In order to evaluate the effect of wetting band depth and magnitude of the matric suction on the stability of

Table 3. The residual volumetric water content

	$D_r=70\%$					$D_r=90\%$		
	SW100	SW95	SW90	SW85	SW80	SW90	SW85	SW80
θ_r	0.038	0.034	0.017	0.026	0.035	0.017	0.026	0.035

Note : θ_r is the value observed by the filter paper method (Yu, 2003)

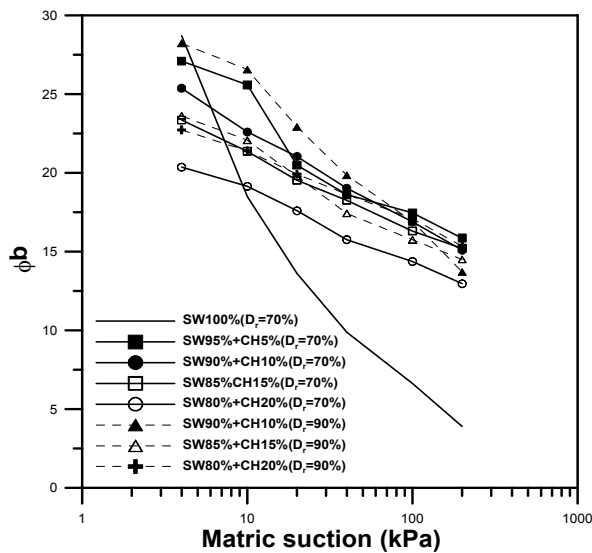


Fig. 10. ϕ^b vs. matric suction

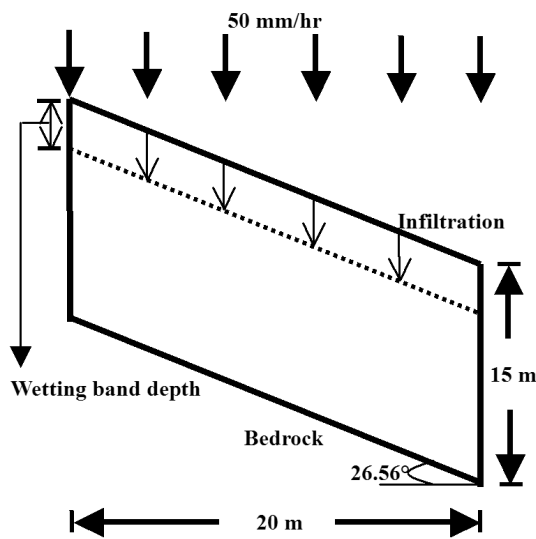


Fig. 11. Finite element mesh (SLOPE/W)

slopes in unsaturated soils, three sets of analysis were conducted using the limit equilibrium based on SLOPE/W program (GEO-SLOPE, 2004). Three infinite slopes –

inclined at 26° , 33° , 45° – were considered, and strength parameter, such as ϕ' , ϕ^b and c' of each mixed soil was fixed as properties of each mixed soil to identify the relation to the only wetting band depth due to rainfall in a slope (Fig. 11). The stability of unsaturated soil slope is analyzed with assumption that the bottom part of infinite slope would be bedrock and the finite element mesh(SLOPE/W) used in this study is shown in Figure 11.

The physical properties of soil mixtures are shown in Table 4. It is shown that the internal frictional angle was decreased as the fines content was increased. But the internal frictional angle was increased as the relative density was increased.

Figure 12 and Figure 13 show the analyzing results of the unsaturated soil slope stability. X-axis means the amount of matric suction with varying volumetric water content when measuring SWCC. If the factor of safety was only affected by the magnitude of wetting band depth, it must increase as the fines content was increased in soil mixtures. However, the factor of the safety decreased by a certain point – slope containing 20% fines content inclined to 26° and 33° hardened 70% relative density came to have 15% fines content inclined to 45° and hardened 70% relative density (Fig. 12), and any slope contained 15% fines content and hardened 90% relative density (Fig. 13). This means that the effect of the wetting band depth on slope stability is somewhat limited to fine content in soil mixtures. That is, the factor of safety is affected by the wetting band depth rather than the variation of strength parameters as the fines content increase, especially the fines content increases as much as 10~15% approximately.

Table 4. Physical properties of soil mixtures

Soil Mixtures	γ_d (kN/m ³)	γ_{sat} (kN/m ³)	c' (kN/m ²)	ϕ' (°)
SW100% ($D_r=70\%$)	11.976	15.889	0	31.84
SW95% ($D_r=70\%$)	12.877	16.482	12.847	27.75
SW90% ($D_r=70\%$)	13.22	16.836	22.948	26.32
SW85% ($D_r=70\%$)	13.436	17.444	26.086	23.85
SW80% ($D_r=70\%$)	13.524	17.655	28.635	20.75
SW90% ($D_r=90\%$)	13.507	17.367	14.21	28.78
SW85% ($D_r=90\%$)	13.782	17.867	16.856	24.03
SW80% ($D_r=90\%$)	14.148	18.202	25.284	22.89

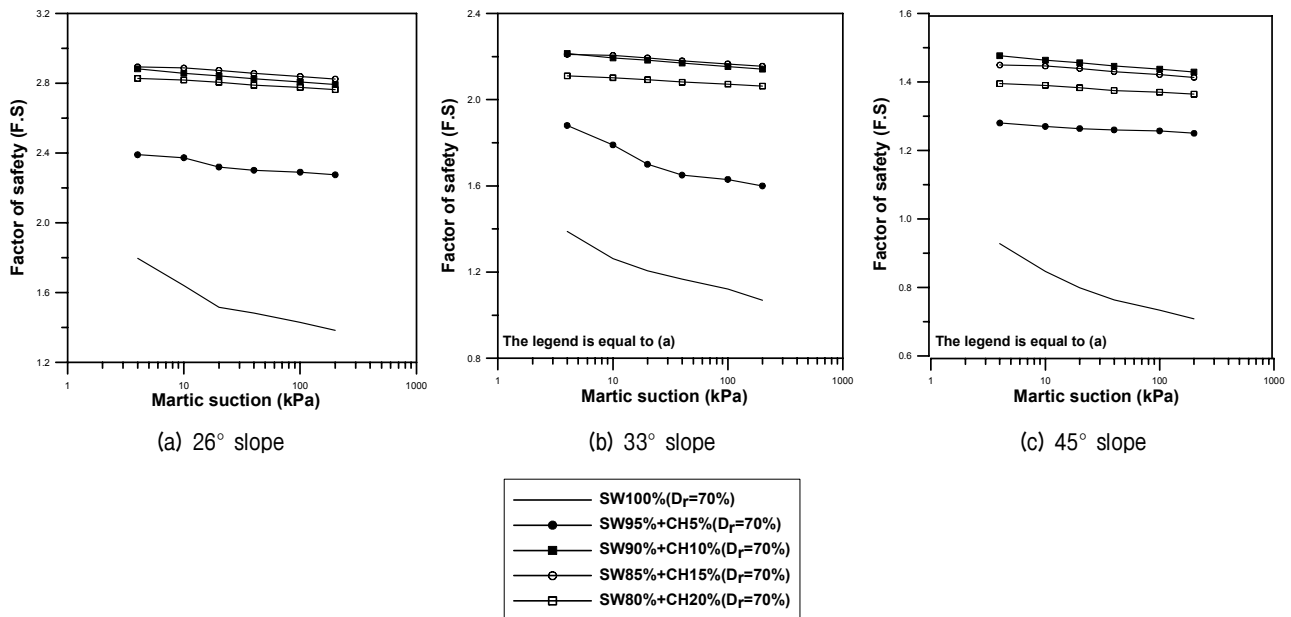


Fig. 12. Factor of safety concerning soil mixtures ($D_r=70\%$)

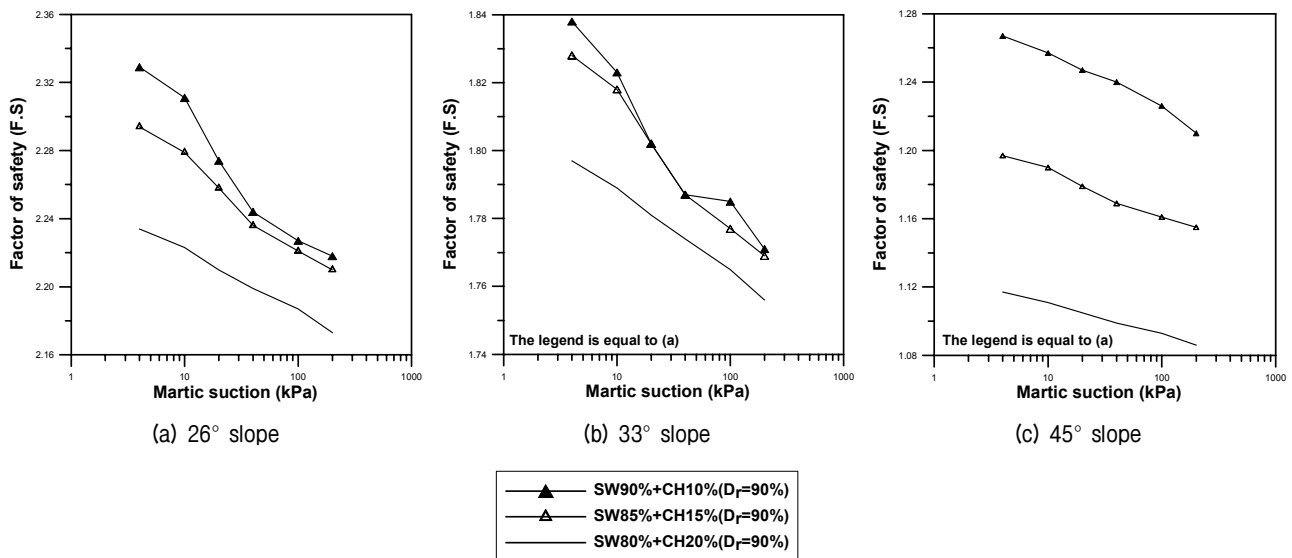


Fig. 13. Factor of safety concerning soil mixtures ($D_r=90\%$)

Besides this range, it is affected by the variation of the strength parameters as the fines content increases.

6. Conclusion

- (1) The volumetric water content decrement was decreased as the fines content of the each soil mixtures and the relative densities were increased. And the volumetric water content had critical distinction between SW100% and other soil mixtures (SW95%+CH5%, SW90%+CH10%, SW85%+CH15%, SW80%+CH20%).
- (2) The increasing rate of the wetting band depth was decreased as the fines contents in the mixtures and the relative densities were increased. These results come from the decrease of the coefficient of permeability and the increase of the soil suction.
- (3) According to the stability analysis result of the unsaturated soil slopes through the SLOPE/W, it is found that the transition from the wetting band depth to the variation of strength parameters which affect the stability of unsaturated soil slopes appears to occur around 10~15% of clay contents in the mixtures.

References

1. Collins, B.D., Znidarcic, D.Z. (2004), "Stability analyses of rainfall induced landslides", *Journal of Geotechnical and Environmental Eng.*, Vol.130, No.4, pp.362-372.
2. Fourie, A.B., Rowe, D. and Blight, G.E. (1999), "The effect of infiltration on the stability of the slope of a dry ash dump", *Geotechnique*, Vol.49, No.1, pp.1-13.
3. Fredlund, D.G. and Rahardjo, H. (1993), *Soil mechanics for unsaturated soils*, John Wiley and Sons, New York, pp.217-259.
4. Fredlund, D.G., Xing, A. and Huang, A. (1994), "Predicting the permeability function for unsaturated soils using the soil-water characteristic curve", *Canadian Geotechnical Journal*, Vol.31, pp.533-546.
5. Fredlund, D.G. and Xing, A. (1994), "Equation for the soil-water characteristic curve", *Canadian Geotechnical Journal*, Vol.31, pp.521-532.
6. Geo-slope. (2004), *User manual for SEEP/W and SLOPE/W. version 6*, Canada, Geo-Slope International Ltd.
7. Kim, J. (2002), *Stability analysis on unsaturated weathered infinite slopes based on rainfall-induced wetting*, Master of Eng. Thesis, Yonsei University.
8. Kim, J., Jeong, S., Park, S. and Sharma, J. (2004), "Influence of rainfall-induced wetting on the stability of slopes in weathered soils", *Engineering Geology*, Vol.75, pp.251-262.
9. Kim, J., Park, S. and Jeong, S. (2006), "Effect of wetting front suction loss on stability of unsaturated soil slopes", *Proceedings of Sessions of Geoshanghai*, Geotechnical special publication No. 148, pp.70-77.
10. Lee, S.J., Lee, S.R. and Jang, B. (2002), "Unsaturated shear strength characteristics of weathered granite soils", *The Journal of Korean Society of Civil Engineers*, Vol.22, No.1, pp.81-88.
11. Lu, N., Likos, W. (2004), *Unsaturated soil mechanics*, John Wiley and Sons, New York, pp.220-241.
12. Ng, C.W.W., Shi, Q. (1998), "A numerical investigation of the stability of unsaturated soil slopes subjected to transient seepage", *Computer and Geotechnics*, Vol.22, No.1, pp.1-28.
13. Ng, C.W.W., Zhan, L.T., Bao, C.G., Fredlund, D.G. and Gong, B.W. (2003), "Performance of an unsaturated expansive soil slope subjected to artificial rainfall infiltration", *Geotechnique*, Vol.53, No.2, pp.143-157.
14. Padilla, J.M., Perera, Y.Y., Houston, W.N. and Fredlund, D.G., "A new soil-water characteristic curve device".
15. Pham, H.Q., Fredlund, D.G. and Padilla, J.M., "Use of the GCTS apparatus for the measurement of soil-water characteristic curves".
16. Vanapalli, S.K., Fredlund, D.G., Pufahl, D.E. and Clifton, A.W. (1996), "Model for the prediction of shear strength with respect to soil suction", *Canadian Geotechnical Journal*, Vol.33, pp.379-392.
17. Yu, N. (2003), *Characteristics of unsaturated weathered soils with varying clay contents*, Master of Eng. Thesis, Yonsei University.

(received on Jan. 17, 2007, accepted on Mar. 20, 2007)

Reliability Analysis of Seismically Induced Slope Deformations

신뢰성 기법을 이용한 지진으로 인한 사면 변위해석

Kim, Jin-Man¹

김진만

요 지

지진하중의 불확실성을 평가할 수 있는 신뢰성기반 해석기법을 제시한다. 이 기법은 종래의 한계평형법과 뉴마크형식의 변형량 계산기법에 확률개념을 도입하였으며 피해 위험성을 몬테카를로 시뮬레이션 해석기법으로 계산한다. 지진파를 작성하고 이들을 사면 내진 해석에 사용하고자 확률변수 프로세스와 RMS 재해 기법을 도입하였다. 지반성질의 변동성과 통계오차도 고려하였다. 신뢰성 해석 결과 지진활동이 활발한 지역에서는, 계산된 사면파괴 위험성과 과도한 영구변형의 관점에서 비교할 때 지진재해 평가가 더 중요한 사항이며, 재료성질의 묘사방법의 차이는 상대적으로 영향이 적다는 사실이 밝혀졌다. 이 결과는 원형 및 비원형 형태의 활동면 파괴에 모두 해당된다.

Abstract

The paper presents a reliability-based method that can capture the impact of uncertainty of seismic loadings. The proposed method incorporates probabilistic concepts into the classical limit equilibrium and the Newmark-type deformation techniques. The risk of damage is then computed by Monte Carlo simulation. Random process and RMS hazard method are introduced to produce seismic motions and also to use them in the seismic slope analyses. The geotechnical variability and sampling errors are also considered. The results of reliability analyses indicate that in a highly seismically active region, characterization of earthquake hazard is the more critical factor, and characterization of soil properties has a relatively small effect on the computed risk of slope failure and excessive slope deformations. The results can be applicable to both circular and non-circular slip surface failure modes.

Keywords : Artificial motion, Monte carlo simulation, Random process, Reliability, Seismic slope stability

1. Introduction

An important step in the slope stability analysis is to identify uncertainties of key design parameter and their statistics. The variability of the various parameters such as material properties, fluctuations of the loads, and the uncertainties of the geometry all contribute to the difficulty of evaluating how the slope actually behaves regardless of the computed factor of safety. In spite of extensive effort, there has not been much consensus on how to

model these uncertainties systematically, leaving them mostly up to the rather subjective judgments of individual engineers. In the past, there have been numerous studies of the various sources of uncertainty and their impact on the risk of damage of slopes subjected to seismic loading. Most approaches, however, have focused either on material uncertainty or on uncertainty of seismic loading (e.g., Pal et al. 1991; Yegian et al. 1991) partly because of computational convenience, and partly due to the practical difficulty in modeling both material and seismic

¹ Member, Assistant Prof., Dept. of Civil Engrg., Pusan National Univ., jmkim@pusan.ac.kr

hazard uncertainties.

Kim (2003) reported the importance of geotechnical variability in the analysis of earthquake-induced slope deformations. This paper reports follow-up analytical and numerical studies that investigated the influence of inherent variability and uncertainty of seismic loading in the analysis of seismic slope stability. Kim (2003) described some of the findings from that study and this paper reports all the remaining findings in details. In this paper, the author presents a reliability-based method that can capture the impact of uncertainty of key material properties and seismic loading in the assessment of seismic slope stability. The uncertainty of seismic loading is approached by generating a large series of hazard-compatible artificial motions, and by using them in subsequent response analyses. The geotechnical variability and sampling errors are also taken into consideration. This approach incorporates probabilistic concepts into the classical limit equilibrium and the Newmark-type deformation techniques. The authors adopt the so-called decoupled approach, where seismic response and deformation analyses are carried out separately, mainly because of its computational efficiency. The risk of damage is then computed by Monte Carlo simulation. Finally, the overall impact of uncertainties and their relative significance on seismic stability of slopes will be judged.

2. Generation of Hazard-Compatible Ground Motions

Due to the random nature of earthquake motions, the definition of the input excitation is one of the major uncertainties in the seismic response analysis. The stochastic representation of the earthquake motion hazard provides, at least theoretically, a systematic way of representing the infinite number of possible scenarios, which correspond to a certain level of hazard.

A series of sinusoids can be used to express a periodic function. With a zero-mean process, it can be represented as:

$$X(t) = \sum_{i=1}^n A_i \sin(\omega_i t + \theta_i) \quad (1)$$

where A_i is the Fourier amplitude, ω_i is the circular frequency, and θ_i is the phase angle of the i^{th} contributing sinusoid. By fixing an array of amplitudes and randomly generating different arrays of phase angles, we can produce different motions with the same general appearance but different details (Gasparini and Vanmarcke 1976). For a stationary random process, the Fourier amplitude A_i is related to the (one-sided) power spectral density function (PSD) $G(\omega)$ as:

$$\frac{1}{2} A_i^2 = G(\omega_i) \Delta\omega \quad (2)$$

The study adopts the following widely quoted form for the power spectral density function (PSD) that is based on Kanai (1957) and Tajimi (1960)'s studies.

$$G(\omega) = G_0 \frac{1 + 4\zeta_g^2 (\omega / \omega_g)^2}{[1 - (\omega / \omega_g)^2]^2 + 4\zeta_g^2 (\omega / \omega_g)^2} \quad (3)$$

where $G(\omega)$ is the energy content at frequency ω , G_0 is some measure of shaking intensity, and ζ_g and ω_g are the parameters termed as "ground damping coefficient and frequency". Each different array of phase angles can be modeled by statistically independent random phase angles θ_i , which are uniformly distributed between 0 and 2π . Equation 1 then becomes (Rice 1954):

$$X(t) = \sum_{i=1}^n \sqrt{2G(\omega_i) \Delta\omega} \sin(\omega_i t + \theta_i) \quad (4)$$

As the number n of sinusoidal motions becomes large, the distribution of the process $X(t)$ approaches Gaussian distribution by virtue of the central limit theorem, as long as A_i is of similar magnitude (Yang 1973). Sample stationary earthquake motion (based on Equation 4) can then be obtained as shown in Figure 1.

The transient character of the intensity content of the earthquake motion can be added by multiplying the stationary motion by a deterministic modulating (envelope) function $m(t)$. The non-stationary motion $Y(t)$ then becomes

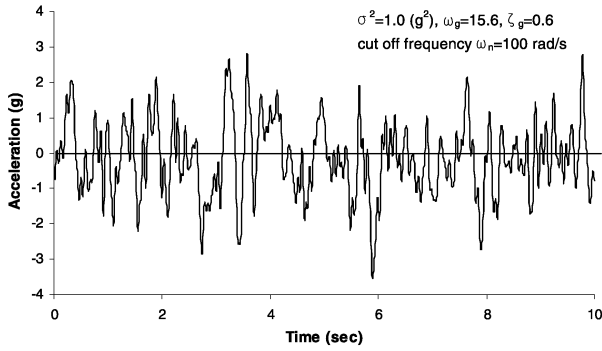


Fig. 1. Sample Stationary Artificial Earthquake Ground Motion for Rock Sites Based on the Frequency Parameters for Firm Soil Proposed by Kanai (1957)

$$Y(t) = m(t)X(t) = m(t) \sum_{j=1}^n \sqrt{2G(\omega_j)\Delta\omega} \sin(\omega_j t + \theta_j) \quad (5)$$

Various modulating functions have been used to incorporate non-stationary aspect of the earthquake ground motions. The most common forms of the modulating function are “Rectangular”, “Exponential”, “Trapezoidal”, and their combination imitates initial build-up followed by a strong-motion part and then a die-down segment of typical recorded ground motions. In their liquefaction-related analytical approaches, Wang and Kavazanjian (1987) proposed a trigonometric modulating function that has two model parameters to define the shape of the modulating function as:

$$m(t) = \sin^\alpha \left(\pi (t/t_d)^\beta \right) \quad (6)$$

where α and β are two parameters to determine the shape of the modulating function and t_d is the duration of motion.

The function is in a normalized form for both intensity and duration such as:

$$0 \leq m(t) \leq 1 \quad \text{and} \quad 0 \leq t/t_d \leq 1 \quad (7)$$

Unlike the conventional models, this model provides a convenient way in developing the statistics of shape parameters since it is in a normalized form and can thus be used independent of the intensity and the duration of the ground motion. For this reason, the model is adopted in our study. Wang and Kavazanjian (1987) also developed the statistics of the model parameters α and β based on their study of 122 Northern California strong ground

motions.

The normalized PSD is obtained by dividing the PSD by the variance as:

$$G^*(\omega) = \frac{1}{\sigma^2} G(\omega) \quad (8)$$

When the stationary process $X^*(t)$ is a normalized process with unit variance and PSD function $G^*(\omega)$, Equation 5 (non-stationary ground motion) can be rewritten in terms of the normalized PSD function and modulating function $m(t)$ as:

$$Y(t) = m(t)X^*(t) = m(t) \sum_{i=1}^n \sqrt{2G^*(\omega_i)\Delta\omega} \sin(\omega_i t + \theta_i) \quad (9)$$

2.1 Intensity

Traditionally, most seismic hazard analyses use either maximum values of ground motion or a response spectrum to characterize the intensity of ground shaking (e.g., Housner 1952, Idriss 1991, Abrahamson and Silva 1996, 1997). However, using a maximum value to characterize the intensity of shaking is often inadequate, especially when dealing with structures whose response depends on total seismic energy rather than peak values of ground shaking. One of the energy-based parameters is the RMS (Root Mean Square) acceleration, which is defined as (Housner 1975):

$$RMS_a = \left[\frac{1}{T_d} \int_{t_0}^{t_0+T_d} a^2(\tau) d\tau \right]^{1/2} \quad (10)$$

where $a(t)$ is an acceleration time history, t_0 is a initial time of interest, T_d is duration of the strong ground shaking. Similarly, temporal RMS can be defined by replacing T_d with a small time interval Δt as:

$$RMS_a(t) = \left[\frac{1}{\Delta t} \int_t^{t+\Delta t} a^2(\tau) d\tau \right]^{1/2} \quad \text{for } \Delta t \rightarrow 0 \quad (11)$$

It is fairly straightforward to relate time-variant RMS to the deterministic modulating function $m(t)$ for the case

when $X^*(t)$ is a normalized process as follows:

$$RMS_Y^2(t) = E[Y^2(t)] = m^2(t)E[X^{*2}(t)] = m^2(t) \quad (12)$$

The time-variant *RMS* of the motion $Y(t)$ is thus identical to the modulating function $m(t)$ in case of the normalized process.

2.2 Frequency Content

There are different methods for characterizing the temporal variation of the spectral content of earthquake motion. A simple, yet efficient, approach is to divide the ground motion into several sections small enough so that stationarity of the frequency content within each section can be assumed without much error (Saragoni and Hart 1974). The proposal by Saragoni and Hart (1974) is based on dividing the motion into three sections of equal time interval as:

$$Y(t) = m(t) \sum_{j=1}^3 (X_j^*(t_j))$$

$$= m(t) \sum_{j=1}^3 \left[\sum_{i=1}^n \sqrt{2G_j^*(\omega_i)} \Delta\omega \sin(\omega_i t_j + \theta_i) \right], \quad t = \sum_{j=1}^3 t_j \quad (13)$$

Once the number of sections is determined, the frequency and damping parameters of Kanai-Tajimi PSD need to be estimated for each section. Based on the approach by Saragoni and Hart (1974), Wang and Kavazanjian (1987) analyzed 80 out of the same set of 122 earthquake records, which were used to estimate the modulating function parameters, and proposed the statistics (i.e., mean and

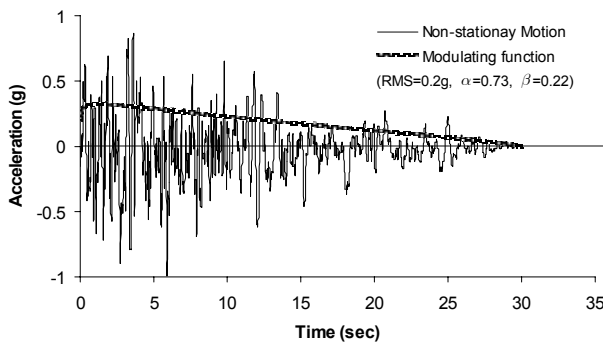


Fig. 2. Sample Time History of Non-Stationary Ground Motion ($RMS=0.2$ g, $\alpha=0.73$, $\beta=0.22$, $t_d=30$ sec)

standard deviation) of the parameter ω_g and ζ_g . Tung et al. (1992) updated the statistics of modulating and PSD function parameters by including an additional set of 36 earthquake records from the 1989 Loma Prieta earthquake. These values are used in our analyses. Figure 2 shows a sample of non-stationary ground motion based on these statistics.

2.3 Duration

There are different definitions of duration including bracketed duration (Bolt 1969) and Arias duration (Trifunac and Brady 1975). 5-95% Arias duration (often called significant duration) is adapted in this study because it provides clear relationship to RMS hazard. The significant duration is nothing but the duration of the 5-95% RMS acceleration. Predictive relationships that relate the mean of 5-95% Arias duration with respect to the distance and moment magnitude (Abrahamson and Silva 1996) are used in this study.

3. Limit State Function and Monte Carlo Simulation

The performance of a structure can be described by a limit state function $g(\mathbf{x})$ such that failure is defined whenever the condition of $g(\mathbf{x}) \leq 0$ is satisfied, where \mathbf{x} is the vector of model variables. The probability of failure is then given by:

$$p_f = P(g(\mathbf{x}) \leq 0) = \int_{g(\mathbf{x}) \leq 0} f(\mathbf{x}) d\mathbf{x} \quad (14)$$

where $f(\mathbf{x})$ is the joint probability density function (PDF) of \mathbf{x} . For deformation-based slope stability under static or seismic loadings, the limit state function can be formulated as:

$$g(\mathbf{x}) = D_a(\mathbf{x}) - D_p(\mathbf{x}) \quad (15)$$

where $D_a(\mathbf{x})$ and $D_p(\mathbf{x})$ denote the allowable and incurred deformations respectively. Particularly, the deformation-based limit-state function of a slope subject to seismic loadings can be obtained through ground response and slope

deformation analyses as shown in Figure 3.

Once the limit state function $g(\mathbf{x})$ and the distribution $f(\mathbf{x})$ are selected, the probability of failure p_f can be estimated by computing the volume of the joint distribution $f(\mathbf{x})$ within the failure domain defined by $g(\mathbf{x}) \leq 0$.

Classic Monte Carlo simulation involves the computation of deterministic solutions for a sufficient number of systematically generated realizations out of all possible scenarios. The resulting set of solutions is statistically analyzed to estimate means, variances, other higher moments, and possibly probability density functions. Recent advances in implementing methodologies, software, fast computing environments, and the use of optimization techniques (e.g., Rubinstein 1986) have made the Monte Carlo simulation one of the widely used practical tools in probabilistic analyses.

The numerical implementation and data flow of the proposed approach are illustrated in Figure 3. The author uses the so-called decoupled approach, in which seismic response and deformation analyses are carried out separately, mainly because of its computational efficiency. The analogy of a block resting on an inclined plane (so-called Newmark's method, Newmark 1965) is used for estimating the permanent displacement of the sliding mass due to earthquake shaking. The computation of yield acceleration is performed with newly developed expressions (Kim and Sitar 2004), which enable the calculation of the yield acceleration directly without iterations.

Probability computations (Equations 14) were carried out with the aid of CALREL, a general-purpose structural

reliability analysis program developed by Liu et al. (1989). The program requires the definition of limit-state functions through user-defined subroutines. These user subroutines are written by the author in such a way that once statistics of seismic hazard, soil properties and geometry of the problem are provided, the program performs all sequential computations from the motion generation to deformation estimation without any interruption.

4. Illustrative Examples

The applicability of developed reliability-based methods is examined, starting from the analysis of seismically induced deformations of an idealized waste fill and ending with comparing the results with those of the seismic stability assessment of a homogeneous slope with a circular slip surface. Various levels of available information are examined in terms of their impact on the computed risk of slope failure.

4.1 Landfill (Non-Circular) Slope Stability

The author considers a problem where we are interested in evaluating the risk of failure of a solid-waste landfill slope along a gently sloping potential slip surface as shown in Figure 4. The geometry of the example landfill slope is very close to that of one of the failed landfill sections at Kettleman Landfill, reported by several researchers (e.g., Seed et al. 1990) and also similar to the damaged slope of Chiquita Canyon Landfills (e.g., Augello et al. 1995).

The key design parameters for both deterministic and probabilistic assessments of the landfill slope stability are given in Table 1. Sliding is assumed to occur only along the liner system underlying the waste-fill, since the foundation soil and waste-fill are judged to be much

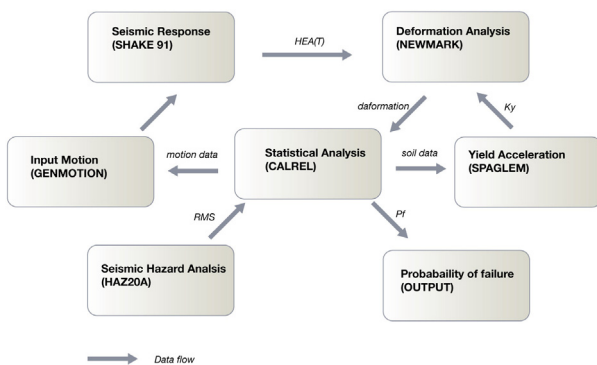


Fig. 3. Numerical Implementation and Data Flow of Probabilistic Seismic Slope Deformation Analysis

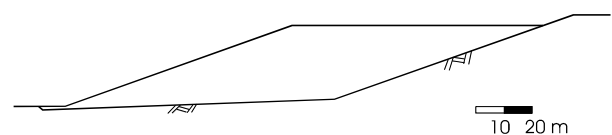


Fig. 4. Geometry of the Landfill Lying on the Gently Sloping Potential Slip Surface

Table 1. Key design material parameters

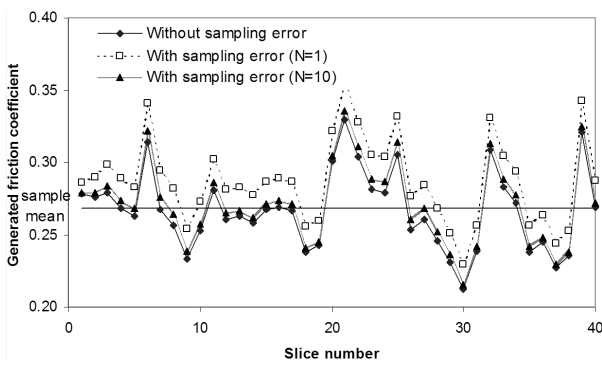
Parameter	Distribution	Mean	c.o.v.	No. of Tests	δ_x	δ_y
$\tan(\phi')$	lognormal	0.268	0.14	10	3 m	3 m
γ	deterministic	12 kN/m ³		10		

stronger than the liner interface (i.e., Kim et al. 2005). Accordingly, only the shear-strength properties of the liner interface, and the average density of the waste-fill deposit and soil cover overlying the lining system need to be considered. Expressions for characterization of material properties developed to incorporate sampling errors, spatial variation that were described in details by Kim (2003) are used, but are not repeatedly described here. The potential sliding mass is divided into 40 slices and Spencer method of analysis (as a subroutine of CALREL) is used

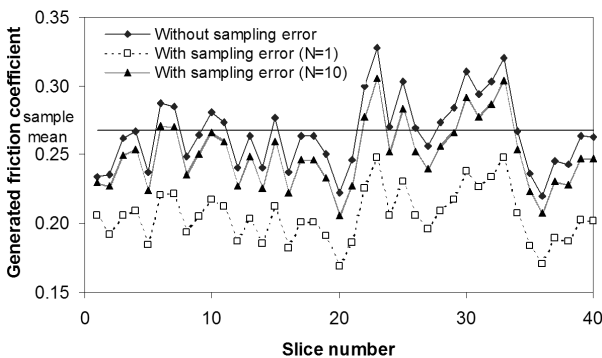
to evaluate the limiting equilibrium. Figure 5 shows two different samples of generated friction coefficients over the 40 slices of the slip surface. It is worthy to note that sampling errors have the effect of shifting the trends of the generated soil properties from the sample mean.

For the purpose of this seismic analysis, the landfill slope is assumed to be in Berkeley, California, in the seismically active San Francisco Bay Area. The major faults affecting the region are the San Andreas, Hayward, and Calaveras faults, all within 30 kilometers of the site. Based on the regional seismicity, seismic hazard analyses, using the empirical RMS attenuation relationship (Kavazanjian et al. 1985), are performed. All the major and minor faults in the vicinity of the site including background sources are considered. The computed RMS hazards are then de-aggregated into several intervals of intensity, magnitude, and distance. In order to generate RMS-compatible ground motion, we need to specify the frequency content and duration in addition to the RMS acceleration. The author adopts the stochastic ground motion parameters suggested by Wang and Kavazanjian (1987) and updated by Tung et al. (1992). Tables 2 and 3 summarize stochastic ground motion parameters used in this study. The frequency content of the ground motion is modeled by dividing the motion into three sections of equal time interval within which stationarity of the frequency content is assumed.

Another strong ground motion parameter, which is important in nonlinear deformation analyses, is duration. The hazard compatible duration can be assigned to each generated ground motion by means of de-aggregation of total hazard into appropriate intervals of earthquake magnitude and distance to site. Kim(2003) reported the



(a) with Trend Higher than the Sample Mean



(b) with Trend Lower than Sample Mean; N: Number of Samples

Fig. 5. Samples of Generated Friction Coefficients over the 40 Slices of the Slip Surface

Table 2. Power spectral density parameters for rock sites (from Tung et al. 1992)

Parameter	Distribution	Segment 1		Segment 2		Segment 3	
		μ	σ	μ	σ	μ	σ
ω_g	Gamma	23.57	3.46	21.12	3.60	18.38	3.50
ζ_g	Gamma	0.352	0.360	0.394	0.380	0.417	0.162

Table 3. Parameters for modulating function (from Wang and Kavazanjian 1987)

Parameter	Distribution	μ	σ
α	Rayleigh	0.73	0.45
β	Exponential	0.22	0.18

significant duration, which is estimated using the empirical relationship proposed by Abrahamson and Silva (1996).

Figure 6 shows the geometry of the problem and the dynamic soil properties, used in the 1-D ground response analyses of the landfill slope, in which the 2-D geometry is approximated by 1-D problem. Modulus reduction and damping curves proposed by Singh and Murphy (1990), and by Schnabel (1973) are used for the waste and base rock respectively. Although shear wave velocity of the solid waste is known to increase with depth, uniform shear wave velocity is assumed so as to be consistent with the assumed homogeneous site condition. The horizontal equivalent acceleration (*HEA*) time history (or the average seismic coefficient k_{ave}) acting on the sliding mass on slope is estimated through seismic response analyses. The procedure needs the shear stress time history $\tau_i(t)$, as described by Bray and Rathje (1998). The shear stress time history at the base of potential sliding mass is evaluated with 1-D wave analyses by using SHAKE91

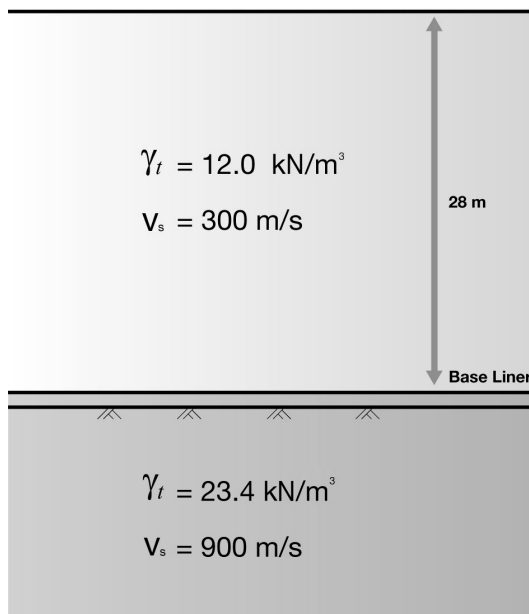


Fig. 6. Geometry of the 1-D Approximation of the Landfill and Dynamic Soil Properties

(Idriss and Sun 1992). Unlike the deformation analyses, the ground response analyses are performed by assuming that the key soil properties are deterministic, hence using mean values of the properties. This approach is adopted, since we employ the decoupled approach, in which ground response and slope deformation analyses are performed separately, by using separate numerical programs (otherwise, in a strict sense, correlations between input parameters of ground response and deformation analyses should be considered). Ideally, the ground response and deformation analyses are performed in so-called coupled mode, thus eliminating the need to provide separate sets of input parameters, as in the case of the decoupled analyses. On the other hand, the coupled analyses such as dynamic FEM are generally time-consuming, and cannot be used routinely, even in the current fast computing environment. This is even more so in inherently time-consuming probabilistic analyses, which generally involve a significant number of repeated analyses of the problem.

The slope is assumed to be able to tolerate up to 300 mm of permanent base displacement. Presently, no standard for acceptable permanent deformation has been established, but in practice it is generally assumed that maximum seismic displacements of 15-30 cm are tolerable for well-designed lined waste fills (i.e., Seed and Bonaparte 1992).

Simulation-based (Monte Carlo) reliability analyses are performed by generating a series of hazard compatible outcrop rock motions, and by using them in subsequent 1-D ground response and slope deformation analyses. The computations are carried out both for the case, where spatial variation is only considered, and the case, where uncertainty arising from sampling is also considered, in order to compare their relative significance on the risk of failure. The results are shown in Figure 7. The seismic hazards (Figure 7a) are the same for the four cases. The difference is the level of uncertainty in soil property determination. The deterministic soil properties represent the lowest level of uncertainty in the property determination, the “with sampling error added” the highest level of uncertainty, and the “spatial variation only” in between these levels. The case of deterministic mean soil

properties provides the lower bound of the risk and the mean minus standard deviation yields the upper bound.

It can be seen in Figure 7b that all three cases except the case of the mean minus standard deviation are almost identical for all RMS levels larger than 0.1 g. In other words, the risk of failure is not sensitive to the uncertainty of material properties. That is possibly due to significant spatial averaging effects and also relatively large number of samplings. It may be thus argued in this particular case that seismic uncertainty is the dominant factor in the assessment of stability of the slope, and that material uncertainty maybe neglected without significant impact on the computed reliability of the problem. The results suggest that in a highly seismically active region, characterization

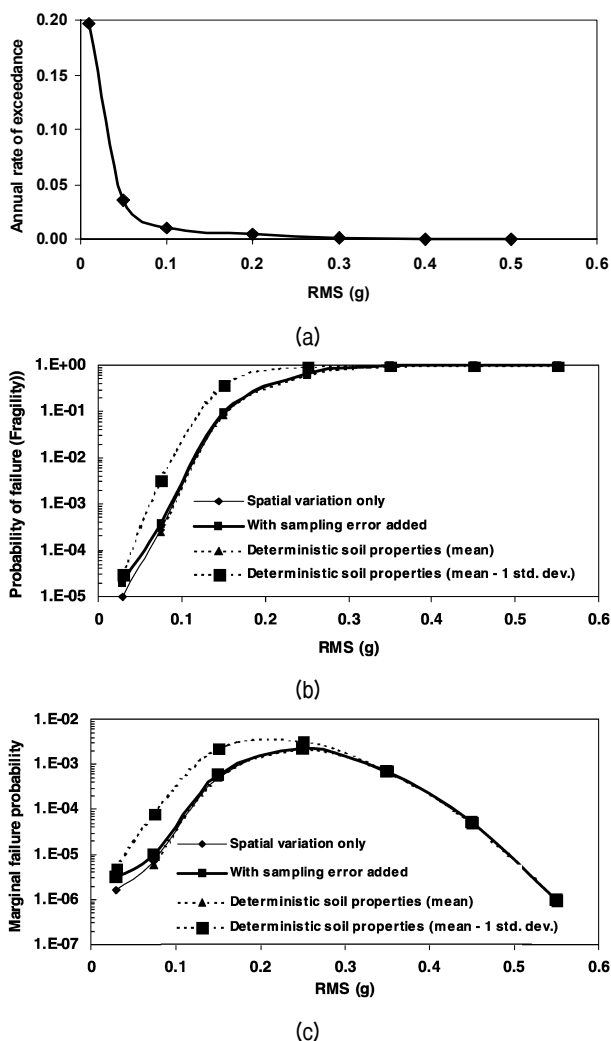


Fig. 7. (a) Annual Hazard Curve (Annual Rate of Exceeding Each Hazard Level); (b) Fragility Curve; (c) Marginal Annual Risk Curve (Annual Probability of Failure with Respect to Each Hazard Level)

of earthquake hazard is the most important and that characterization of soil properties, if in a reasonable range, have a relatively small effect on the computed risk of the slope failure.

Figure 7c shows that the most probable failure event will come from the RMS hazard of 0.2-0.3 g due to their relatively high rates of occurrence and damaging effects. This information may be useful in case we need to determine earthquake scenarios that are associated with the corresponding probabilistic hazard level.

4.2 Circular Slip Surface

The slope (Figure 8) reported by Kim (2003) is revisited in order to see the consistency of findings in the analysis above persists in different types of slope. The results were described by Kim (2003) and therefore, are briefly discussed here only for comparison purpose. This paper, however, reports some of findings from the follow-up study that examines the influence of scales of fluctuation in the seismic slope stability.

Three vertical borings are carried out and 10 soil samples are taken at the specific locations shown in Figure 8. Laboratory tests yield a sample mean value $\bar{c} = 45 \text{ kN/m}^2$ with standard deviation $s_c = 13.5 \text{ kN/m}^2$ for undrained shear strength, and $\bar{\gamma} = 18 \text{ kN/m}^3$ and $s_\gamma = 0.9 \text{ kN/m}^3$ for soil density. The soil deposit is modeled as a statistically homogeneous random field with two different scales of fluctuation (a measure of correlation distance) $\delta_x = 5 \text{ m}$ and $\delta_y = 1 \text{ m}$, and $\delta_x = 25 \text{ m}$ and $\delta_y = 5 \text{ m}$, respectively. In addition to the shear strengths it is assumed that the shear wave velocity measured at the site may be around

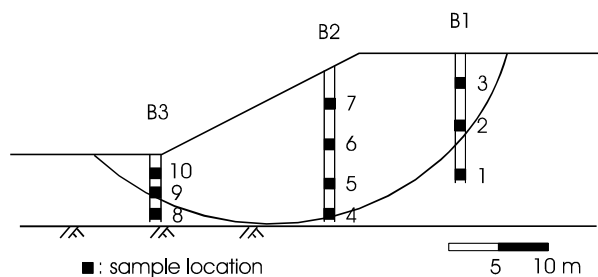


Fig. 8. Geometry and Sample Location of a Slope with a Circular Slip Surface (Kim 2003)

200 m/sec. The potential sliding mass is divided into 40 vertical soil slices of equal width, for subsequent seismic stability and deformation analyses.

The slope is also assumed to be in Berkeley. Unlike the preceding example, only the Hayward fault that is the closest major fault to the site is considered here.

The computations were carried out with the soil properties modeled with various approaches including conditional, unconditional and deterministic methods (Kim 2003). Figure 9 shows the probabilities of failure given the certain hazard levels (often called *fragility curve*), for five different characterizations of soil properties. It is interesting to observe that the differences in the probabilities of failure for the different cases are significant at the lower level of hazard (< 0.1 g) and gradually decrease with increasing hazard level, being negligible at the higher level (> 0.2 g) except for the case of the mean minus one standard deviation (i.e., conservative assessment of soil properties). For relatively small correlation lengths ($\delta_x = 5\text{ m}$ and $\delta_y = 1\text{ m}$), the difference between the conditional and unconditional (with sampling error) approaches is minimal. Increasing correlation ($\delta_x = 25\text{ m}$ and $\delta_y = 5\text{ m}$) yields a similar trend, but the risk level for the unconditional approaches becomes higher due to small variance reduction. Thus, in this particular problem, uncertainty of soil properties has a significant impact on the computed risk of slope failure at relatively low levels of seismic hazard, but it has little impact on the computed risk if the slope is exposed to relatively high levels of hazard. In this particular problem, the uncertainty of soil properties arising from the spatial variation and sampling errors does

not have much impact on the reliability of the slope for the RMS hazard level higher than 0.2 ~ 0.3 g. The results are consistent with those from the previous non-circular slope case

5. Summary and Conclusions

The effects of the material and seismic load uncertainties on the performance of different types of slopes were investigated and a new reliability-based method for evaluating permanent deformations of slopes was presented. The stochastic nature of seismic loading was accounted for by generating a large series of hazard-compatible artificial motions, and by using them in subsequent response analyses. The uncertainty of material properties was also considered. The developed method can model both material and seismic hazard uncertainties at the same time unlike other previous studies.

The RMS acceleration was adopted to characterize the intensity of ground shaking. The RMS procedure proved to be useful for generation of a large number of hazard-compatible motions, unlike the conventional procedures that usually can generate only a small number of motions that match deterministic targets such as design response spectra.

It is found that for relatively small correlation lengths, the difference between the conditional and unconditional (with sampling error) approach is minimal. Increasing correlation yields a similar trend, but the risk level for the unconditional approaches becomes higher due to small variance reduction.

Two example problems show that the characterization of material properties has a considerable influence on the probability of failure for a slope that is exposed to relatively low levels of seismic hazard. On the other hand, it shows a little impact on the computed risk in case of relatively high levels of seismic hazard.

The results suggest that in a seismically active region like the Western States of USA, Taiwan and Japan, characterization of earthquake hazard is the more critical factor in the computed risk, and a moderate variability in material properties and its characterization have a

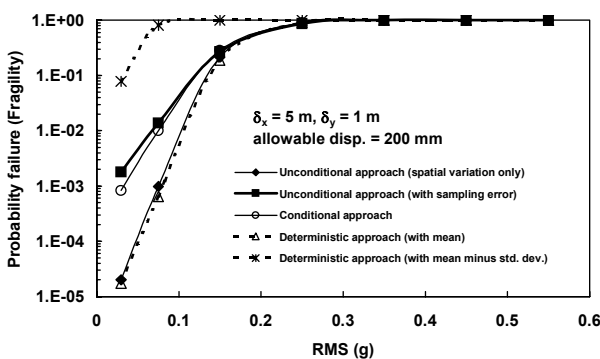


Fig. 9. Probability of Failure Given the Certain Hazard Levels (Fragility Curve)

relatively small effect on the computed risk of slope failure and excessive slope deformations. On the other hand, in a seismically less active region like the Mid-Western States of USA, Britain and Korea, characterization of material properties may be equally important to that of earthquake hazard, and therefore cannot be neglected.

Acknowledgments

This research was supported for two years by the Pusan National University Research Grant. The author thanks professor Sitar of University of California at Berkeley for reviewing the manuscript.

References

1. Abrahamson, N., and Silva, W. (1996), *Empirical Ground Motion Models, Draft Report*, Brookhaven National Laboratory.
2. Abrahamson, N., and Silva, W. (1997), "Empirical Response Spectral Attenuation Relations for Shallow Crustal Earthquakes", *Seismological Research Letters*, Vol.68, No.1, pp.94-127.
3. Augello, A. J., Matasovic, N., Bray, J. D., Kavazanjian, J., E., and Seed, R. B. (1995), "Evaluation of Solid Waste Landfill Performance During the Northridge Earthquake", *Geotechnical Special Publication*, No.54, ASCE, pp.17-50.
4. Bolt, B. A. (1969), "Duration of Strong Ground Motion", *Proceedings of Fourth World Conference on Earthquake Engineering*, Santiago, Chile, pp.1304-1315.
5. Bray, J. D., and Rathje, E. M. (1998), "Earthquake-Induced Displacements of Solid-Waste Landfills", *Journal of Geotechnical and Geoenvironmental Engineering*, ASCE, Vol.124, No.3, pp.242-253.
6. Gasparini, D. A., and Vanmarcke, E. H. (1976), *Evaluation of Seismic Safety of Buildings Report No. 2: Simulated Earthquake Motions Compatible with Prescribed Response Spectra*, Publication No.R76-4, Department of Civil Engineering, Massachusetts Institute of Technology, Cambridge, Massachusetts.
7. Housner, G. W. (1952), *Intensity of Ground Motion During Strong Earthquake*, California Institute of Technology, Earthquake Research Laboratory.
8. Housner, G. W. (1975), "Measures of Severity of Earthquake Ground Shaking", *Proceedings U.S. National Conference on Earthquake Engineering*, Ann Arbor, Michigan.
9. Idriss, I. M. (1991), *Selection of Earthquake Ground Motions at Rock Sites*, Report prepared for the Structures Division, Building and Fire Research Laboratory, NIST.
10. Idriss, I. M., and Sun, J. I. (1992), *User's Manual for SHAKE91 - A Computer Program for Conducting Equivalent Linear Seismic Response Analyses for Horizontally Layered Soil Deposits*, Center for Geotechnical Modeling, Department of Civil and Environmental Engineering, University of California, Davis, California.
11. Kanai, K. (1957), "Semi-Empirical Formula for the Seismic Characteristics of the Ground", *Bulletin of the Earthquake Research Institute*, Tokyo University, Vol.35, pp.308-325.
12. Kavazanjian, J., E., Echezuria, H., and McCann, J., M. W. (1985), "RMS Acceleration Hazard for San Francisco", *Soil Dynamics and Earthquake Engineering*, Vol.4, No.3, pp.106-123.
13. Kim, J. (2003), "The Importance of Geotechnical Variability in the Analysis of Earthquake-Induced Slope Deformations", *Journal of Korean Geotechnical Society*, Vol.19, No.2, pp.123-133.
14. Kim, J., Bray, J., Riemer, M. (2005), "Dynamic Properties of Geosynthetic Interfaces", *Geotechnical Testing Journal*, ASTM, Vol.28, Issue 3, pp.288-296.
15. Kim, J., and Sitar, N. (2004), "Direct Estimation of Yield Acceleration in Seismic Slope Stability Analyses", *Journal of Geotechnical and Geoenvironmental Engineering*, ASCE, Vol.130, No.1, pp.111-115.
16. Liu, P. L., Lin, H. Z., and Der Kiureghian, A. (1989), *CALREL User Manual*, Report No. UCB/SEMM-89/18, Department of Civil Engineering, University of California at Berkeley, Berkeley, California.
17. Newmark, N. M. (1965), "Effects of Earthquakes on Dams and Embankments", *Geotechnique*, Vol.15, No.2, pp.139-160.
18. Pal, S. K., Rahman, M. S., and Tung, C. C. (1991), "A Probabilistic Analysis of Seismically Induced Permanent Movements in Earth Dams", *Soils and Foundations*, Vol.31, No.1, pp.47-59.
19. Rice, S. O. (1954), "Mathematical Analysis of Random Noise", *Selected Papers on Noise and Stochastic Processes*, N. Wax, ed., Dover Publications, New York, pp.133-294.
20. Rubinstein, R. Y. (1986), *Monte Carlo Optimization, Simulation and Sensitivity of Queueing Networks*, John and Wiley & Sons, New York.
21. Saragoni, G. R., and Hart, G. C. (1974), "Simulation of Artificial Earthquakes", *Earthquake Engineering and Structural Dynamics*, Vol.2, pp.249-267.
22. Schnabel, P. B. (1973), *Effects of Local Geology and Distance from Source on Earthquake Ground Motions*, Ph.D. Dissertation, University of California, Berkeley, California.
23. Seed, R. B., and Bonaparte, R. (1992), "Seismic Analysis and Design of Lined Waste Fills: Current Practice", *ASCE Special Conference on Stability and Permanent Deformation of Slopes and Embankments*, II, Reston, Va, pp.1152-1187.
24. Seed, R. B., Mitchell, J. K., and Seed, H. B. (1990), "Kettleman-Hills Waste Landfill Slope Failure. 2: Stability Analyses", *Journal of Geotechnical Engineering*, ASCE, Vol. No.4, pp.669-690.
25. Singh, S., and Murphy, B. (1990), "Evaluation of the Stability of Sanitary Landfills", *Geotechnics of Wastefills - Theory and Practice*, ASTM STP 1070, ASTM, pp.240-258.
26. Tajimi, H. (1960), "A Statistical Method of Determining the Maximum Response of a Building Structure During an Earthquake", *Proceedings of the Second World Conference on Earthquake Engineering*, Tokyo, pp.781-797.
27. Trifunac, M. D., and Brady, A. G. (1975), "A Study of the Duration of Strong Earthquake Ground Motion", *Bulletin of the Seismological Society of America*, Vol.65, pp.581-626.
28. Tung, A. T. Y., Kiremidjian, A. S., Wang, J. N., and Kavazanjian, J., E. (1992), "Statistical Parameters of AM and PSD Functions for the Generation of Site-Specific Strong Ground Motions", *Earthquake Engineering, Tenth World Conference*.

29. Wang, J. N., and Kavazanjian, J., E. (1987), *A Nonstationary Probabilistic Model for Pore Pressure Development and Site Response due to Seismic Excitation*, Report No.84, The John A. Blume Earthquake Engineering Center, Stanford University.
30. Yang, J.-N. (1973), "On the Normality and Accuracy of Simulated Random Processes", *Journal of Sound and Vibration*, Vol.3, pp.417-428.
31. Yegian, M. K., Marciano, E. A., and Ghahraman, V. G. (1991), "Earthquake-Induced Permanent Deformations - Probabilistic Approach", *Journal of Geotechnical Engineering*, ASCE, Vol.117, No.1, pp.35-50.

(received on Jan. 18, 2007, accepted on Mar. 20, 2007)

Relationship between the State Parameter and Cone Resistance of Busan Sand

부산모래의 상태정수와 콘저항치 상관관계

Kim, Seung-Han ¹	김 승 한	Lee, Moon-Joo ¹	이 문 주
Choi, Sung-Kun ¹	최 성 근	Hong, Sung-Jin ¹	홍 성 진
Lee, Woo-Jin ²	이 우 진		

요 지

일련의 CID 삼축압축시험과 실내콘관입시험을 통하여 부산모래에서의 상태정수와 정규화된 콘저항치의 상관관계를 파악하였다. 삼축압축시험결과를 토대로 부산모래의 한계상태선을 도출하였으며 3개의 한계상태정수는 $M = 1.39$ ($\phi_{cs} = 34^\circ$), $\Gamma = 1.07$ 및 $\lambda = 0.068$ 인 것으로 산출되었다. 부산모래의 상태정수와 정규화된 콘저항치의 상관관계는 $(q_c - p)/p' = 27.6 \exp(-10.9\psi)$ 의 식으로 표현되었으며, 이는 응력이력에 관계없이 동일함을 확인하였다. 문헌조사를 통해 얻은 다른 모래시료의 정규화된 콘저항치 기울기 m 및 $\psi = 0$ 에서의 절편값 κ 를 비교 분석한 결과, 부산모래는 유사한 λ_{ss} 값을 갖는 모래시료 중 가장 큰 κ 값을 보였으나, m 과 κ 가 λ_{ss} 와 갖는 관계는 기존에 발표된 자료와 일치함을 확인하였다.

Abstract

A series of CIDC triaxial tests and cone penetration tests in calibration chamber were performed to investigate the relationship between state parameter and normalized cone resistance for dredged Busan sand. From the results of the triaxial tests, the critical state line of Busan sand was established, and the critical state parameters found to be $M = 1.39$ ($\phi_{cs} = 34^\circ$), $\Gamma = 1.07$ and $\lambda = 0.068$. By analyzing the state parameters and corresponding cone resistances for calibration chamber specimens, the relationship between normalized cone resistance and state parameter for Busan sand was defined as $(q_c - p)/p' = 27.6 \exp(-10.9\psi)$. This relationship was also shown to be independent of the stress history. From the comparison of the slope of the normalized cone resistance, m , and the normalized cone resistance at $\psi = 0$, κ , with those of various sandy soils from over the world, the relationship of m and κ with λ_{ss} of Busan sand was concluded to show a good agreement with the result published previously, while Busan sand had the largest κ among the soils with similar λ_{ss} values.

Keywords : Busan sand, Calibration chamber, Cone resistance, Critical state, Shear response, State parameter

1. Introduction

Korea, as well as other neighboring countries, has invested both public and private funds for the construction

of a number of harbors and airports in order to facilitate transportation and preoccupy international logistics service market. In Korea, Busan new port is under construction with the aim of serving as a gateway hub for the Northeast

¹ Member, Graduate Student, Dept. of Civil and Environmental Engineering, Korea Univ., Seoul

² Member, Associate Professor, Dept. of Civil and Environmental Engineering, Korea Univ., Seoul, woojin@korea.ac.kr, Corresponding Author

Asia. A large amount of sand was dredged from the offshore seabed for reclamation. Hence, investigating the shear behavior of Busan sand deserves academic attention.

The behavior of sandy soil subjected to drained shear can be contractive, intermediate, or dilative. For a dilative specimen, the void ratio decreases to a minimum transient value, known as the characteristic state (Luong, 1980), prior to the peak strength and then increases again until its void ratio reaches the critical state. For a contractive specimen, the void ratio continuously decreases toward the void ratio at the critical state. The critical state is defined as the ultimate state at which the soil continues to deform with a constant stress and void ratio. The response of a specimen can be captured in 3-D space in terms of the void ratio (e), mean principal stress ($p' = (\sigma_1' + 2\sigma_3')/3$), and deviator stress ($q = (\sigma_1 - \sigma_3)$). For simplicity, the projections of the critical state line in two planes ($p' - q$ and $e - \log p'$ plane) are commonly used, where three critical state parameters are able to be determined. The slope of the critical state line in the $p' - q$ plane is expressed in terms of the critical state friction angle, ϕ_{cs} .

$$M = \left(\frac{q}{p'} \right)_{cs} = \frac{6 \sin \phi_{cs}}{3 - \sin \phi_{cs}} \quad (1)$$

The critical state line projected in the semi-logarithmic $e - \log p'$ plane is expressed in terms of the intercept, Γ , and slope, λ .

$$e_{cs} = \Gamma - \lambda \log \left(\frac{\sigma'_{cs}}{1 \text{ kPa}} \right) \quad (2)$$

The critical state line stands for a reference state affected by various physical properties of a sandy soil, such as the compressibility, internal friction angle, grain size distribution and shape, mineralogy, and extreme void ratios. Theoretically, the critical state line represents a condition of zero volume change during shear (Poulos, 1981). The shear behavior of a sandy soil can be either contractive or dilative depending on whether the initial void ratio is greater or lesser than the void ratio of the critical state. Actually, the further a material state is from the critical state condition, the stronger will be the

tendency for a volume change during shear. Quantification of this tendency for a specimen to change its volume is achievable using the concept of state parameter (ψ).

The two most influential factors affecting the behavior of a given soil are the void ratio and stress level. The state parameter combines the influence of both of these factors, and can be used to describe the shear behavior of a sandy soil. The state parameter is defined as the difference between the void ratio of a soil and the void ratio on the ultimate (steady or critical) state line at the same mean effective stress, as illustrated in Fig. 1. Actually, despite of some controversy, the ultimate state of a soil has been reported to be independent of the initial stress state (Ishihara, 1993, Vaid and Thomas, 1995, Chu, 1995), initial fabric (DeGregorio, 1990, Ishihara, 1993), loading condition (DeGregorio, 1990, Been et al., 1991), and drainage condition (Been et al, 1991, Chu, 1995), even though the shear response and quasi-steady state may differ. In this study, therefore, the critical state line was assumed to be identical to the steady state line.

Finding the relationship between the cone resistance and state parameter is initiated based on the fact that the small strain behavior, such as shear modulus or compressibility, does not correlate well with the state parameter; whereas, the correlation between the state parameter and the large strain behavior, such as drained angle of shearing resistance, is considered acceptable. Been et al. (1986) provided a better relationship between the cone resistance and state parameter for a sandy soil using data collected from available chamber testing programs. Concluding that the relationship relies on the characteristics of the soil,

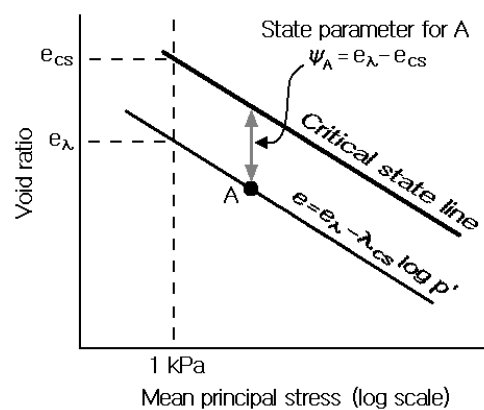


Fig. 1. Definition of state parameter ψ

Been et al. (1986) suggested the following correlation in terms of the slope, m , and the intercept, κ .

$$\frac{q_c - P}{p'} = \kappa \exp(-m\psi) \quad (3)$$

In this paper, the critical state of Busan sand was determined using a series of conventional CIDC tests, and then the chamber cone tests data were correlated with the state parameter. Also, the gradient and intercept of the $q_c - \psi$ relationship of Busan sand were evaluated and compared with other values published previously.

2. Experimental Program

2.1 Property of Busan Sand

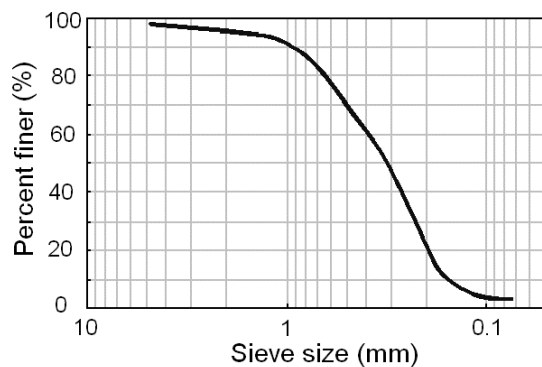
Busan sand is natural soil dredged near Yokji Island in the South Sea. Its properties are summarized in Table 1. The basic properties were evaluated using standardized techniques, KSF2308 (specific weight), KSF2302 (sieve analysis), and DIN18126 (extreme void ratios). The particle size distribution and SEM images are shown in Fig. 2. Distinguished characteristics of Busan sand are its high content of crushed shell.

2.2 CIDC Test

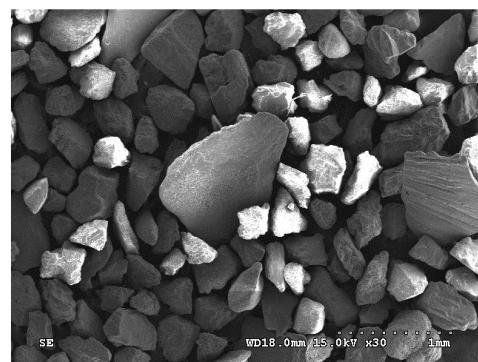
The specimen for the triaxial test had a diameter of

70.6 mm and height of 156.0 mm. Porous stones with a Norton mixture number of P260 were used with a sheet of filter paper at the top and bottom plates. In this paper, eighteen drained shear tests were performed with different relative densities and confining pressures. The complete CIDC triaxial test program is summarized in Table 2.

Dense and medium specimens were formed using the air-pluviation method. For loose and very loose specimens, both the air-pluviated and moist-tamped specimens were tested to monitor the differences in the shear behavior. Moist-tamping is considered adequate for preparation of a loose specimen close to the maximum void ratio; whereas, the air-pluviated loose specimen shows dilative behavior, regardless of its void ratio (Been and Jefferies, 1985). For air-pluviation, a funnel and a diffuser are required to prevent material segregation and to regulate the soil deposition rate and energy, which determine the resulting density. The drop heights of the air-pluviation system are predetermined according to the densities. For moist-tamping, soils are mixed to have moist content of 5%, and then placed in ten layers to the predetermined height of a mold. This procedure has to be performed with great caution to enhance the homogeneity. Before the mold was disassembled, the specimen was held with a vacuum pressure of 35 kPa (5 psi) constantly maintained using a regulator. Saturation was achieved in three phases; firstly, specimen was flushed with carbonate water, then



(a) Particle size distribution



(b) SEM image

Fig. 2. Particle size distribution and a microphotograph

Table 1. Properties of Busan sand

G_s	$e_{\max} (\gamma_{d\min})$	$e_{\min} (\gamma_{d\max})$	D_{50} (mm)	D_{10} (mm)	C_u	C_c	Particle Shape	Mineralogy (%)
2.62	1.063(1.27)	0.658(1.58)	0.315	0.162	0.71	2.35	Angular to sub-angular	SiO ₄ (84.69), CaCO ₃ (7.25)

Table 2. CIDC test program

Confinement	Moist tamping		Air-Pluviation			
	20%	40%	20%	40%	60%	80%
100 kPa	M21	M41	A21	A41	A61	A81
200 kPa	M22	M42	A22	A42	A62	A82
400 kPa	M24	M44	A24	A44	A64	A84

saturated using de-aerated water. Because of the high solubility of carbon dioxide in water, rapid and complete saturation is insured; back-pressure was finally applied until B value of at least 0.97 was achieved. The same value of back-pressure (100 kPa) was applied for all specimens. With increment of 50 kPa per two minutes, the isotropic consolidation pressure was applied to the target effective confining pressure. After the completion of the isotropic consolidation, the strain-controlled shear tests were performed with a 0.5%/min strain rate until an axial strain of 30% was reached. Time, axial strain, volumetric strain, deviatoric stress, and total and effective confining stresses were recorded every 1 second using an automatic data acquisition system.

2.3 Chamber Cone Penetration Test

The Korea University Calibration Chamber System (KUCCS) was devised to simulate in-situ tests under various boundary conditions and stress states. The system consists of a calibration chamber, control panel, and data acquisition system. The calibration chamber, 1.2 and 1.0 meters in diameter and height, respectively, is capable of performing K_0 consolidation, using a servo-controlled double wall and piston underneath the base-plate (Fig. 3), as well as consolidation following arbitrary stress path under four boundary conditions. Chamber cone penetration test is able to be conducted using cone-probe adapters located on the top plate.

As the chamber-to-cone diameter ratio and boundary condition are known to have a significant influence on the results of the cone penetration test, a number of correction methods have been suggested to account for the effects of the chamber size and boundary condition. In this paper, the chamber size standardization factors suggested by Been et al. (1986) were used, which defines

the correction factors according to the boundary condition and chamber-to-cone diameter ratio based on the data of Hokksund sand. Although this standardization technique is based on limited test data, for the sake of consistency with previously published papers, the calibration chamber test results were corrected using this technique.

The chamber specimen was prepared using a large scale pluviation method. This technique was preferred due to its effectiveness, and repeatability in forming identical samples with spatial homogeneity. The KUCCS raining equipment, as shown in Fig. 4, consists of a storage chamber, lower and upper molds, and a diffuser sieve,

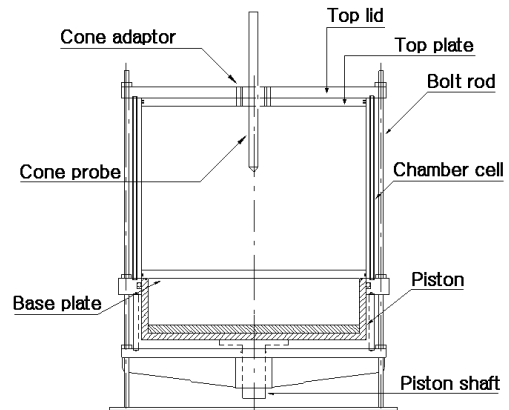


Fig. 3. Schematic of calibration chamber

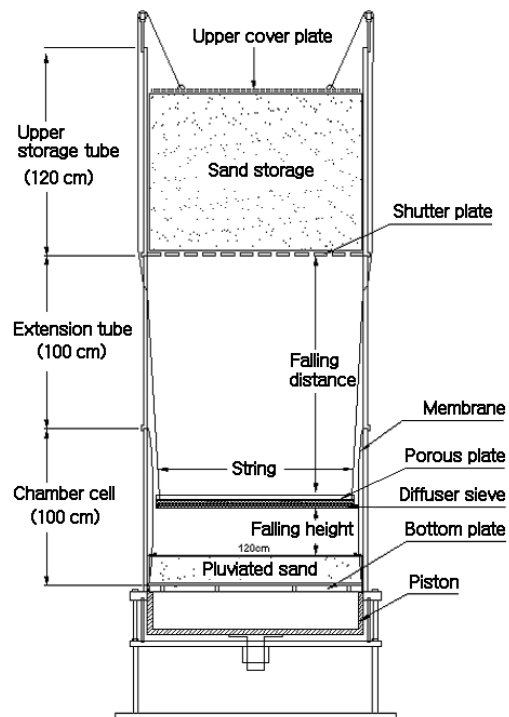


Fig. 4. Raining equipment

Table 3. Chamber cone penetration test program

Vertical confining pressure	Relative density		
	40%	60%	80%
100 kPa (OCR=1)	CN41	CN61	CN81
200 kPa (OCR=1)	CN42	CN62	CN82
400 kPa (OCR=1)	CN44	CN64	CN84
200 kPa (OCR=2)	CO42	CO62	CO82
100 kPa (OCR=4)	CO44	CO64	CO84
50 kPa (OCR=8)	CO48	CO68	CO88

which is capable of maintaining a constant drop height with the elevating diffuser sieve. The relative density of the specimen is governed by the opening size of the diffuser and the drop height, and these values were predetermined from a series of preliminary raining tests.

After assembling the spilt mold and rubber membrane, the specimen was pluviated using the raining system. The upper plate was mounted onto the specimen and was sealed with membrane and O-rings. Once the specimen was held with a vacuum pressure, the split mold was disassembled and the initial volume was measured. The double wall chamber cell, upper lid, and reinforcing plate were assembled and the inner and outer cells then completely filled with de-aerated water. The confining pressure was increased to a target value with increments of 50 kPa per every hour. By unloading from a vertical preconsolidation pressure of 400 kPa, the specimens with OCR of 2, 4 and 8 were prepared. The volume change in the specimen was measured by reading the water level in two vessels connected to the piston and chamber cell. Once the chamber specimen had stabilized at the desired consolidation pressure, the hydraulic thruster was located above the cone adapter on the reinforcing plate and cone probe is penetrated into the specimen at a standard penetration rate of 2 cm/sec. Eighteen cone penetration tests were performed according to the test program summarized in Table 3.

3. Experimental Results

3.1 Critical State Line of Busan Sand

Fig. 5 shows the results of the CIDC triaxial tests for

Busan sand with different initial void ratios and effective confining pressures. Due to the dilating behavior of the air-pluviated specimen, Figs. 5 and 6a were plotted based on data acquired from the air-pluviated loose and medium specimens, as well as the moist-tamped dense and very dense specimens. From Fig. 5, as long as the confining pressures are the same, the shear strength of the soil converges to a certain residual value, regardless of the initial void ratio. The void ratios of the dense specimens, however, did not converge to the same value. The development of a shear band during shear may induce strain localization, which would affect the global void ratio. In addition to the strain localization effect, the end platen effect triggered by friction between the plates and the bordering soils plays a significant role in preventing the specimen from dilating, as a result, lowering the global void ratio. The transient void ratio, which is known to appear as a minimum void ratio prior to the peak strength in medium-dense or dense specimens, can be seen clearly with a specimen under a large confining pressure. It can be clearly observed in the specimen with 400 kPa confinement, whereas it is indistinguishable in the specimen with 100 kPa confinement. Figure 6b shows the difference between the shear responses of the moist-tamped samples and the air-pluviated samples. The air-pluviated samples turned out to be dilative even though the moist-tamped specimens at the same void ratio showed contractive behavior.

On the basis of the test data, including axial strain, void ratio, deviatoric stress, and confining stress at the critical

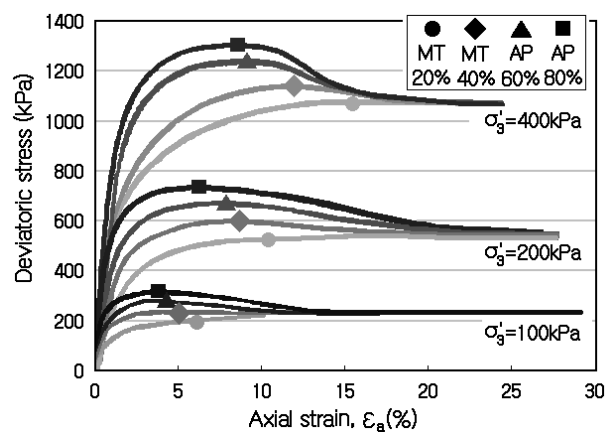
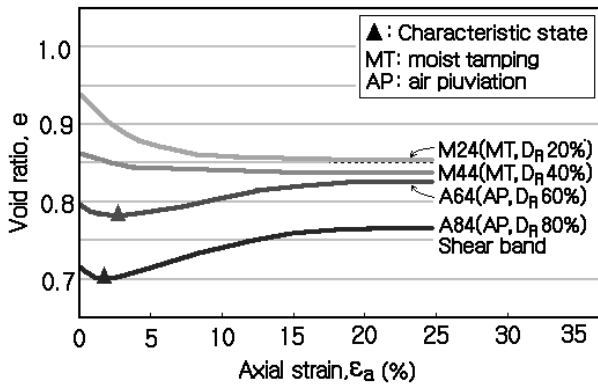
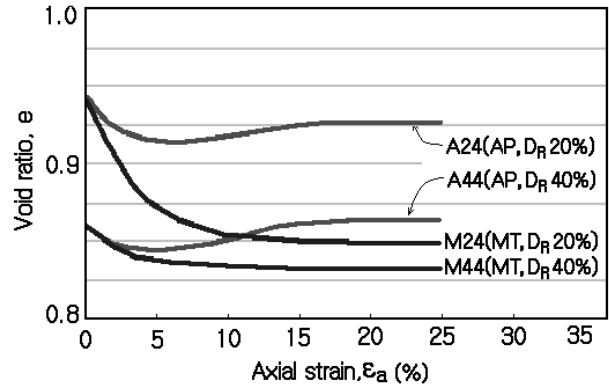


Fig. 5. Drained shear response

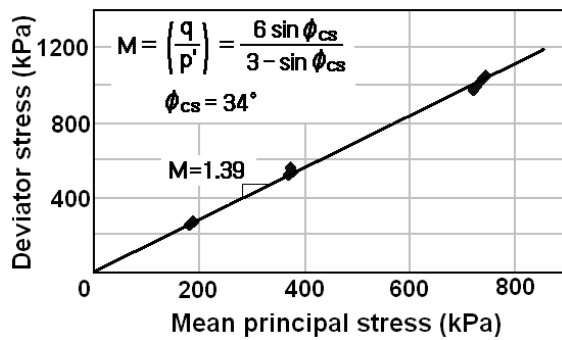


(a) Evaluation of critical void ratio

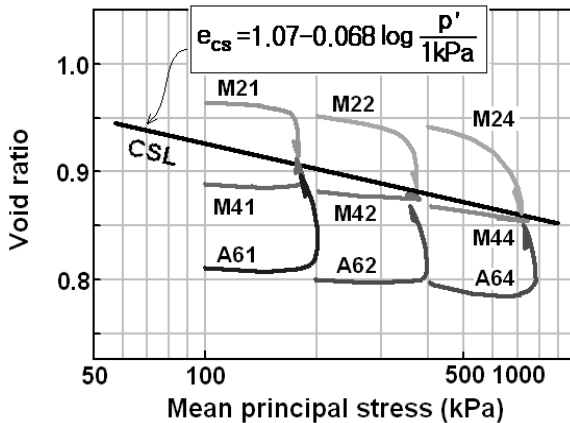


(b) Volumetric response for specimens formed by different methods

Fig. 6. Variation of void ratio with axial strain ($\sigma'_3 = 400$ kPa)



(a) CSL on $p'-q$ plane



(b) CSL on $e-\log p'$ plane

Fig. 7. Critical state line for Busan sand

state, obtained from a series of CIDC tests, the critical state line and three parameters were determined, as illustrated in Fig. 7. It should be noted that, due to the insufficient void ratio convergence of the dense specimens, the shear responses of $D_R = 80\%$ specimens were excluded when determining the critical state line. The computed critical state parameters of Busan sand are $M = 1.39$, Γ

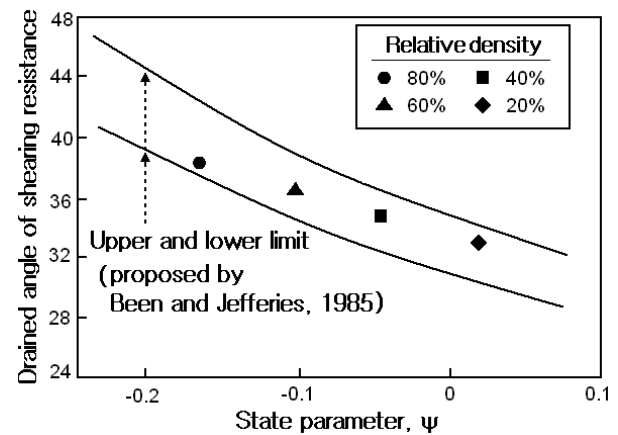


Fig. 8. Peak friction angle of Busan sand as a function of ψ

$= 1.07$, and $\lambda = 0.068$. The friction angle at the critical state, ϕ_{cs} , was determined to be 34° , which is in good agreement with the typical value of ϕ_{cs} suggested by Bolton (1986), which was 33° for quartz sands.

Fig. 8 shows the relationship between the peak friction angle and state parameter for Busan sand. It was within the range proposed by Been and Jefferies (1985). Although the trends of decreasing ϕ'_{peak} with increasing ψ were quite similar, the gradient of the extreme limits was steeper than that for Busan sand. This indicates that the maximum dilation angle, ψ_{max} , of Busan sand is likely to be smaller than that of other sands, as reflected in the fact that the slope of the critical state line, which is basically a measure of the compressibility of soil, was relatively large for Busan sand.

3.2 Chamber Cone Penetration Test Result

The state parameters of the chamber specimens were calculated based on the void ratio after the completion of each K_0 consolidations. The representative cone resistance was determined as the value when the cone resistance measured during cone penetration into calibration chamber became constant. Also, the cone resistance was corrected using the chamber size standardization factor, and the normalized cone resistance was obtained. From a series of preliminary raining tests, a 20% relative density was impossible to achieve and, as a result, data for $D_R=20\%$ specimens was not obtained in the calibration chamber.

The points in Fig. 9 indicate the void ratio and stress state of each chamber specimen, all of which were below the critical state line. All the chamber specimens had negative state parameters, indicating a dilative shear response. The void ratio of the OC specimen was slightly smaller than that of the NC specimen due to the unrecoverable deformation during unloading. Fig. 10 shows the relationship between normalized cone resistance and the state parameter established for Busan sand. It is shown that the cone resistance increases as the density of the specimen increases, i.e. as the state parameter decreases. It was also observed that the linear regression lines of the NC and OC specimens show no discrepancy. Therefore, it can be concluded that the stress history does not affect the relationship between the cone resistance and state parameter when the cone resistance is normalized with respect to the mean effective normal stress. From the relationship,

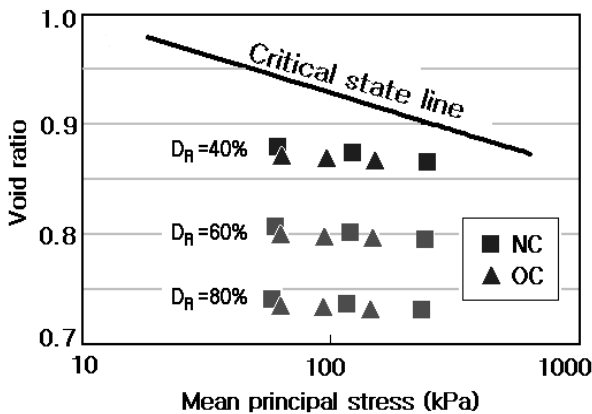


Fig. 9. State parameter for cone chamber specimen

the values of m and for κ Busan sand were found to be 10.9 and 27.6, respectively.

Fig. 11 shows the contour lines determined by assigning specific numbers in place of the state parameter in Equation (3). The numbers in the figure represent the state parameter, e.g. 04 means $\psi = -0.04$. It was observed that the slope of the plot between $q_c - p$ and p' was closely related to the state parameter, and provided a good estimation for the state parameter of each chamber specimen.

Figs. 12a and 12b show the plots of the slope of the normalized cone resistance, m , and the normalized cone resistance at $\psi = 0$, κ , with respect to the slope of the steady state line, λ_{ss} , for various sandy soils from over the world. The data point for Busan sand is located at almost the same position with that of Reid Bedford in

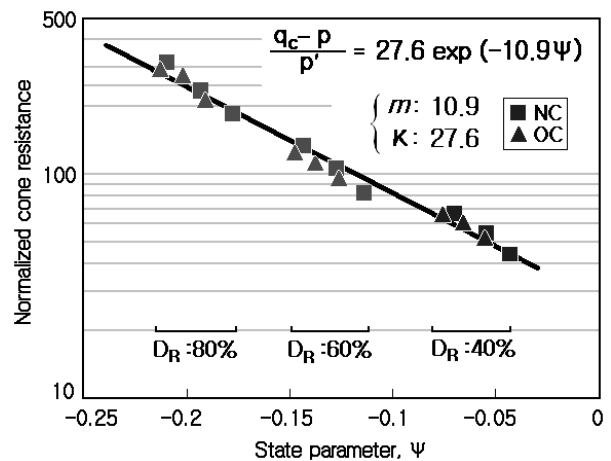


Fig. 10. Relationship between the state parameter and normalized cone resistance

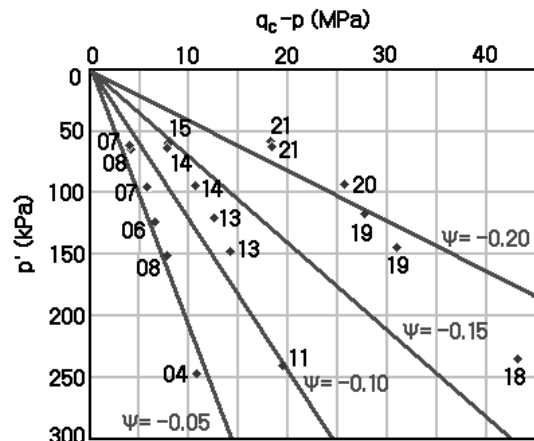
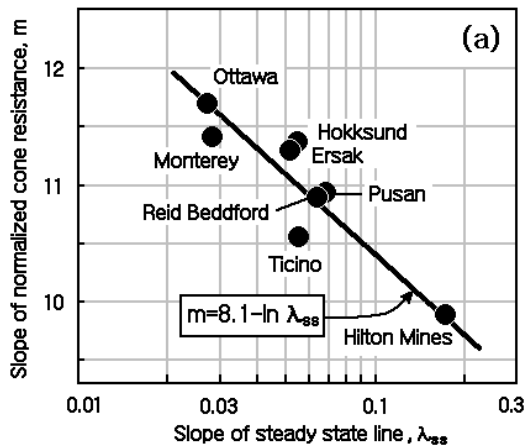
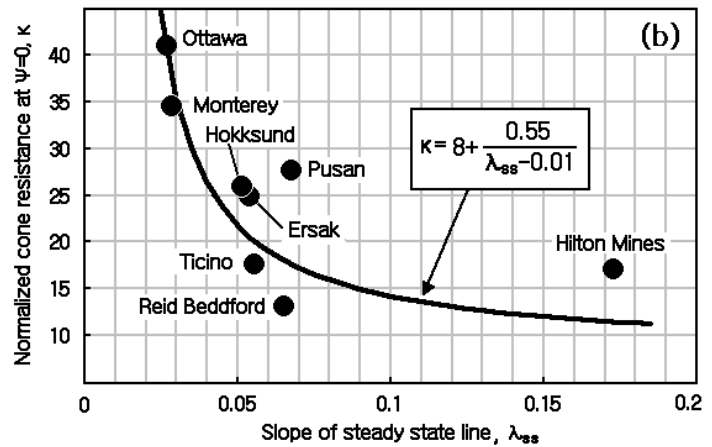


Fig. 11. Proportionality of the state parameter to the normalized cone resistance



(a) Relationship between m and λ_{ss}



(b) Relationship between κ and λ_{ss}

Fig. 12. Correlation of m and κ with λ_{ss} (after Been et al., 1987)

Figure 12a, while Busan sand shows the largest κ among the soils with similar λ_{ss} in Figure 12b. The reason the κ did not correlate well with the previously published data may be explained by the high strength of quartz sand. Although the compressibility of Busan sand was the second largest of the various sands, the mineralogy or material strength of Busan sand is believed to be large enough to resist grain rupture during cone probe penetration. Therefore, comparatively high cone resistance and κ are likely to be obtained.

4. Conclusions

From a series of CIDC triaxial tests and the cone penetration tests in a calibration chamber, the relationship between the state parameter and normalized cone resistance for Busan sand dredged from the South Sea was investigated and the following conclusions were drawn.

- (1) Using the results of the triaxial tests on specimens showing contractive and dilative responses during shear, the critical state line was established and the critical state parameters of Busan sand were determined as $M = 1.39$ ($\phi_{cs} = 34^\circ$), $\Gamma = 1.07$, and $\lambda = 0.068$. It was also observed that the peak friction angle of Busan sand decreased with increasing state parameter with relationship obtained being within the range suggested by Been and Jefferies (1985).
- (2) By evaluating the state parameters for the calibration

chamber specimens and the corresponding cone resistances normalized with respect to the mean effective normal stress, the relationship between the normalized cone resistance and state parameter for Busan sand was established to be $(q_c - p)/p' = 27.6 \exp(-10.9\psi)$. It was also shown that this relationship was independent of the stress history when the cone resistance was normalized with respect to the mean effective normal stress.

- (3) The slope of the normalized cone resistance, m , and the normalized cone resistance at $\psi = 0$, κ , for Busan sand were compared with those of various sandy soils by plotting the data in the relation of m and κ with respect to the slope of the steady state line λ_{ss} . The relationship between the m and λ_{ss} of Busan sand showed a good agreement with the result of Been et al. (1987), while Busan sand was found to have the largest κ among the soils with similar λ_{ss} .

Acknowledgement

This paper is supported by the Construction Core Technology Program (C104A1000009-06A0200-00800) under the KICTTEP Grant.

References

1. Been, K., Crooks, J.H.A., Becker, D.E., and Jefferies, M.G. (1986), "The cone penetration test in sands: Part I, State parameter

- interpretation”, *Géotechnique*, Vol.36, No.2, pp.239-249.
2. Been, K., and Jefferies, M.G. (1985), “A state parameter for sands”, *Géotechnique*, Vol.35, No.2, pp.99-112.
 3. Been, K., Jefferies, M.G., Crooks, J.H.A., and Rothenburg, L. (1987), “The cone penetration test in sands: Part II, General inference state”, *Géotechnique*, Vol.37, No.3, pp.285-299.
 4. Been, K., Jefferies, M.G., and Hachey, J. (1991), “The critical state of sands”, *Géotechnique*, Vol.42, No.3, pp.365-381.
 5. Bolton, M.D. (1986), “The strength and dilatancy of sands”, *Géotechnique*, Vol.36, No.1, pp.65-78.
 6. Cho, G.C. (2003), “Determination of critical state parameters in sandy soils from standard triaxial testing (I): Review and application”, *Journal of Korean Geotechnical society*, Vol.19, No.1, pp.61-75.
 7. Cho, G.C. (2003), “Determination of critical state parameters in sandy soils from standard triaxial testing (II): Experiment and recommendation”, *Journal of Korean Geotechnical society*, Vol.19, No.1, pp.77-92.
 8. Chu, B. (1995), “An experimental examination of the critical state and other similar concepts for granular soils”, *Canadian Geotechnical Journal*, Vol.32, pp.1065-1075.
 9. DeGregorio, V.B. (1990), “Loading systems, sample preparation, and liquefaction”, *Journal of Geotechnical Engineering*, Vol.116, No.5, pp.805-821.
 10. Frost, J.D., and Park, J.Y. (2003), “A critical assessment of the moist tamping technique”, *Geotechnical Testing Journal*, Vol.26, No.1, pp.57-70.
 11. Ishihara, K. (1993), “The Rankine Lecture: Liquefaction and flow failure during earthquakes”, *Géotechnique*, Vol.43, No.3, pp.351-415.
 12. Jefferies, M.G., and Been, K. (1987), “Note: Use of critical state representations of sand in the method of stress characteristics”, *Canadian Geotechnical Journal*, Vol.24, pp.441-446.
 13. Luong, M.P. (1980), “Stress-strain aspects of cohesionless soils under cyclic and transient loading”, *International Symposium on Soils under Cyclic and Transient Loading*, Swansea, pp.315-324.
 14. Poulos, S.J. (1981), “The steady state of deformation”, *Journal of Geotechnical Engineering*, Vol.107, No.GT5, pp.553-562.
 15. Robertson, P.K., and Campanella, R.G. (1983), “Interpretation of cone penetration tests. Part I: Sand”, *Canadian Geotechnical Journal*, Vol.20, pp.718-733.
 16. Vaid, Y.P., and Thomas, J. (1995), “Liquefaction and post-liquefaction behavior of sand”, *Journal of Geotechnical Engineering*, Vol.121, No.2, pp.163-173.

(received on Jan. 31, 2007, accepted on Mar. 26, 2007)

Case Studies of Penetration Characteristics of DCM Wall Using Spiral Mixing Blades in Soil Layers

특수교반날개를 사용한 DCM 공법의 지반 관입 특성에 대한 사례연구

Jung, Doo-Hoi¹ 정 두 회
Jeong, Gyung-Hwan² 정 경 환
Yang, Tae-Seon³ 양 태 선

요 지

DCM 공법(심층혼합처리 공법)은 흙막이 벽체 등 구조물 구성에 적용하였다. 이러한 DCM 벽체는 경질층에서 관입능력이 있어야 한다. DCM 장비에 부착된 교반날개에 의해 경질지반의 관입능력이 증가되는 알아보기 위해 특수교반날개가 고안되었다. 경질점토층에 관입되는 특수교반날개의 관입특성은 김해와 인천현장에서 조사하였다. 고안한 특수교반날개는 관입속도가 다소 느려도 N=30 이상 되는 지반까지 관입되었고 관입시 효율이 경질지반에서 낮아질 수 있으므로 경제적인 교반날개의 관입깊이를 분석하였다.

Abstract

DCM (Deep Cement Mixing Method) has been applied to build structures such as self-supported earth retaining walls. DCM columns should be penetrability into the stiff layer to assure the self-supporting ability. On the penetration increase of blade attached to the DCM mixing tools, a spiral mixing blade has been revised. Penetration characteristics of spiral blades in the stiff soil layer were evaluated through Gimhae and Incheon areas. The spiral mixing blades could penetrate into the stiff soil layers which have the N-value of greater than 30 although the penetration rate is somewhat slow. Penetration characteristics and economical efficiency should be discussed to determine the critical depth of the spiral mixing blade because the penetration efficiency can decrease in the stiff layer in this paper.

Keywords : Construction efficiency, Spiral mixing blades, Penetration characteristics

1. Introduction

For the development of DCM, design strength and elastic modulus can be studied. Self-supported earth retaining systems have been employed to minimize the use of bracing components while securing the stability and to maximize the construction efficiency. These tech-

nologies include the use of PS beam or IPS method in which a pre-stress is introduced to widen the spacing of struts, a self-supported diaphragm wall incorporated with a counter-fort wall, or a self-supported DCM wall without a bracing component. Among these, a self-supported DCM wall is highly applicable to wide excavation works, underground structures with a complicated configuration,

1 Member, Prof., Dept of Civil Engrg., Pukyong National Univ.

2 Member, CEO, Dong-A Geological Engrg. Co., Ltd., ghjeong@dage.co.kr, Corresponding Author

3 Member, Associate Prof., Dept. of Construction Information Engrg., Kimpo College

or shallow excavation works not exceeding 10 m in depth. In Korea, DCM method has been employed for land applications to support structures, to prevent settlement, or to support excavation works since it was applied to build Su-Young waste water treatment plant in Busan in 1985. In recent days, the accumulated length of DCM wall construction in Korea is increasing.

Deep cement mixing (DCM) technologies have been applied to build self-supported earth retaining walls supporting underground excavation works. For the self-supported DCM wall to assure the self-supporting ability, DCM columns should be penetrated into the stiff layer to derive a sufficient passive resistance against the lateral forces acting on the wall. However, a conventional mixing blade attached to the DCM mixing tool was originally developed for soft soils and therefore the penetration efficiency of conventional blades is significantly lowered in the stiff layer. The construction efficiency of DCM method in the stiff soil layer largely depends on the penetration characteristics of blade attached to the DCM mixing tool. A spiral mixing blade has been revised to increase the construction efficiency of DCM method in the stiff layer while building a self-supported DCM wall in Incheon area. Trial constructions have been carried out to evaluate the penetration characteristics of new blades both in Gimhae and Incheon areas. Penetration characteristics of spiral blades employed to build a self-supported DCM wall in the stiff soil layer are presented herein in terms of soil types and their stiffness.

2. DCM Method

2.1 Overseas Trends

In the late 1960's, Scandinavian countries and Japan independently developed a deep lime mixing (DLM) method using quicklime or slaked lime as binding materials. Today, in Sweden and Finland, a combination of lime and cement are extensively used in the deep mixing method. Lime or lime-cement is introduced in the form of dry powder. In 1975, Japanese CDIT (Coastal Development Institute of Technology) developed a DCM method in which

binding materials are introduced in the form of slurry. The deep mixing method utilizes such agents as quicklime, slaked lime, cement, slag, fly ash or a combination of these agents. The accumulated volume of treated soil using the deep mixing method reached over 1,000,000 m³ in Sweden and Finland since 1966. From 1977 to 1998, the accumulated volume of treated soil using the DCM method reached 38,000,000 m³ in Japan. The deep mixing methods were first introduced as a preventive measure against liquefaction in the United States in 1987. The deep mixing method has been applied to several highway projects such as Central Artery highway construction and is becoming a viable construction technology in the United States. In recent days, the deep mixing method is also applied to a variety of construction projects in Asian countries.

2.2 Domestic Trends for Land Application

In Korea, the DCM method was first introduced as a SEC (Special Earth Concrete) method for the construction of Su-Young waste water treatment plant in 1985 and it was applied to build a self-supported earth retaining wall and a foundation.

The treatable depth with the DCM method largely depends on the capacity of equipment. The earlier version of equipment, 110P, could improve soils up to the depth of 20~25 m. However, a modern version of equipment, 170P, can improve soils up to the depth of 35~37 m. In the introductory stage of DCM method in Korea, a two-shaft mixing tool (ϕ 1,000×2rod) was used for foundation applications whereas a three-shaft mixing tool



(a) 135P

(b) 170P

Fig. 1. DCM mixing rigs on land application

(ϕ 550 \times 3rod) was employed for the construction of earth retaining walls. Afterwards, a four-shaft mixing tool (ϕ 1,000 \times 4rod) has been developed to meet a demand for a variety of improving configuration. The four-shaft mixing tool has several advantages over the two-shaft mixing tool. They include the higher construction efficiency due to a wider improving area, a better mixing efficiency and a higher stability of earth retaining wall due to a better overlapping.

3. Case Studies

3.1 Plan of Self-supported DCM Wall

The subsurface soil at the site of Hak-ik waste water treatment facility in Incheon consists of reclaimed soil, alluvial clay, weathered soil and weathered rock. A self-supported DCM wall was planned to be constructed

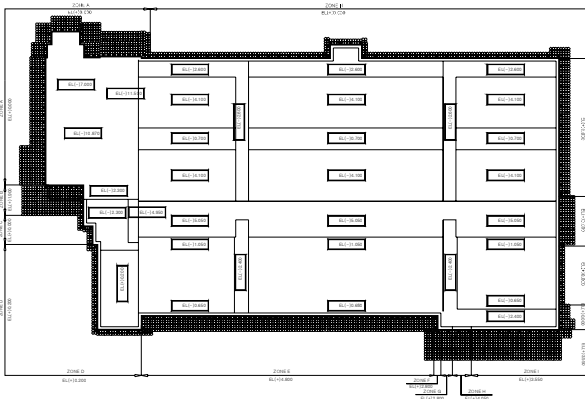


Fig. 2. Plan view of self-supported DCM wall

as an excavation support system as shown in Figures 2 and 3. A number of DCM columns were determined based on the excavation depth to assure the stability of the excavation work.

3.2 Characteristics of Subsurface Soils

Based on the standard penetration test performed during the subsurface investigation, the N-value of upper reclaimed layer was less than 20/30 and showed a wide scatter. The N-value of alluvial clay layer ranged 1/30~50/30, and the N-value of weathered soil and rock exceeded 50. The ground water table is located 0~7.9 m below the ground surface.

3.3 Alteration of Original Design

Incomplete DCM columns were found in the stiff clay

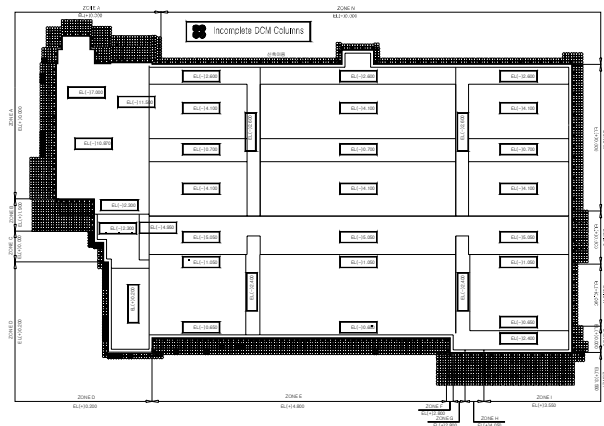


Fig. 4. Plan view of incomplete DCM columns

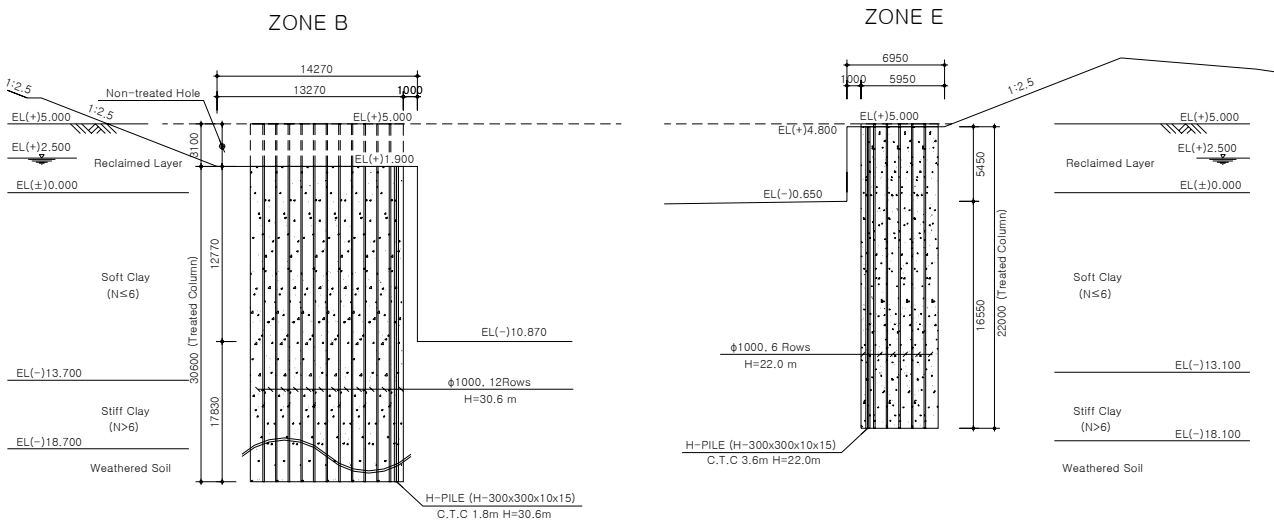


Fig. 3. Cross sectional view of self-supported DCM wall

ZONE-A(Final Excavation Depth 7.0m)

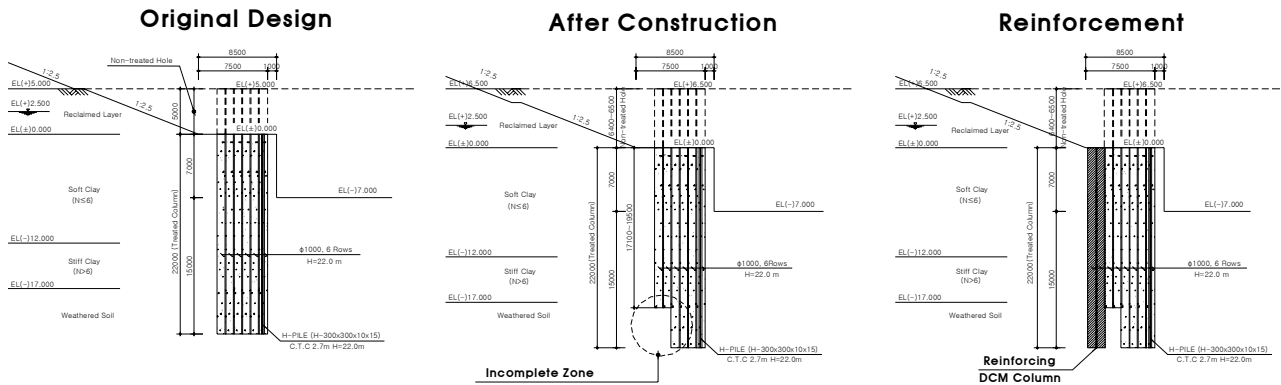


Fig. 5. Cross sectional view of reinforcement in the stiff soil layer

and weathered soil layers during the construction of DCM wall. The uncompleted thickness ranged 0.1~5.0 m as presented in Figure 4. A reinforcement was planned to assure the stability of DCM wall as presented in Figure 5. In addition, two types of mixing blades were revised to facilitate a penetration into the stiff soil layer.

4. Development of Mixing Blades to Penetrate into Stiff Soils

4.1 Characteristics of Conventional Blade Used in Soft Soils

Mixing blades used in domestic DCM methods were developed for an application to the soft clay layer and employed a two-stroke type in which water is introduced in the process of penetration. In recent days, a one-stroke type where slurry is introduced and mixed both in the

process of penetration and retrieval is mainly employed. The one-stroke method is proved to be effective for a quality control. Figure 6 shows a conventional mixing blade employed in soft clayey soils.

Figures 7 and 8 show penetration characteristics of one-stroke DCM mixing tool equipped with a conventional mixing blade employed to form DCM columns with a diameter of 1,000 mm in Gimhae area located in the

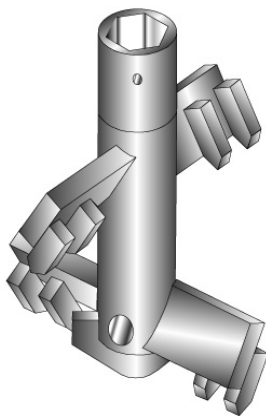


Fig. 6. A configuration of conventional mixing blade for soft soils

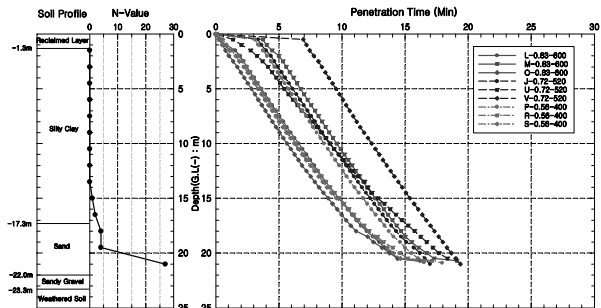


Fig. 7. Penetration time (Gimhae)

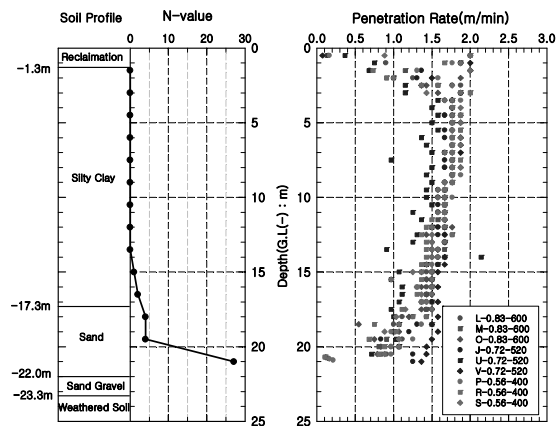


Fig. 8. Penetration rate (Gimhae)

southern coastal area over which a thick soft clay deposit is distributed. A four-shaft mixing tool, 135P was employed in the project. As presented in Figure 10, time required for the penetration into the reclaimed layer and the sand layer with greater N-values appeared to be irregular and long whereas the penetration time in the silty clay layer was consistent. It took 16~19 minutes to penetrate the whole design depth of 21 m.

Figure 8 shows a variation of penetration rate with depth. The penetration rate appeared to be slower in reclaimed soil and dense sand layers than in silty clay layer. The penetrating rate appeared to be almost constant in the silty clay layer. The slower penetration rate recorded in the reclaimed-soil layer may be attributed to larger particles mixed in the reclaimed soil. However, the penetration rate decreased because it requires a longer mixing time to assure a complete formation of DCM column end in the dense sand layer. The penetration rate appeared to be 1.3~1.9 m/min in the soft silty clay layer.

4.2 Penetration Characteristics of Conventional Mixing Blade in Stiff soils of Incheon

Clay soils in Incheon area tend to have higher N-values or contain more silt or sand components compared to those in southern coastal area. The penetration efficiency of DCM equipment can decrease in this area. Thus, a re-evaluation of penetration capability of DCM equipment equipped with a conventional mixing blade was required to treat stiff clays ($N > 4$) as well as dense sandy soils ($N > 10$).

A trial construction was performed by using a two-stroke type instead of using a one-stroke type in order to increase the penetration depth. In the two-stroke type, water is introduced in the process of penetration and slurry is then introduced and mixed in the repeated process of penetration and retrieval. Penetration time and rate obtained from the trial construction are presented in Figures 9 and 10. Penetration time appeared to be similar in both the one-stroke and the two-stroke types. The critical penetration depth appeared to be 26 m where a sand layer ($N=30$)

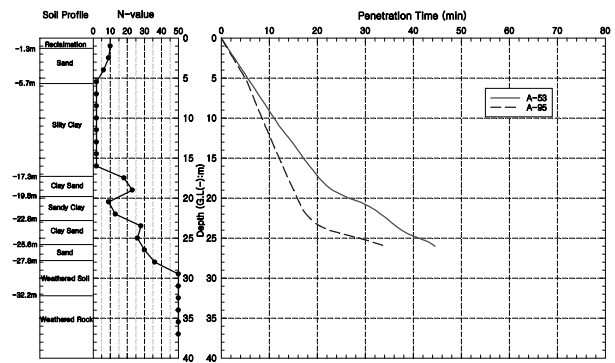


Fig. 9. Penetration time of conventional mixing blade (Incheon)

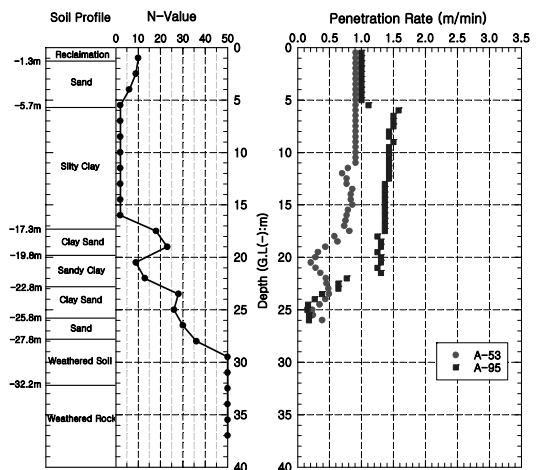


Fig. 10. Penetration rate of conventional mixing blade (Incheon)

exists.

As indicated in Figure 10, the penetration rate based on the two-stroke type ranged 1.0~1.5 m/min and decreased to 0.5 m/min in the depth of below 20 m where a stiff layer exists. In the stiff layer, the penetration rate decreased both in the one-stroke and two-stroke types if a conventional mixing blade is employed. In addition, the penetration was impossible in the sand layer with a N-value of greater than 30.

4.3 Penetration Characteristics of Spiral Mixing Blade in Stiff Soils

4.3.1 Demands for the Development of Spiral Mixing Blade

The penetration capability of conventional mixing blade significantly decreased in the stiff layer distributed over Incheon area and also the penetration was impossible in the stiff layer with a N-value of greater than 30.

Therefore, a special mixing blade is required to be developed to improve the penetration capability of DCM equipment in the stiff layer.

4.3.2 Types of Special Mixing Blades

Two types of mixing blades were revised to increase the penetration capability of DCM mixing tool in the stiff layer as shown in Figure 11. The special mixing blades

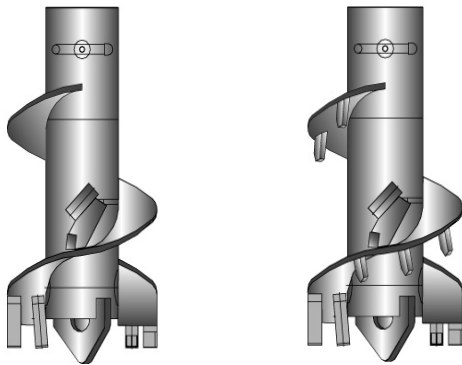


Fig. 11. Configuration of spiral mixing blades (Type1, Type2)

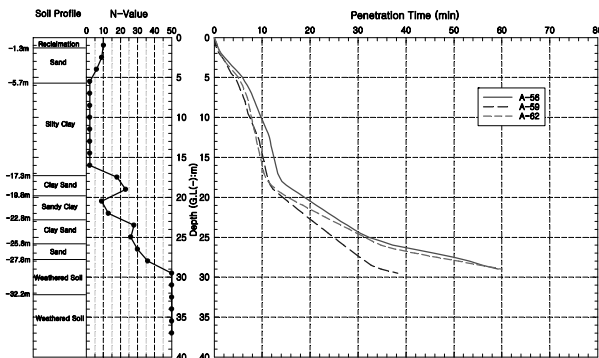


Fig. 12. Penetration time (Type1 blade)

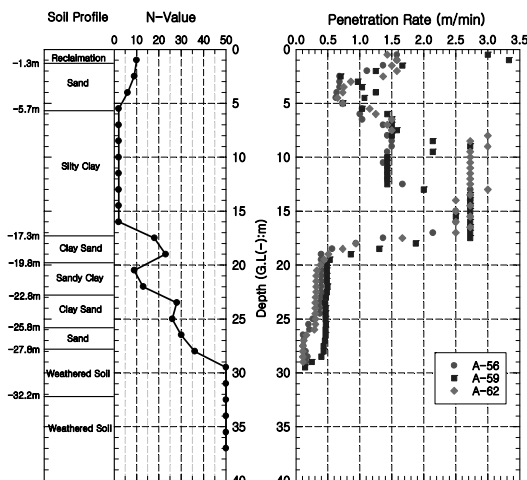


Fig. 13. Penetration rate (Type1 blade)

are equipped with a spiral auger and it facilitates a removal of the cuttings while penetrating into the ground. Special bits are attached to the bottom of Type 1 blade whereas special bits are attached to blade of the helical auger as well as to the bottom of Type 2 one.

4.3.3 Penetration Characteristics of Type 1 Blade

Based on trial constructions, penetration characteristics of Type 1 blade are presented in terms of penetration time and penetration rate in Figures 12 and 13.

Although the penetration characteristics of Type 1 blade were similar to those of a two-stroke conventional blade in the soft soils ($N = 0-4$ for clay, $N = 0-10$ for sand), the penetration time was reduced by about 10 minutes and also the penetration rate increased in the stiff layer ($N = 4-15$ for clay, $N = 10-30$ for sand). However, Type 1 blade was able to penetrate into the stiff layer such as dense sand ($N > 30$) and weathered soil layers where the conventional blade could not. As shown in Figure 12, the penetration rate was measured to be 0.3~0.5 m/min in the sand and the weathered soil layers ($N > 30$) and 0.1~0.3 m/min in the weathered soil layer with a N-value of greater than $N > 50$.

However, in the sand and the weathered soil layers with N-values of greater than 30, the penetration rate decreased below 0.5 m/min and the constructability was lowered.

4.3.4 Penetration Characteristics of Type 2 Blade

The penetration characteristics of Type 2 blade obtained from trial constructions are presented in Figures 14 and

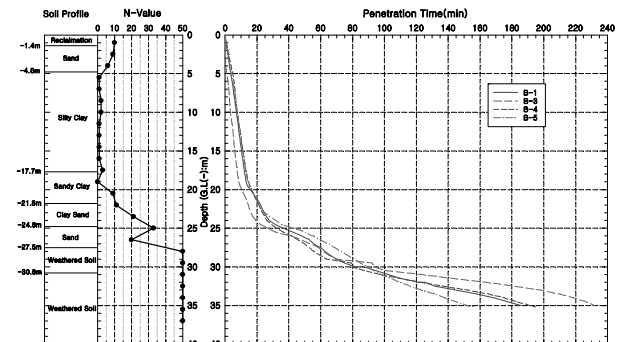


Fig. 14. Penetration time (Type 2 blade)

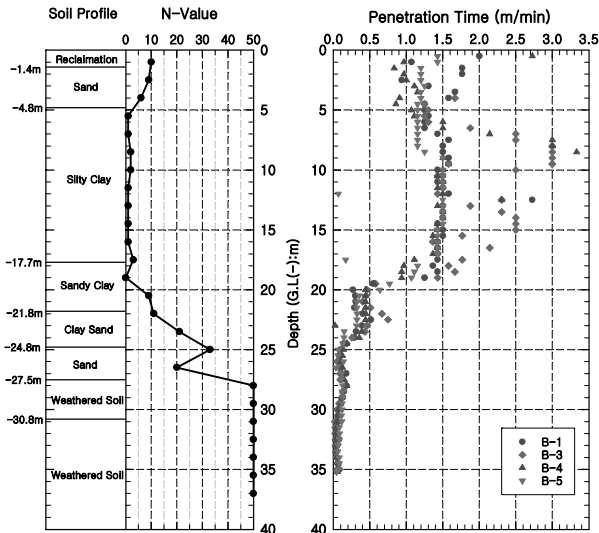


Fig. 15. Penetration rate (Type2 blade)

15. The penetration time of Type 2 blade was similar to that of Type 1 blade up to the depth of 28~29 m where N-value increases to about 50. Nevertheless, Type 2 blade could penetrate into the weathered rock layer ($N > 50$) where Type 1 blade could not. However, the penetration efficiency of Type 2 blade was lowered to 0.1~0.2 m/min in the weathered layer with a N-value of greater than $N > 50$.

4.4 Correlation of Penetration Characteristics

The penetration rates of various blades, measured from trial constructions, were analyzed based on N-value to evaluate the penetration characteristics of DCM equipment depending on soil type and their stiffness. Their correlations are presented in Figures 16 through 18. N-values of greater than 50/30 were converted to the number of blows for the 30 cm of penetration.

A correlation of penetration rate and N-value obtained from both Gimhae and Incheon areas is presented in Figure 16. As indicated in Figure 16, the penetration rate tends to decrease as the N-value increases.

After eliminating the converted N-value of greater than 100, a correlation of penetration rate and the converted N-value of soil layers to which the DCM method can be applied is presented in Figure 17. The penetration rate tends to decrease as the N-value increases. The scatter of correlation tends to decrease as the converted N-value

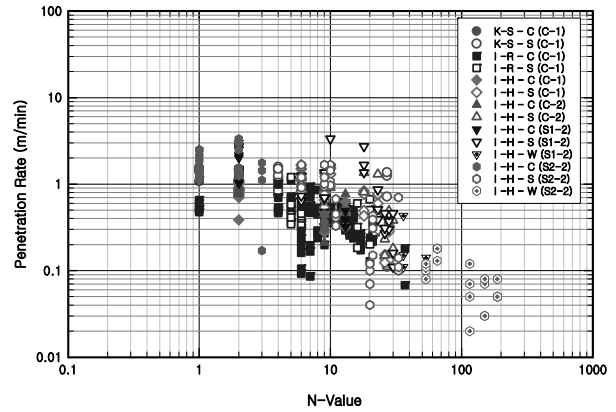


Fig. 16. N-value vs. Penetration rate

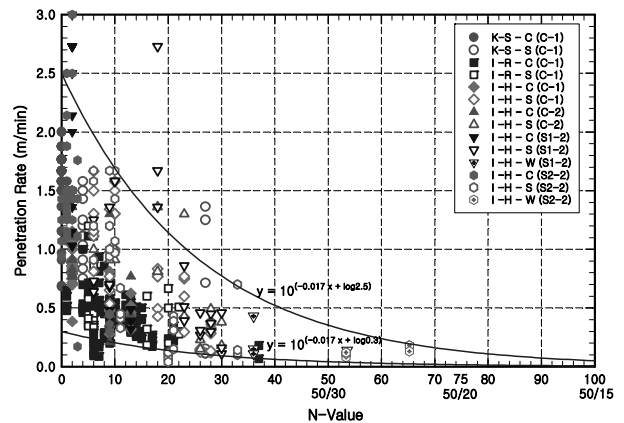


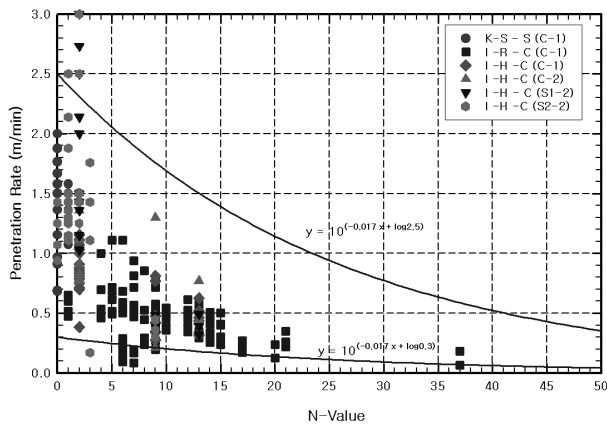
Fig. 17. Correlation of N-Value and Penetration rate (summary)

increases.

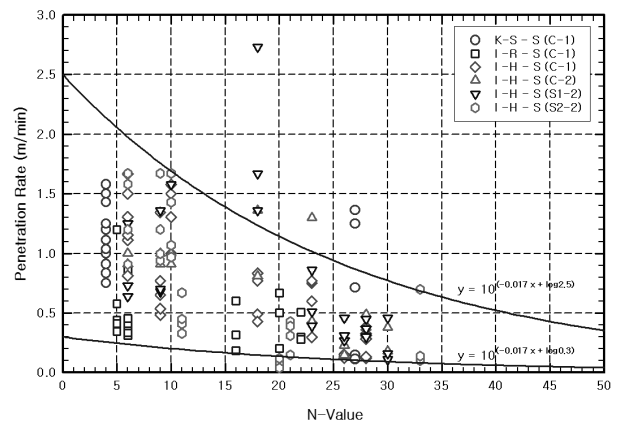
Figure 18 (a) shows a correlation of penetration rate and N-value in the clay layer. The penetration rate tends to decrease as the N-value increases. The average penetration rate was about 1.0 m/min for the N-value of 0~4 but it decreased to 0.50 m/min for the N-value of 4~15. The average penetration rate appeared to be slower than 0.3 m/min for the N-value of greater than 15.

A correlation of penetration rate and N-value in sand layer is shown in Figure 18 (b). The average penetration rate was 1.0 m/min for the N-value of 0~10 and it decreased to 0.5 m/min for the N-value of 10~30. For the N-value of greater than 30, the average penetration rate decreased below 0.3 m/min.

In Japan, a standard penetration rate of 1.0 m/min is established as a criterion to select a soil type where an application of DCM is possible. Based on Japanese criterion, DCM can be applied to clay soils with an N-value of less than 4 and to sandy soils with an N-value



(a) Clay



(b) Sand

Fig. 18. Correlation of N-Value and Penetration rate

of less than 8. Penetration rates obtained from trial constructions fall within Japanese criterion.

Penetration rates in the clay layer appeared to be slower than those in the sand layer which has a similar N-value.

5. Conclusions

Based on the case studies of penetration characteristics of mixing blades employed for the trial constructions of a self-supported DCM wall in Gimhae and Incheon areas, conclusions are as follows.

- (1) The penetration efficiency of a conventional mixing blade decreased in the stiff soil layer distributed over Incheon area and the conventional mixing blade could not penetrate into the stiff layer if the depth exceeds certain limit.
- (2) A spiral mixing blade revised to improve the penetration capability of DCM mixing tool can penetrate into the thick and stiff layer where the conventional blade can not. Penetration characteristics and economical efficiency should be considered to determine the critical depth of the spiral mixing blade because the penetration efficiency can decrease in the stiff layer.
- (3) Results of construction areas showed correlations of

penetration rate and N-value falls within a limited range. The penetration rates of mixing blades used in Korea may be similar to those in Japan.

- (4) The DCM method was developed to improve soft foundation soils or to build an earth retaining wall to support excavation works. The development of DCM, design strength and elastic modulus can be studied.

References

1. Jung, Doohoi, Jeong Gyunghwan et al., 2005. Characteristics of Self-Supported Counterfort Diaphragm Wall. ISOPE-2005 Seoul, Korea, 596~603
2. Jeong Gyung hwan, Kim Yongwan et al., 2006. Application for Self-Supported Retaining Wall Using Deep Cement Mixing. KGS Spring Conference 2006, Korea, 257~267. (in Korean)
3. Jeong Gyunghwan, Bae Jonggyeon et al., 2006. Study on Development of Special Rotary Wing of DCM in Hard Soil. Proceedings of Technical Committee on Dredging and Reclaiming, Korea Geotechnical Society, 2006, Korea, 193~200. (in Korean)
4. Yang Taeseon, Jeong Gyunghwan, Yeo Bonggu, Lee Sangsoo, 2000. A Study on Design Strength and Elastic Modulus using Deep Cement Mixing Method, Proceedings of Fall Conference of Korea Society of Civil Engineers, 2000, Korea, 193~200. (in Korean)
5. Broms, B. B., 1975, Lime Stabilization Column, Proceedings of the 5th Asian Regional Conference on Soil Mechanics and Foundation Engineering, 1975
6. Costal Development Institute of Technology, 2002, The Deep Cement Mixing Method(Principal Design And Construction), 2002 (in Japanese)

(received on Feb. 5, 2007, accepted on Mar. 10, 2007)

Evaluation of the Dynamic P-Y Curves of Soil-Pile System in Liquefiable Ground

액상화 가능성이 있는 지반에 놓인 지반-말뚝 시스템의 동적 p-y 곡선 연구

Han, Jin-Tae¹ 한 진 태
Kim, Sung-Ryul² 김 성 렬
Kim, Myoung-Mo³ 김 명 모

요 지

말뚝의 동적 응답 해석을 위한 다양한 방법들이 개발되어 있으며, 이 중에서 비선형 스프링, p-y 곡선을 이용하여 지반-말뚝 상호작용을 고려하는 방법이 널리 사용되고 있다. 그러나, 현재 사용되는 동적 p-y 곡선은 정적 또는 주기 하중에 의한 횡방향 재하 시험에 의해 개발되었다. 또한, p-y 곡선에 scaling factor를 도입하여 액상화에 의한 지반-말뚝 상호작용의 영향을 모사하고자 하는 시도가 이루어져 왔으나, 지금까지 정확한 scaling factor를 산정하지 못하고 있는 실정이다. 이에 본 연구에서는 1g 진동대 실험으로부터 구한 말뚝 주변 지반의 과잉간극수압과 지반-말뚝 시스템의 고유진동수 관계 및 수치해석으로부터 구한 말뚝 주변 지반의 탄성계수의 변화와 지반-말뚝 시스템의 고유진동수 관계로부터, 말뚝 주변 지반의 탄성계수의 변화로 표현되는 p-y 곡선의 scaling factor를 구하였다. 그 결과, scaling factor는 과잉간극수압비에 따른 지수 함수의 형태로 나타났다.

Abstract

Various approaches have been developed for the dynamic response analysis of piles. In one of the approaches, the soil-pile interaction is approximated by using parallel nonlinear springs, namely the p-y curves. Currently available p-y curve recommendations are based on static and cyclic lateral load tests. Other researchers have attempted to extend the p-y curves by incorporating the effects of liquefaction on soil-pile interaction and derived scaling factors of p-y curves to account for the liquefaction. However, opinions on the scaling factors vary. In this study, the scaling factors, which reflect the variation of the elastic moduli of surrounding soils, were established combining the relationship between excess pore pressures and the natural frequencies of a soil-pile system obtained from 1g shaking table tests and the relationship between the elastic moduli of surrounding soils and the natural frequencies of a soil-pile system obtained from numerical analyses. As a result, the scaling factors were presented in an exponential function.

Keywords : Excess pore pressure, Liquefaction, Natural frequency, Pile, Shaking table test

1. Introduction

Predicting the performance of pile foundations in

liquefying ground under earthquake loading is a complex problem requiring consideration of the inertial loads from the superstructure and the kinematic loads from the

1 Member, Post Doctoral Researcher, Engrg. Research Institute, Seoul National Univ., Seoul, Korea, jimmy76@snu.ac.kr, Corresponding Author

2 Member, Full-time Lecturer, Dept. of Civil & Environmental Engrg., Dong-A Univ., Busan, Korea

3 Member, Prof., Dept. of Civil Engrg., Seoul National Univ., Seoul, Korea

surrounding soil. Liquefaction changes these loads because of its influence on free-field soil response and soil-pile-structure interaction. Analyses and design procedures for piles in liquefying ground generally include large uncertainties due to the lack of physical data and the lack of correct understanding of the mechanism involved in the interaction phenomena. These uncertainties must be resolved for earthquake hazard remediation.

Various approaches have been developed for the dynamic response analysis of single piles. In one approach, the soil-pile interaction is approximated by using parallel nonlinear soil-pile (p-y) springs (Matlock, 1978). Currently available p-y curve recommendations (API, 1993) are based on static and cyclic lateral load tests. Other researchers have attempted to extend the recommended p-y curves by incorporating the effects of liquefaction on soil-pile interaction. The Architectural Institute of Japan (AIJ, 1988) and Japan Road Association (JRA, 1980) codes include the scaling factor, that is p-multiplier, of p-y curves to account for liquefaction. Liu and Dobry (1995) also suggested that the scaling factor from centrifuge tests would vary linearly with excess pore pressure ratio and Wilson (1998) found that appropriate p-multipliers were 0.10~0.20 for liquefying loose soil, and 0.25~0.35 for liquefying medium dense soil.

However, there is yet a variety of opinions on the

scaling factors. To obtain the exact scaling factors, it is necessary to evaluate the stiffness of the liquefying soil as a function the magnitude of excess pore pressure. Therefore, in this study, the variation of the natural frequency of the soil-pile system and the stiffness of the liquefying soil according to the magnitude of excess pore pressure were investigated by 1g shaking table tests and three dimensional FE analyses.

2. Test Program

A series of shaking table model tests were performed to evaluate the dynamic characteristics of a soil-pile system. The dimensions of the soil box were 100 x 44 x 60 cm (length x width x height), and the soil box was made of transparent acrylic plates. Figure 1 shows the test section of the model and the locations of the measurement instruments. The model pile was made of a steel plate and was installed with 7 strain gauges, 2 LVDTs, 6 pore pressure transducers, and 7 accelerometers. The dimensions of the model pile were 60 x 4 x 600 mm (width x thickness x length). And the flexural rigidity (EI) of the model pile was calculated by using the result of one(-) point loading test. Jumoonjin sand was used as the model soil, which is typical clean uniform sand in Korea. The effective grain size, D10, was 0.38 mm and the

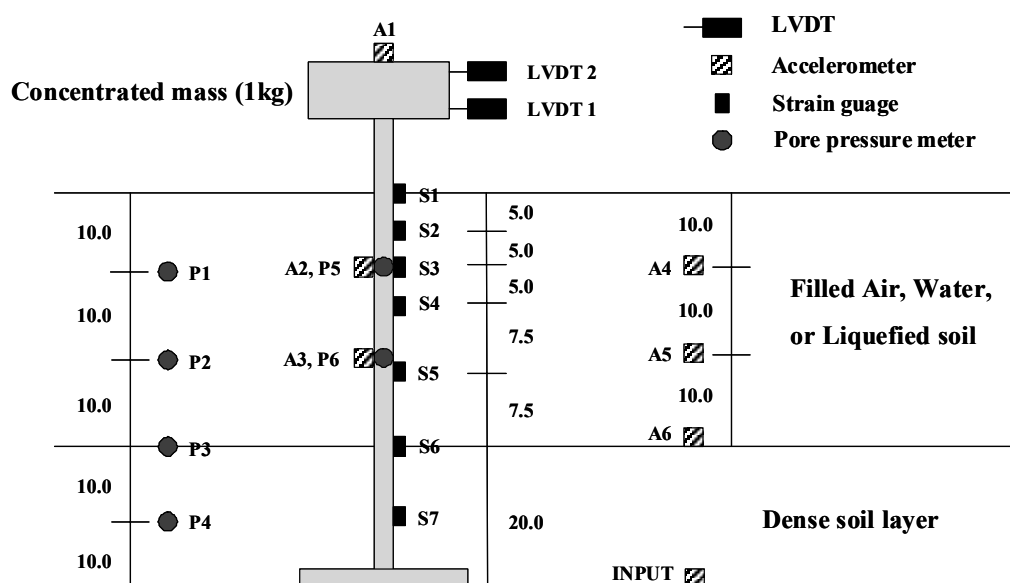


Fig. 1. Test section

coefficient of uniformity was 1.58. The maximum and minimum dry unit weights were 15.99 kN/m³ and 13.05 kN/m³, respectively.

Table 1 summarizes the test program used in this study. The shaking table tests were classified into different cases depending on the fill materials in the upper part of the model box. The materials were either air (case 1), water (case 2), or liquefiable soil (case 3). And three different types of tests were performed on the model pile, whose upper part was surrounded by liquefiable soil. In the first test, input acceleration of small amplitude was applied to prevent liquefaction in the soil (case 3a). In the second test, large input acceleration was applied to induce liquefaction in the soil (case 3b). In the third test, a small input acceleration was applied to re-shake the liquefied model system of case 3b (case 3c). The liquefiable layer of 30 cm was prepared by water sedimentation method in every frequencies and the resulting relative density of the soil was about 20% (case 3b). The bottom foundation layer of 20 cm was prepared by pre-shaking the soil. The resulting relative density of the soil was about 80%. Sinusoidal waves of various amplitudes and frequencies were used to produce the input base motions.

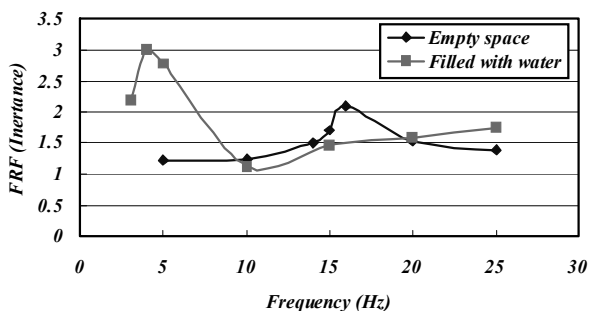
3. Test Results

Hwang (2004) previously performed shaking table tests to determine the natural frequency of a liquefied quay wall system using a random wave as input motion. However, the tests were not successful because the excessive pore pressure did not increase to the liquefaction level under the moderate amplitude of random wave acceleration. Thus, sine waves were used in this study.

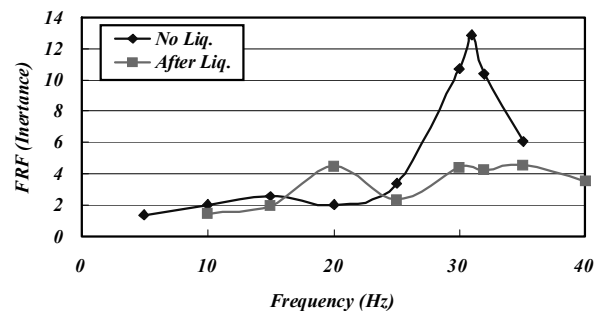
Figure 2 shows the acceleration FRF (Frequency Response Function= Fourier amplitude of upper acceleration / Fourier amplitude of input acceleration) of the soil-pile system for each case of the tests, except case (3b). Acceleration FRF is defined as the pile top acceleration divided by the input base motion for corresponding frequencies, and the 1st natural frequency f_n is taken as the frequency corresponding to the first peak value of FRF. In case (3b), the natural frequency could not be evaluated by FRF because the natural frequency varied with the magnitude of the excess pore pressure in the surrounding soil of the pile. Therefore, the natural frequency in case (3b) was determined differently. Figure 3 shows the excess pore pressure ratio at the center of the liquefiable soil with time and shows the acceleration

Table 1. Test program

Cases	Pile environment (upper layer : 30 cm)	Amplitude of input acc. (g)	Frequency of input acc. (Hz)	Remark
1	Empty space	0.1	5, 10, 14, 15, 16, 17, 20, 25	–
2	Filled with water	0.1	3, 4, 5, 10, 15, 20, 25	–
3a	Filled with liquefiable soil	0.015	5, 10, 15, 20, 25, 30, 31, 32, 35	No liquefaction occurred
3b		0.2	3, 4, 5, 6, 10, 15, 20	Liquefied
3c		0.015	10, 15, 20, 25, 30, 32, 35, 40	Retested after liquefaction



(a) Empty space (Case 1), filled with water (Case 2)



(b) No liquefaction (Case 3a), After liquefaction (Case 3c)

Fig. 2. FRF of soil-pile system

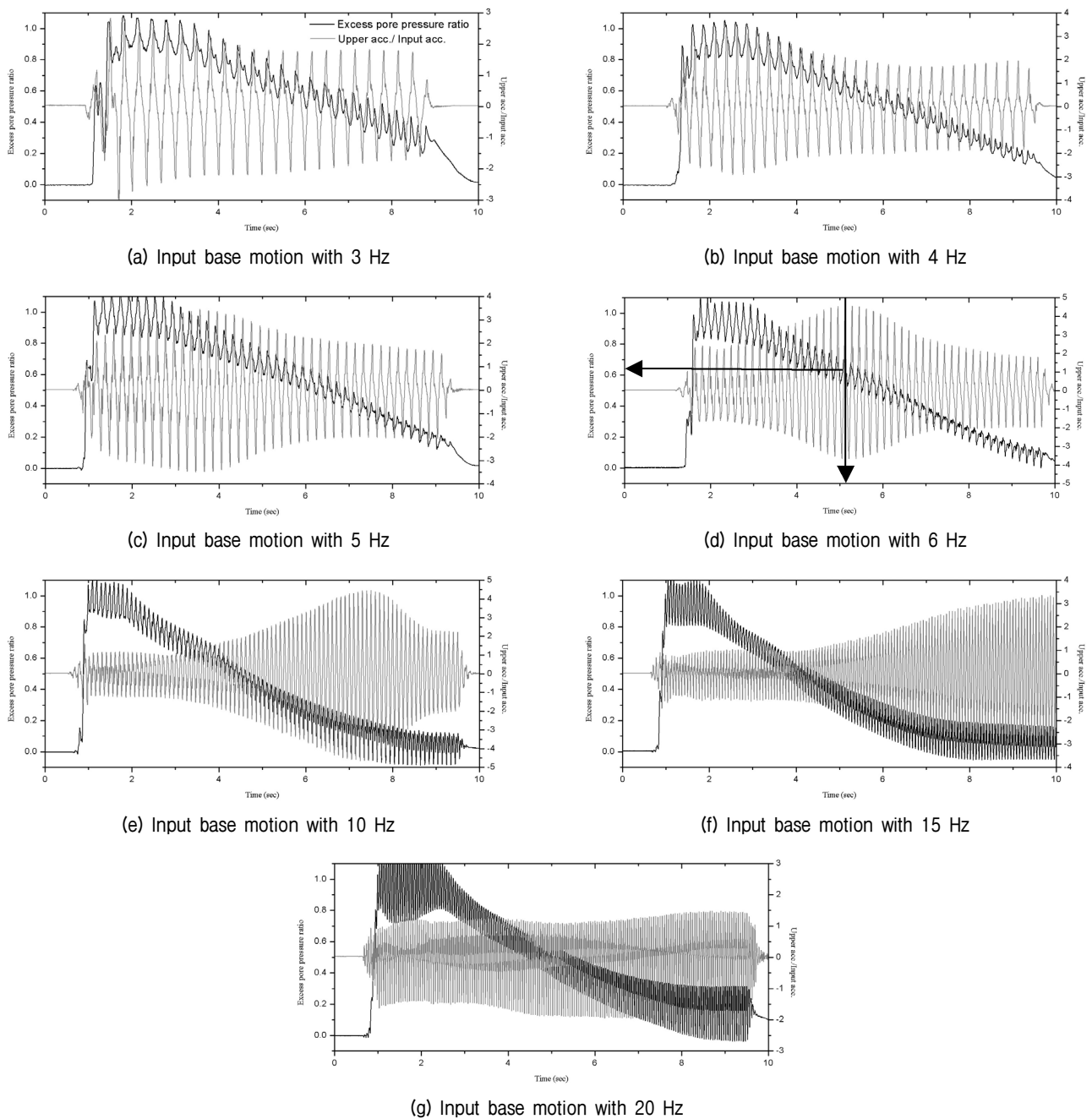


Fig. 3. Excess pore pressure ratios vs. acceleration amplification ratio (case 3b)

amplification ratio with time, which is the ratio of pile top acceleration to the input base motion. As shown in Figure 3, when the frequencies of the input base motion were 3 and 4 Hz, the pile top acceleration amplified greatly during liquefaction (i.e., when the excess pore pressure ratio was about 1.0). Thus, it can be said that the natural frequencies of the soil-pile system during liquefaction are around 3 to 4 Hz. From Figure 3, the natural frequency of the soil-pile system can be determined for various excess pore pressure ratios by correlating the maximum

acceleration ratio with the magnitude of excess pore pressure ratio for each input acceleration frequency. For example, as shown in Figure 3(d), in the case of 6 Hz, when the acceleration amplification ratio is peak, the time is 5.2 sec and the excess pore pressure ratio is 0.65 at this time. Therefore, when the excess pore pressure ratio is 0.65, the natural frequency of the soil-pile system is 6 Hz. Figure 4 shows the variation of the natural frequency of the soil-pile system according to the excess pore pressure ratio, which is the ratio of the excess pore

Table 2. The natural frequency of soil-pile system

Type (Case No.)	Empty space (1)	Filled with Water (2)	No Liq. (3a)	Filled with liquefiable soil Liquefaction (3b)	After Liq. (3c)
N.F. (Hz)	16	4	15	3~4	20

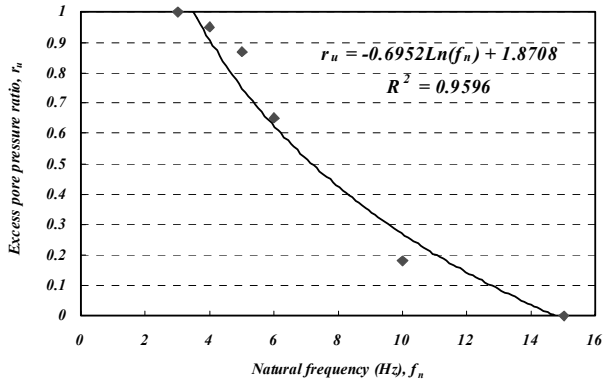


Fig. 4. Natural frequencies of soil-pile system vs. excess pore pressure ratio of surrounding soil (case 3b)

pressure to the vertical effective stress, obtained from Figure 3. It is seen in Figure 4 that the natural frequency of the soil-pile system increases as the excess pore pressure ratio decreases.

The natural frequencies of all cases are summarized in Table 2. The natural frequency of the soil-pile system in case (1) was 16 Hz and in case (2), 4 Hz. In the case of liquefiable soil, the natural frequency was 15 Hz before liquefaction, 3 to 4Hz during liquefaction, and 20 Hz after liquefaction. The natural frequency during liquefaction was similar to that of case (2). This result confirms that the liquefied soil behaves like water. After liquefaction, the natural frequency became larger than that of the no-liquefaction case (3a) probably by the increase of the stiffness due to the densification of the soil during liquefaction.

4. Numerical Analysis

The elastic modulus of the pile surrounding soil of various excess pore pressure ratios, thus, of a pile-soil system with various natural frequencies was calculated by three dimensional FE analyses with a commercial program ABAQUS (1998). In the FE analysis, the model pile and surrounding soil were modeled as an elastic continuum, and the soil-pile system was assumed to be undamped.

Table 3. Input parameters of model pile and surrounding soil for FE analysis

Input parameter	Pile (steel)	Surrounding soil
Elastic modulus	200 GPa	Variation
Poisson's ratio	0.3	0.33
Mass density	7700	1860

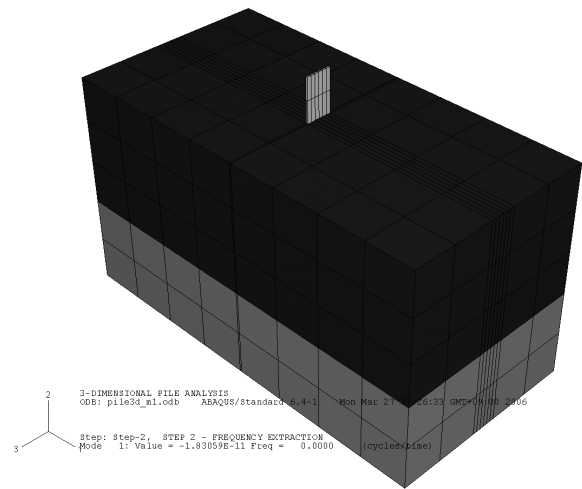


Fig. 5. Mesh for FE analysis of soil-pile system

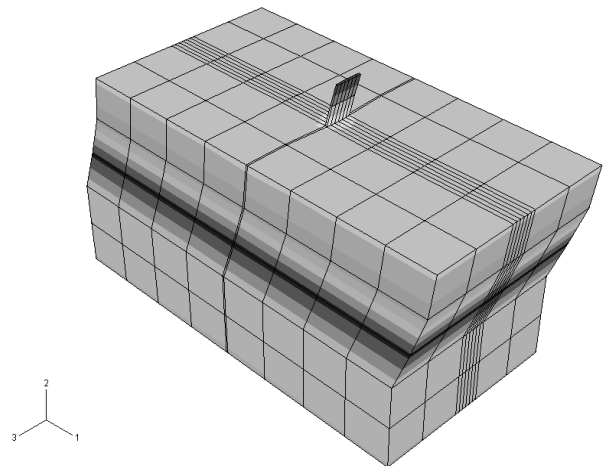


Fig. 6. 1st mode shape of soil-pile system

Important parameters affecting the natural frequency of a soil-pile system are the mass density, elastic modulus and Poisson's ratio of the model pile and the surrounding soil. Input parameters for the numerical analysis are summarized in Table 3. The typical values of the elastic modulus and Poisson's ratio of steel were selected for

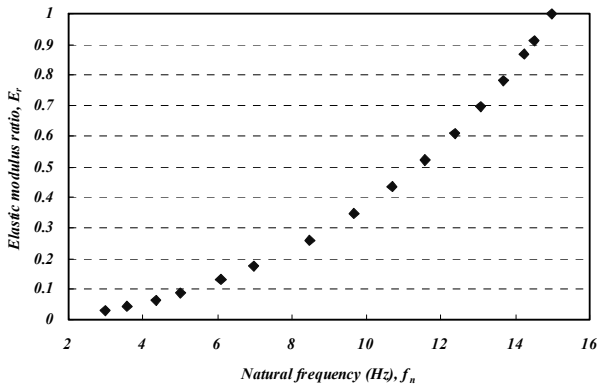
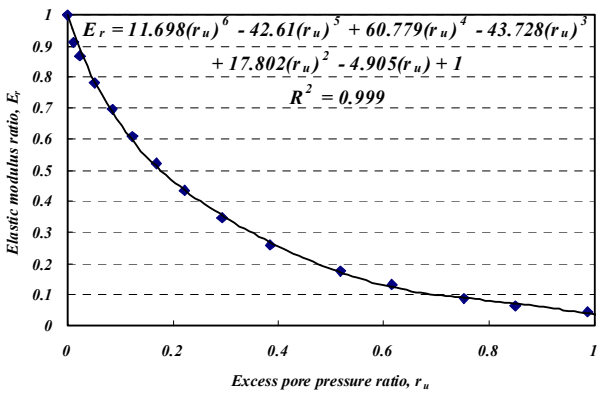
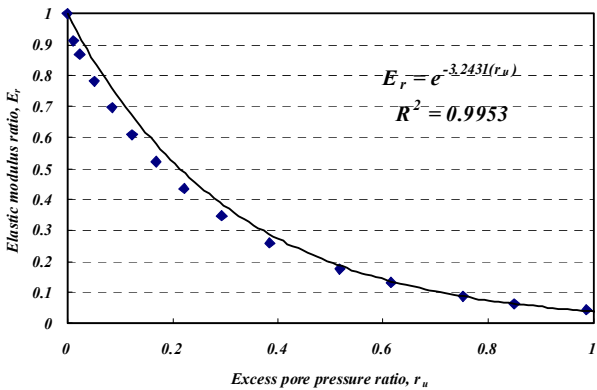


Fig. 7. Elastic modulus ratios of surrounding soil vs. natural frequencies of soil-pile system



(a) Fitting to sixth order polynomial



(b) Fitting to exponential function

Fig. 8. The elastic modulus ratio vs. the excess pore pressure ratio of surrounding soil

the model pile. The mass density of the surrounding soil was the value of saturated Jumoonjin sand. The Poisson's ratio of the surrounding soil was assumed to be 0.33. Figure 5 shows the mesh for the FE analysis. Figure 6 shows the deformed shape of the 1st mode of the soil-pile system.

The natural frequency of the soil-pile system was 15

Hz when the excess pore pressure ratio was zero, and the natural frequencies of the soil-pile system during liquefaction were around 3 to 4 Hz.

From FE analyses, the elastic modulus of the surrounding soil was estimated for the soil-pile system of natural frequencies between 3 and 15 Hz. The results are shown in Figure 7. In this figure, elastic modulus ratios, which are the ratios of respective elastic modulus of surrounding soil of the various states to the soil's elastic modulus of the soil-pile system with the natural frequency of 15 Hz, are plotted against the natural frequencies.

If the natural frequency values in Figure 7 are replaced by the excess pore pressure ratios using the correlation established in Figure 4, an elastic modulus ratio vs. excess pore pressure ratio curve is obtained, as shown in Figure 8. After all, the variation of the elastic moduli of surrounding soils reflects the scaling factor of p-y curve to account for the liquefaction. Two different regression lines are shown in the figures. For easy application in practice, the exponential function correlation (Equation (1)) is recommended.

$$E_r = e^{-3.2431(r_u)} \quad (1)$$

where, E_r : elastic modulus ratio

r_u : excess pore pressure ratio

5. Conclusions

From 1 g shaking table tests, the empirical relations between the excess pore pressures mobilized in a soil ground and the natural frequencies of a soil-pile system were established. From numerical analyses, the relations between the elastic moduli of the soil ground and the natural frequencies of the soil-pile system were also established. Combining these two relations, the relations between the elastic modulus ratios, that is, the scaling factors of p-y curves to account for the liquefaction, and the excess pore pressures of the soil ground were obtained as an exponential function. In pseudo-static analysis, the lateral resistance of liquefied soil is represented as a scalar multiple of its static drained lateral resistance and these scaling factors. Even if the specific results may only apply

to the model system tested in this study, they have much potential, because a methodology has been established to find such a correlation, which will be essential for predicting the scaling factors of p-y curves to account for the mobilization of excess pore pressures in soil-structure interaction problems.

References

1. ABAQUS. User's Manual – Standard version 5.7, Hibbitt, Karlsson and Sorenson, Inc., 1998.
2. American Petroleum Institute (API). Recommended Practice for Planning, Designing and Constructing Fixed Offshore Platforms – Working Stress Design, API Recommended Practice 2AWSD (RP 2A-WSD), 20th edition, 191p., 1993.
3. Architectural Institute of Japan (AIJ). Recommendations for design of building foundations, 1988 (in Japanese).
4. Hwang, J. I. (2004), "Behavior of piles subjected to flow of liquefied soil and verification of similitude law for 1g shaking table tests", Ph. D. dissertation, Seoul National University, Korea.
5. Japan Road Association (JRA). Specifications for highway bridges, 1980 (in Japanese).
6. Matlock, H., Foo, S.H., and Bryant, L.L. (1978), "Simulation of lateral pile behavior", *Proc. Earthquake Engineering and Soil Dynamics*, ASCE, 600-619.
7. Liu, L. and Dobry, R. (1995), "Effect of liquefaction on lateral response of piles by centrifuge model tests", *National Center for Earthquake Engineering Research (NCEER) Bulletin*, 9(1), January, 7-11,
8. Wilson, D.W. (1998), "Soil-pile-superstructure interaction in liquefying sand and soft clay", Ph. D. dissertation, University of California at Davis, USA.

(received on Feb. 20, 2007, accepted on Mar. 20, 2007)